

OPTICAL STUDIES OF
INSECT FLIGHT AT LOW ALTITUDE

by
Michael John Farmery

A thesis submitted to
the University of York for
the degree of Doctor of Philosophy

Department of Physics

March 1981

CONTENTS

		<u>Page</u>
ACKNOWLEDGEMENTS	vi
DECLARATION	viii
ABSTRACT	ix
INTRODUCTION	x
<u>CHAPTER 1</u>	<u>BACKGROUND</u>	1
1.1	THE IMPORTANCE OF INSECT PEST CONTROL FOR WORLD FOOD PRODUCTION ..	1
1.2	THE ROLE OF INSECT FLIGHT IN RELATION TO PEST CONTROL ..	5
1.3	THE APPLICATION OF RADAR TO THE STUDY OF BIRD AND INSECT FLIGHT ..	6
1.4	THE LIMITATIONS OF THE RADAR TECHNIQUE FOR INSECT FLIGHT STUDIES ..	8
1.5	A NEW SYSTEM TO SUPPLEMENT THE RADAR TECHNIQUE ..	10
1.6	REQUIREMENTS FOR THE NEW SYSTEM	13
1.7	DESIGN CONSTRAINTS ON THE PROPOSED SYSTEM	13
1.8	CONCLUSIONS	14
<u>CHAPTER 2</u>	<u>THEORETICAL EVALUATION OF PROPOSED SYSTEM</u>	16
2.1	INTRODUCTION	16
2.2	PRINCIPLES OF OPERATION ..	16
2.3	SIGNAL AND NOISE CONSIDERATIONS	17
2.3.1	Ratio of Transmitted to Received Power	17
2.3.2	Noise at the Receiver ..	22
2.3.3	Transmitter Requirements ..	29

<u>CHAPTER 2</u>		<u>Page</u>
2.4	SAMPLE VOLUME	32
2.4.1	Alignment and Choice of Field of View	32
2.4.2	Calculation of Volume of Air Sampled	34
<u>CHAPTER 3</u>	<u>SOURCE-DETECTOR COMBINATION</u> ..	40
3.1	INTRODUCTION ..	40
3.2	DEFINITION OF TERMS RELATING TO DETECTOR CHARACTERISTICS ..	40
3.2.1	Dark Current	40
3.2.2	Spectral Responsivity ..	41
3.2.3	Quantum Efficiency ..	41
3.2.4	Noise Equivalent Power ..	41
3.2.5	Detectivity	42
3.2.6	Specific Detectivity ..	42
3.3	DETECTORS OF NEAR INFRA-RED RADIATION	43
3.3.1	Photoconductive Devices ..	43
3.3.2	Photovoltaic Devices ..	44
3.3.3	Photoemissive Devices ..	45
3.4	SOURCES OF NEAR INFRA-RED RADIATION	48
3.4.1	Conventional Sources ..	48
	(a) Tungsten filament lamps ..	48
	(b) Arc lamps	51
	(c) Xenon flash tubes ..	52
3.4.2	Laser Sources	53
	(a) Neodymium - Yag Lasers ..	53
	(b) Gallium-arsenide semiconductor lasers	53
	(c) Ruby lasers	54
3.5	CONCLUSIONS	55

	Page
<u>CHAPTER 4</u> <u>DESCRIPTION OF OPERATIONAL SYSTEM</u>	59
4.1 BACKGROUND 	59
4.2 RECEIVERS 	60
4.2.1 Mark I (Single Channel) ..	60
4.2.2 Mark II (Two Channel) ..	62
4.3 TRNASMITTER 	64
4.4 OPERATIONAL SYSTEM ..	65
4.5 CALIBRATION METHODS ..	68
4.5.1 Receiver Performance ..	69
4.5.2 Transmitter-Receiver Alignment ..	70
4.5.3 Transmitter Performance ..	70
4.5.4 Instrumentation Recorder Tape Speed	71
 <u>CHAPTER 5</u> <u>DATA ANALYSIS</u>	 73
5.1 DESCRIPTION OF TYPICAL SIGNALS ..	73
5.2 CALCULATION OF AERIAL DENSITY ..	75
5.3 WING BEAT FREQUENCY MEASUREMENTS	79
5.4 CALCULATION OF TARGET SPEED AND DIRECTION	82
5.5 TOWARDS AUTOMATIC IN-FIELD DATA ANALYSIS	85
 <u>CHAPTER 6</u> <u>LABORATORY STUDIES</u> ..	 87
6.1 TETHERED FLIGHT EXPERIMENTS ..	87
6.1.1 Background 	87
6.1.2 Variation of Wing Beat Frequency With Wing Length 	87
6.1.3 Wing Beat Frequency as an Aid to Species Identification 	90
6.1.4 Variation of Received Signal with Relative Position of Transmitter, Insect and Receiver	91

<u>CHAPTER 6</u>	<u>Page</u>
6.2 POLARISATION EFFECT ..	92
6.3 COMPUTER SIMULATION OF RECEIVED SIGNALS	95
6.3.1 Scattering and Reflectivity Properties of Insect Wings	95
6.3.2 Computed Model of Flapping Flight	97
6.4 VARIATION OF RESPONSIVITY ACROSS A PHOTOMULTIPLIER PHOTOCATHODE ..	101
 <u>CHAPTER 7</u> <u>FIELD STUDIES</u>	 104
7.1 REVIEW OF FIELD WORK UNDERTAKEN	104
7.1.1 Background	104
7.1.2 Armyworm Studies, Kenya, March - April 1978	104
7.1.3 Grasshopper Studies, Mali, September - November 1978	108
7.1.4 Armyworm Studies, Kenya, March - April 1979	110
7.1.5 Armyworm Studies, Kenya, February-April 1980	113
7.2 RESULTS FROM INSECT SPEED AND DIRECTION MEASUREMENTS	115
7.3 RESULTS FROM FIELD STUDIES ..	116
7.3.1 Aerial Density Measurements ..	116
(a) Low altitude density profile ..	116
(b) General pattern of armyworm activity at low altitude ..	117
(c) Meteorological effects ..	119
7.3.2 Wing Beat Frequency Measurements ..	120
(a) Effect of temperature on wing beat frequency	120
(b) Identification	123
(c) Wing beat frequency as a function of wing length	124
7.3.3 Aggregation of Armyworm Moths in Trees	125
7.3.4 Post Dusk Take Off "Descending Flight"	127
7.4 CONCLUSIONS	131

		<u>Page</u>
<u>CHAPTER 8</u>	<u>CONCLUSIONS AND FURTHER PROSPECTS</u>	134
 <u>APPENDICES</u>		
<u>APPENDIX A</u>	<u>CIRCUIT DIAGRAMS</u>	
A1	Photomultiplier Tube Dynode Chain and Current Amplifier Circuitry. ..	I
A2	Photodiode Current Amplifier Circuitry (Photovoltaic Configuration) ..	II
A3	Automatic EHT System ..	III
A4	Counter System ..	VII
A5	Calibration Frequency Unit ..	IX
<u>APPENDIX B</u>	<u>RECORDER NOISE</u> ..	XI
<u>APPENDIX C</u>	<u>COLLECTED DATA</u> ..	XV
C1	Mali 1978 ..	XVI
C2	Kenya 1979 ..	XVII
C3	Kenya 1980 ..	XIX
C4	Kenya 1978 ..	XXIII
<u>APPENDIX D</u>	<u>LOW LEVEL RADIOMETER</u> ..	XXV
<u>APPENDIX E</u>	<u>DESIGN STUDY FOR MODULATED TRANSMITTER</u>	XXXIII
<u>REFERENCES</u>	137

ACKNOWLEDGEMENTS

I would first like to express my sincere gratitude to my supervisor Professor O.S. Heavens, whose tremendous initial enthusiasm for the work has never wavered.

The project would not have been possible without the support of my co-sponsors: the Agricultural Aviation Research Unit (AARU) of Ciba-Geigy (UK) Ltd. and the Centre for Overseas Pest Research (COPR). I am very grateful to the many people from both organisations who have helped in different ways. In particular I am indebted to Professor R.J.V. Joyce of AARU for his help and encouragement in setting up the project.

The close collaboration with the COPR radar group has been especially enjoyable and I thank Dr. J.R. Riley, Dr. D. Reynolds and Mr. A. Smith for their companionship and assistance in the field and many useful discussions.

In Kenya I received valuable logistic assistance from the COPR Armyworm team. I am particularly indebted to Derek Rose and his family for their kind hospitality. Thanks also go to the Kenyan Agricultural Research Institute and the Desert Locust Control Organisation for East Africa for the use of their facilities.

The technical staff at York have been very helpful particularly in their quick response to rather tight deadlines. I am especially grateful to Mr. L. Jarvis and Mr. I. Wright for their skill and ingenuity in the construction of the equipment. Special thanks go to Mrs. Pirozek for her first class typing and to Mr. A. Gebbie for his photographic work. I have also had the pleasure of secretarial assistance (particularly just prior to field projects)

from Ms. Christine Upton.

I am extremely grateful to Dr. J.R. Riley for his unfailing moral support, constructive criticism and stimulating conversation both in England and overseas.

Finally I would like to thank my family for their continual encouragement and inspiration.

DECLARATION

The original idea for the project was suggested by the candidate.

The results presented in Section 7.3 for the 1979 Armyworm project are contained in a comprehensive joint radar-optical report on that project.

The rest of the thesis, excluding the construction of the mechanical parts of the optical system, was the work of the candidate.

List of publications

Riley J.R., Reynolds D.R. and Farmery M.J., (1981)

Radar observations of spodoptera exempta, Kenya 1979
COPR Miscellaneous Report No. 54, 1981.

ABSTRACT

The use of radar for the study of insect flight is described and the two major limitations of the technique are identified, namely low altitude coverage and target identification.

A solution in the form of an optical system which is capable of measuring insect aerial density, speed and direction of flight and wing beat frequency up to 30 m above ground level (AGL) is described.

A computer simulation of the signal received from a flying insect is shown to agree with laboratory measurements. Possible methods for measuring insect orientation and discriminating between moths and grasshoppers are deduced.

The potential of the optical system is illustrated by a selection of results from a joint radar-optical field study of the flight behaviour of the African Armyworm Moth (*spodoptera exempta*). In particular, the density and size structure of the aerial population in the range 10 - 30 m AGL are shown to be similar to those observed by the radar at 70 m AGL, whereas activity at ground level is seen to follow a different pattern, which is closely related to the emergent behaviour of the moth. Field results are also presented which suggest strongly that the wing beat frequency of armyworm moths is dependent on ambient air temperature.

INTRODUCTION

The growing world population is placing an increasingly heavy demand on world food production. There is therefore considerable pressure on the agricultural community to reduce crop losses due to depredations of insect pests. Unfortunately traditional pest control strategies are often unsuccessful because they fail to take account of insect mobility.

Radar studies have made a valuable contribution to the understanding of the role of insect flight in the population dynamics of some insect pests. However, the considerable potential of radar for this work is limited in two areas, namely low altitude coverage and species identification. A solution was proposed in the form of an optical system capable of supplementing the radar observations. No such system was known to exist and, in fact, optical methods have found little application in the study of insect flight, a surprising fact when their wide use in remote sensing and short range tracking is considered.

The performance of a suitable system has been analysed by calculating the transmitter power requirements for a specified signal-to-noise ratio at the receiver, for different types of detector. The resulting design criteria were used to select components which were suitable for the purpose on both technical and practical grounds.

The development of the prototype into an operational system

was made using experience gained on field trials. The system has found most application in a combined radar-optical study of the flight of the African Armyworm Moth (spodoptera exempta). For such a study, low altitude observations were of special importance, since both long range flight and local flight are involved. Local flight can be observed only using the optical system and so a complete account of the migration behaviour could be obtained only by the combination of optical and radar methods.

The results obtained have demonstrated the value of the optical system both in supplementing the radar observations and as an entomologically useful tool in its own right. In particular, the results show the aerial density profile of Armyworm Moths at an outbreak site to be reasonably constant from 10 m above ground level (AGL) to the minimum height accessible to the radar (70 m AGL). It is therefore fair to assume that the activity detected by the radar is typical of that below its minimum operating height. Comparison of the radar derived wing beat frequencies with those obtained by the optical system from moths which had been visually confirmed to be Armyworm has helped considerably to identify behaviour attributable to Armyworm. On most occasions the size structure of the airborne population was found to be effectively constant with height in the 10 - 70 m AGL range.

In its own right the optical system has produced valuable field results to support the accumulating laboratory data which indicate strongly that the wing beat frequency in small moths is dependent on the ambient air temperature.

The signal received from a flying insect has been studied in the laboratory and has been found to be dependent on the aspect of the insect presented to the receiver. A polarisation effect has been noted which offers a possible method for discriminating between moths and grasshoppers. Both of these effects are now understood as a result of a computer simulation of flapping flight.

Throughout the development of the system emphasis has been placed on affecting a balance between technical sophistication and operational reliability. The result is considered to be a useful entomological tool.

CHAPTER I

BACKGROUND

1.1 THE IMPORTANCE OF INSECT PEST CONTROL FOR WORLD FOOD PRODUCTION

"For a nation has come up against my land
powerful and without number;
Its teeth are lions teeth,
and it has the fangs of a lioness.

It has laid waste my vines
and splintered my fig trees;
It has stripped off their bark and thrown it down,
their branches are made white."

The Devestation of Locusts.

(Joel, Chap. 1, vs 6 - 7)

The locust is probably the most widely known and sensational insect pest. The damage that it causes is legendary. A large swarm can cover an area of over 100 Km², have a total mass in excess of 80,000 tonnes and consume its own weight in vegetation each day, (Baron, 1972).

The locust plague is not a modern phenomenon. The Eighth Plague of Egypt described in Exodus is presumed to have visited that country 3,500 years ago. However the recent resurgence in activity during the period 1940 - 1960 inspired a large research effort into the forecasting and control of locust plagues. As a result internationally funded organisations were established which continue to monitor their activity and apply the control methods developed, where appropriate, (e.g. in East Africa, the Desert Locust Control Organisation (DLCOEA); in West Africa, the Organisation Commune de

Lutte Antiacridienne et de Lutte Antiaviaire (OCLALAV)). The destructive power of a large locust swarm is enormous. In 1954 in the Sous Valley of the Moroccan Atlas Mountains the entire citrus fruit crop valued at £4½ million was destroyed, (Baron, 1972). However, because the infestations are sporadic and often occur in areas of poor agricultural yield, their effect on world food production is not as great as their reputation might suggest.

There are many less known insect species which have until now existed undisturbed. It is only because of increased world demand for food and agricultural products that man has now to compete with them. For example in the coniferous forests of Eastern North America the larvae of the Spruce Budworm Moth (Choristoneura Jumiferana) cause considerable damage to mature trees. There is evidence to suggest that outbreaks of this insect have constituted a regular part of the cycle of forest regeneration since at least 1770 (Morris, 1963), and it is likely that it was man's very efforts to protect the forests from attack that has caused the major control problems there (Miller, 1971).

We can see the importance of losses to insect pests most dramatically in relation to world demand for food. The world population is at present approximately 4 billion, with an annual growth rate of 2%. It has been projected by demographers that the world population will rise to 6 - 7 billion by the year 2000 and to 10 - 16 billion by 2100 (NAS, 1975). Assuming no change in the amount of available arable land, this would result in a reduction of the world per capita arable land from 0.38 hectares to 0.1 hectares.

Which can be put into perspective by considering that the average diet in the United States is provided from about 0.62 hectares per capita (Pimentel and Pimentel, 1978).

It can be argued that the increase in available food supplies through the use of improved technology has been a major cause of the rapid increase in population (Malthus, 1798). Morally, however, it seems necessary to continue to increase world food production to alleviate the widespread malnutrition in the hope that in the meantime an effective method for limiting world population growth can be found.

There are several ways of increasing world food production including (a) the improvement of the intrinsic crop yield through development of new high yield hybrid crops, (b) the creation of new arable land through such schemes as irrigation and (c) the reduction of crop losses to pests.

Irrigation schemes have been successful although their cost is high in economic, social and environmental terms. Their use is limited and certainly offers no realistic prospects of doubling the available arable land (Pimentel and Pimentel, 1978).

New varieties of crops bred especially for their high yield have improved production in some areas but their advantages have often been offset by the need for sophisticated fertilizers and by their increased vulnerability to attack by pests. Continued progress however can be expected in this direction.

In this work I shall concern myself with the reduction of crop losses due to pests, particularly insect pests. Post harvest crop losses due to micro-organisms, insects and rodents have been

estimated to range from 9% in the United States (USDA, 1965) to 20% in some of the developing nations especially in the tropics. If pre-harvest and post-harvest losses are added together then total food losses due to pests amount to 45% (Pimentel and Pimentel, 1978). Total losses attributable to insects alone are likely to be about 15 - 30% (Cramer, 1967).

The impact of insect pests on world food production has been well illustrated by considering the example of rice, which is the world's most important crop (staple diet for over 2 billion people) (Smith and Calvert, 1978). They calculate that in India where there is inadequate crop protection the rice crop losses amount to 36% whereas in Japan which uses "maximum" insect pest control measures the corresponding loss is only 2%. If India could achieve the Japanese yields then her production would be sufficient for twice the population of South East Asia.

Clearly dramatic improvements in food production can be achieved by properly designed insect pest control programmes and through their implementation many areas could become self sufficient in food production. However as we shall see in the next section simplistic approaches to protecting crops often do not work. Considerable care must be taken to prevent the enthusiasm for insect control from causing economic and environmental disaster.

1.2 THE ROLE OF INSECT FLIGHT IN RELATION TO PEST CONTROL

The relationship between pest control and insect flight is extremely complex and its proper consideration is beyond the scope of this work. For a comprehensive evaluation the reader is referred to Joyce (1976). In what follows I shall briefly describe the important issues which have been raised.

Conventional agricultural pest control has traditionally assumed that insect pests are immobile (Headley, 1972) and economic entomologists have adopted a purely empirical approach to crop protection. They have applied a regulator (usually a chemical pesticide) and have been concerned only with its effect on the final crop yield, without monitoring intermediate effects such as the mortality rate of the pests involved. The concepts of adaptive dispersal (synonymous with migration) developed by Johnson (1960, 1963, 1966, 1969) have had little effect on the control methods used. In the past insect control has been considered to be the individual farmer's responsibility. He has been forced by economics to adopt the cheapest method of control (usually a pesticide) regardless of its wider consequences. Unfortunately because insects can move about pesticides affect insects which originate beyond the treated fields, an effect which has been a common cause for conflict between environmentalists and pesticide users. Insect mortality can also seriously reduce the effectiveness of a pesticide, since redistribution of an imperfectly controlled population can completely nullify the original control effort.

Many insect pest species engage in flight activity at some

time during their life cycle, often as young adults prior to sexual maturation (Johnson, 1969). In some cases this flight takes them out of their "Boundary layer," which was defined by Taylor (1958) as that region near the ground "in which air movement is less than the insects' flying speed, or within which the insects' sensory mechanisms and behaviour permit active orientation to the ground." Their dispersal is then controlled by large scale wind systems. It is thus obviously important to understand the role of flight in the population dynamics of an insect pest in order to achieve successful pest management (Joyce, 1976). The fact that insect flight studies have been extremely difficult to do in the past may partially explain why many control strategies have failed to take into account insect mobility. Recently, however, X-band radar has proved very useful for this study. It has allowed observations to be made during the day and night of insects flying at heights and over distances at which they were previously quite inaccessible.

1.3 THE APPLICATION OF RADAR TO THE STUDY OF BIRD AND INSECT FLIGHT

The first biological application of radar was to the study of bird flight, following on from experience gained during World War II (Lack and Varley, 1945). Later the subject of Radar Ornithology became well established (Eastwood, 1967) and since then a great deal of insight into bird migration has been gained.

The feasibility of detection of insects by radar was first demonstrated by Crawford (1949) and independently suggested by Rainey in 1950 (Rainey, 1955) for the study of locust swarms. Probably the first entomologically useful information about insect flight concerned the density and extent of locust swarms (Ramana Murty et al., 1964; Muzumder, Bhaskara Rao and Gupta, 1965). Several pioneering experiments were attempted after this (Roffey, 1969; Schaefer, 1969; Schaefer, 1971; Roffey, 1972; Riley, 1974) which clearly demonstrated the large amount of insect activity which had previously gone undetected. Recently more comprehensive studies have been made (Schaefer, 1976; Riley and Reynolds, 1979; Greenbank, Schaefer and Rainey, 1980). These have incorporated observations from many different sources, including ground surveys and meteorological stations, so that a clearer understanding of the insect behaviour and its response to the environment might be achieved. The development, use and limitations of radar as a tool for the study of insect flight has been well reviewed by Riley (1979) and will be summarised only briefly here. Basically it has been possible, using commercially available X-band marine radars with high gain parabolic antennas, to detect individual moths and grasshoppers at ranges of approximately 1500m and 2500m respectively. Concentrations of insects have been detected out to several tens of kilometres. This represents a very significant advance since prior to the advent of radar the maximum range for nocturnal observations had been 100m (Roffey, 1963). The following flight parameters have been measured using radar.

- (i) Insect aerial density,
- (ii) insect speed and direction,
- (iii) insect headings,
- (iv) rates of climb and descent,
- (v) flight duration,
- (vi) wing beat frequency.

All of the above can be measured as functions of height and time.

The last parameter, wing beat frequency, is measured by detecting the modulation of the returned signal resulting from the insect body movement associated with flapping (Riley, 1979), and has proved very useful for identification purposes. Wing beat frequency appears to be inversely related to wing length (Figure 1.1) and therefore may be used to provide valuable information about the size structure of the airborne population. Unfortunately it cannot generally be used alone for identification since there is normally a substantial amount of inter-species overlap.

Radar has become a unique tool for the study of insect flight and its importance is likely to increase as growing world demand for agricultural products encourages the development of large monocultures, which are especially susceptible to pest problems (Joyce, 1976).

1.4 LIMITATIONS OF THE RADAR TECHNIQUE FOR INSECT FLIGHT STUDIES

Despite the great potential of radar for contributing to the development of strategy for the control of mobile insect pests, its

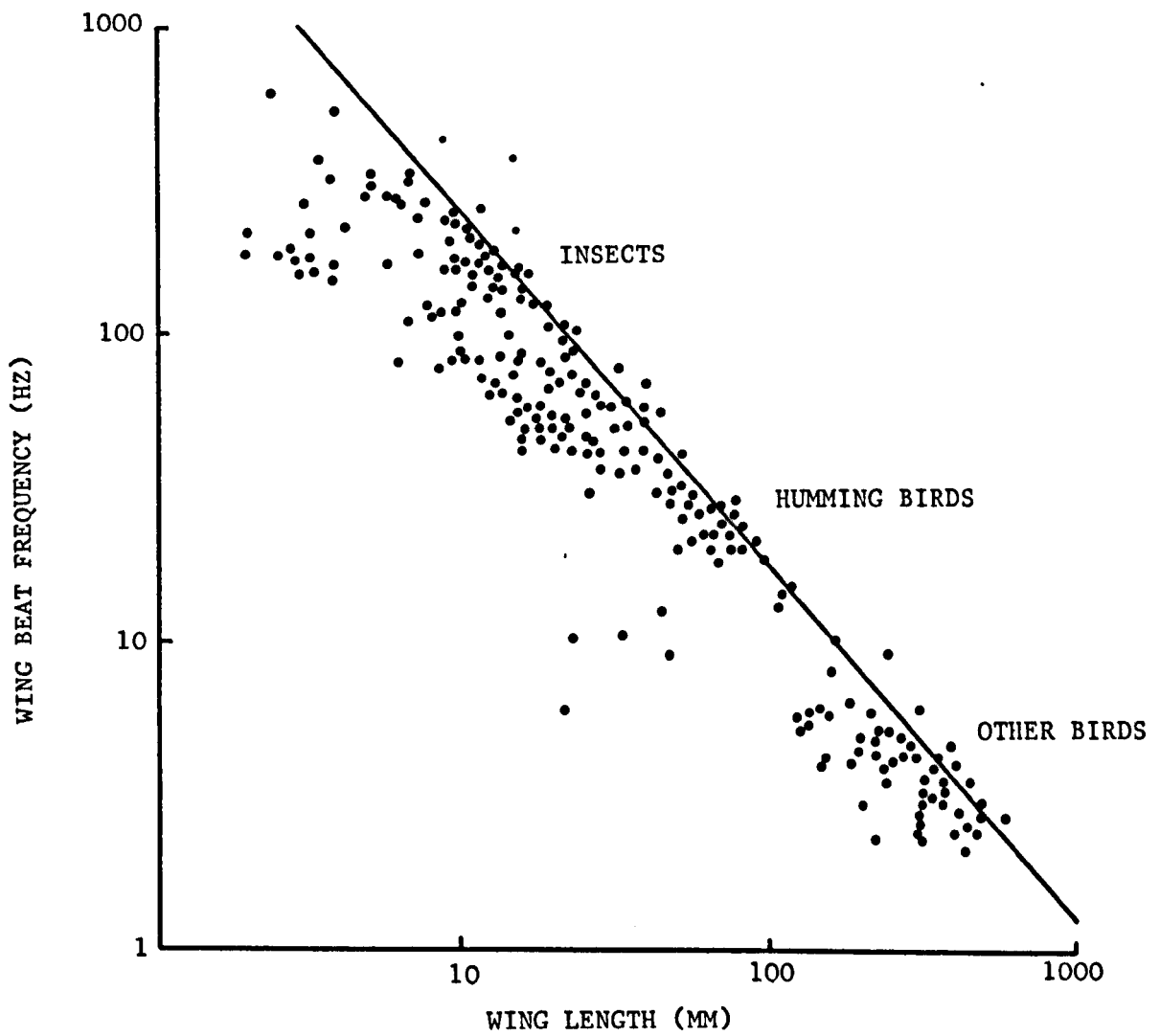


FIGURE 1.1 Relationship between wing beat frequency and wing length for birds and insects. Boundary line has equation $(\text{freq}) \times (\text{length})^{1.15} = 3540$ (from Greenwalt, 1962).

effectiveness is reduced by two serious limitations, namely:-

- (a) identification of species being observed,
- (b) observations close to the ground.

It is obviously important, while making observations on the behaviour of a particular pest, to be absolutely confident that the insects being observed are really the species of interest. As already mentioned, wing beat frequency may indicate the size distribution of the insects observed, but this is not species specific. In some cases the problem can be sidestepped by restricting observations to situations where the species of interest dominate the aerial fauna. The synchronised emergence of the Spruce Budworm Moth in New Brunswick has provided such a situation (Greenbank, Schaefer and Rainey, 1980). In most cases however very careful interpretation of indirect evidence about identity has been required.

The second limitation is caused by ground clutter, which is the result of side lobes in the radiation pattern of the aerial. At low antenna elevations energy in the side lobes is reflected off the ground and back into the receiver. The size of this signal far exceeds that expected back from a typical insect target in the main beam, and therefore swamps the signals from insect targets. With careful siting it has been possible to reduce the minimum height for observations to 20 - 30m above ground level (AGL) (Schaefer, 1976). It is however crucially important to quantify insect activity below this height for a complete understanding of flight behaviour. The purpose of the project described in this thesis was to develop and use techniques for the study of insect flight in this region. The objective was not only to supplement the radar coverage at low altitude but also to help

resolve the identification problem by measuring the wing beat frequencies of insects flying at altitudes low enough to permit them to be visually identified.

1.5 A NEW SYSTEM TO SUPPLEMENT THE RADAR TECHNIQUE

The author conceived the idea for this work while working on the Sudan Aphid Project (supported by Agricultural Aviation Research Unit of Ciba-Geigy (UK) Ltd.) for Schaefer at Cranfield Institute of Technology. The project was designed to study aphid flight above a wheat crop by detecting the sunlight scattered from the aphids' wings as they flew across a specially prepared dark background (Farmery and Sills, 1976). Whilst on the project the author tried some experiments at night using a modified version of the equipment with a searchlight to provide illumination. During these experiments it became clear that night flying moths and grasshoppers could be detected by an optical technique. The exciting idea of applying this technique to supplement radar observations of nocturnal insect flight at low altitude immediately became apparent to the author. It became clear that a system was required which was capable of measuring the same parameters of insect flight as did the radar, but in the height range 0 - 30m AGL. The optical approach seemed particularly well suited for this purpose for the following reasons:-

- (a) narrow, well-defined optical beams are easily generated for the low altitude observations, and

- (b) many well-tried sources and detectors are available at optical wavelengths.

Optical systems have been used widely to study atmospheric parameters such as aerosol densities and clear air turbulence. Original studies used powerful searchlights (Synge, 1930; Hulbert, 1937; Friedland et al., 1956; Elterman, 1966) and more recent work has used lasers (Fiocco and Simullin, 1963; Lawrence, Crownfield and McCormick, 1967). Application of these techniques to the study of animal flight has, however, received little attention. Richards (1955) observed modulated signals from a photoelectric cell pointed at the sun. He deduced that these were due to flying insects interrupting the sunlight falling on the detector and suggested that the method might be useful as a technique for studying daytime insect flight. Searchlights have been used to extend the range of visual observations at night of both bird (Cauthreaux, 1969) and insect (Roffey, 1963; Brown, 1970) flight. These searchlight techniques provided useful qualitative observations but suffered from difficulties with identification, quantification and the perturbing effect of the bright light on insect behaviour.

Clearly to be really useful an optical system would have to operate at wavelengths to which the insect eye was insensitive and be able to make the following measurements:-

- (i) aerial density
- (ii) speed and direction of flight
- (iii) wing beat frequency.

All of these parameters need to be measured as functions of

time and height up to 30m AGL. It was envisaged that the lowest radar and highest optical observations would ideally overlap to allow comparisons between the two sets of results.

In 1977 the Centre for Overseas Pest Research (COPR) initiated a major and comprehensive study of the African Armyworm (spodoptera exempta. walk) in collaboration with the Desert Locust Control Organisation for East Africa (DLCOEA) and the Kenya Agricultural Research Institute (KARI). The Armyworm is a serious pest of grasses and granineous crops in East Africa. It is thought to fly considerable distances downwind in the moth stage to infest new areas, often in regions of wind convergence (Brown, Betts and Rainey, 1969). The new studies were designed to provide the basis for a comprehensive Armyworm forecasting and control strategy for East Africa (Rose, 1979(a) and (b)), Radar was to be used to provide general information about the flight of Armyworm moths, and in particular to help resolve questions about the relative importance of long range as opposed to local flight. It became clear that the proposed optical system could conveniently fill the gap between ground and radar observations. Its use would make possible the measurement of relative numbers of moths embarking on low and high altitude flights and so the crucial long range/local flight question might be better resolved.

Although it was thought that the high densities of moths at an outbreak site (Rose, 1979(a)) would simplify radar identification it was considered essential that wing beat frequency be used as confirmatory evidence. The optical system could contribute by

measuring wing beat frequency distributions of moths visually identified as Armyworm.

The optical system was therefore developed with these Armyworm studies in mind.

1.6 REQUIREMENTS FOR THE NEW SYSTEM

The operating waveband for the system had to be chosen to be outside the spectral sensitivity of the Armyworm eye (Figure 1.2). The ultraviolet region ($\lambda < 340$ nm) was considered unsuitable for two reasons. Firstly it was not clear, because of insufficient data that the Armyworm eye was, in fact, insensitive in this region. Secondly, since the transmission of ordinary glasses decreases dramatically in this region, the optical system would require special quartz elements. This requirement would have the effect of increasing cost and reducing choice, without possessing any particular advantages. It was therefore considered more convenient to operate in the near infra-red region ($\lambda > 700$ nm), where ordinary glass is transparent up to 2.0 μ m. Reasons for the exact choice of waveband will be described in Chapter 3.

1.7 DESIGN CONSTRAINTS ON THE PROPOSED SYSTEM

There were two major constraints on the design of the optical system. Firstly, the capital expenditure on the main system was

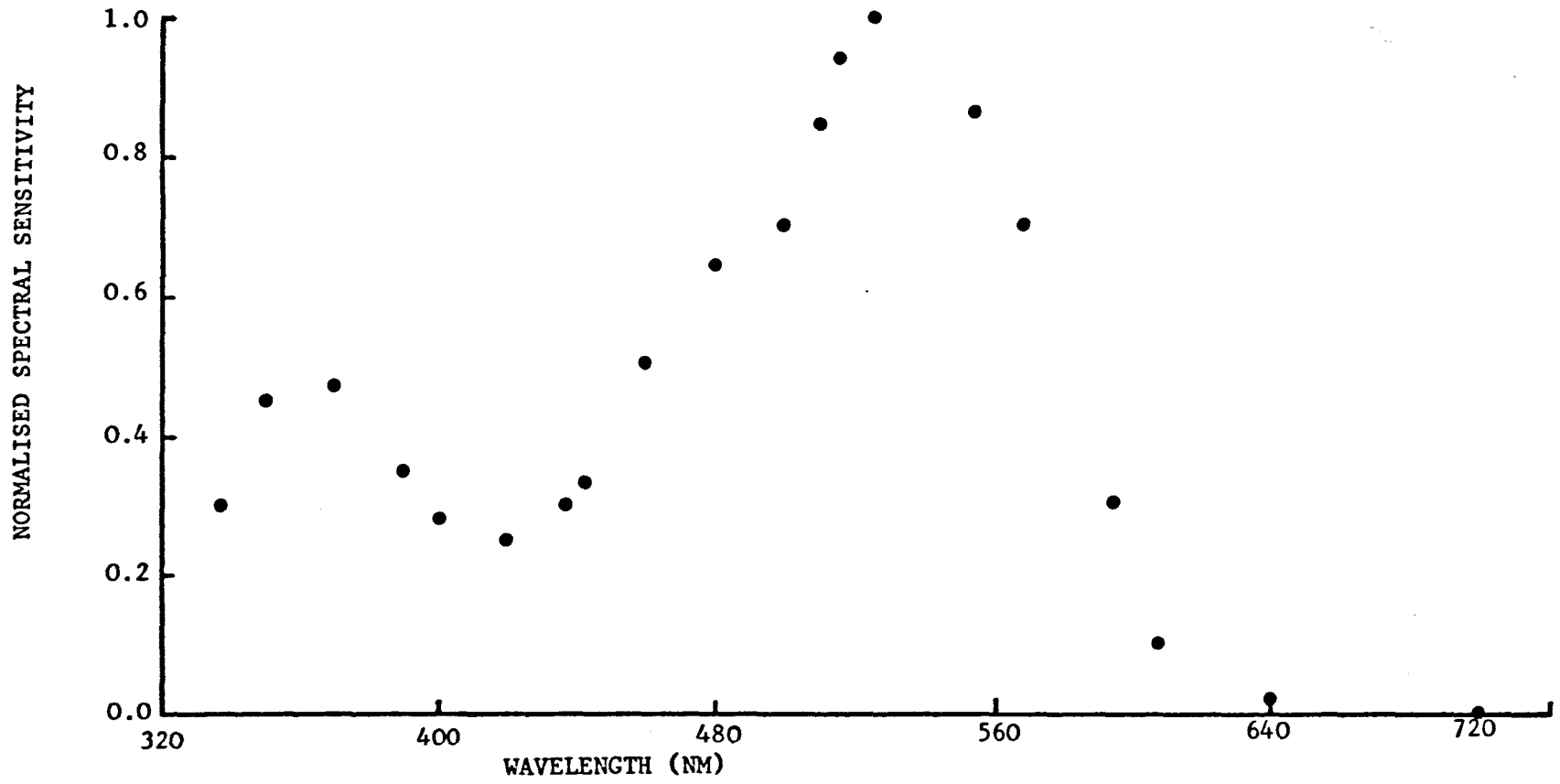


FIGURE 1.2 Spectral sensitivity of s. exempta eye (from Langar et al., 1979).

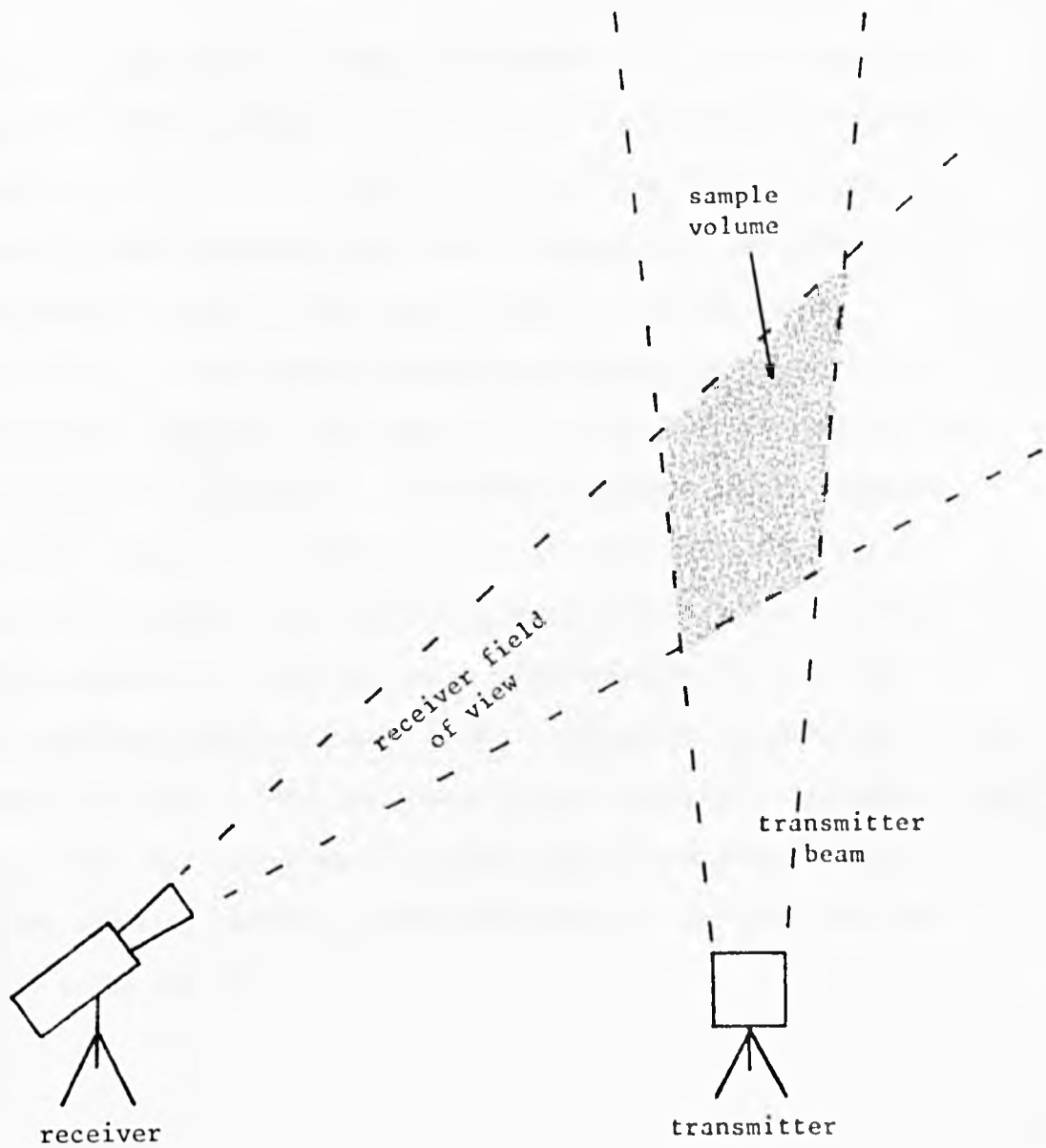


FIGURE 1.3 The bistatic method.

limited to approximately £3000 and secondly the system needed to be compatible with operation in isolated and hostile field conditions. Together, these two constraints effectively limited the degree of technical sophistication that could be employed in the system. Consequently instead of adopting a pulsed system for range measurement, as with most microwave and optical radars, a bistatic approach was employed. In this method the transmitter and receiver are physically separated by a distance comparable to the proposed detection range, in an arrangement as illustrated in Figure 1.3. Range information is then provided geometrically, a sample volume being defined by the intersection of the receiver field of view and the transmitter beam (Skolnik, 1962). The major disadvantage of this method is in the critical alignment of the two beams. However it was decided that the system should operate in a fixed geometry as a passive sampling system, so that difficulties with alignment were likely to be minimal.

1.8 CONCLUSIONS

The study of published work shows that radar has made a valuable contribution to the study of insect flight in relation to pest control, but that the inability of radar to obtain information at low altitudes constitutes a serious limitation. I have considered the feasibility of using an optical system and have established that such a system should substantially improve the radar

coverage, and the credibility which can be attached to its results. I have deduced that for the system to be useful it should operate at near infra-red wavelengths in a bistatic mode, and be capable of detecting Armyworm sized moths up to at least 30m AGL. It should be able to make measurements similar to those made by the radar and, like the radar, it should operate reliably even in hostile field conditions. I shall describe the development and use of such an optical system in the rest of this thesis.

CHAPTER 2

THEORETICAL EVALUATION OF PROPOSED SYSTEM

2.1 INTRODUCTION

In the first half of this chapter the principles of operation are outlined and the signal-noise ratio (S_N) required of the system is calculated for various environmental conditions. The results are used to arrive at criteria for the transmitter and receiver performances which are then used in Chapter 3 where the choice of source detector combination is discussed.

The sample volume formed by the intersection of the receiver field of view and the transmitter beam is examined in Section 2.4. Problems of alignment are also investigated here and a method for calculating the volume of air sampled is described.

2.2 PRINCIPLES OF OPERATION

The original experiment (Section 1.5) showed that the light flux reflected from a flying insect is heavily modulated at the insect wing beat frequency. This is easy to understand since the open wings form the major reflecting area of the insect and the wing area projected in any particular direction varies during the wing beat cycle. The reflected light flux consists of a d.c. component attributable to the body reflection with an a.c. modulation superimposed on it. By sensing the modulated light flux with a photodetector and performing

a frequency analysis of the resulting electrical signal the insect wing beat frequency can be measured. (More detailed analysis of the wing beat action is described in Section 5.3.)

The excursion of the received signal above a certain threshold indicates the presence of an insect in the sample volume. Simple counting of the number of targets detected provides a measure of insect aerial 'activity'. The more quantitative measurement of aerial density can be made by dividing the number counted in a particular period by the volume of air sampled during that period.

Two important parameters, viz. insect aerial density and wing beat frequency, can thus be measured by detecting the reflected light flux.

Measurement of insect speed and direction requires more complex procedures and the method adopted to make these measurements is explained in Section 4.3.1.

The questions of whether the received signals are large enough to be detected and what is the volume of air sampled will be examined in the two next sections.

2.3 SIGNAL-NOISE CONSIDERATIONS

2.3.1 Ratio of Transmitted To Received Powers

The scattered power received from a typical insect flying through the sample volume is now calculated in terms of the power

transmitted by the illuminator. The bistatic configuration which has been used for these calculations is the same as that shown in Figure 1.3.

The transmitter-receiver separation was made equal to the maximum height of interest H , and the transmitter beam intensity profile was initially assumed to be flat. The more realistic case of an approximately Gaussian intensity profile is considered in Section 2.4. One advantage of an optical system is that the receiver gain is constant across its field of view and can be made to fall sharply to zero at the edges with the use of aperture stops. Evidence to support this assumption for the detector used in this system will be presented in Section 6.4. If the transmitted power is P_T watts and the beamwidth is β rad, then the power density of the target at altitude H within the beam is given by

$$I_T = \frac{4 P_T}{\pi H^2 \beta^2} \quad (2.1)$$

Assuming the Armyworm Moth to have an open wing area of $A \text{ m}^2$ and a reflectivity η , the power reflected by the moth becomes

$$P_m = I_T \times A \times \eta$$

$$P_m = \frac{4 P_T A \eta}{\pi H^2 \beta^2} \quad (2.2)$$

In this analysis the scattering area of the insect has been taken to be the maximum wing area. The small body contribution has been ignored and no account has been taken of the variation of the

presented wing area during the wing beat cycle. These aspects will be dealt with in more detail in Sections 5.1 and 6.3. If the receiver aperture has a diameter of d m, the optics have a transmission factor K , and the power reflected by the insect is assumed to be uniformly scattered into a hemisphere below the moth, then the power incident on the detector in the receiver at a distance $\sqrt{2} H$, will be given by P_R where

$$P_R = \frac{P_m d^2 K}{16 H^2} \quad (2.3)$$

Combining (2.2) and (2.3) we obtain

$$P_R = P_T \times \frac{A \eta d^2 K}{4 \pi \beta^2 H^4} \quad (2.4)$$

The ratio of received power to transmitted power (P_R/P_T) has been plotted against transmitter beamwidth for different sample heights in Figure 2.1, with the following typical values assumed for the other parameters:-

$$A = 2 \times 10^{-2} \text{ m}^2$$

$$K = 0.5$$

$$\eta = 0.2$$

$$d = 6 \times 10^{-2} \text{ m} \quad .$$

Clearly reducing the transmitter beamwidth increases the received power for a given transmitted power. However there is a limit to the extent to which beamwidth can be reduced, which is set by the minimum acceptable target transit time. The linear width of the

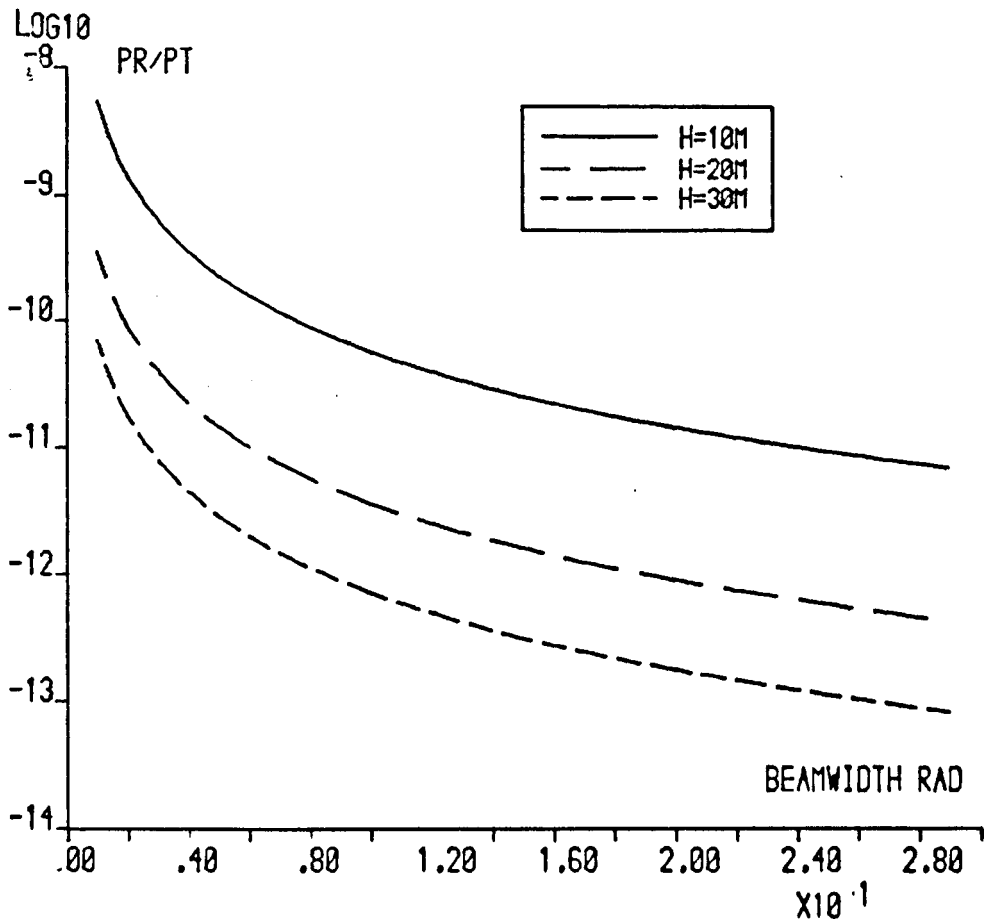


FIGURE 2.1 Ratio of received power to transmitted power (the range factor) as a function of transmitter beamwidth.

beam S, at height H m, for a beamwidth β is given approximately by

$$S = \beta H \text{ m} \quad (2.5)$$

For an insect flying downwind at $v_i \text{ ms}^{-1}$ with a wind of speed $v_w \text{ ms}^{-1}$, the transit time across the beam is

$$t_b = \frac{S}{(v_i + v_w)} \text{ sec} \quad (2.6)$$

If the insect has a wing beat frequency of $f \text{ Hz}$, the number of wing beat cycles completed whilst in the beam will be given by

$$n_b = t_b \times f .$$

Substituting from (2.6) gives

$$n_b = \frac{f S}{(v_i + v_w)} \quad (2.7)$$

There is a minimum number of wing beat cycles n_R required before spectrum analysis is possible. Therefore

$$n_b > n_R .$$

Substituting from (2.7) and (2.5) gives

$$\beta > n_R \frac{(v_i + v_w)}{f H} \quad (2.8)$$

The justification of the choice of n_R for this analysis will be described in Section 5.3. Here the following typical values for the other parameters are assumed:-

$$n_R = 5$$

$$f = 40 \text{ Hz}$$

$$v_i = 2.0 \text{ ms}^{-1}$$

$$v_w = 8.0 \text{ ms}^{-1}$$

The following condition is thus obtained for the beamwidth β_H which is suitable for detecting insects at height H .

$$\beta_H \geq \frac{1.25}{H} \text{ radians} \quad (2.9)$$

Values of β_H are given in Table 1. The required width of the sample volume at each height is 1.25m.

TABLE 1

<u>Height of observations</u>	<u>Approximate Beamwidth required</u>	<u>Ratio of received to transmitted power</u>
<u>H m</u>	<u>β_H rad.</u>	<u>$\frac{P_R}{P_T}$</u>
10	0.12	5×10^{-11}
20	0.06	1×10^{-11}
30	0.04	5×10^{-12}

Table 1 also includes the ratio of received to transmitted power for each of the beamwidth - height combinations. The values of $\frac{P_R}{P_T}$ are approximately the same and the minimum value will be used, together with the results of the next subsection, to calculate the required transmitted power.

2.3.2 Noise At The Receiver

In the operational system (Chapter 4) the electrical output of the photodetector is recorded as a frequency modulated signal on magnetic tape. The recorded data consist of the signal caused by the insect, plus the noise generated by the detection system, and any signals due to background illumination. The ratio of signal-to-noise required for target measurement, and the absolute value of the system and background noise, thus together define the minimum received power needed for detection. This value, together with the results of the previous section enable the required transmitter power output to be determined.

To proceed further some generality must be lost by considering the type of detector used in the receiver. The performance of the two most important sensitive detectors of near infra-red radiation, namely the photomultiplier tube and the silicon photodiode will be analysed here. These devices and some of the terms used to characterise them are described in Chapter 3. The photomultiplier tube will be considered first.

Operating the photomultiplier tube in the configuration shown in Appendix A1 with a current to voltage amplifier to amplify the anode current, the output signal includes noise from the following sources:-

- (i) Shot noise associated with signal current.
- (ii) Shot noise associated with the current due to background illumination.
- (iii) Shot noise associated with the dark current.

- (iv) Johnson (thermal) noise associated with the feedback resistor.
- (v) Shot noise associated with the input bias current of the operational amplifier.

The total noise current i_N at the amplifier input can thus be written (Lawrence, Crownfield and McCormick, 1967),

$$i_N = \mu \left[2eB(i_S + i_B + i_D) \right]^{\frac{1}{2}} + \left[\frac{4kTB}{r} \right]^{\frac{1}{2}} + (2eB i_{OA})^{\frac{1}{2}} \quad (2.10)$$

where

- μ is the photomultiplier gain
- e is electronic charge
- B is electronic bandwidth of detection system
- i_S is signal current at photocathode
- i_B is background current at photocathode
- i_D is dark current at photocathode
- k is Boltzman's constant
- T is Absolute temperature
- r is feedback resistor
- i_{OA} is input bias current of operational amplifier.

The thermal noise contribution, i_{JN} in equation (2.10)

$$i_{JN} = \left[\frac{4kTB}{r} \right]^{\frac{1}{2}}$$

is small compared to shot noise terms and can be neglected. For example, its value for a feedback resistor of $5.6 \text{ M}\Omega$ at room temperature with a bandwidth of 300 Hz is $i_{JN} = 10^{-12} \text{ A}$, which is the same as the shot noise current at the anode associated with a

signal current of only 10^{-18} A (6 electrons sec^{-1}) for a typical photomultiplier gain of 10^5 .

The amplifier-generated noise can be disregarded for similar reasons. The shot noise current associated with a worst case figure of $i_{OA} = 3 \mu\text{A}$ is the same as the thermal noise current, namely 10^{-12} A.

Equation (2.10) can therefore be rewritten as

$$i_N = \mu \left[2eB(i_S + i_B + i_D) \right]^{\frac{1}{2}} \quad (2.11)$$

The signal-to-noise ratio (S_n) at the output of the current amplifier is given by

$$S_n = \frac{\mu i_S F}{\mu i_N F} \quad \text{where } F \text{ is the feedback resistor}$$

which gives

$$S_n = \frac{i_S}{\left[2eB(i_S + i_B + i_D) \right]^{\frac{1}{2}}} \quad (2.12)$$

The next step is to calculate the current at the photocathode due to background illumination. The spectral sky irradiance is shown in Figure 2.2 for different day and night conditions. It can be seen to be approximately flat in the near infra-red region (0.7 - 1.0 μm) and we assume a value of $4 \times 10^{-8} \text{ W m}^{-2} \text{ nm}^{-1}$ for clear night sky conditions. For these calculations, however, the nocturnal spectral radiance is required since the observing system received radiation from only a finite solid angle of sky. This has been given by Roach (1963) as $L_\lambda = 10^{-8} \text{ W m}^{-2} \text{ sr}^{-1} \text{ nm}^{-1}$ in the

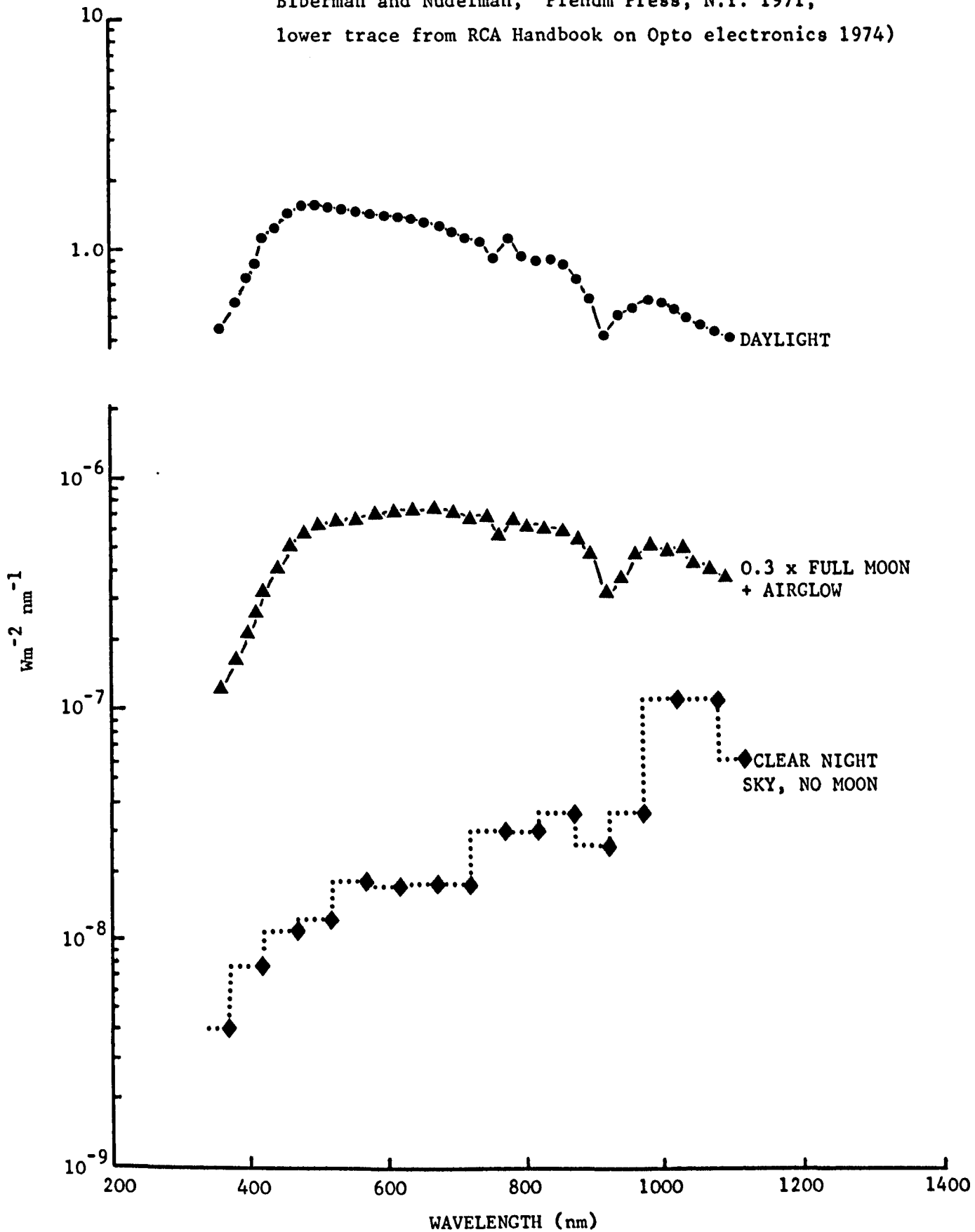
FIGURE 2.2

SPECTRAL IRRADIANCE DAY AND NIGHT

(Upper two traces from Photoelectric Imaging Devices,

Biberman and Nudelman, Plenum Press, N.Y. 1971;

lower trace from RCA Handbook on Opto electronics 1974)



waveband 0.7 - 1.0 m and is consistent with the value of irradiance assumed above. The background power P_B incident on the detector can be written as

$$P_B = P_B(\lambda) \Delta\lambda \quad (2.12a)$$

where

$$P_B(\lambda) = \Omega \frac{\pi d^2}{4} L_\lambda K \quad (2.12b)$$

here, Ω is the solid angle of receiver in steradians

d is the diameter of receiver aperture

$\Delta\lambda$ is the spectral bandwidth of receiver filter

K is the transmission of receiver optics

$P_B(\lambda)$ is the spectral radiant background flux.

The received background power can be reduced by restricting the receiver field of view. However, in order to facilitate alignment and to adjust the vertical extent of the sample volume to 10m (see Section 2.4.1) a typical receiver field of view of 15° ($\Omega = 0.06$ sr) was chosen. Assuming the following values for the other parameters in equation (2.12)

$$d = 6 \times 10^{-2} \text{ m}$$

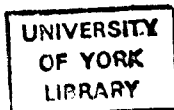
$$K = 0.5$$

we obtain

$$P_B(\lambda) = 9.0 \times 10^{-13} \text{ W nm}^{-1}$$

The photocathode current, i_B , generated by this flux can be calculated from

$$i_B = P_B R \quad (2.13)$$



where R is the responsivity of the photocathode in the spectral region of interest. If an average value of $R = 8 \times 10^{-3} \text{ A W}^{-1}$ for a typical S-20 photocathode (see Section 3.3.3) in the waveband $0.7 - 0.85 \text{ } \mu\text{m}$ is assumed the background current is computed to be

$$i_B = 7.0 \times 10^{-15} \text{ A nm}^{-1}$$

which can be compared to a typical value for an S-20 photocathode dark current of

$$i_D = 2.0 \times 10^{-15} \text{ A} .$$

The background current is clearly dependent on the spectral bandwidth of the receiver filter. Laser sources are narrowband emitters, and provide an opportunity to reduce the background current by using a matched narrowband spectral filter in the receiver. Interference filters have the narrowest bandwidths easily available, typically of the order of 1.0 nm wide. Even for this bandwidth it can be seen that the signal-to-noise ratio for the photomultiplier tube is background limited, that is, it is dominated by the noise from the background induced current rather than by the internal dark current.

The case of using a silicon photodiode as detector is now considered. The photodiode will be operated in the photovoltaic mode (i.e. without external bias) using a current to voltage amplifier to amplify the generated photocurrent (Appendix A2).

There is no dark current in a photovoltaic device; the internal noise current, i_{IN} , is the Johnson noise current associated with the dynamic resistance of the device. The sensitivity of photovoltaic cells is usually quoted in terms of the Noise Equivalent Power (NEP) (see Section 3.2), related to the internal noise current in the following way

$$NEP = \frac{i_{IN}}{R(\lambda)} \quad (2.14)$$

where $R(\lambda)$ is the responsivity of the device at the wavelength of interest. In practice the sensitivity of photovoltaic devices has been found to be limited not by the Johnson noise current but by the noise generated by the current to voltage amplifier, which, because the photovoltaic cell has no internal gain, is generally greater than the shot noise associated with the signal and background photocurrents. Optimum performance from these devices is obtained by combining the photodiode and a low noise J-FET current to voltage amplifier in the same package. The quoted NEP's for these hybrid units is calculated from the internal noise current which takes into account the Johnson noise current and the amplifier input noise current. The noise voltage at the output of one of these devices is given by

$$v_N = G \left[(2eB (i_S + i_B))^{\frac{1}{2}} + i_{IN} B^{\frac{1}{2}} \right] \quad (2.15)$$

where G is the feedback resistor

i_S is the signal photocurrent

i_B is the background photocurrent.

Rewriting equation (2.15) in terms of the received and background powers, P_R and P_B defined by

$$i_S = R P_R \quad (2.16)$$

$$i_B = R P_B \quad (2.17)$$

gives

$$v_N = G \left[(2eBR (P_R + P_B))^{1/2} + i_{IN} B^{1/2} \right] \quad (2.18)$$

For a typical transmitted power of 10 w and spectral bandwidth of 100 nm, the received and background powers take the values

$$P_R = 5 \times 10^{-11} \text{ w}$$

$$P_B = 9 \times 10^{-11} \text{ w}$$

Substituting these with an average value of 0.2 A W^{-1} for the responsivity R in equation (2.18) gives

$$v_N = G B^{1/2} \left(6.7 \times 10^{-15} + i_{IN} \right) \quad (2.19)$$

The value of i_{IN} for a typical photodiode (e.g. United Detector Technology UDT-500, $NEP = 5.10^{-12} \text{ W (Hz)}^{-1/2}$ calculated from equation (2.14) is $1.5 \times 10^{-12} \text{ A (Hz)}^{-1/2}$. The internal noise current i_{IN} is clearly the dominant term in the expression (2.19) for the hybrid device noise voltage, and the signal-to-noise ratio for the device reduces to

$$S_N = \frac{G i_s}{G i_{IN} B^{\frac{1}{2}}}$$

i.e.
$$S_N = \frac{i_s}{i_{IN} B^{\frac{1}{2}}} \quad (2.20)$$

The analysis continues by combining these results with the calculated ratio of received to transmitted power to arrive at suitable criteria for the transmitter performance.

2.3.3 Transmitter Requirements

Rewriting equation (2.11) in terms of the signal current, gives

$$i_s = (eB)S_N^2 + \left[(eB)^2 S_N^4 + 2(eB) S_N^2 (i_B + i_D) \right]^{\frac{1}{2}} \quad (2.21)$$

The ratio of received to transmitted power (the range factor), γ was calculated in Section 2.3.1

$$\gamma = \frac{P_R}{P_T} \quad (2.22)$$

Substituting for P_R in equation (2.22) from equation (2.16)

$$i_s = \gamma P_T R \quad (2.23)$$

For this analysis the spectral distribution of the transmitted

radiation $P_T(\lambda)$ will be assumed to be flat over the waveband $\Delta\lambda$, which is the spectral bandwidth of the receiver filter.

Equation (2.23) can then be written

$$i_S = P_T(\lambda) \Delta\lambda R \quad (2.24)$$

where R is taken as the average value in the waveband $\Delta\lambda$.

Combining (2.21) and (2.24) gives

$$P_T(\lambda) = \frac{1}{\gamma \Delta\lambda R} \left((eB) S_N^2 + \left[(eB)^2 S_N^4 + 2(eB) S_N^2 (i_B + i_D) \right]^{\frac{1}{2}} \right) \quad (2.25)$$

Combining (2.12a) and (2.13) the background current can be expressed thus

$$i_B = P_B(\lambda) \Delta\lambda R \quad (2.26)$$

substituting in (2.25) gives

$$P_T(\lambda) = \frac{1}{\gamma \Delta\lambda R} \left((eB) S_N^2 + \left[(eB)^2 S_N^4 + 2(eB) S_N^2 (P_B(\lambda) \Delta\lambda R + i_D) \right]^{\frac{1}{2}} \right) \quad (2.27)$$

Equation (2.27) defines the required spectral brightness of the transmitter (in units of $W \text{ nm}^{-1}$) in terms of the required signal-to-noise ratio, the range factor, background power and detector characteristics for a photomultiplier tube. The corresponding equation for the case of a photovoltaic cell as detector is considerably simpler, and is obtained by combining (2.20) and (2.24) viz.

$$P_T(\lambda) = \frac{1}{\gamma \Delta\lambda R} \left(S_N i_{IN} B^{\frac{1}{2}} \right) \quad (2.28)$$

$P_T(\lambda)$ has been plotted against the spectral bandwidth of the system for each of the two detectors considered above (Figure 2.3). The details of the parameters assumed in these calculations are listed in Table 2.

TABLE 2
VALUES OF THE PARAMETERS USED IN THE EVALUATION
OF EQUATIONS (2.27) AND (2.28) FOR FIGURE (2.3)

<u>Parameter</u>	<u>Photomultiplier</u>	<u>Photodiode</u>
<u>Device Type</u>	EMI 9558 B	UDT - 500
Responsivity, R	$8 \times 10^{-3} \text{ A W}^{-1}$	0.2 A W^{-1}
Dark Current, i_D	$2.0 \times 10^{-15} \text{ A}$	-
Internal noise current i_{IN}	-	$1.5 \times 10^{-12} \text{ A (Hz)}^{-\frac{1}{2}}$
Range Factor, γ	5×10^{-12}	5×10^{-12}
Signal-to-noise ratio, S_n	5	5
Electronic bandwidth B	300 Hz	300 Hz
Background spectral Radiant flux, $P_B(\lambda)$	$9.0 \times 10^{-13} \text{ W nm}^{-1}$	$9.0 \times 10^{-13} \text{ W nm}^{-1}$
<u>Other relevant features</u>		
Diameter of active area	51 mm	10 mm
Cost	£250	£100

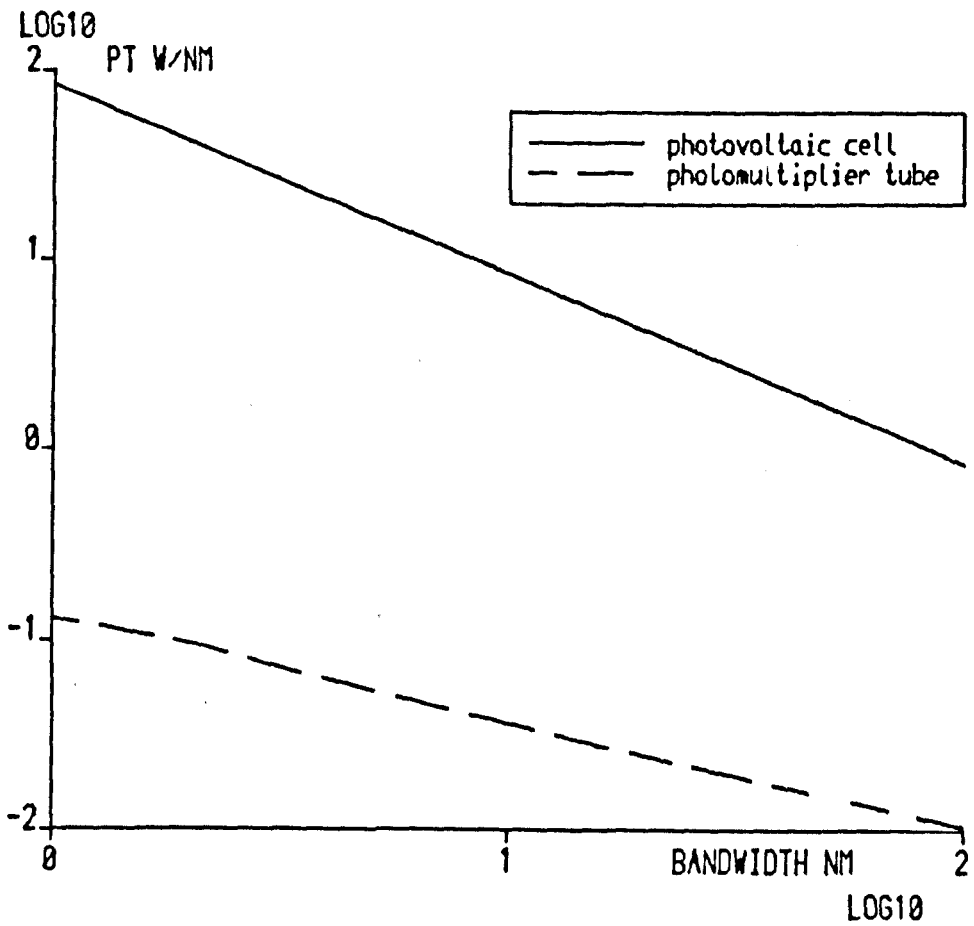


FIGURE 2.3 Transmitter spectral radiance required for a signal-noise ratio of 5 for different detectors.

2.4 SAMPLE VOLUME

2.4.1 Alignment and Choice of Field of View

The adoption of a bistatic configuration for the optical system reduced the level of technical sophistication compared to that for a monostatic system. With a monostatic system, achievement of a range resolution of 5m entails gating the received pulses with an accuracy of better than 30 nS . In the bistatic system such information is provided by simple geometrical relationships. However in using the bistatic system we lost one of the advantages of a monostatic system, namely that the alignment of the receiver field of view and transmitter beam is automatically assured. The problems of ensuring correct intersection of the transmitter and receiver axes at a height of 30m AGL when the transmitted beam was invisible to the naked eye were considerable. The problems could have been alleviated by using theodolite-like mounts for the transmitters and receivers but the number required (6) placed this solution beyond the project budget.

The strategy adopted followed from the argument below. The transmitter beam was aligned as near vertical as possible on its photographic-type tripod. The problem then was to align the optical axis of the receiver in azimuth and elevation. The accuracy of alignment in elevation was not considered as important as that in azimuth since errors in elevation would only result in a slightly different height being sampled. Errors in azimuthal alignment, however, could mean complete failure of the axes to intersect.

The required precision for alignment in azimuth was considered to have to be better than the order of $(\alpha + \beta)$ where α was the field of view of the receiver and β the beamwidth of the transmitter. For the system to give optimum performance the receiver and transmitter beam diameters should be made equal at the point of intersection and the two beams should generate a sample volume whose horizontal dimension is set by the transit time condition. For a sample volume at 30m AGL these conditions mean $\alpha \sim \beta \sim 2^\circ$, and consequently if the azimuthal alignment of the transmitter and receiver beams is worse than $\pm 4^\circ$ then they will not intersect at all. Clearly the required accuracy of alignment can be reduced by increasing either α or β from their optimum values and accepting the corresponding loss of performance. The option $\alpha \gg \beta$ was chosen, which gave the sample volume the shape of a section of a cone. Its vertical extent was defined by the field of view of the receiver and its horizontal dimension was set by the transmitter beamwidth. The alternative of putting $\beta \gg \alpha$ would have created an inconveniently shaped sample volume.

The optical system was originally designed to monitor activity at three heights, viz. 10m, 20m and 30m. The sample volumes were arranged to extend 5m above and below each design height. This gave a system with no overlap and a reasonable sample rate. The condition for the sample to have a 10m vertical extent fixed the value of α at 0.25 rad (15°) for the 30m level.

The scheme outlined above possessed the added advantage that the size of the sample volume could be changed by simply adjusting the receiver field of view, thus allowing different aerial densities to be accommodated.

2.4.2 Calculation of Volume of Air Sampled

The optical system described in this thesis is a passive sampling system. Targets are detected only if they pass through the stationary sample volume. The rate of detection \dot{n} depends on the aerial density of insects ρ , their ground speed v and the cross sectional area A of the sample volume presented perpendicular to the direction of insect movement.

$$\text{Thus} \quad \dot{n} = \rho v A \quad (2.29)$$

The rate of detection is calculated from the number of signals which are counted during a convenient time period. For the purposes of this analysis the ground speed v_g will be assumed equal to the sum of insect flying speed v_i and wind speed v_w . Evidence to justify this assumption (that the insects fly predominantly downwind) will be presented in Section 7.2. The remainder of this analysis is concerned with the calculation of the effective cross sectional area of the sample volume which is presented to the flying insects.

To be counted an insect must not only intersect the sample volume, but must produce a signal of adequate size and duration to produce a frequency spectrum from which its wing beat frequency can be measured. The methods used in the frequency analysis and the criteria for what are 'good' spectra will be described in Section 5.3. Here we shall use the results deduced in that section which imply the following requirements:

- (i) The recorded signal voltage must be twice the system noise level.

(ii) The signal must contain at least five wing beat cycles. Only signals satisfying these criteria will be counted. The problem is now to calculate the cross sectional area of the sample volume such that an insect of a particular size passing through that area will satisfy (i) and (ii) above. This is termed the effective cross sectional area (ESCA), and its method of calculation will be described with reference to Figure 2.4.

The cone TXY represents the approximate extent of the transmitter beam. In these calculations the measured beam intensity profile will be used rather than the flat, sharply defined profile assumed in Section 2.2. The profiles were measured using a 1 cm diameter calibrated photodiode at a range of 10m (Section 3.4.1). Results for the narrowest and widest beams are shown in Figures 4.4 and 4.5. The total transmitted power in the waveband 0.7 - 0.85 μm is approximately the same in each case, namely 1.2 W. For the purposes of these calculations attempts were made to find analytical representations for these profiles, but the results were unsatisfactory. Figure 2.5 shows the attempts to fit different distributions to the widest beam profile. The problem was overcome by incorporating a subroutine into the main computer program which interpolated the required values from the experimentally measured data, with an accuracy of better than 1%. The lines RP and RQ represent the lower and upper bounds of the receiver field of view α . The insects are assumed to be moving in the direction AB. The calculation was developed in the form of an interactive computer program which proceeds in the following way.

- • • Measured profile
 - - - Gaussian, $Y = \exp -2.7 \frac{x^2}{\Gamma^2}$
 - · - · - Hyperbolic secant, $Y = \operatorname{sech} \left(\frac{x \cdot 2.68}{\Gamma} \right)$
 - · · · · · Lorentzian $Y = \frac{\Gamma/2}{x^2 + (\Gamma/2)^2}$
- } All normalised
and arranged to
have same full
width at half
maximum (Γ) as
measured profile

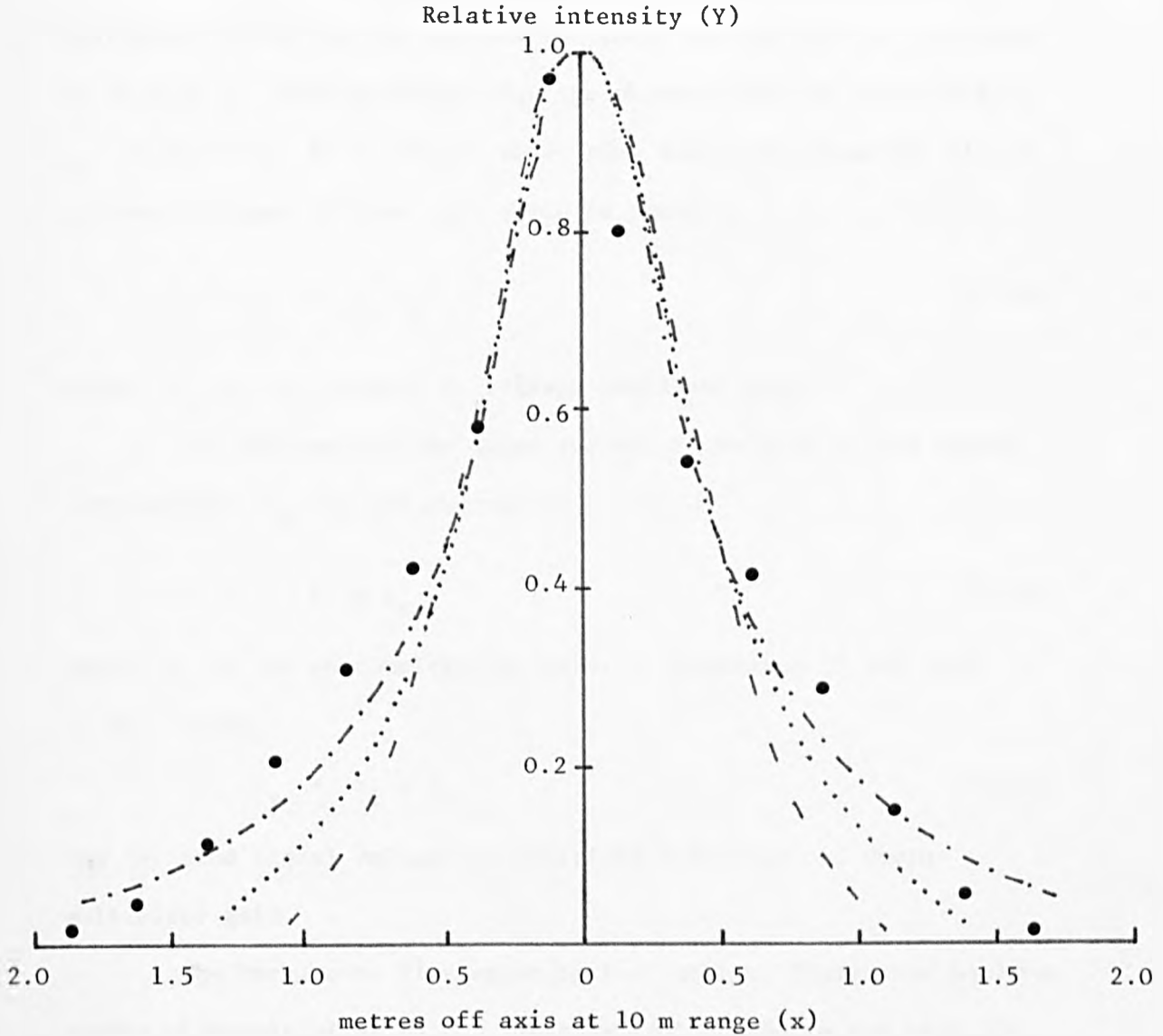


FIGURE 2.5 Different attempts to fit analytical distributions to the measured beam profile of a defocussed aldis lamp

A point O is chosen on the transmitter axis TZ , and the first test establishes whether the point lies within the receiver field of view. If it does, the program proceeds to calculate the received signal photocurrent i_s from a target at that position, in a similar manner to that described in Section 2.2 except that the measured beamprofile is used rather than the flat idealised case.

The detectors used in the operational system were photomultiplier tubes and the reasons for their choice will be described in Chapter 3. Here it is noted that the photomultiplier anode current i_a is amplified by a current to voltage amplifier (Appendix A1) to produce a signal voltage v_s which is given by

$$v_s = i_a r_f \quad (2.30)$$

where r_f is the current to voltage amplifier gain.

The photomultiplier anode current is related to the signal photocurrent i_s by the expression

$$i_a = \mu i_s \quad (2.31)$$

where μ is the photomultiplier gain. Combining (2.30) and (2.31) gives

$$v_s = r_f \mu i_s \quad (2.32)$$

The recorded signal voltage is therefore a function of photomultiplier gain.

The background flux entering the receiver limits the maximum usable photomultiplier gain. That is if the gain is too high the background photocurrent saturates the tube. An automatic system was

therefore developed (see Chapter 4) which adjusted the photomultiplier gain to its optimum value for the current background flux. The recorded signal voltage was therefore a function of the background power P_b ,
i.e.

$$v_s = r_f \times i_s(P_b) \quad (2.33)$$

The received signal voltage v_s was calculated from equation (2.33) and compared to the recorder noise voltage v_n , which was found to be the limiting noise factor in the operational system (for explanation see Appendix B1). This procedure was repeated at intervals along the trajectory AB and the length of the trajectory s , for which the signal voltage was greater than the noise voltage, was thus determined.

The next step in the calculation was to test whether the time taken for the insect to transit the calculated length of trajectory permitted completion of the required number of wing beat cycles for satisfactory spectrum analysis. The number of wing beat cycles n_T completed during the transit was calculated using equation (2.7)

$$n_T = \frac{f \times s}{(v_i \times v_w)}$$

If the number completed was found to be greater than the number required (i.e. $n_T > n_R$) then the point O was accepted as being within the effective cross sectional area of the sample volume.

The program then tested points (e.g. O¹) progressively further off the beam axis until the horizontal extremities of the effective sample volume were defined at that particular height.

The height of the point 0 was incremented and the whole procedure repeated until the outer boundary of the points which satisfied the criteria (i) and (ii) above was delineated. The effective cross sectional area A_E enclosed within this boundary was calculated and used to compute the effective volume sample rate of air, V_E using

$$V_E = A_E (v_i + v_w) \quad (2.34)$$

The volume sample rate depends not only on system performance but also on the environmental parameters wind speed and direction and background illumination. Results illustrating these characteristics are presented in Section 5.2.

Equation (2.34) relies on the assumption already made that insects fly predominantly downwind (see Section 7.2 for verification), so that their ground speed can be taken as the sum of flying speed and wind speed. When the wind speed is zero, the insects fly in random directions. For the narrow transmitter beam configuration used in this system, the value of V_E was found to be largely independent of wind direction. It was therefore possible to use equation (2.34) without modification to describe the volume sample rate down to zero wind speeds.

In this analysis the effective volume of air sampled has been calculated for only one size of target. Clearly the volume is reduced for small targets and vice versa. Accurate calculation of the aerial density therefore requires prior knowledge of the size

structure of the aerial population. A similar problem is encountered in the computation of aerial densities from the radar data, which has been analysed by Riley (1979).

A corresponding analysis has not been performed for the optical system because it was felt that the results were sufficiently accurate to prove the feasibility and usefulness of the optical system.

CHAPTER 3

SOURCE-DETECTOR COMBINATION

3.1 INTRODUCTION

This chapter will begin by defining some of the terms used to characterise the performance of optical detectors. This will be followed by brief descriptions of the three main classes of photo-detectors and their respective advantages for this work. The various sources of near infra-red radiation will then be considered in relation to the performance criteria established in Section 2.3.3; finally, the reasons for the choice of source-detector combination that has been used in the operational system will be outlined.

3.2 DEFINITION OF TERMS RELATING TO DETECTOR CHARACTERISTICS

Many different terms have been used to describe the performance of optical detectors, in this section only those in common usage will be defined (for a more comprehensive review the reader is referred to Ross, (1962)).

3.2.1 Dark Current

Dark current is the current that flows in a photodetector in the absence of signal and background radiation. Its average or

d.c. value is identified by the symbol i_D .

3.2.2 Spectral Responsivity

This term describes the spectral sensitivity of the photo-sensor and is the ratio of the output current in amperes to the input flux in watts, at a particular wavelength. It is denoted by the symbol $R(\lambda)$.

3.2.3 Quantum Efficiency

The quantum efficiency is defined as the ratio of the number of photoelectrons (or electron-hole pairs) created for each incident photon at a particular wavelength. The quantum efficiency η is related to the spectral responsivity thus (RCA Optoelectronics Handbook 1972 pp 149)

$$\eta = \frac{1.24 R(\lambda)}{\lambda} \quad (3.1)$$

where the wavelength λ is in μm .

3.2.4 Noise Equivalent Power

The Noise Equivalent Power (NEP) is defined as the rms value of the sinusoidally modulated radiant power falling on the detector which will give rise to a rms signal current equal to the

rms noise current in the detector, i.e. it is the radiant flux incident on the detector which gives a signal-to-noise ratio of unity. The detector noise current is proportional to the square root of the electronic bandwidth, so the NEP is usually defined at some modulation frequency (e.g. 1 kHz) for a 1 Hz bandwidth at a particular wavelength. The units of NEP are watts $(\text{Hz})^{-\frac{1}{2}}$. It can be interpreted as the minimum detectable signal for unit bandwidth. The NEP and noise current i_N in a detector are related thus

$$\text{NEP} = \frac{i_N}{R(\lambda)} \quad (3.2)$$

3.2.5 Detectivity

Detectivity D, is the reciprocal of NEP and is expressed as $\text{Hz}^{\frac{1}{2}} \text{W}^{-1}$. It is a figure of merit providing the same information as NEP but describes the characteristics such that a higher value of detectivity indicates an improvement in detection capability.

3.2.6 Specific Detectivity

The noise current in many optical detectors is proportional to the square root of the sensitive area. The specific detectivity, D^* takes this into account so that detectors with different active areas may be compared. It is related to the detectivity in the following way, (Ross, 1962, pp 63)

$$D^* = A^{\frac{1}{2}} D \quad (3.3)$$

where A is the detector area. The normal units of D^* are $\text{cm} \cdot (\text{Hz})^{\frac{1}{2}} \text{W}^{-1}$.

3.3 DETECTORS OF NEAR INFRA-RED RADIATION

3.3.1 Photoconductive Devices

In this type of device, energy absorbed from incident radiation excites charge carriers from non-conducting to higher energy states where they can contribute to the electrical conductivity. Incident radiation thus causes a decrease in the electrical resistance of the device. There are two basic types:

(a) Semiconductors, e.g. Germanium, Lead Sulphide. These are characterised by high dark currents at room temperature. They are sensitive to radiation from $0.5 - 20 \mu\text{m}$, with typical specific detectivities of $10^{10} \text{cm Hz}^{\frac{1}{2}} \text{W}^{-1}$.

(b) Insulators, e.g. Cadmium Sulphide. These have lower dark currents at room temperature but slower response times, and specific detectivities of the order of $10^{11} \text{cm Hz}^{\frac{1}{2}} \text{W}^{-1}$.

The low specific detectivities for these devices make them unsuitable for our purpose and they will not be considered further. For example, the transmitted power required for a signal-to-noise ratio of unity for a 1 cm^2 area device at a bandwidth of 300 Hz is 600 W .

3.3.2 Photovoltaic Devices

Absorption of a photon generates an electron-hole pair in the vicinity of a p-n junction. The electron and hole move apart under the influence of the potential barrier at the junction. This generates a current without the need for external bias. Photovoltaic devices can be operated with external bias as photodiodes. In this way, their speed of response is increased but so is their internal noise, in the form of shot noise associated with the bias current.

One of their major advantages for this work is that their spectral sensitivity extends from 0.45 - 1.20 μm (see Figure 3.1) making them suitable for use as detectors with sources which emit at wavelengths beyond the long wavelength cut off of photoemissive devices. Although photovoltaic cells have high quantum efficiencies giving high responsivities, their sensitivity is limited, as we have seen in Section 2.3, by the noise generated in the amplification of the photocurrent. They therefore require high transmitted power.

The signal to noise ratio for a background limited detector is

$$S_N = \frac{i_S}{[(i_S + i_B) 2eB]^{\frac{1}{2}}} \quad (3.4)$$

where the symbols have their usual meaning. Rewriting in terms of signal and background powers gives

$$S_N = \frac{P_S R^{\frac{1}{2}}}{[(P_S + P_B) 2eB]^{\frac{1}{2}}} \quad (3.5)$$

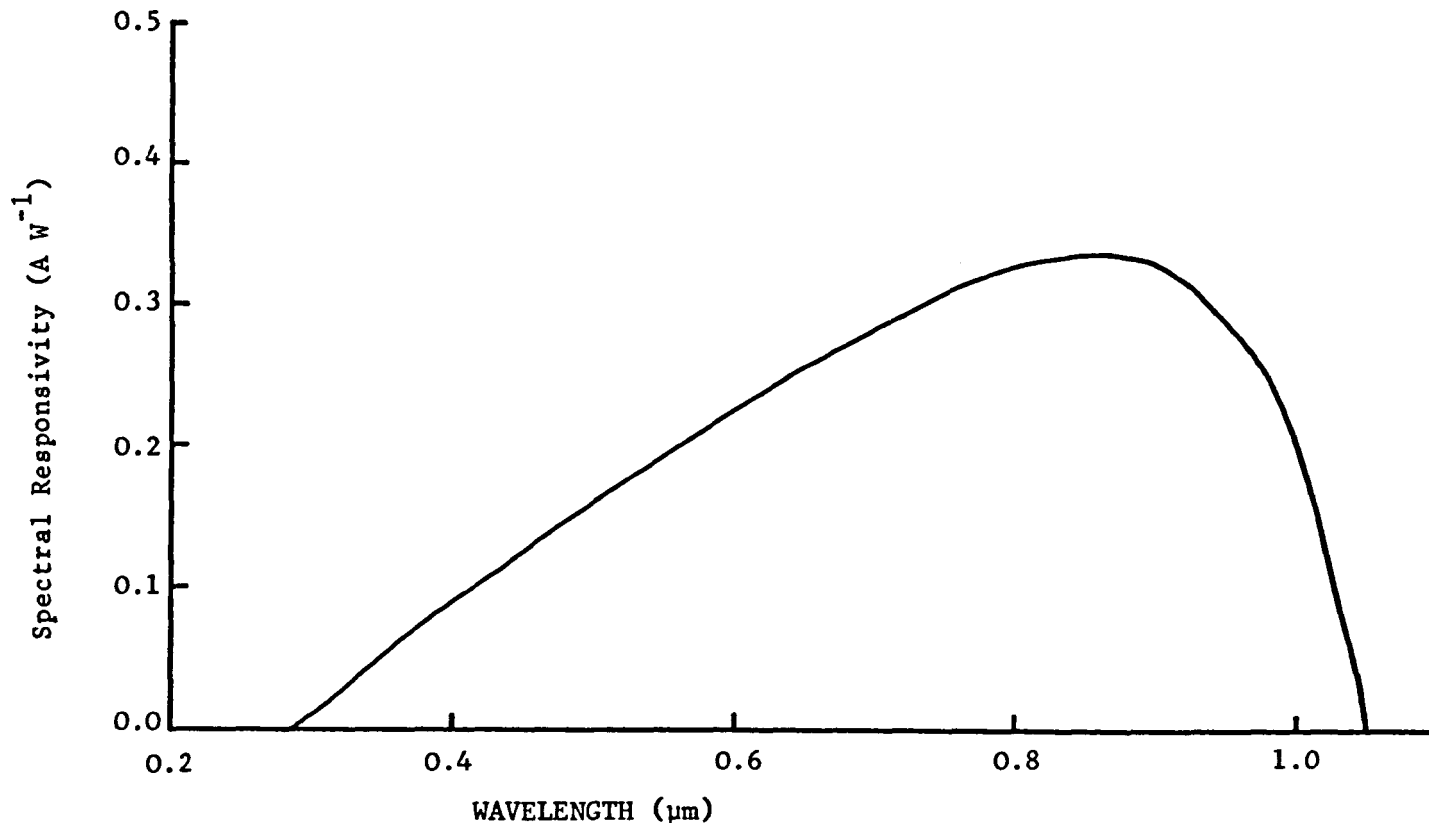


Figure 3.1 Spectral responsivity for typical silicon photodiode.
(UDT PIN 125DP)

The signal to noise ratio is thus proportional to the square root of the responsivity. Therefore in applications where photovoltaic devices are background limited their high responsivity offers the best discrimination of signal against background power. Other advantages of these devices for this work are their small size, ease of operation, ruggedness and low cost. The largest active areas available are typically only 1.0 cm diameter.

3.3.3 Photoemissive Devices

This type of device is based on the photoelectric effect. In this process, when a photon of energy $h\nu$ (where h is Planck's Constant and ν is the frequency of the radiation) is absorbed by a surface of work function ϕ , an electron is emitted with a kinetic energy of $\frac{1}{2}mv^2$ (where m is the electron mass and v is electron velocity).

The process is described by the Einstein equation:

$$h\nu = \phi + \frac{1}{2}mv^2 \quad (3.6)$$

Photoemission only occurs if the photon energy $h\nu > \phi$, the work function. There is thus a threshold for photoemission which is frequency rather than intensity dependent. The practical consequences of this are shown in Figure 3.2 where the spectral responsivities of several photocathode materials are presented.

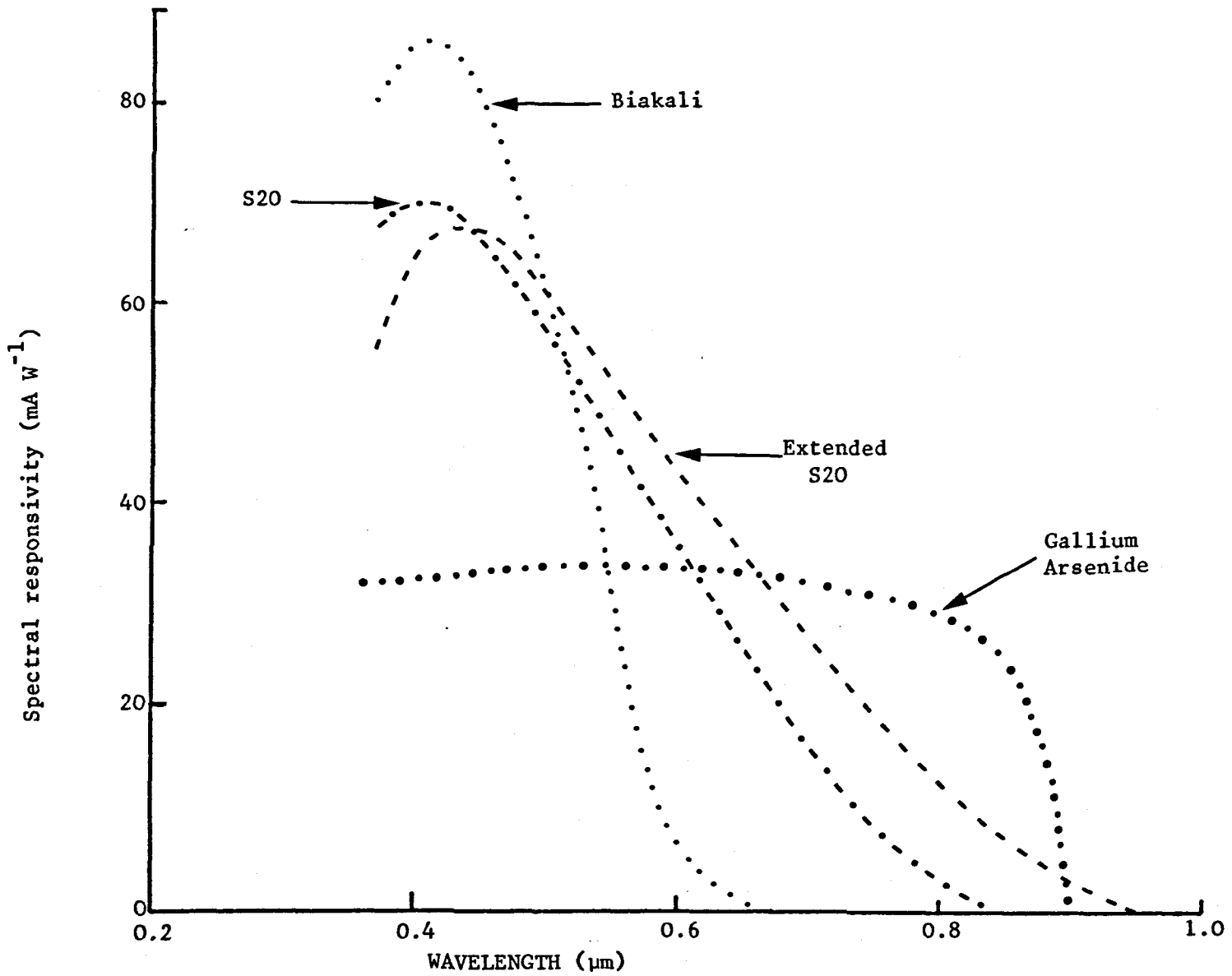


Figure 3.2 Spectral responsivities of common photocathode materials.
 (from Young, (1972) and RCA)

Beyond 900 nm photoemission can only be obtained from photocathodes made from either gallium arsenide or cesium.

At the beginning of this project devices made from these materials were difficult to obtain, expensive and reportedly unreliable for use in the field (R.C.A. pers comm). Furthermore the low work function of the photocathode materials means that the dark current from thermionic emission is significantly greater than that from S20 photocathodes. The tubes are therefore constructed with small photocathodes (typically 23 x 8 mm) which made them inconvenient for this application. Gallium arsenide/cesium photoemissive devices were thus not considered further for this work.

The most important type of photoemissive device is the photomultiplier tube, which has the advantage of providing internal gain. The photomultiplication principle is outlined with reference to Figure 3.3. Photoelectrons emitted from the photocathode are accelerated toward an electrode D (known as a dynode) by a positive potential E . The electrons collide with the dynodes generating secondary electrons, typically four per primary electron. The process is repeated for, say, 10 dynodes and current gains of 10^6 are easily obtainable. The electrons are collected by the positive anode.

The major source of noise in a photomultiplier is due to the dark current generated by thermionic emission from the photocathode. It is more of a problem with low work function photocathodes but in all cases may be reduced if necessary by cooling the tube.

The important aspect of the multiplication process described above is that it is very nearly noise free. Assuming Poisson

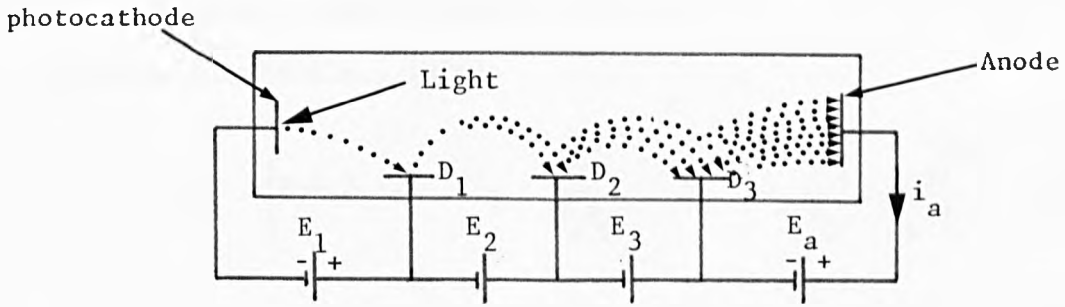


Figure 3.3 Photomultiplier schematic diagram.

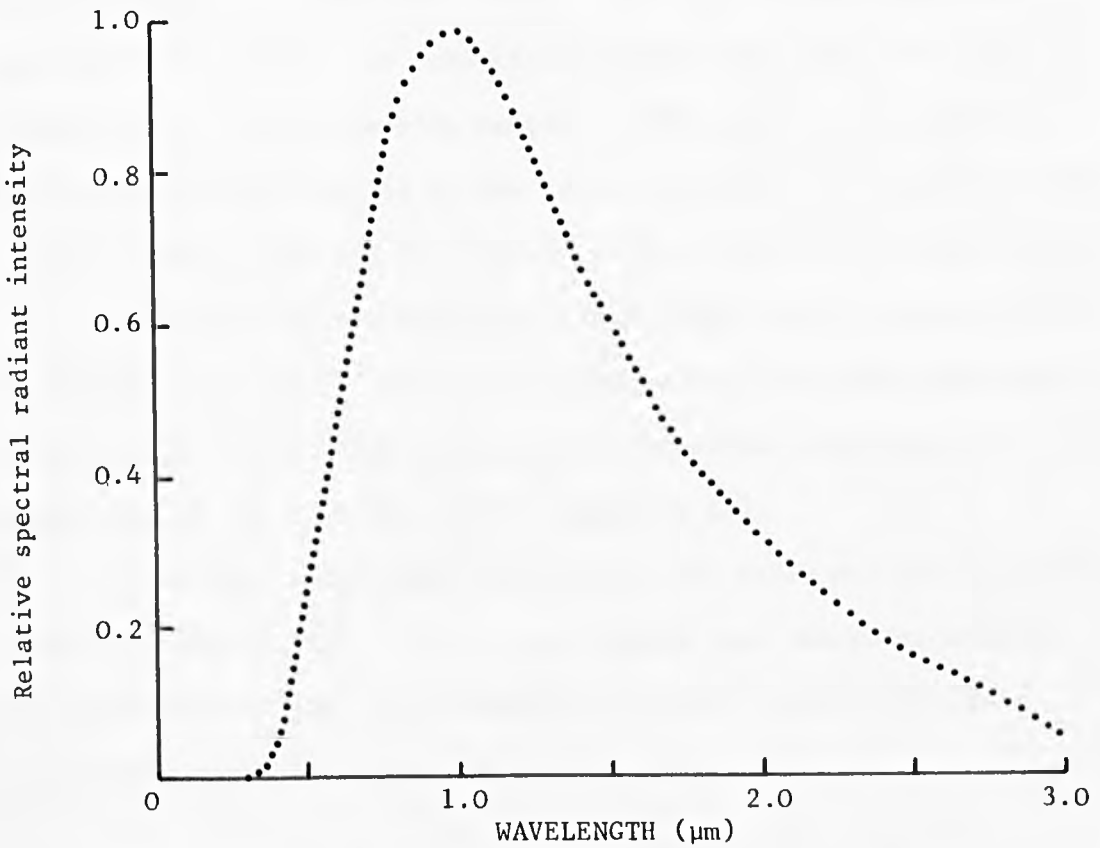


Figure 3.4 Spectral distribution of 3000^o K tungsten lamp
(from Forsythe & Adams, (1945))

statistics for the secondary emission process, the complete expression for the rms shot noise current at the anode of a photomultiplier can be written as (R.C.A., 1974)

$$i_N = \mu \left[2eB I \left(1 - \frac{1}{\delta_1} - \frac{1}{\delta_1 \delta_2} - \dots - \frac{1}{\delta_1 \delta_2 \dots \delta_k} \right) \right]^{\frac{1}{2}} \quad (3.7)$$

where I is the total photocathode current

$\delta_1 \delta_2 \dots \delta_k$ are the secondary emission gain factors for each of the dynode stages

$\mu = \delta_1 \delta_2 \dots \delta_k$ is the total gain of the photomultiplier

B is the electronic bandwidth

e is the electronic charge.

The largest contribution to the noise generated by secondary emission comes from the first stage. If δ_1 is large then the multiplication process is essentially noise free, since the $1/\delta$ terms become negligible with respect to the one. For a typical secondary emission gain of 4, the increase in rms noise current over that of a perfect amplifier, calculated from equation (3.7) is about 15%. Other sources (Shockly and Pierce, 1938) give a value of 20%. In practice, the cathode to first dynode voltage is well stabilised, usually with a zener diode, to prevent additional noise due to variations in δ_1 (see EMI, 1979; Appendix A1).

Photomultiplier tubes are made in two basic designs viz: end window and side window. In the end window case the photocathodes are circular with typical diameters of 4.5 cm, and are available with a wide range of photocathode materials.

The internal gain and low noise equivalent power of the photomultiplier tube make it a detector well suited for this work. Its major disadvantages are that the efficiency of the photoemissive process decreases rapidly in the near infra-red and that it requires a well stabilised high voltage supply for operation.

3.4 SOURCES OF NEAR INFRA-RED RADIATION

3.4.1 Conventional Sources

(a) Tungsten filament lamps

As can be seen in Figure 3.4 these lamps emit predominantly in the near infra-red. The power output of a 60W 11v bulb in the range 0.7 - 0.85 μm has been measured using a calibrated silicon photodiode. To do this, it was first necessary to calculate the "effective responsivity" R_{eff} of the photodiode to light with a spectral distribution $\phi(\lambda)$ characteristic of the bulb in question. The effective responsivity over the wavelength range λ_1 to λ_2 can be written as

$$R_{\text{eff}} = \frac{\int_{\lambda_1}^{\lambda_2} R(\lambda) \phi(\lambda) d\lambda}{\int_{\lambda_1}^{\lambda_2} \phi(\lambda) d\lambda} \quad (3.8)$$

where $R(\lambda)$ is the spectral responsivity of the photodiode. The

values of λ_1 and λ_2 were chosen as 0.7 μm and 0.85 μm respectively. The lower limit was defined by sensitivity of the insect eye (Figure 1.2) and the upper limit by the approximate long wavelength cut off of conventional photomultiplier tubes (Figure 3.2). The waveband λ_1 to λ_2 thus represented a likely operating range for the optical system. The colour temperature of the bulb in question was given by the manufacturers (Rank Pullin Controls Ltd.) as 3000 $^{\circ}\text{k}$. The relative spectral distribution $\phi(\lambda)$ appropriate to this temperature (Figure 3.4) was obtained from Forsythe and Adams (1945). Unfortunately the absolute value of $\phi(\lambda)$ could not be inferred because of uncertainty in the value of the candlepower output of the bulb as supplied by the manufacturers. This, however, did not present a serious problem since the scaling factor cancels in equation (3.8).

The integrals in equation (3.8) were evaluated numerically at 10 nm intervals using the data from Figures 3.1 and 3.4 to give a value for R_{eff} of 0.30 A W^{-1} .

The bulb was mounted in an Aldis signalling lamp (a convenient, narrow beam searchlight, see Section 4.3) and the intensity profile across the beam measured at a range of 10 m using the photodiode (see Figure 3.5). For this exercise the lower wavelength limit λ_1 was defined by an infra-red filter ("cutting on" at 0.7 μm) (see Section 4.3) and the upper limit λ_2 by a filter ("cutting off" at 0.85 μm) mounted over the photodiode. The beamshapes of the narrowest and widest beams obtainable from the Aldis lamp are shown in Figures 4.4 and 4.5.

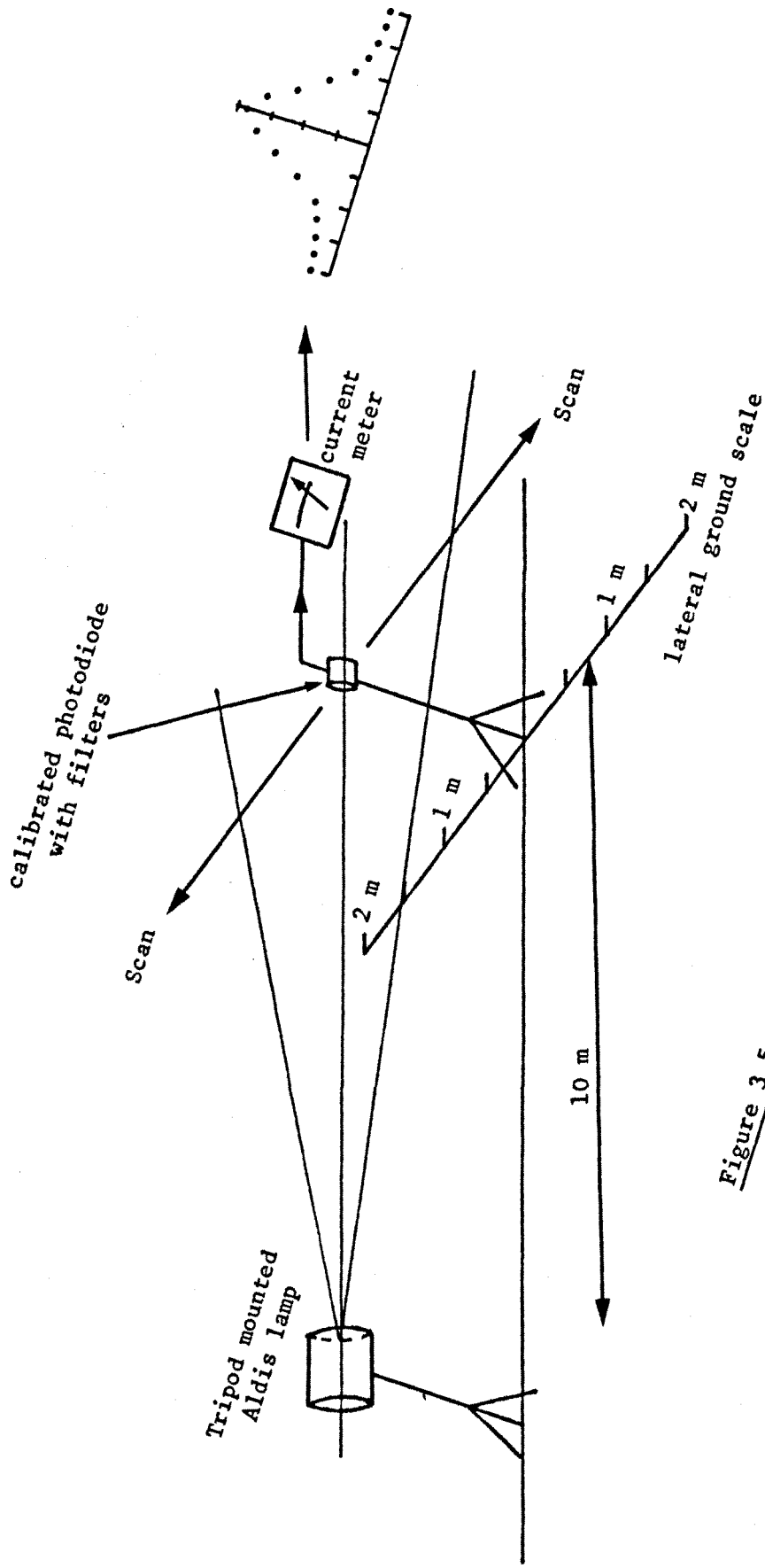


Figure 3.5
 Experiment to measure intensity profile of the beam from an Aldis lamp.

The total power output of the bulb/aldis lamp combination was then calculated by numerically integrating the measured intensity profile of the narrowest beam (Figure 4.4). The total power output was found by this method to be given by

$$P = \frac{I_{10}}{4.56} \quad (3.9)$$

where I_{10} is the on-axis intensity at a range of 10 m. This can be compared to the case for a Gaussian beamshape where

$$P = \frac{I_{10}}{8.5} \quad (3.10)$$

From equation (3.9) the power output of the lamp in the 0.7 - 0.85 μm waveband was found to be 1.20 W, which represented an efficiency of 2%.

The spectral radiant flux from the lamp over the 150 nm wide band is therefore $8 \times 10^{-3} \text{ W nm}^{-1}$. This is approximately equal to the transmitter spectral radiance required for a spectral bandwidth of 150 nm with a photomultiplier tube as detector (see Section 2.3.3 and Figure 2.3). Such a bulb/lamp combination was therefore considered suitable for this work in conjunction with a photomultiplier tube as detector. The lamp had the added advantages of reliability, ruggedness and low cost (see Section 4.3).

The required spectral radiance for the lamp with a photovoltaic cell as detector operating in the waveband 0.7 - 1.2 μm is 0.17 W nm^{-1} (from Figure 2.3) i.e. a total power output of 85 W.

Assuming a calculated efficiency of approximately 15% for generating power in this waveband, the power consumption of a tungsten lamp suitable for use with a photovoltaic cell was calculated to be about 500w. This combination was therefore disregarded.

(b) Arc lamps

The emission spectra for a Xenon Short arc lamp has a broad peak between 0.8 - 0.85 μm superimposed on a continuous spectrum (Figure 3.6). The performance of these lamps has been analysed by considering their power output in two wavebands, viz. 0.7 - 0.85 μm and 0.7 - 1.2 μm , which correspond to the usable spectral ranges of the photomultiplier tube and photovoltaic cell respectively. The results of this analysis are summarised in Table 3 below •

TABLE 3

Waveband	Detector	Lamp efficiency in waveband	Power in waveband for 150w lamp	Average Spectral Radiant Flux in waveband	Required Spectral Radiant Flux
			W	W nm ⁻¹	W nm ⁻¹
0.7 - 0.85 μm	PM tube	0.1	15	0.1	5.0 x 10 ⁻³
0.7 - 1.20 μm	Photovoltaic cell	0.6	90	0.18	0.17

Comparison of the data in the fifth and sixth columns of Table 3.1 shows clearly that the 150 W Xenon short arc lamp could be used in the

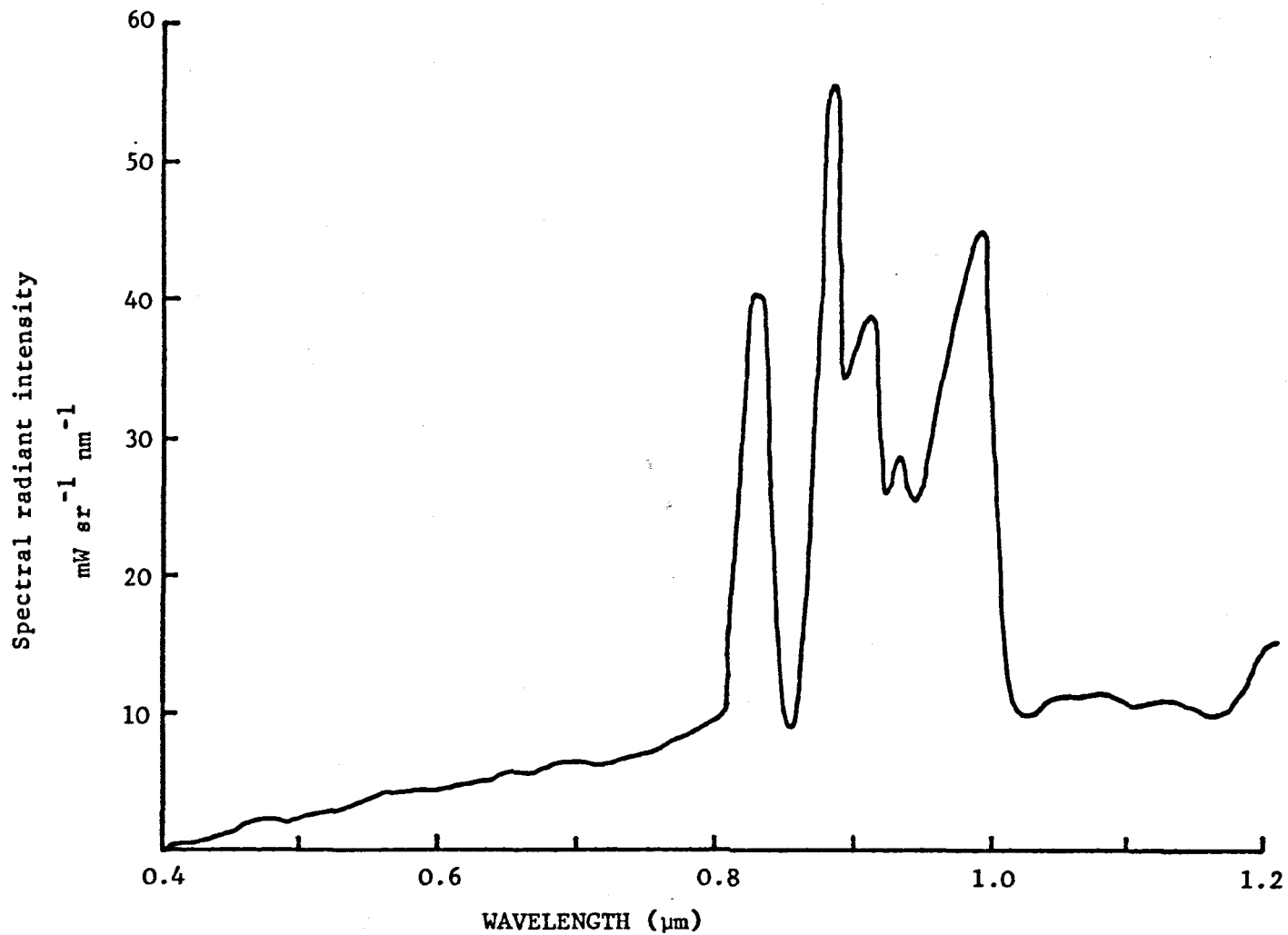


Figure 3.6 Emission Spectra of 150w Xenon Short Arc
(from R.C.A. Optoelectronic Handbook, 1974)

system with a photomultiplier tube as detector. The alternative of using the lamp with a photovoltaic cell is marginal, and because of the inherent advantages of the photomultiplier tube, it has not been considered further.

One of the major advantages of the Xenon short arc lamp for this work is that it can be modulated electrically at suitable frequencies (e.g. 1 kHz) by operating in the 'Simmer Mode'. This technique will be described in Appendix E where a method for discriminating against background illumination is presented.

Zirconium arc lamps exhibit a continuous emission spectrum with a well defined line structure in the 0.75 - 0.85 μm region (Figure 3.7). They are difficult to modulate, the depth of modulation decreasing with increasing frequency (only 20% at 1 kHz). These lamps offered no significant advantages for this work over the tungsten filament lamp or the Xenon short arc lamp and have not been considered further.

(c) Xenon flash tubes

These generate very high energy flashes. The pulse repetition frequency is however low (< 60 Hz) because of the long recovery time of the gas. This would preclude the determination of the target wing beat frequencies at approximately 40 Hz and so study of these lamps has not been pursued.

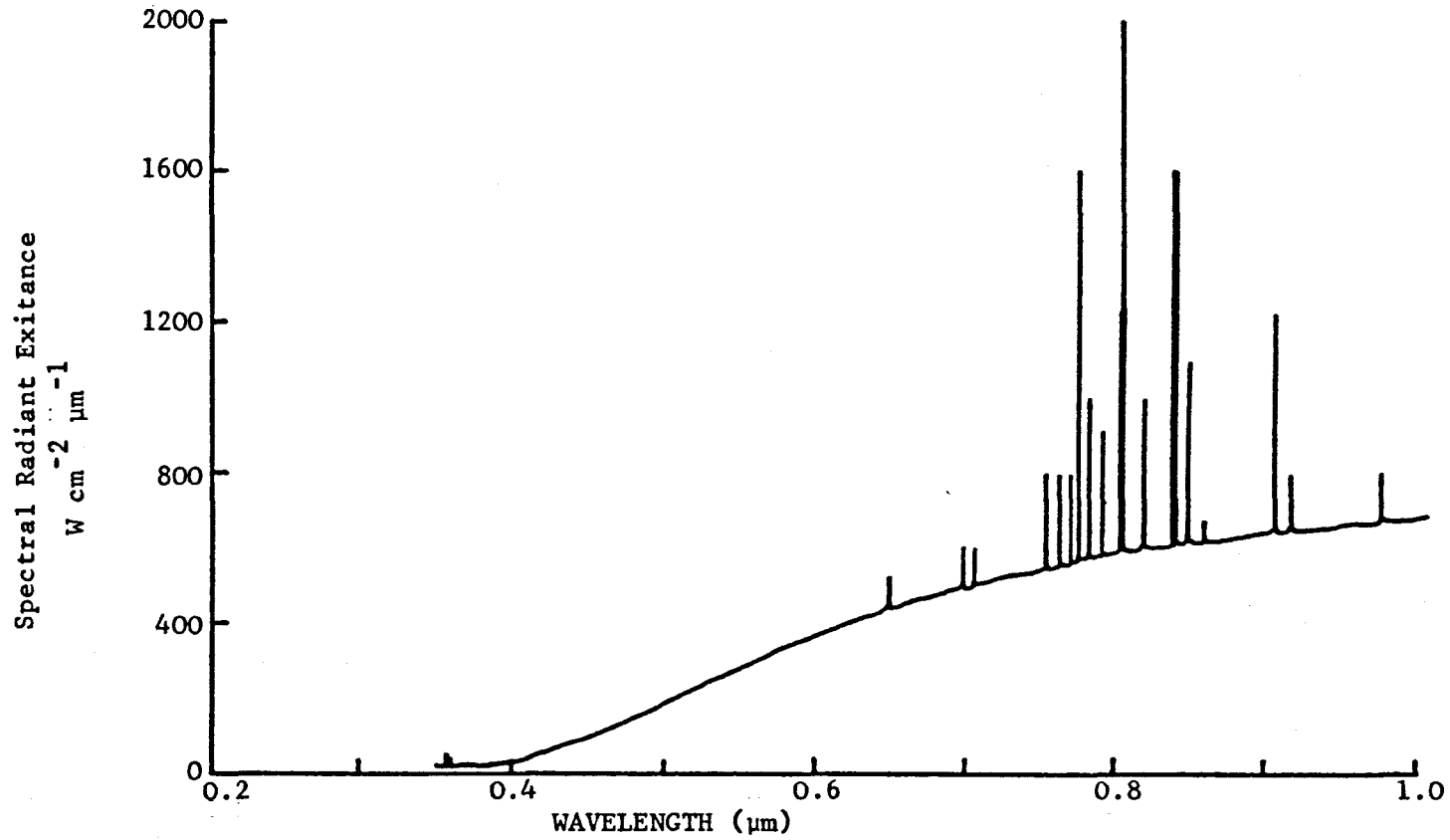


Figure 3.7 Spectral distribution of 100w Zirconium concentrated-arc lamp
(from RCA Optoelectronic Handbook, 1974)

3.4.2 Laser Sources

(a) Neodymium - Yag

As this laser operates at $1.06 \mu\text{m}$ a silicon photovoltaic cell must be used as detector. The typical spectral bandwidth of this type of laser is $<0.1 \text{ nm}$. The system bandwidth may therefore be limited to 1.0 nm by the bandwidth of the receiver interference filter. For this bandwidth the required transmitter spectral radiance is found from Figure 2.3 to be $8.4 \times 10^1 \text{ W nm}^{-1}$ for a photovoltaic detector. The required laser output power is therefore approximately 84 W . Pulsed Neodymium:Yag lasers with peak power outputs of this order are available but their high cost combined with their unsuitability for field use have prevented them from being considered further.

(b) Gallium arsenide (GaAs) semiconductor lasers

These devices operate in the region $0.8 - 0.95 \mu\text{m}$ depending on the doping levels. It is therefore feasible to combine them with either a photomultiplier tube or photovoltaic cell as detector. The spectral width of GaAs laser diodes is approximately 5.0 nm . From Figure 2.3 the minimum required spectral radiance for the device is 0.05 W nm^{-1} (using a photomultiplier tube), which means a total transmitted power of 0.25 W .

The semiconductor diode laser suffers seriously from internal heating which limits the power output of the devices to about 20 m W for continuous operation (e.g. Valtec type LCW5). In pulsed operation peak output powers of 100 W can be easily obtained with

either arrays or stacks of diodes. These are, however, still limited by internal heating to duty cycles of typically 2×10^{-4} . For a pulse repetition frequency of 1 kHz this limits the pulse length to 200 ns. The energy per pulse is calculated to be

$$\begin{aligned} E_p &= 100 \times 200 \times 10^{-9} \text{ J} \\ &= 2 \times 10^{-5} \text{ J} \end{aligned}$$

Energy received from one pulse, E_R is

$$E_R = \gamma E_p$$

where γ is the range factor, substituting values we obtain

$$E_R = 10^{-16} \text{ J}$$

Photon energy at $\lambda = 0.8 \text{ } \mu\text{m}$

$$E_p = 2.5 \times 10^{-17} \text{ J}$$

Thus, even with peak transmitted powers of 100w, the low duty cycle limits the received signal to approximately 4 photons. The photon counting techniques needed to detect such small signals were considered to be beyond the scope of this project for practical as well as economic reasons. Laser diodes were therefore deemed unsuitable as sources for this work because of their restriction to low duty cycles to prevent internal overheating.

(c) Ruby lasers

Although ruby lasers operate at the convenient wavelength of $0.69 \text{ } \mu\text{m}$ they are, like semiconductor diode lasers, restricted to low

average power outputs to prevent internal overheating. They have been developed to generate 'giant pulses' at very low repetition frequencies (~ 0.06 Hz). These limitations and their excessive cost barred them from further consideration for this work.

3.5 CONCLUSIONS

In the last two sections I have examined the different sources and detectors of near infra-red radiation which are available, and have used the analysis of Section 2.3 to investigate which combinations were suitable for my application. The analysis of Section 2.3 was necessarily general and assumed idealised parameters for detectors and sources. For example, both the spectral responsivity of the detector were assumed to be flat over the waveband of interest. No attempt was made to incorporate the real device characteristics exactly into the analysis and so the results have been necessarily approximate. However, I feel that the analysis has been sufficiently accurate to demonstrate which source detector combinations were feasible, and which could be disregarded.

Laser sources are often used in optical radar systems where their advantages of narrow beamwidth and narrow spectral bandwidth can be fully exploited to yield systems which are practically insensitive to background radiation (where low pulse repetition frequencies can be tolerated), (Lawrence, Crownfield and McCormick, 1967).

However, for this application larger beamwidths were required so that sufficiently large volumes of air could be sampled. Some of the intrinsic properties of laser systems (e.g. Neodymium:Yag) are therefore of no advantage, and the advantages that remain are easily offset by their high cost and unsuitability for field work.

The performance criteria analysed so far were not the only factors considered in the selection, other practical aspects were considered important. For example the prototype system had to (a) be reasonably quick to implement so that operational results could be obtained at an early stage (only three field trials were planned), (b) be reliable in the field and (c) cost less than £1000 per sample volume. Modulated systems were not considered for the prototype, it was thought to be sensible to demonstrate the feasibility, usefulness and problems of the technique using an intrinsically simpler (and therefore more reliable) c-w system.

The combination of tungsten filament lamp and photomultiplier tube was chosen for the prototype system. The tungsten lamp had several attractive features viz:

- (a) tungsten lamps mounted in searchlight-type units were available,
- (b) tungsten lamps were relatively inexpensive,
- (c) power supply requirements for tungsten lamps were simple,
- (d) simplicity of the lamp/power supply made it amenable to field repair.

The Xenon short arc lamp offered good performance but its extra cost, shorter lifetime and more complex power supply

requirements made them less attractive for the prototype system. They were however considered suitable for the second generation modulated system outlined in Appendix E.

The photomultiplier tube had the advantage in this combination of being background, rather than device limited. This meant that, if necessary, the system performance could be improved by reducing the background radiation (e.g. by reducing the receiver field of view). It was also fortuitous that the diameter of the image formed by a standard 35 mm camera lens was approximately the same (45 mm) as the diameter of the active area of one standard size of photomultiplier tube. The use of standard 35 mm camera lenses in the receivers meant that their cost could be reduced and their flexibility increased.

The exact type of photomultiplier was selected as follows. From Figure 3.2 it can be seen that the photocathode materials most suitable for use in the near infra-red region are termed S20 and "extended S20". These are both used in 51 mm diameter, 11-stage photomultiplier tubes. Table 4 summarises the characteristics of two tubes using these materials and manufactured by EMI Tube Division Ltd..

TABLE 4

Photo-cathode	Tube type	Effective Responsivity for tungsten filament lamp $\lambda > 0.7 \mu\text{m}$	Dark Current	Cost
S20	9558B	8.12 mA W ⁻¹	2×10^{-15} A	£285
extended S20	9659	13.20 mA W ⁻¹	5×10^{-15} A	£424

For the background limited case the signal-to-noise ratio is proportional to the square root of the responsivity (equation (3.5))

$$\text{i.e. } S_N \sim R^{\frac{1}{2}}$$

The original calculations in Section 2.3.3 were made for an S20 photocathode. Employing an extended S20 photocathode increases the signal.to.noise ratio by $(13.2/8.12)^{\frac{1}{2}}$ i.e. 28%. This improvement did not justify the extra 50% cost of the 9659 tube, since at least five tubes were required for the operational system. The 9558B tube was therefore used.

The arguments used in the selection of the source-detector combination are summarised in Figure 3.8.

	<u>Photovoltaic Device</u>	<u>Photomultiplier Tube</u>
Advantages	Low cost, ruggedness, ease of operation, high responsivity extending to 1.1 μm .	Internal gain therefore high sensitivity realised in practice, large diameter active area.
Disadvantages	Sensitivity limited by amplifier noise, small active area.	Spectral response limited to 0.85 μm , stabilised eht power supply required.
Laser sources	Possible use with Nd:Yag laser at 1.06 μm but prohibitively high cost.	Spectrally suitable lasers e.g. GaAs or ruby, unsuitable on power and p.r.f. grounds.
Arc lamps	Xenon short arc possible candidate but small active area outweighs advantages.	Good combination with Xenon short arc lamp - in simmer mode for chopped system.
Tungsten Filament lamps	High power (600 W) bulbs needed, impractical.	60 W bulb adequate, conveniently mounted in Aldis lamp to give narrow beam.

Figure 3.8 Brief summary of the arguments used in the selection of the source-detector combination.

CHAPTER 4

DESCRIPTION OF OPERATIONAL SYSTEM

4.1 BACKGROUND

The objective of this project was to devise a means to study insect flight activity as a function of height and time in the altitude range 0 - 30 m AGL. The original plan for obtaining the height profile had been to use a single transmitter-receiver pair (as in Figure 1.3) and to sample different heights by changing the angle of elevation of the receiver. It was planned that the selected heights be sampled sequentially and that each sample be long enough to obtain a statistically significant measurement.

The first operational field trial of the prototype system was held in Mali, West Africa during September and October 1978. It formed part of the Centre for Overseas Pest Research (COPR) radar study of the migration of Sahelian Grasshoppers (Riley and Reynolds, 1979). This trial, which is described in more detail in Chapter 7, demonstrated clearly that the sequential sampling method outlined above was not suitable for field operations. The dwell times at each height to obtain a significant sample were found to be excessively long (~ 30 mins) for the aerial densities found. It was therefore difficult to relate the activity at one height with that at another. It was also discovered that the insect aerial density could change rapidly over a narrow height range. From these results it became clear that, for the system to have maximum potential, it should be able

to sample continuously and simultaneously at several different heights. The sample heights chosen for the Armyworm studies were 10, 20 and 30 m AGL, but these were varied according to the experiments planned (Chapter 7).

It was also evident from the Malian field trial that, in terms of supplementing the radar and entomological observations, the most important parameters that the optical system could measure were aerial density and wing beat frequency. Measurements of insect speed and direction were needed to confirm the assumption made in Chapter 2 that insects fly predominantly downwind, but those measurements were of secondary importance for the collaborative studies.

Two types of receiver were therefore developed to make the necessary observations. The Mark I receiver was designed simply to detect insects flying through the sample volume and thereby provide aerial density and wing beat frequency measurements. The Mark II receiver was designed to have the added capability of measuring insect speed and direction. Both of these will be described below.

4.2 RECEIVERS

4.2.1 Mark I (Single Channel)

The Mark I receiver shown in Plate 1 was designed to be simple to deploy, rugged and compatible with operation in hostile field conditions. It consisted basically of a primary (zoom) lens which imaged the sample volume on to the photocathode of a photomultiplier tube.

The receiver body was made from $3/16$ " thick aluminium plate, which gave a strong, rigid and reasonably light construction. The low total weight of 3.5 kg made it possible to mount the Mark I receivers on lightweight and relatively inexpensive photographic-type tripods.

The photomultiplier tube was mounted securely in a split-cylindrical carrier with its photocathode in the image plane of the primary lens. Its dynode chain was of a standard linear design recommended by the tube manufacturers (EMI, 1979). The anode current was amplified by a current to voltage amplifier (see, for example, pp 332, Operational Amplifiers, Burr Brown, 1971) mounted behind the tube. Both the dynode and amplifier circuitry is shown in Appendix A1.

The primary lens used was a 100 - 300 mm zoom lens manufactured by Messrs. Vivitar Ltd.. The zoom facility provided field of view adjustment over the range 8° - 23° which allowed flexibility in the choice of sample volume size and transmitter-receiver separation. The transmission coefficient of the lens was measured to be approximately 0.5 at a wavelength of $0.7 \mu\text{m}$.

A Ramsden eyepiece was incorporated into the receiver so that the field of view could be checked visually. This proved to be an extremely useful feature, particularly during alignment. Insertion of the eyepiece blocked off light to the photomultiplier tube and removed the near infra-red input filter. This filter, which was mounted just behind the zoom lens restricted the radiation incident on the photomultiplier to the range $0.7 - 2.0 \mu\text{m}$ (see Figure 4.1).

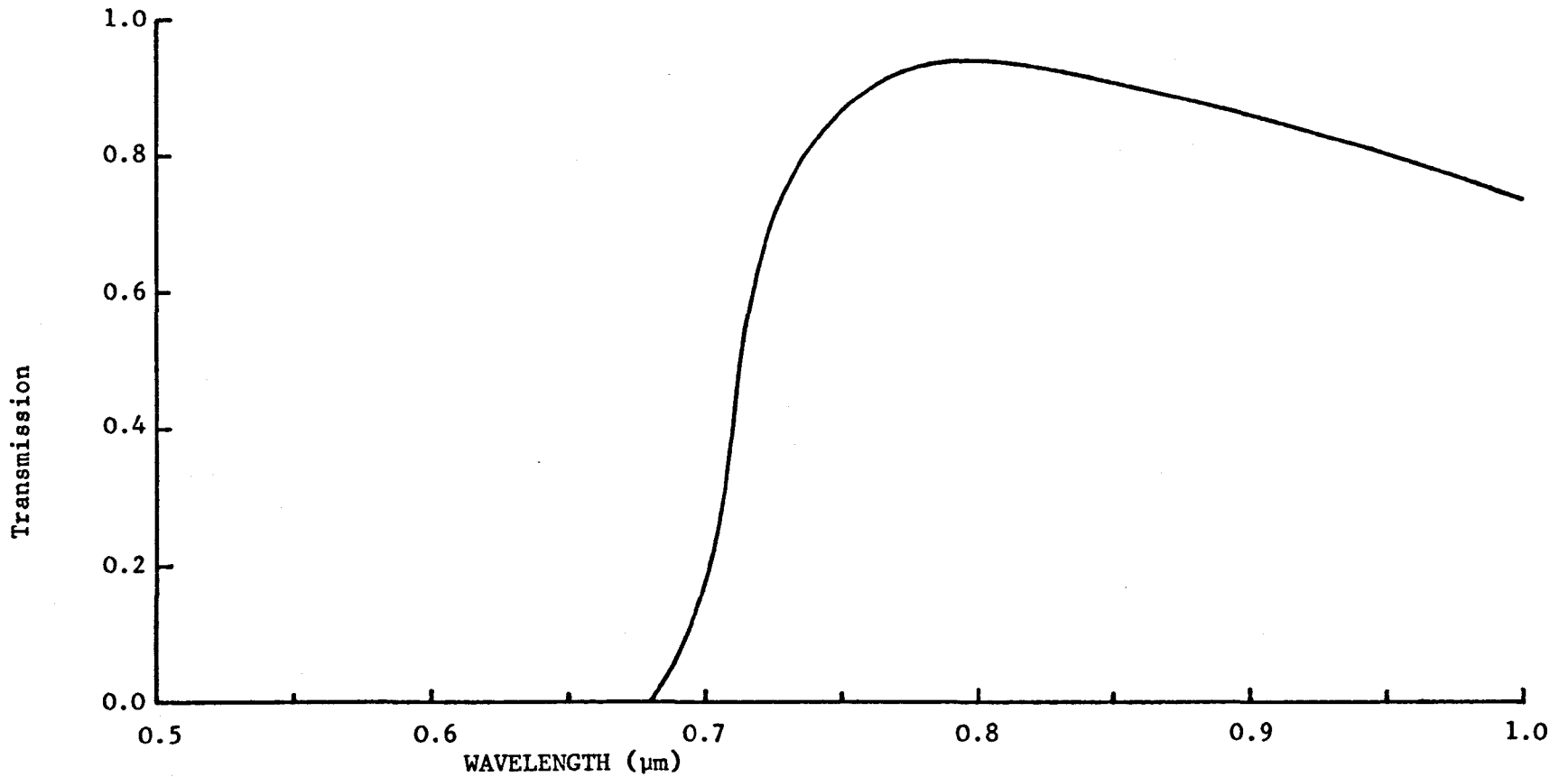


FIGURE 4.1 Transmission characteristic of infra-red glass filter used in receivers and transmitters.

(Type AFV 18, data supplied by manufacturers, Grubb Parsons Ltd.)

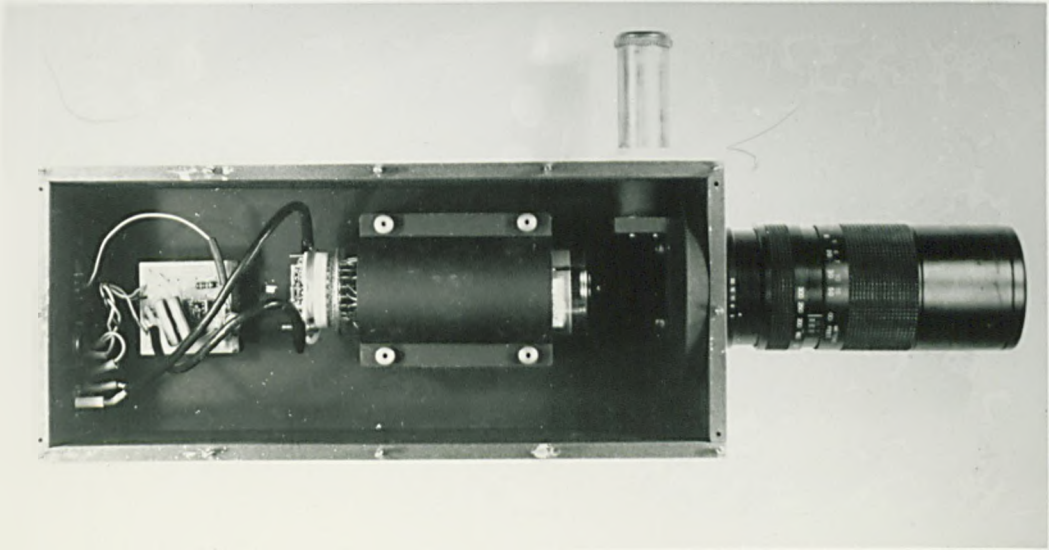


PLATE 1 The Mark I (single-channel) receiver with top cover removed to show the internal layout.



PLATE 2 Mark I receivers with weather shrouds fitted. The Mark II (two-channel) receiver can be seen next to the Landrover.

Since the long wavelength limit of sensitivity for the photomultiplier tube was $0.85 \mu\text{m}$, the receiver sensitivity was effectively restricted to the waveband $0.70 - 0.85 \mu\text{m}$.

In use, the receivers were protected by weather-proof shrouds (Plate 2). These allowed the system to function during the frequent rain storms experienced in Kenya and prevented condensation on the zoom lenses.

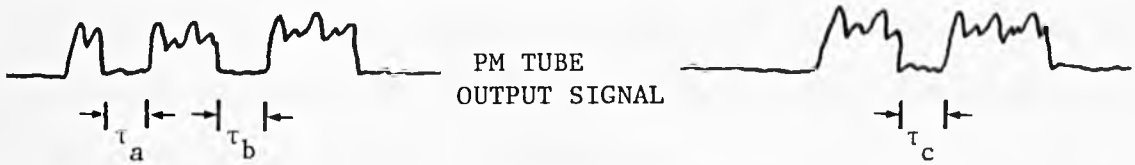
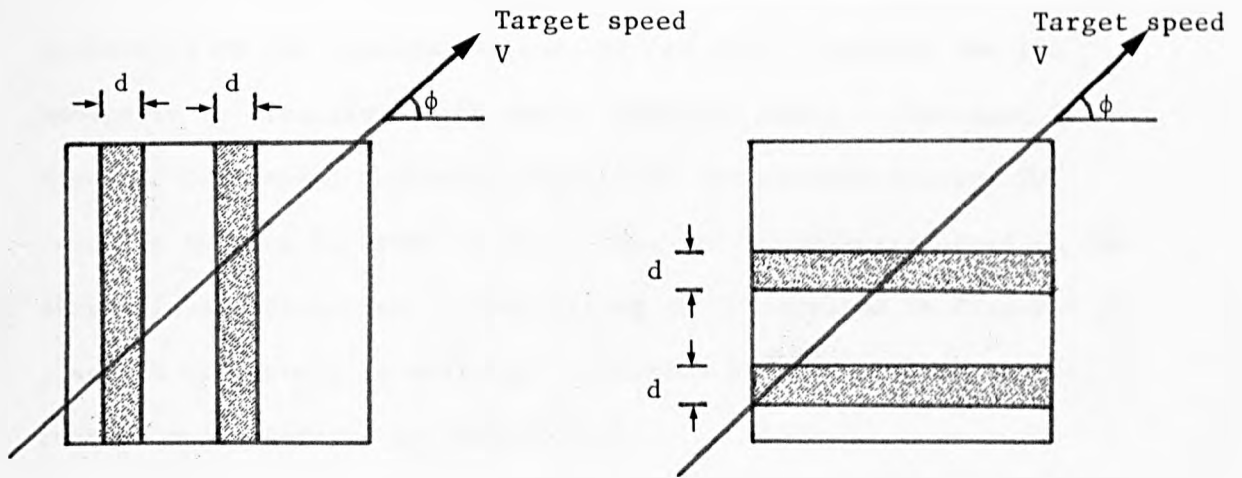
4.2.2 Mark II (Two Channel)

The technique developed to measure target speed and direction will be presented below, followed by a description of the Mark II receiver, which was designed to employ this technique.

The image of the sample volume formed by the primary lens is split into two identical images by a beamsplitter. Each image is focussed on to the photocathode of a separate photomultiplier tube. The image of an insect flying through the sample volume moves across the photocathodes at a speed proportional to the insect flying speed. Optical masks consisting of alternate opaque and transparent bars placed in front of the photocathodes intercept the images as they move across the focal planes and so interrupt the signal to the tube. The time for which the signal is 'off' is proportional to the speed of the image in a direction perpendicular to that of the bars and hence proportional to the insect flying speed in the corresponding direction through the sample volume. The opaque bars are repeated across the mask at the same width to allow averaging of the 'off time'. The

Channel 1

Channel 2



$$\tau_1 = \frac{\tau_a + \tau_b}{2}$$

$$\tau_2 = \tau_c$$

$$V \cos \phi = \frac{d \times R}{\tau_1 \times f}$$

$$V \sin \phi = \frac{d \times R}{\tau_2 \times f}$$

where R is the insect range and f is the focal length of the lens (for $R \gg f$).

$$\text{Hence } V = \frac{d + R}{f} \left(\frac{1}{\tau_1^2} + \frac{1}{\tau_2^2} \right)^{\frac{1}{2}}$$

$$\text{and } \phi = \tan^{-1} \frac{\tau_1}{\tau_2}$$

FIGURE 4.2 Measurement of target speed using optical masks.

width of the transparent bars is incremented across the mask so that inspection of the resulting change of 'on time' resolves the 180° ambiguity in direction which would otherwise exist. The mask in front of the second photomultiplier tube was rotated through 90° relative to that in front of the first, and so measures speed in the perpendicular direction. This action is illustrated in Figure 4.2, a sample trajectory is analysed in Section 5.4 and experimental results are presented in Section 7.2.

This method measures target velocity only in the plane normal to the optical axis of the receiver; data on radial motion cannot be obtained. To measure target track and ground speed the receiver is directed vertically with illumination from the side, a reversal of the normal single channel configuration.

Plate 3 shows the layout of the inside of the Mark II receiver and the corresponding ray diagram is presented in Figure 4.3. The eyepiece-filter arrangement was the same as that used in the Mark I version. The image of the sample volume is formed by the zoom lens approximately 4 cm behind the lens mount. To accommodate the beamsplitter, eyepiece and extra photomultiplier tube the image distance had to be increased by using an intermediate lens. The optical masks were made into 35 mm slides and mounted in slide holders positioned at the image planes of the intermediate lens. The photomultiplier tubes were mounted just behind the slide holders in cylindrical carriages. All the optical components inside the Mark II receiver were mounted on a precision sliding track so that their relative positions could be changed to allow different system

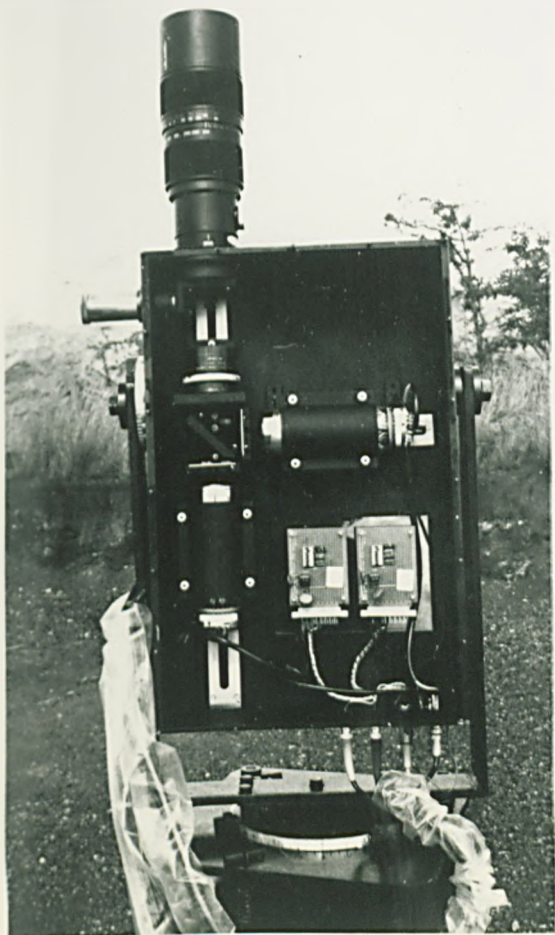
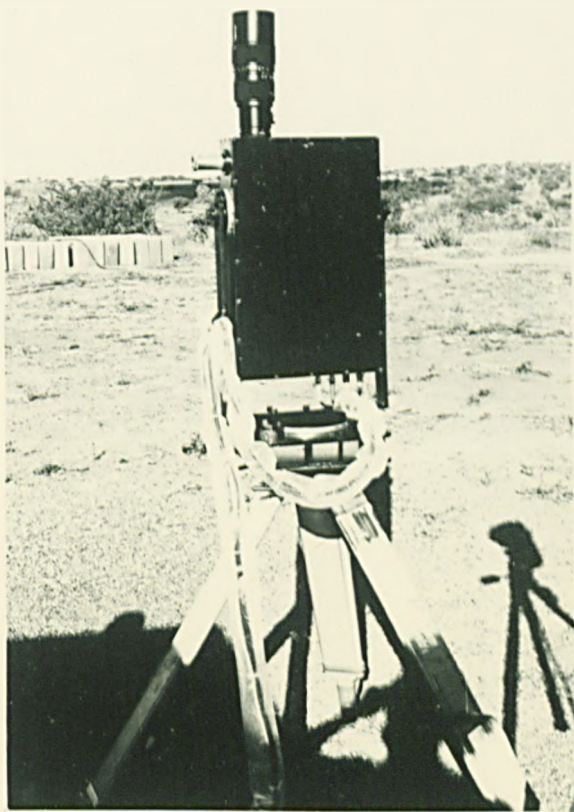


PLATE 3 The Mark II (two-channel) receiver with top cover removed to show the internal layout.

PLATE 4 The Mark II (two-channel) receiver mounted on theodolite tripod.



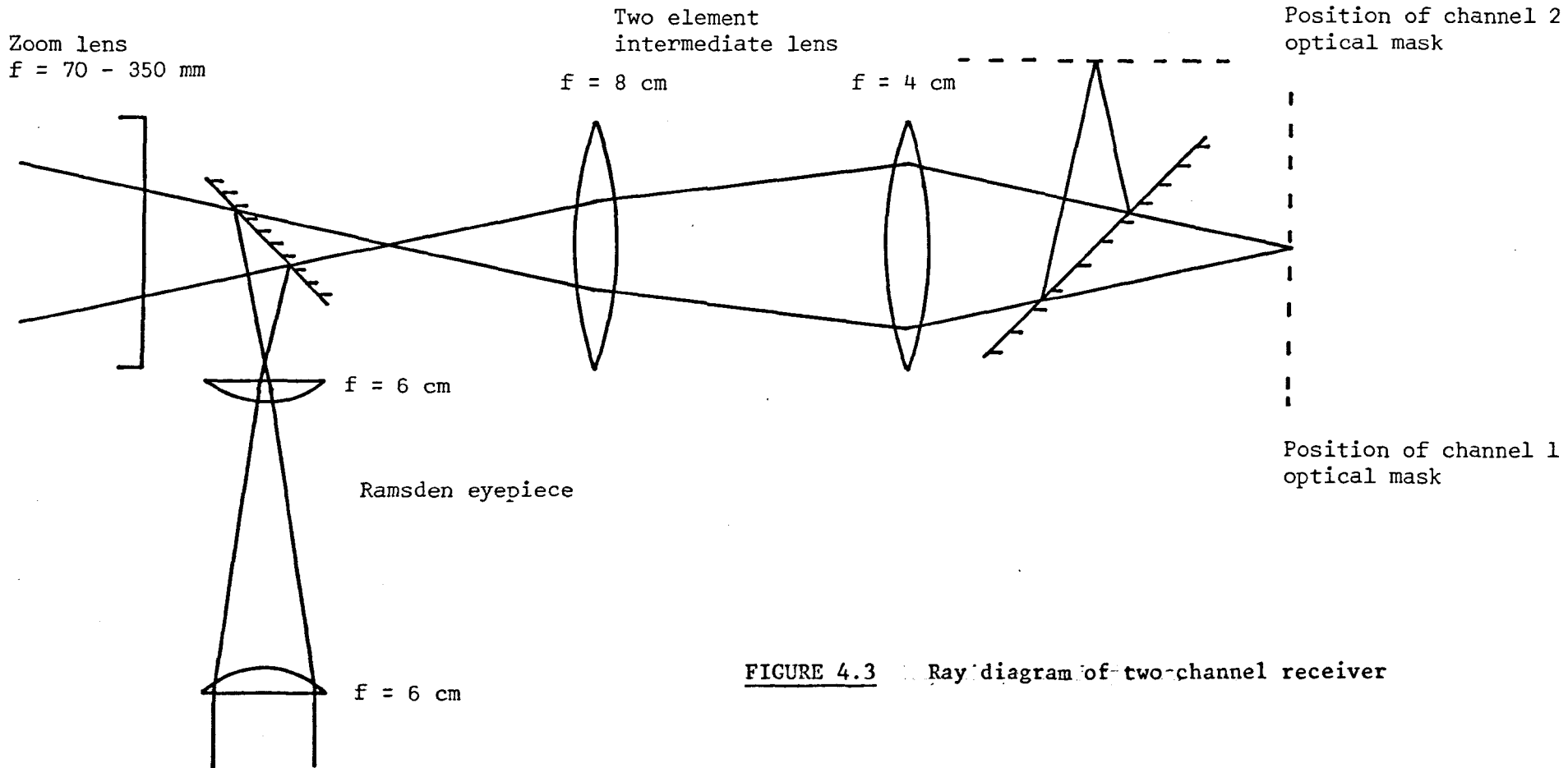


FIGURE 4.3 Ray diagram of two-channel receiver

configurations to be used when necessary.

Two current to voltage amplifiers were mounted in the receiver and both tubes were operated from the same non-automatic EHT supply. The dynode and amplifier circuits were the same as those used in the Mark I (Appendix A1). A 15 m long composite cable comprising two signal, one eht and one amplifier power supply cable connected the receiver to the main control electronics.

The Mark II channel receiver was significantly larger than the Mark I, and despite being made out of aluminium, required a heavy duty theodolite tripod to support it. A special mounting was designed which allowed movement about three axes and accurate leveling. The receiver is seen mounted in Plate 4.

4.3 TRANSMITTER

The transmitter, which as we have already seen (Section 3.5) was to be based on a tungsten filament lamp, needed to be rugged and lightweight and to have a narrow beamwidth. These features were found to be conveniently combined in an Aldis Signalling Lamp (Plate 5). This lamp uses inexpensive and easily replaceable 11 volt 60 Watt bulbs which give a power output of about 1.2 W in the waveband 0.7 - 0.85 μm (Section 3.4.1(a)). The beam shape of the standard lamp was found by experiment (Section 3.4.1(a)) to be as shown in Figure 4.4, and this shape may be expanded to that shown in Figure 4.5 by simple axial movement of the lamp's parabolic reflector.

Visible radiation was filtered from the lamp output by a 6 inch

Figure 4.4
INTENSITY PROFILE ACROSS FOCUSSED ALDIS BEAM

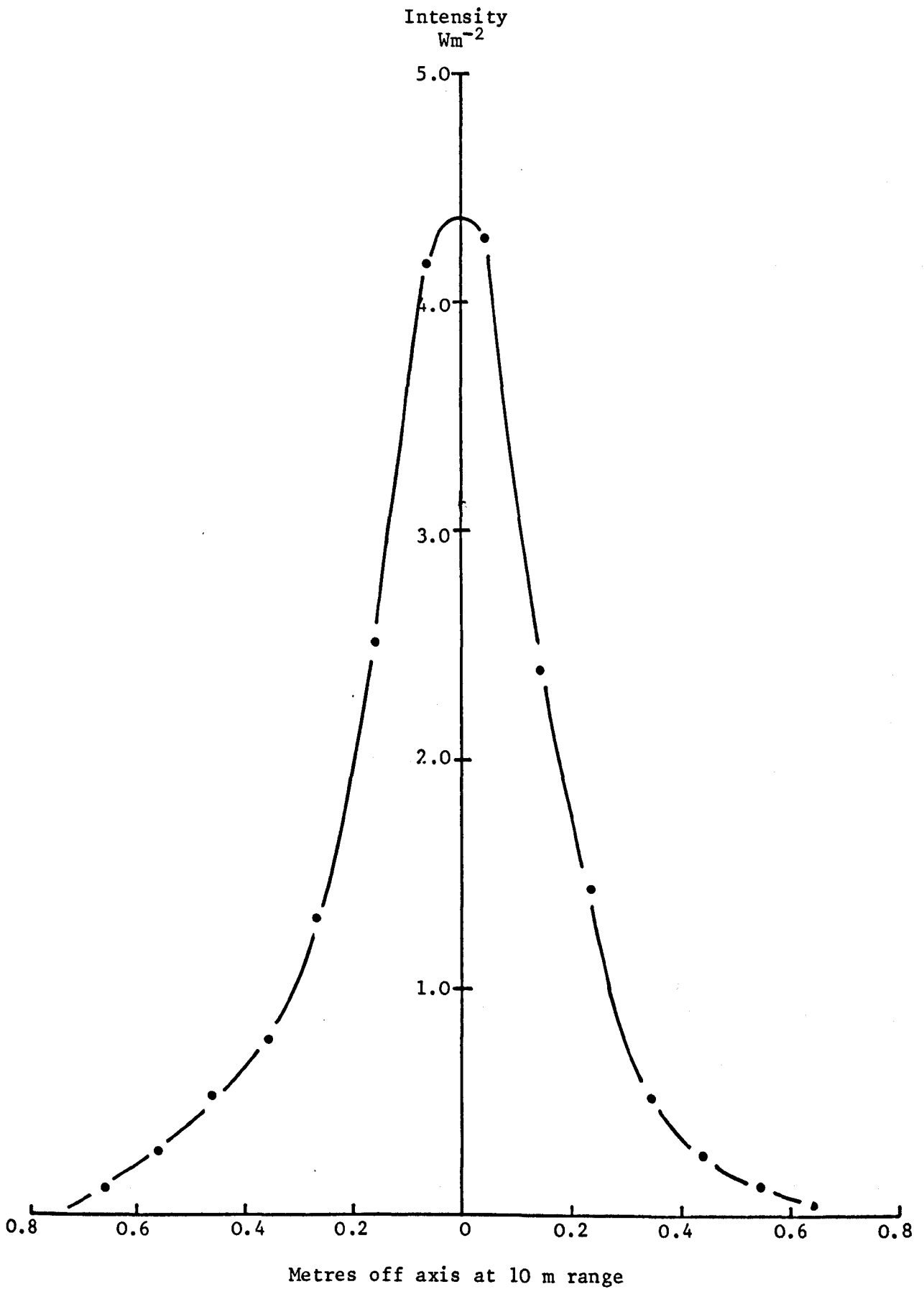


Figure 4.5

INTENSITY PROFILE OF DEFOCUSSED ALDIS BEAM AT 10 M RANGE

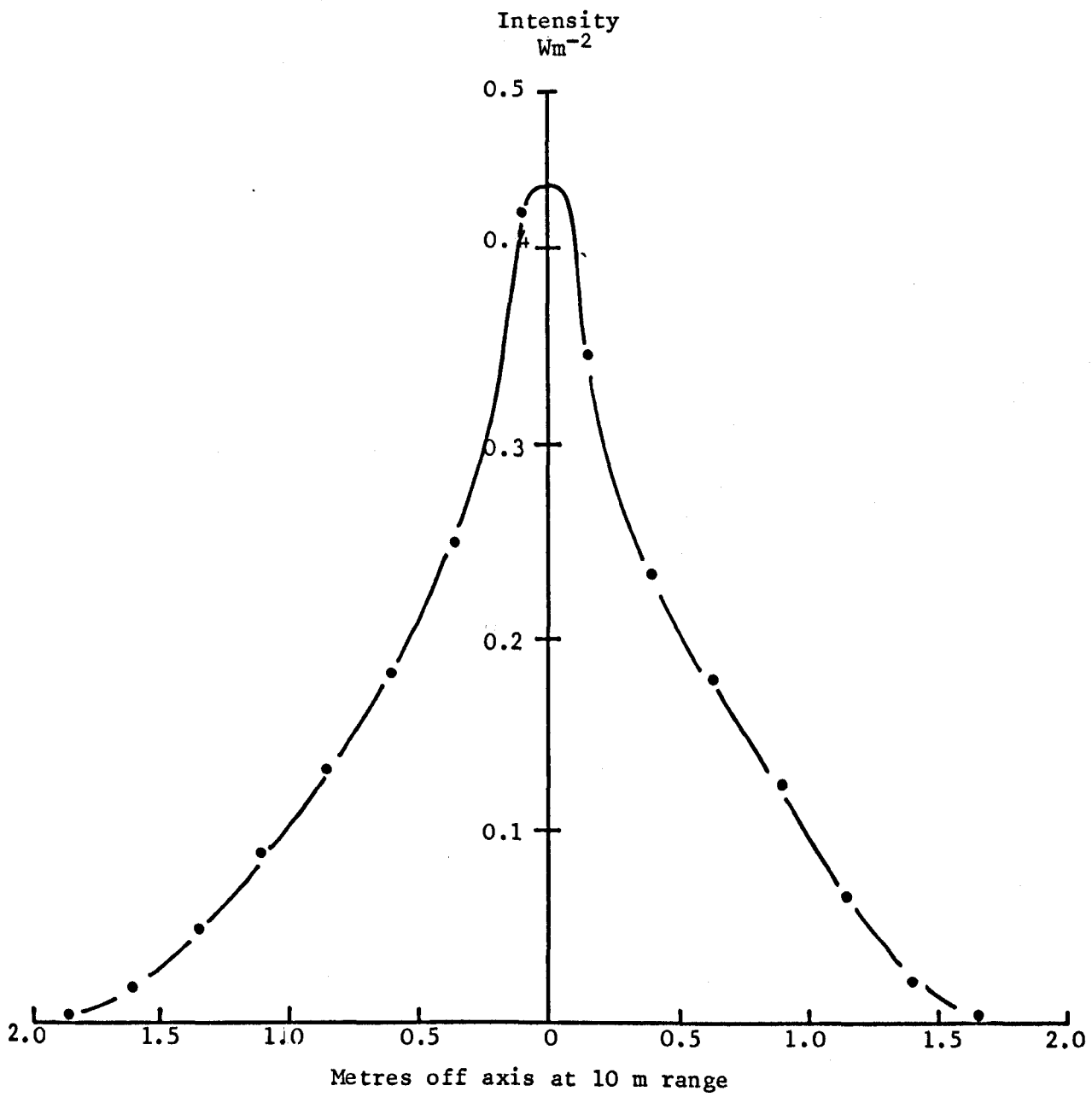




PLATE 5 Aldis lamp with
infra-red glass filter
in place.

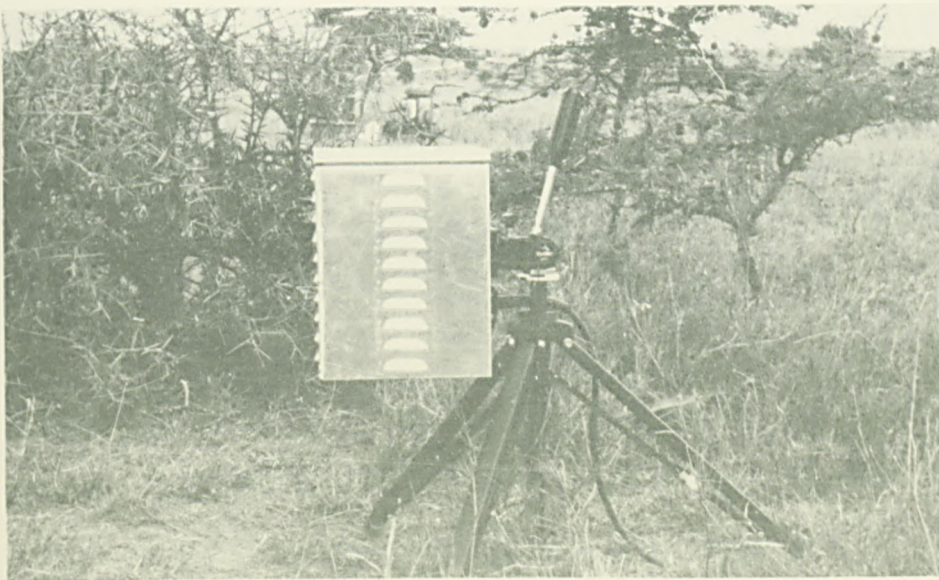


PLATE 6 Aldis lamp with protective weather shroud.

diameter infra-red glass filter mounted on the front. The transmission characteristic of this filter was identical to those used in the receivers ('cutting on' at 0.7 μm , see Figure 4.1). During operations, the absorbed power increased the temperature of the glass filter to typically 40^oC above ambient. It was therefore necessary to stop rain from coming into contact with the filter to prevent cracking. Protective covers with perspex windows were used for this purpose and one is shown in use in Plate 6.

The aldis lamps were easily mounted on lightweight photographic tripods and powered by a 12 v switched-mode power supply, which had a capacity of 30 amperes and weighed only 2 kg (Farnell Instruments Ltd., type G12-30).

4.4 OPERATIONAL SYSTEM

A block diagram of the operational system is shown in Figure 4.6. It was organised to fulfil two roles viz. to make aerial density and wing beat frequency measurements continuously and automatically at three different heights throughout the night, and secondly to measure insect speed and direction at a chosen height and at selected times during the night. The system was designed to be operated from and transported in a long wheelbase landrover, with electrical power being supplied by a 2 kVA 240 v petrol generator.

The continuous aerial density and wing beat frequency measurements were made using three separate transmitter-receiver pairs. In the standard configuration the transmitters were all vertically pointing and powered from the 12 v 30 amp switched mode

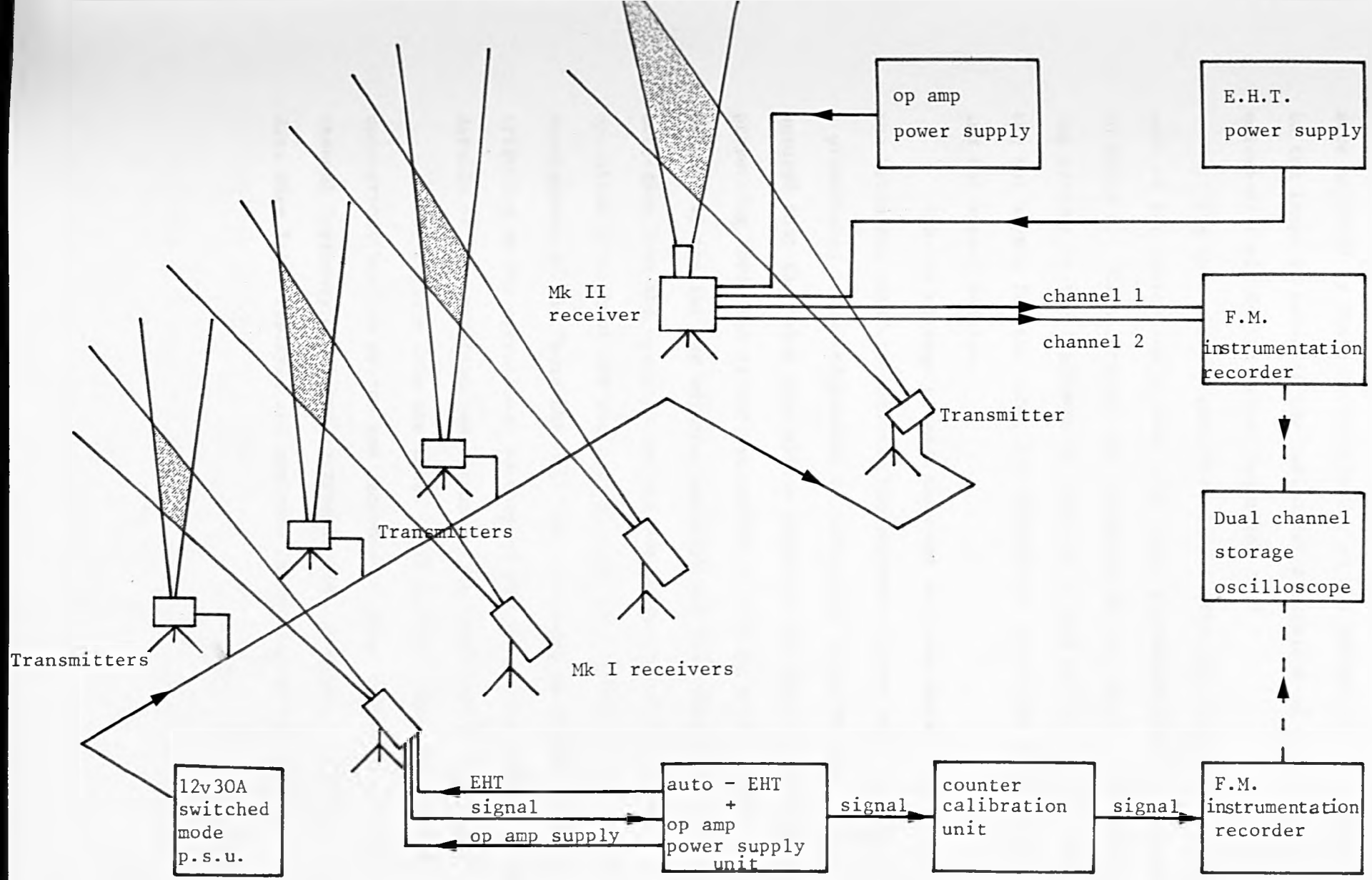


Figure 4.6 Schematic Diagram of Operational System

power supply, which was positioned close to the transmitters to reduce power loss along the cables. The transmitter beamwidths were adjusted by suitable positioning of the parabolic reflectors in the lamps to maintain the horizontal dimensions of each sample volume at their design values (equation 2.9).

The three Mark I receivers used in the continuously recording part of the system can be seen with their corresponding transmitters in Plate 7. Each receiver was connected to the control and recording systems in the landrover by three 30 m long cables, which carried the eht supply for the tube, the operational amplifier power supply and the signal voltage.

The eht voltage to each tube was adjusted automatically by the "auto-ehv unit" to maintain the photomultiplier anode current at a preselected value independent of background illumination. This ensured that the tubes were always adjusted for their optimum gain, preventing them from either saturating or lacking sensitivity. Originally the eht was adjusted manually but this required constant attention from the operator and was not suitable for continuous operation throughout the night (e.g. from 1900 - 0600 hours). The development of the "auto-ehv unit" was therefore an important contribution to the operational success of the three level system. The details of its operation and circuitry are described in Appendix A3.

The signals from the three receivers were fed through the counter-calibration system and recorded on three channels of a four channel frequency modulated instrumentation recorder. The recorded data were later replayed and analysed in England by the methods



PLATE 7 The Operational layout in the field
(Hopcraft Ranch outbreak site, Kenya 1980)

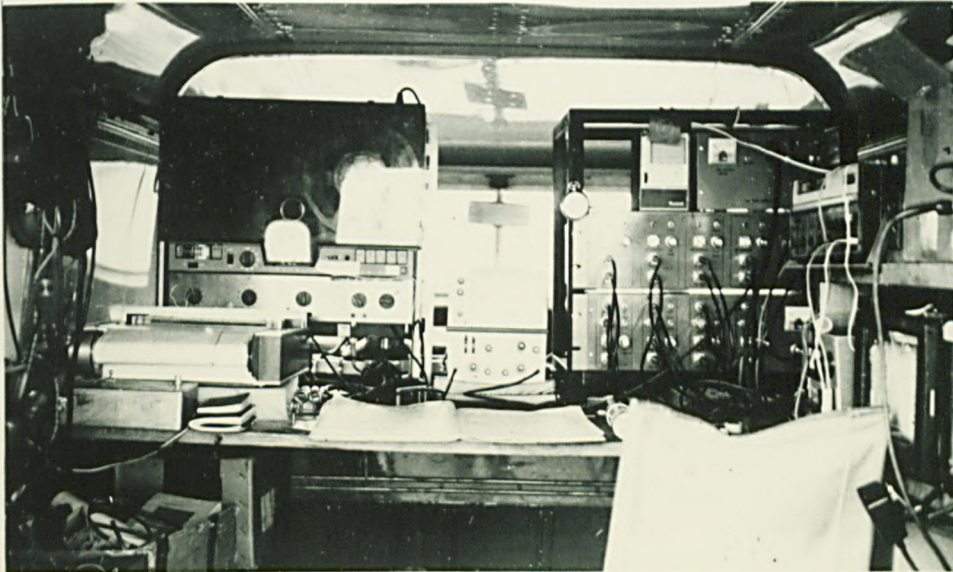


PLATE 8 The control and recording equipment mounted in the rear of the Landrover (Instrumentation recorder to left, monitor oscilloscope in centre, autoht and counter/calibration to right, anemographs on extreme right.)

described in Chapter 5. This "after the event" analysis was necessary because it was impractical for the experimenter to simultaneously monitor the recording and conduct the analysis using currently available methods. It was, however, often found useful to have some measure of what was happening, while it was actually happening, so that changes to observational strategy could be made if necessary. A counter system was therefore developed which was capable of limited real-time analysis. It formed part of the counter-calibration unit and worked in the following way. If the signal voltage from a particular receiver rose above a preset level, indicating the presence of a target in the sample volume, an 'event' was counted by marking the appropriate channel of a four channel event recorder. These marks provided an indication in real time of the relative activity at different heights (see, for example, Figure 7.23). It has enhanced the automatic capability of the system by allowing the operator to look back at activity which occurred during periods when he was otherwise engaged. It has also proved useful for conveniently directing attention towards periods meriting detailed analysis in England. The calibration function of this unit will be described in the next section, and the circuitry appears in Appendix A4.

A dual channel storage oscilloscope was used to monitor the received signals as they were recorded on the instrumentation recorder, a voice commentary being put on the fourth channel. A tape speed of $15/16$ ips was employed which gave a bandwidth of 300 Hz and a playing time of approximately eight hours for a 2300 feet long

instrumentation tape. The control and recording electronics are shown mounted in the rear of the landrover in Plate 8.

The "speed and direction" equipment was made independent of the three channel section described above, and was only operated at selected times. The transmitter was similar to those used above and used the same power supply. The eht voltage for the two photo-multiplier tubes in the receiver was adjusted manually and the two signal voltages were recorded on two channels of a second instrumentation recorder. The two data channels were monitored by the storage oscilloscope when necessary. The method of analysing the data collected by this system is described in Section 5.4 and some of the results are presented in Section 7.2

4.5 CALIBRATION METHODS

In order to maintain a high level of confidence in the results obtained from the automatic system it was necessary to check regularly the following parameters.

- (i) Receiver performance.
- (ii) Transmitter-receiver alignment.
- (iii) Transmitter performance.
- (iv) Instrumentation recorder tape speed.

The methods used for calibrating these parameters will be discussed in turn below.

4.5.1 Receiver Performance

The "auto-eht unit" controls the gain of each photomultiplier tube and as noted in Section 5.2 it is necessary to know the gain in order to calculate the volume of air sampled and hence the aerial density. One method adopted to measure the receiver gain was to note the receiver response to a known light flux incident on the photocathode. A small unit was constructed which contained an infra-red emitting 'beta light' manufactured by Messrs. Saunders Roe Developments Ltd.. This acted as a standard source and consisted of a glass envelope (5 x 5 x 2 mm), coated on the inside with an infra-red emitting phosphor and filled with tritium gas, which is a low energy β -emitter with a half life of approximately 9 years. The device emits continuously in the near infra-red (650 - 950 nm) and has a total power output of 100 nW. It was mounted behind a segmented rotating disc to give a chopped signal. The unit was routinely positioned at a range of 2 m at the centre of the receiver field of view. It is shown in Plate 11 mounted on a vertical post.

It was not practical to use this unit to check regularly the gains of the three receivers since this procedure would have required the operator's attention every 15 minutes throughout the night.

Instead, in the field work conducted so far, the receiver gains have been inferred from concurrent radiometer measurements of the background illumination (see Section 5.2). Ideally an automatic method is required in which a standard illuminator is contained within each receiver and at regular intervals (e.g. every 15 minutes) a modulated signal from it is directed onto the photocathode of each

photomultiplier tube. The calibration signal would thus be recorded with the normal data and could be read off during analysis.

4.5.2 Transmitter-Receiver Alignment

The question of alignment has already been considered (Chapter 2) and its effect on the size of the sample volume has been reduced by the choice of transmitter beamwidth and receiver field of view. Checks have been made during operations by viewing the unfiltered aldis beam (normally made visible by scattering from airborne dust) through the receiver eyepiece. Experience has shown that if the receiver and transmitter tripods are firmly positioned then the correct alignment is maintained. It would, of course, be preferable to have some system of regularly testing the alignment of each transmitter-receiver pair without undue disturbance. However it has not been possible to develop such a procedure which is compatible with field operations.

4.5.3 Transmitter Performance

The calculation of the effective volume of air sampled used in the aerial density computations assumes a constant transmitter power output. Ideally then the output should have been monitored regularly to test this assumption, and if it was found invalid then the measured power output should have been used in the calculations. However, spot checks have shown that the output power remained constant within $\pm 5\%$ during the observational periods. The radiant output from a new bulb was found to decrease, from an initially high

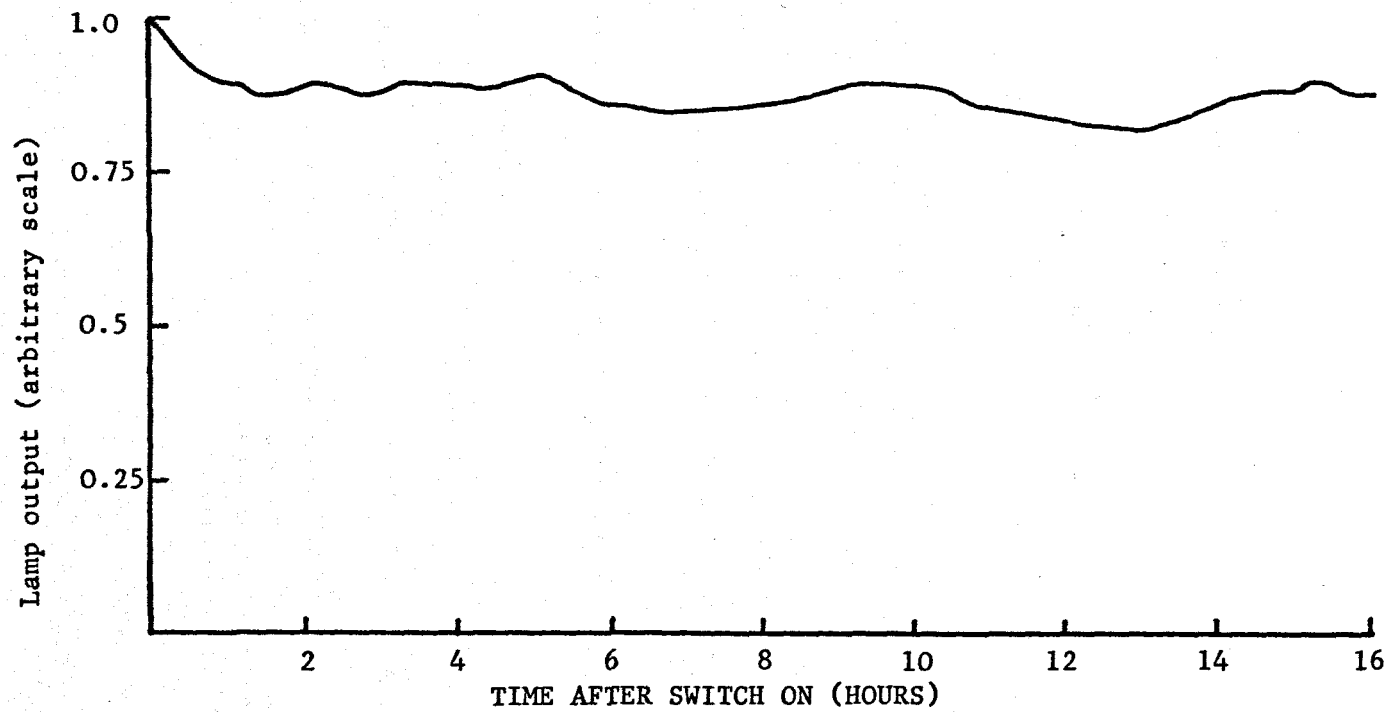


FIGURE 4.7 Measured power output of Aldis lamp with a new bulb as a function of time after switch on.

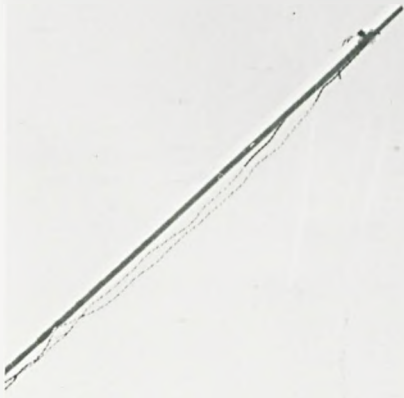
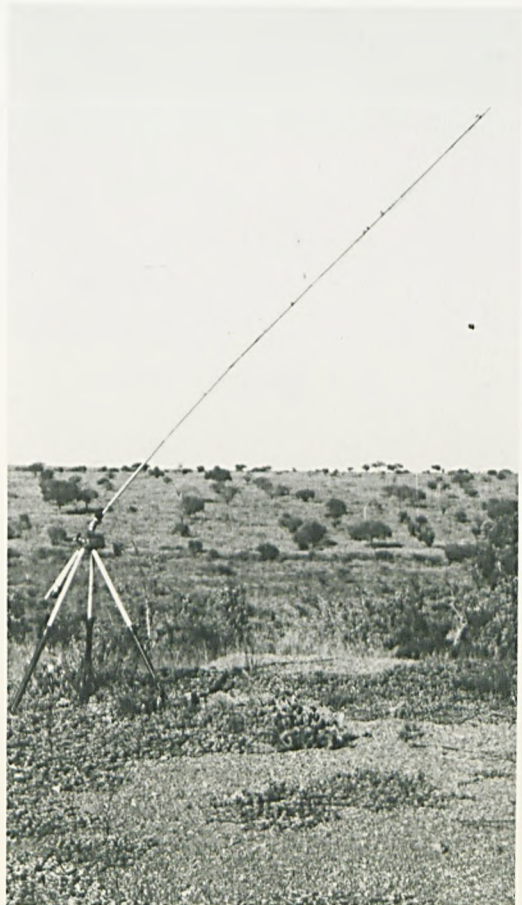


PLATE 9 Artificial Insect target.

PLATE 10 Artificial Insect target on suspension system.



value, during the first two hours of operation and then maintain a steady output (Figure 4.7). After 50 hours of use the reflector in the prefocussed bulbs was found to be slightly blackened but the corresponding reduction in output power was only 3%.

Although it is clear that the output power of the lamps can be confidently assumed to be reasonably constant it would, of course, be slightly desirable to have regular confirmatory measurements. It is envisaged that a small photodiode mounted on the front of each lamp to intercept a small fraction of the light flux would be suitable. The output of each photodiode could then be recorded on the appropriate channel of the tape recorder at, for example, 15 minute intervals after the receiver calibration signal.

A procedure was adopted to measure occasionally the transmitter output indirectly. This involved the use of an artificial insect target, which was developed to provide a known target at a specified range. It allowed field tests to be made on the combined transmitter-receiver performance and was used as an aid in alignment experiments. A vane, the approximate size of the Armyworm open wings, was attached to the spindle of a small d.c. motor (Plate 9). This was supported in space by a structure similar to a large fishing rod (Plate 10). Rotation of the vane at the appropriate rate crudely simulated the insect wing beat action (Figure 7.1).

4.5.4 Instrumentation Recorder Tape Speed

During analysis if the replay speed of the tape recorder differs from that when the data were recorded, then the wing beat

frequencies will be shifted from their true value. The performance of the recorder was monitored by recording a short burst (~ 1 sec) of a signal of reliably known frequency and amplitude, at 15 minute intervals, in parallel with the data. This signal was then used during analysis to confirm that the recorder was performing correctly. The circuitry used in this system is described in Appendix A5, and in practice formed part of the counter-calibration unit. The 48.12 Hz calibration signal was derived from a 100 k Hz quartz oscillator and was inserted on to all tape recorder channels every 15 minutes. In the analysis of the data collected so far no significant error in the replay speed has been found in any of the recordings. Timing marks were also put on the fourth channel of the event recorder used in the counter system to aid interpretation.

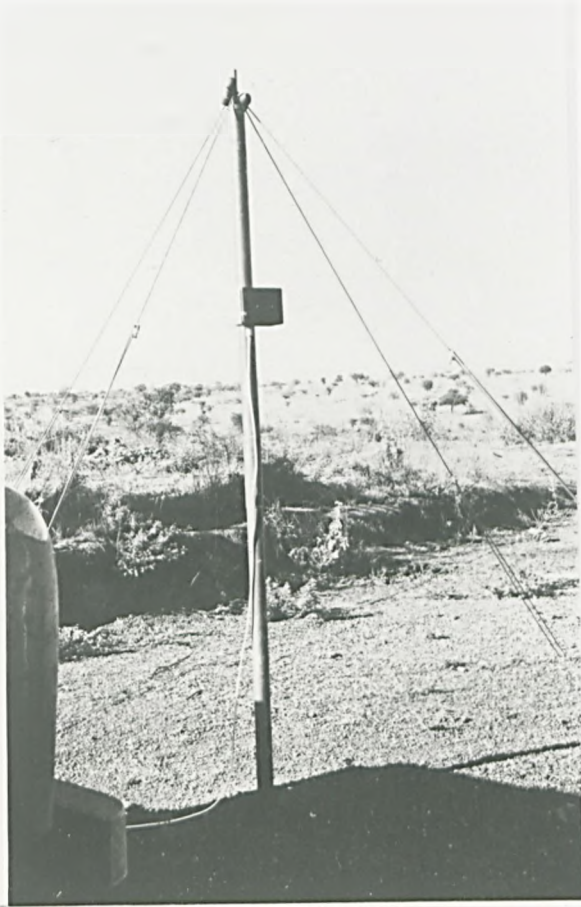


PLATE 11 Beta-light
calibration
unit.

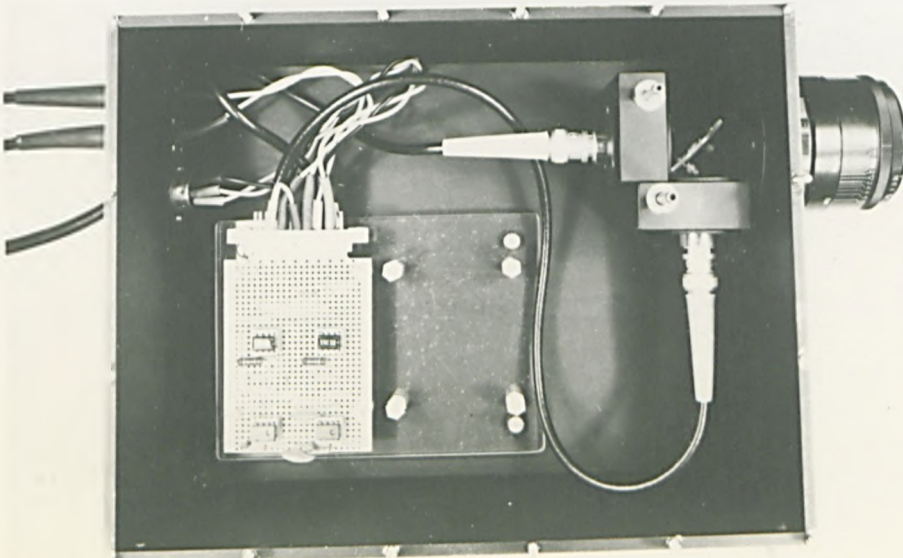


PLATE 12 Internal layout of laboratory receiver.

CHAPTER 5

DATA ANALYSIS

5.1 DESCRIPTION OF TYPICAL SIGNALS

The received light flux from a flapping insect consists of a modulated component which is scattered from the wings superimposed on a steady component which represents scattering from the insect body. Generally, because of the difference in the surface areas of the body and wings, the amplitude of the wing beat modulation is much larger than the body component. These features are illustrated in Figure 5.1 where typical signals from a laboratory, field and an artificial specimen are presented. The d.c. component in the case of the artificial insect target is abnormally large because of the large surface area of the motor body (Section 4.5.3). The shape of the received signal (the wing beat pattern) is discussed fully in Chapter 6. Here it is sufficient to note that the main peak is due to scattering from the wings on the downbeat and the small peak corresponds to the upbeat. The fundamental modulation frequency is the wing beat frequency but the distribution of power between the harmonics depends on the orientation of the insect to the receiver (Section 6.1).

The horizontal dimension of the sample volume was arranged so that, for the highest likely wind speed and a wing beat frequency of 50 Hz, at least five wing beat cycles were recorded as the insect

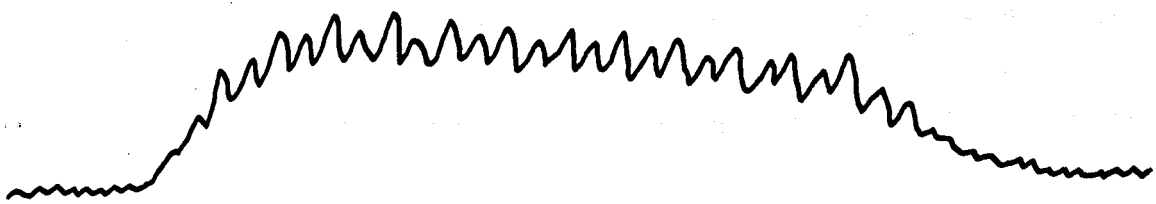
20 mS



(a) Tethered flight in laboratory.



(b) Natural flight in the field.



(c) Artificial insect target

FIGURE 5.1 Typical signals received from different specimens.

traversed the beam. Signals lasting for twenty wing beat periods were often obtained during calm conditions.

The size of the sample volume was arranged so that even at high densities (approximately one insect per 10^3 m^3) on average only one insect transected it at a time. The problem of unravelling multiple frequencies and harmonics was thus avoided. It should be noted, however, that in principle, the frequencies of several individuals simultaneously crossing the sample volume can be detected since the signals from each insect simply add at the receiver. Interference effects between radiation scattered from different insects are negligible because (a) the wavelength of the radiation is small compared to the likely path differences and, (b) the coherence length of the tungsten filament lamp is very short.

In the case of 3 cm wavelength radar interference effects pose serious problems for insect studies. When there are a few targets simultaneously within the pulse volume the individual returns interfere at the receiver and quantitative interpretation of received signal is very difficult.

In the radar case the calculation of aerial density simplifies when there are many targets within the pulse volume because the interference effects are smoothed out and volume reflectivity can be measured. However, wing beat frequency measurements are not normally possible when there is inter-target interference, which represents a serious limitation on radar observations of high density phenomena. The independence of the

optical system from these effects is therefore a valuable feature.

The above summary of the nature of the signals received by the optical system from flying insects is followed in the next three sections by descriptions of the methods used to calculate insect aerial density, wing beat frequency and flying speed and direction. One of the important developments envisaged for the optical system is the provision of automatic in-field data analysis. This is discussed briefly in the final section.

5.2 CALCULATION OF AERIAL DENSITY

The results presented here follow from the method described in Section 2.4 for the calculation of the effective volume sample rate V_E . If the aerial density of insects is ρ and the rate of detection is \dot{n} then

$$\dot{n} = \rho V_E \quad (5.1)$$

In practice, in order to obtain reasonable statistics \dot{n} was determined by counting the number of insects detected over a period of 30 minutes. However from the data recorded, averages over other periods can be determined if needed.

The way the effective volume sample rate depends on the environmental parameters (wind speed, direction and background illumination) is illustrated below for the particular case of the sample volume positioned at 10 m AGL at the Hopcraft Ranch Armyworm

outbreak site, Kenya 1980 (see Section 7.1).

As noted in Section 2.4.2, the values of photomultiplier tube gain used for the calculation of V_E were inferred from the measured values of nocturnal irradiance. This was considered a satisfactory interim method after spot measurements of the applied EHT to the tubes had shown a significant correlation at the 5% level with the radiometer output (VRAD). The least squares fit linear regression line shown on the scatter plot of Figure 5.2 has the form

$$\text{EHT} = a \times \text{VRAD} + b \quad (5.2)$$

where $a = 45.2 \pm 14.8$ (95% confidence interval)

$b = 65.2 \pm 83.0$ (" " ")

and explains 70% of the variation.

Measurements of the applied photomultiplier voltage E and the resulting gain G for tube used in this sample volume are shown in Figure 5.3. The least squares polynomial fit to the data is represented as the solid line and has the equation

$$\text{Log } G = -4.29 + 1.77 \times 10^{-2} E - 1.11 \times 10^{-5} E^2 + 2.51 \times 10^{-9} E^3 \quad (5.3)$$

The receiver gain was thus calculated using equations (5.2) and (5.3) from values of VRAD averaged over half hourly periods, which were obtained from the radiometer records. It should be noted that VRAD represents a logarithmic scale of irradiance.

The system parameters relevant to the sample volume under

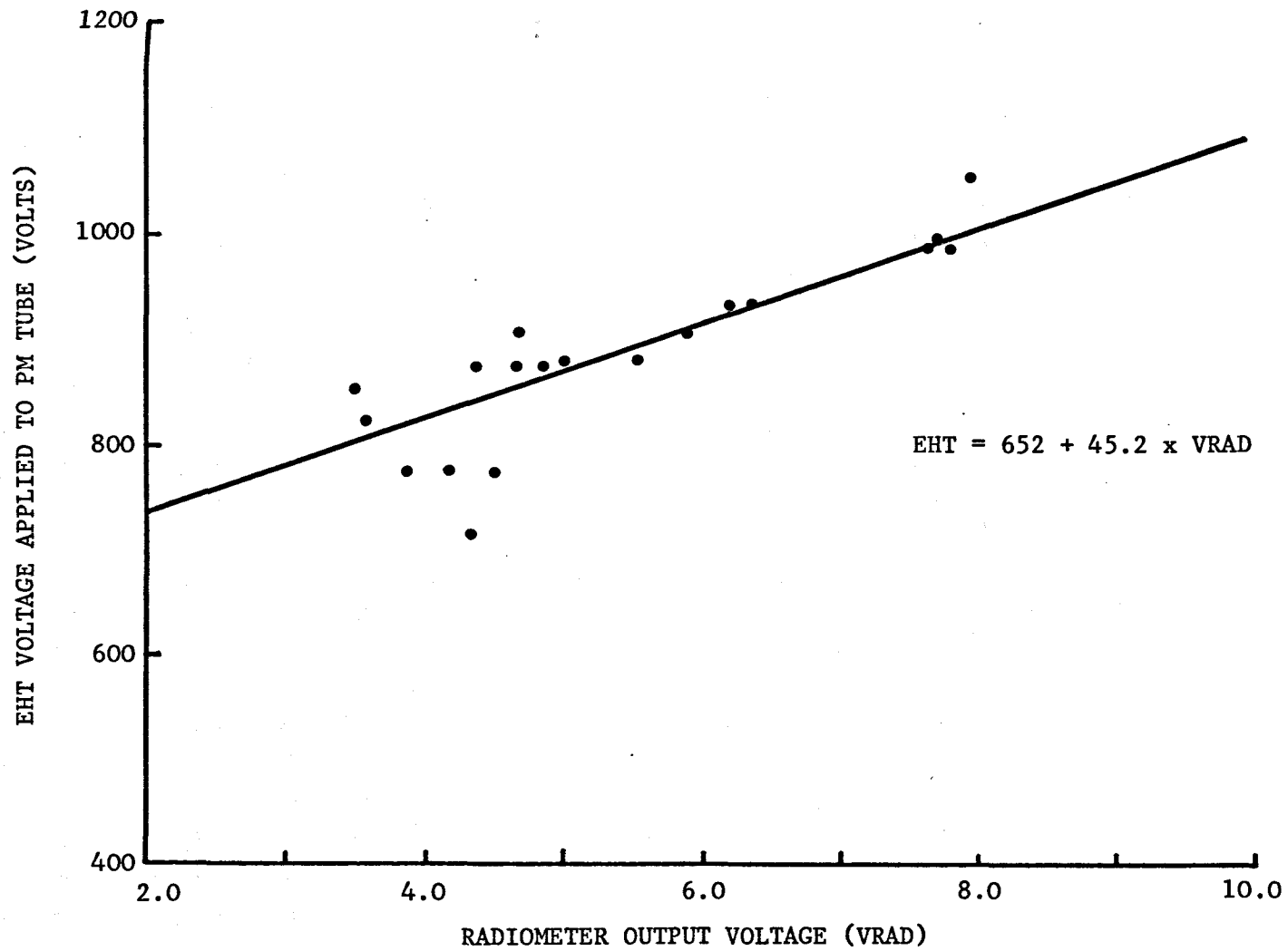


FIGURE 5.2 Spot measurements of EHT applied to one of the single channel receivers (Ch 2) and radiometer output at Hopcraft Ranch outbreak. The solid line represents the least squares fit regression line.

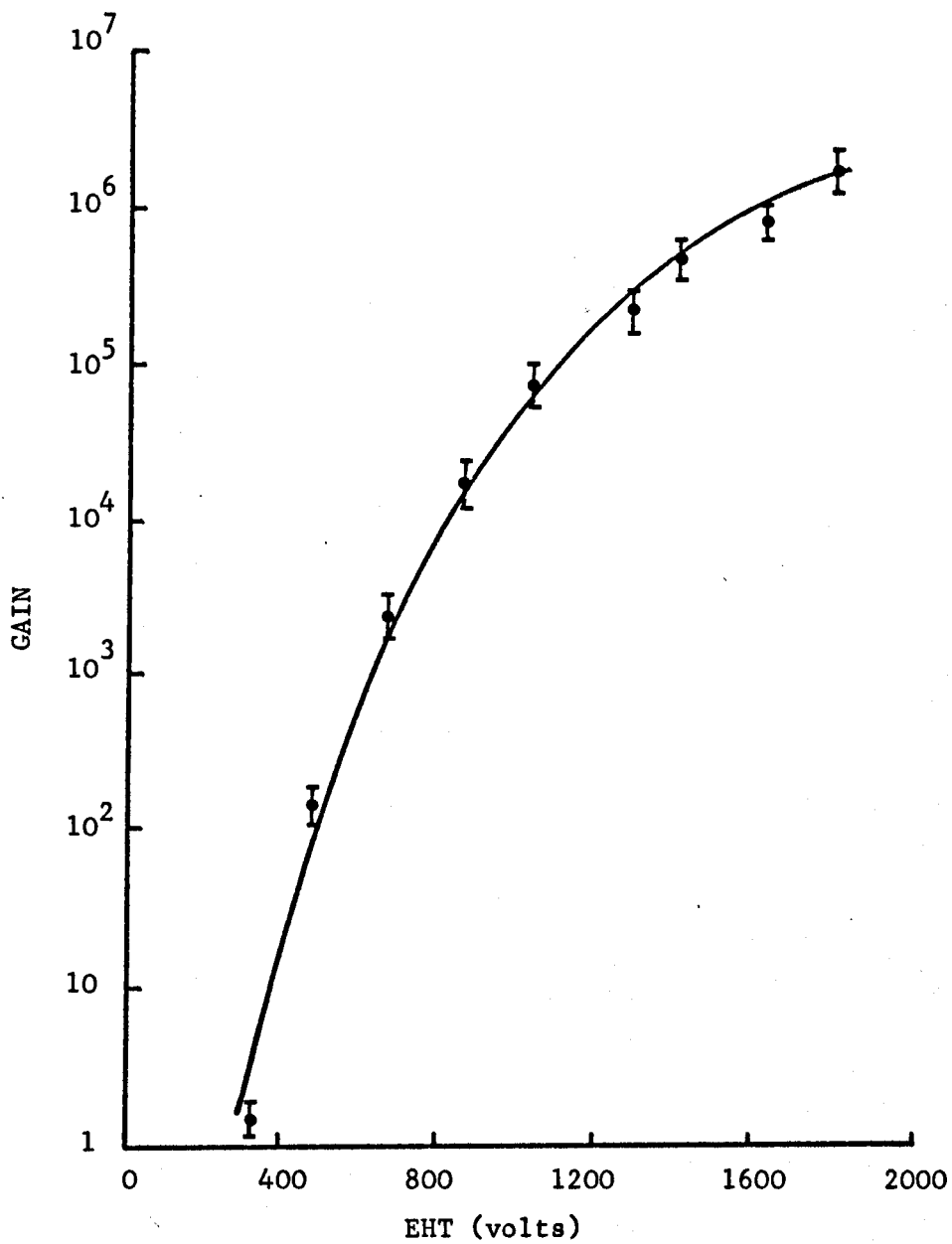


FIGURE 5.3

Measured gain as a function of applied voltage for 11-stage photomultiplier (EMI type 9558B). Solid line represents polynomial least squares fit (equation (5.4) in text).

consideration are listed in Table 5.

TABLE 5

Height of sample volume (mid pt)	10 m
Upper and lower limits of sample volume	5,15 m
Transmitter beamwidth (FWHM)	0.03 rad.
Receiver field of view	23°
Receiver elevation	45°
Transmitter-receiver separation	10 m
Receiver bearing from transmitter	0°

One of the advantages of the narrow transmitter beamwidth adopted in this system can be seen in Figure 5.4. This shows the computed value of the volume sample rate to be largely independent of wind direction for a typical wind speed of 3 ms^{-1} and $\text{VRAD} = 8.0$ (corresponding to starlight conditions). The calculation of V_E for randomly directed insects, and the real time interpretation of the aerial activity as recorded by the counter system, were therefore both simplified considerably.

The sensitivity of the effective sample rate to the background illumination level is clearly demonstrated in Figure 5.5 where V_E is plotted against the ratiometer output VRAD. The horizontal

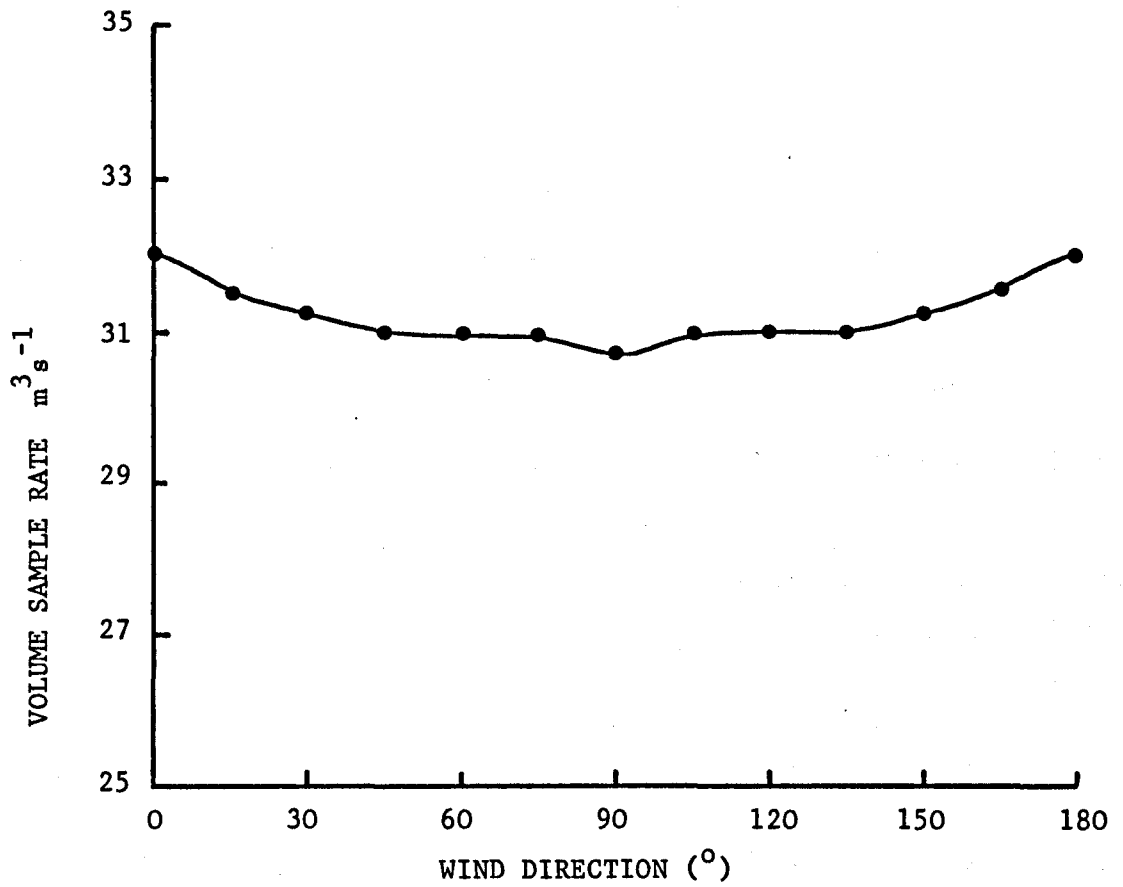


FIGURE 5.4 Volume sample rate as a function of wind direction for $V_w = 3.0 \text{ ms}^{-1}$, $\text{VRAD} = 8.0 \text{ v}$.

scale of VRAD has also been calibrated in terms of irradiance and approximate photomultiplier gain. The maximum irradiance level for operation is approximately equivalent to the illumination from full moon at zenith ($L = 10^{-3} \text{ W m}^{-2}$, in the waveband 375 - 825 nm). One practical limitation of this for the Armyworm studies was that the system was not operational until about 20 minutes after sunset and therefore missed the dusk take off flight (Section 7.3). Although this represented a serious limitation it has not prevented the collection of very useful data (Section 7.3). Plans have been made (Appendix E) to reduce the susceptibility of the system to background radiation but the demonstration of the usefulness of the system was considered the major priority.

The effective volume sample rate is related to the effective cross sectional area A_E according to equation (2.34) thus

$$V_E = A_E (v_i + v_w)$$

The dependence of A_E on the wind speed v_w for different values of VRAD is shown in Figure 5.6. The decreasing nature of A_E with increasing wind speed is a direct result of the transit time condition imposed in the calculation. The effective volume sample rate plotted in Figure 5.7 against v_w exhibits a 'humped' structure characteristic of the product of a decreasing and an increasing function, and the rapid fall off of V_E after the peak value for all VRAD values is a consequence of the narrow beamwidth of the transmitter.

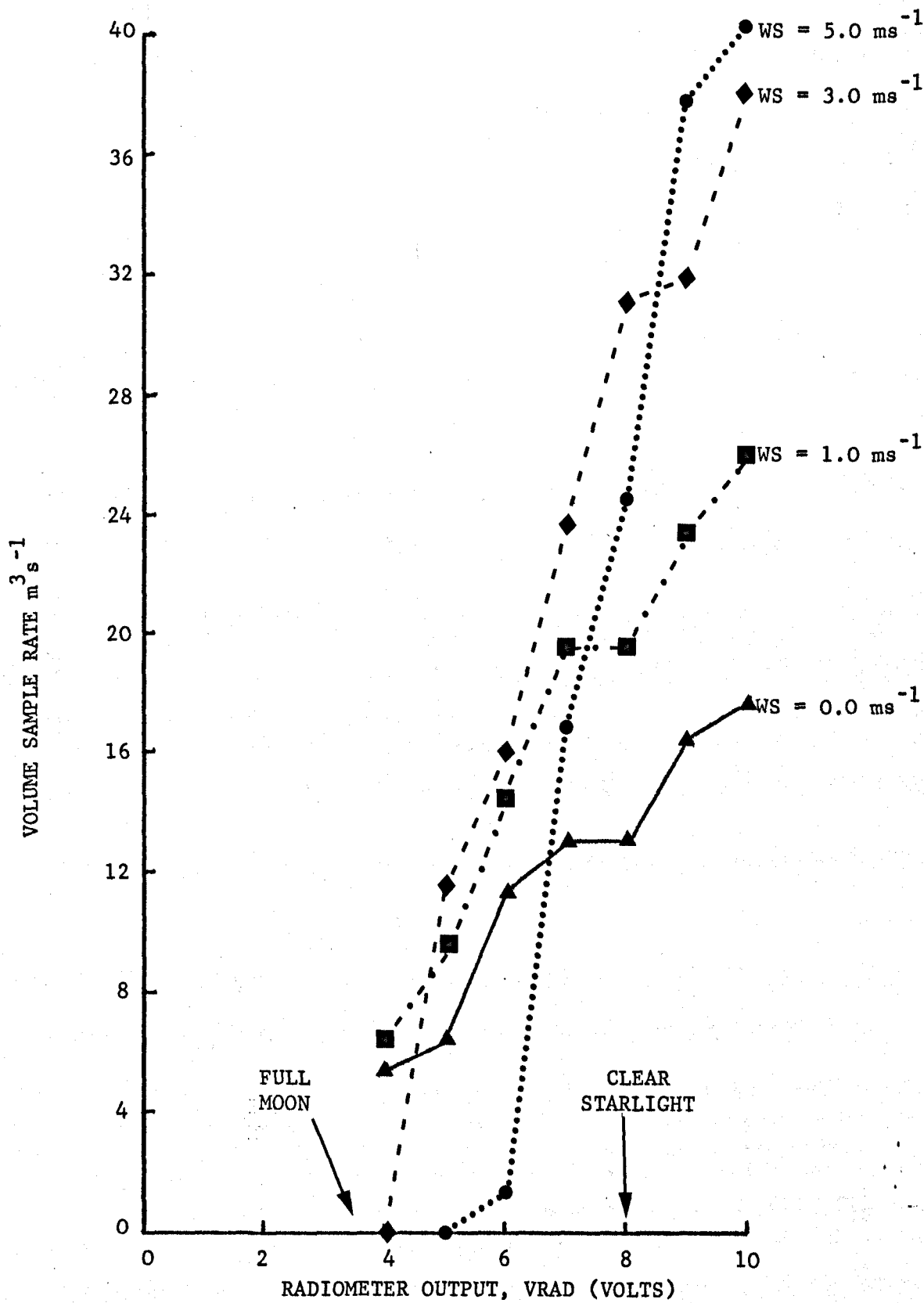


FIGURE 5.5

Volume Sample rate as a function of background illumination.

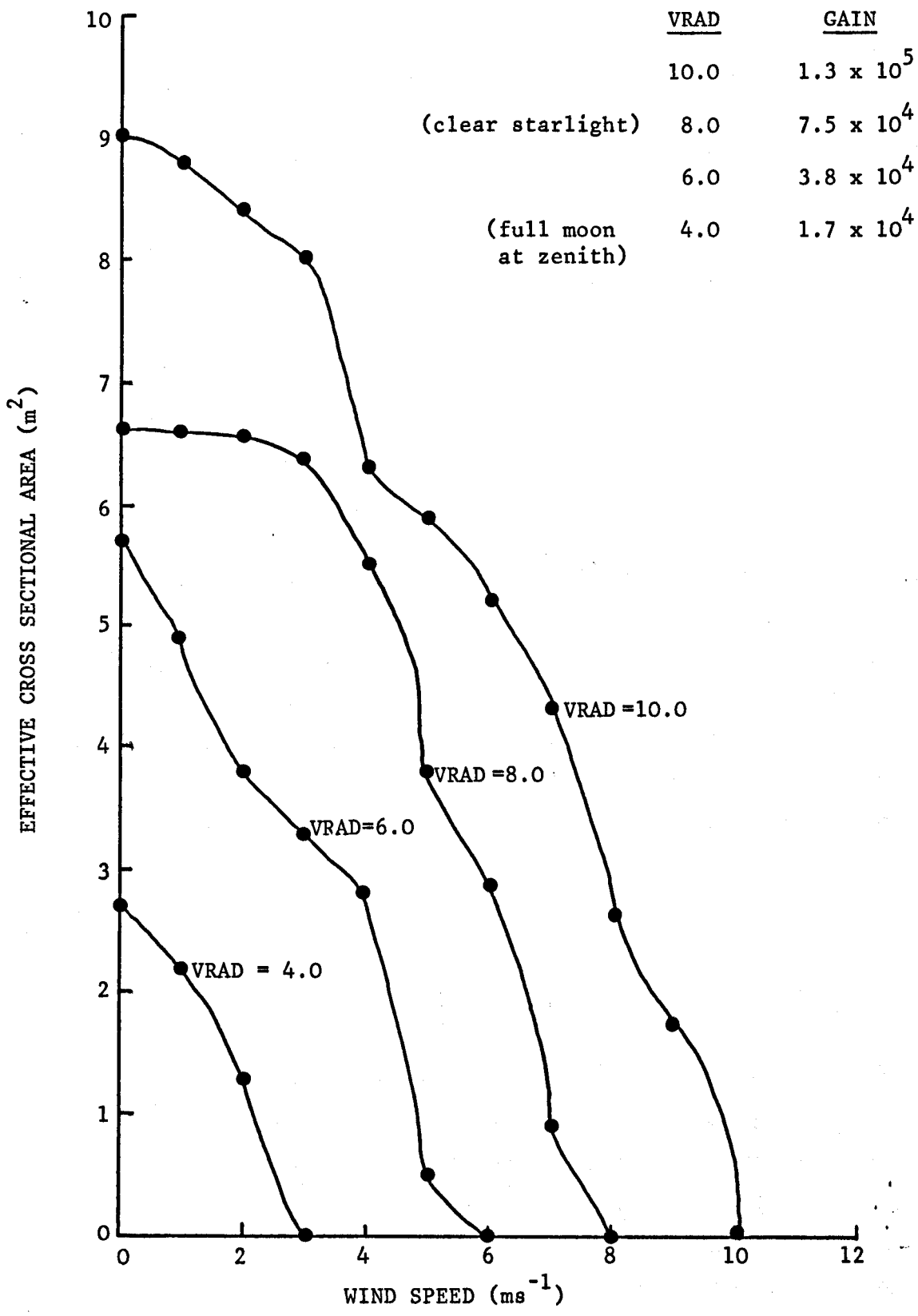


FIGURE 5.6

Effective cross sectional area of sample volume as a function of wind speed for different background illuminations.

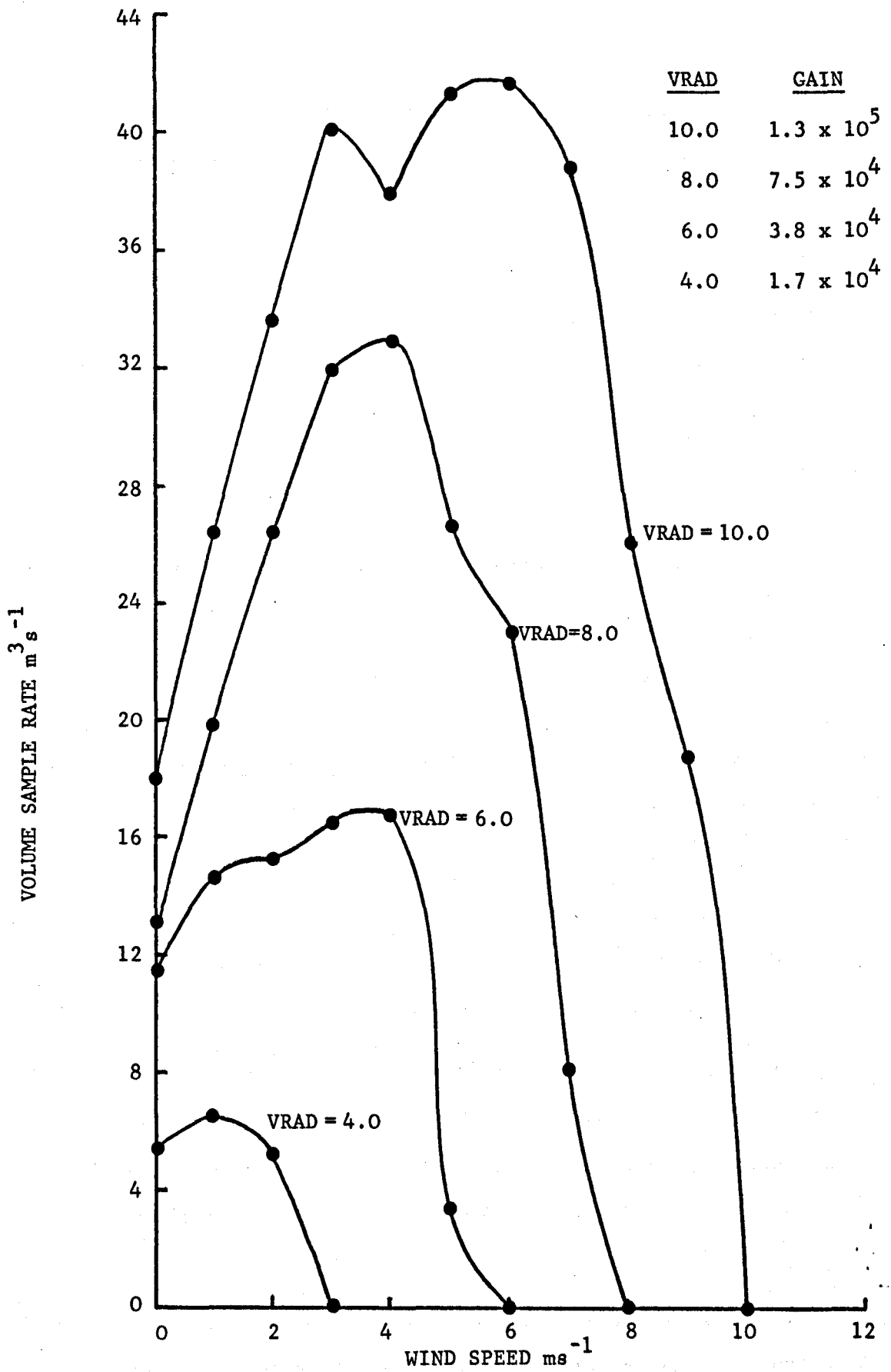


FIGURE 5.7

Volume Sample rate as a function of wind speed for different background illuminations and a wind direction of 0° .

In the analysis of the field results collected so far the effective volume of air sampled has been calculated for each 30 minute period from the average values of wind speed, direction and background illumination (VRAD) during each period. This method has been quite satisfactory for analysis of data in the laboratory. However, because of the large computational requirement it is not suitable for automatic data analysis in the field. It is envisaged that analysis systems for use in the field will be based on microcomputer techniques and the individual calculations will be replaced by either nomograms or 'look-up' tables derived from the results presented here.

5.3 WING BEAT FREQUENCY

In this section we first look at the method used to obtain the frequency spectrum of the recorded data. This is followed by a brief discussion of some aspects of the theory of frequency analysis and an examination of the mode of operation of the spectrum analyser used. The section concludes with a description of the criteria which were used to decide which spectra were 'good'.

The recorded data were frequency analysed using the COPR Radar Group's spectrum analyser facility at the Royal Signals and Radar Establishment, Malvern. This was a semi-automatic system based on a Ubiquitous UA14 - A Spectrum Analyser (Figure 5.8). The data were replayed one channel at a time, through the analyser. The resulting frequency spectra were examined visually on a CRT

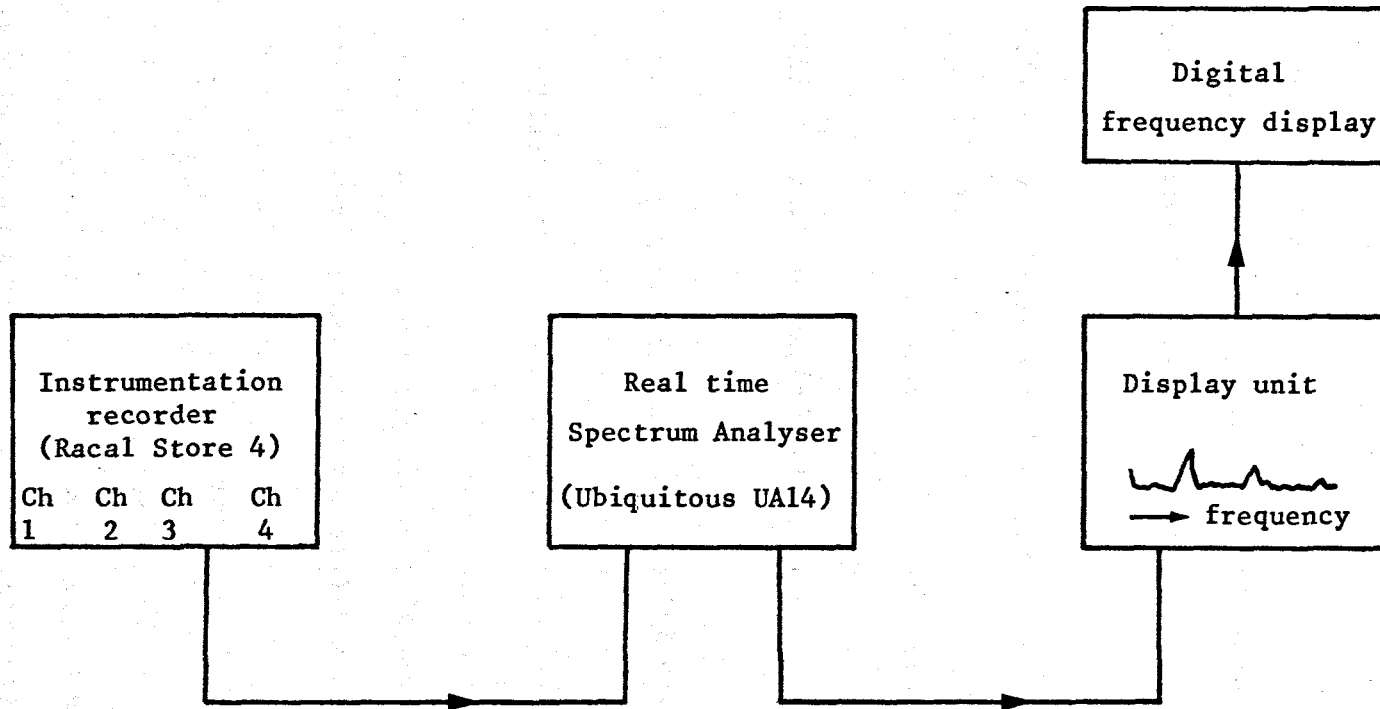


FIGURE 5.8 Block diagram of frequency analysis system for recorded data.

and the fundamental frequency, measured with an electronic calibrated cursor, was noted together with its tape position, which indicated the time of occurrence.

The theory of frequency analysis can be considered only briefly here; for a more comprehensive treatment the reader is referred, for example, to Enochson and Otnes (1968). A signal $x(t)$ in the time domain can be examined in the frequency domain by taking the fourier transform of $x(t)$, which is defined by

$$X(f) = \int_{-\infty}^{\infty} x(t) \exp\{-i 2\pi f t\} dt \quad (5.4)$$

For digitised data, the discrete fourier transform is written

$$X(f) = \Delta_t \sum_{k=0}^N x_k \exp\{-i 2\pi f k \Delta t\} \quad (5.5)$$

where Δ_t is the sampling period. Direct calculation of equation (5.5) on a digital computer is an inefficient process and the Fast Fourier Transform (FFT) algorithm has been developed which speeds up the calculation of (5.5) considerably by reducing the number of arithmetical operations. It is envisaged that an automatic frequency analysis system will operate on digitised data using an FFT program.

Analogue frequency analysis is performed by passing the signal through a narrow band filter and observing the output. A frequency range is covered by either a series of filters with incremented centre frequencies or by using a single filter and

incrementing the centre frequency after each passage of the signal. The second method is time consuming as it requires passing the signal through the filter N times in succession, where N is the number of frequency bins. The first method is usually expensive as it requires N high quality filters.

The Ubiquitous UA 14-A spectrum analyser employs the second method of sequential sampling using one narrow band incremented filter, but overcomes the time factor by using a 'time-compression' technique. The input signal is sampled by an analogue to digital convertor and the resulting values are placed in a recirculating memory. The sample rate is set at $3 \times F$, where F is the upper limit of the analysis range, to prevent problems with aliasing. The samples are entered into the memory in sequence and circulate at 40 k Hz. The frequency shifted samples are passed through a narrow bandwidth filter whose centre frequency is incremented after each pass of the memory contents. A complete 400 line frequency scan is thus performed in

$$\frac{400}{40000} = 0.01 \text{ sec.}$$

The sample rate corresponding to the 100 Hz frequency range used for this analysis was 300 Hz. The resolution available from a 400 line scan over a 100 Hz range is 0.25 Hz. This requires a sample length of 4.0 seconds (see equation (5.8)) which at a sample rate of 300 Hz is equivalent to 1200 data points. This is in fact equal to the analyser memory size. The "time compression" effect

is clearly demonstrated by noting that the frequency analysis of 4.0 seconds of signal is completed in 0.01 seconds, a 'speed-up' of 400 : 1.

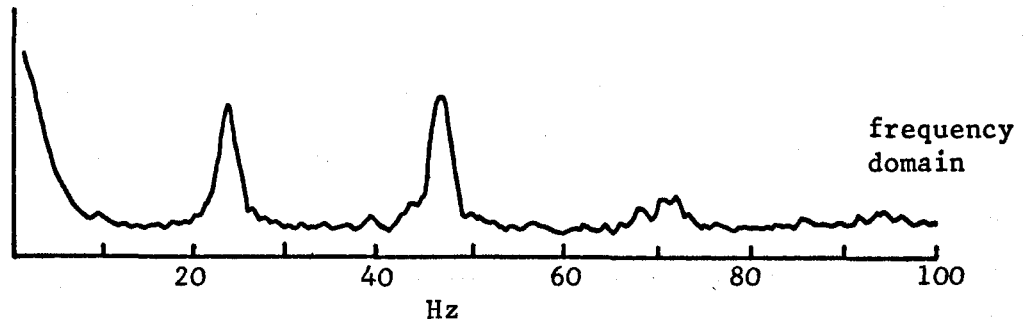
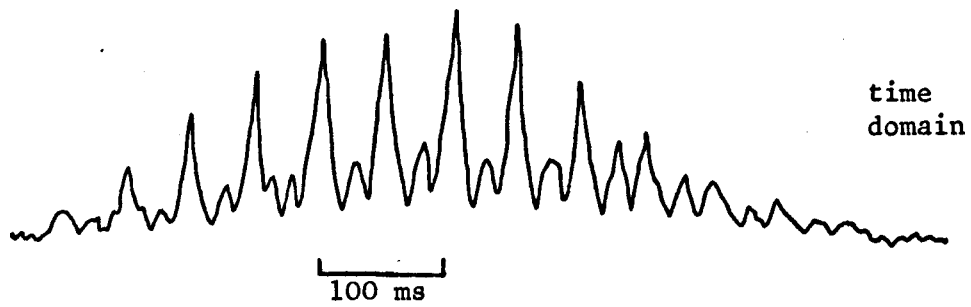
The width Δf of the frequency spectrum of a signal is related to the sample duration Δt by

$$\Delta f = \frac{1}{\Delta t} \quad (5.6)$$

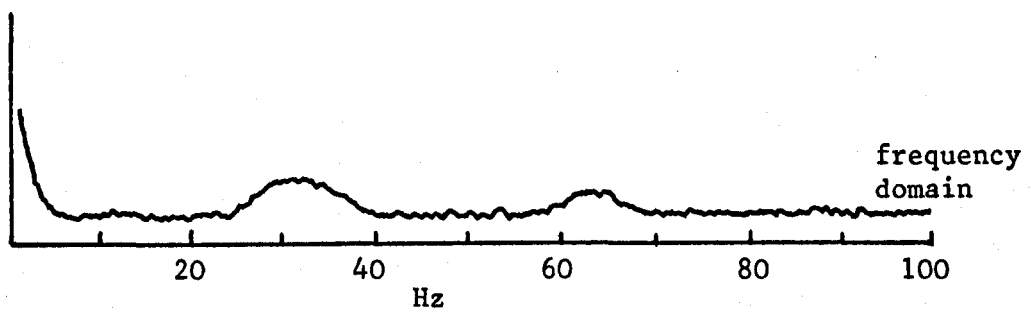
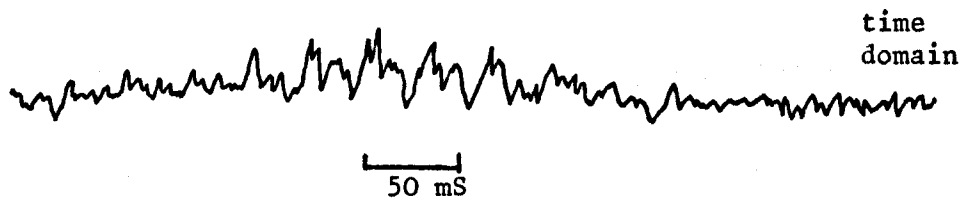
When the signal exists for the entire sample period (in this case 4.0 seconds) the width of the spectrum is equal to the resolution (0.25 Hz). For shorter duration signals the resolution remains constant since the sample length remains unchanged but the spectrum width is increased (as per equation (5.6)). Short duration signals therefore produce broad spectra and in practice a point is reached when the spectra are too wide to estimate the centre frequency. Experimentally this was found at a spectral width of 10 Hz on the 100 Hz analysis range, equivalent to a signal duration of 0.1 seconds (or 5 wing beat cycles at a wing beat frequency of 50 Hz). It was also found that the signal amplitude had to be at least twice the noise level. Examples of the minimum acceptable signal and a typical signal are shown in Figure 5.9 in the time and frequency domains respectively.

5.4 CALCULATION OF TARGET SPEED AND DIRECTION

Measurements of target speed and direction were made using the two channel receiver which is described, with the principle of



(a) typical signal



(b) Minimum acceptable signal

FIGURE 5.9 Examples of recordings in the time and frequency domains showing (a) a typical signal, and (b) a minimum acceptable signal.

operation, in Section 4.2.2. The collected data have been analysed manually using the method illustrated in the example below and the results are presented in Section 7.2

The technique used is summarised in Figure 4.2 and a typical record is shown in Figure 5.10. The two channels of data in Figure 5.10 were output simultaneously on a two channel X-T plotter and the off times τ_a , τ_b , τ_c measured using a ruler. The smallest error associated with the measurement of the distance corresponding to the off time was taken as ± 1.0 mm, equivalent to an error in τ of ± 0.005 seconds. This estimate included the uncertainty of judging the precise beginning and end of the 'off period', which is clearly a minimum when the image is in sharp focus at the slide (Figure 5.11). The definition of the beginning and end of the 'off period' is further complicated by the variation of signal strength during the wing beat cycle. The error here is estimated to be of the order of $\pm \frac{1}{4}$ x (wing beat period), which for a 50 Hz signal is ± 0.005 seconds, comparable to the error estimated above.

The target speed in a direction perpendicular to the opaque bars is given by

$$v = \frac{Rd}{f\tau} \quad (5.7)$$

for $R \gg f$

where R is the object range

f is the focal length of lens

τ is the off time

d is the width of the opaque bar

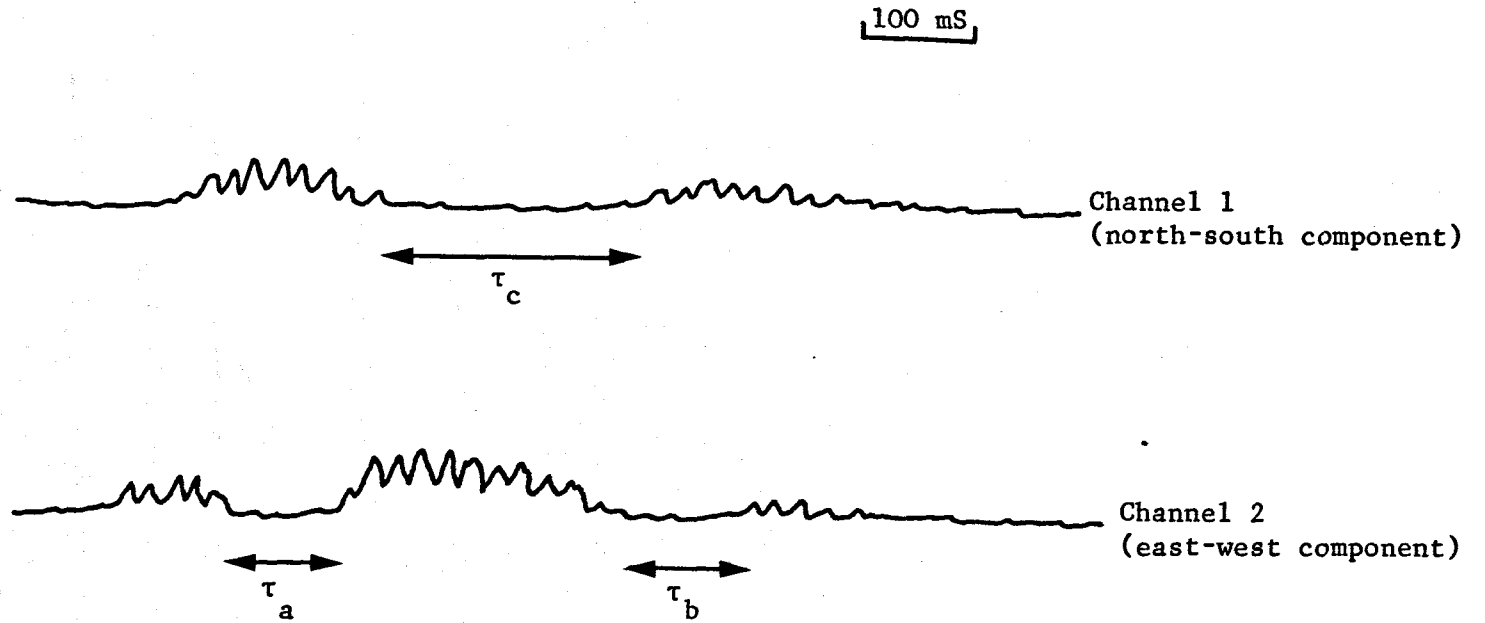


FIGURE 5.10

Typical signal to illustrate the method used to calculate speed and direction.

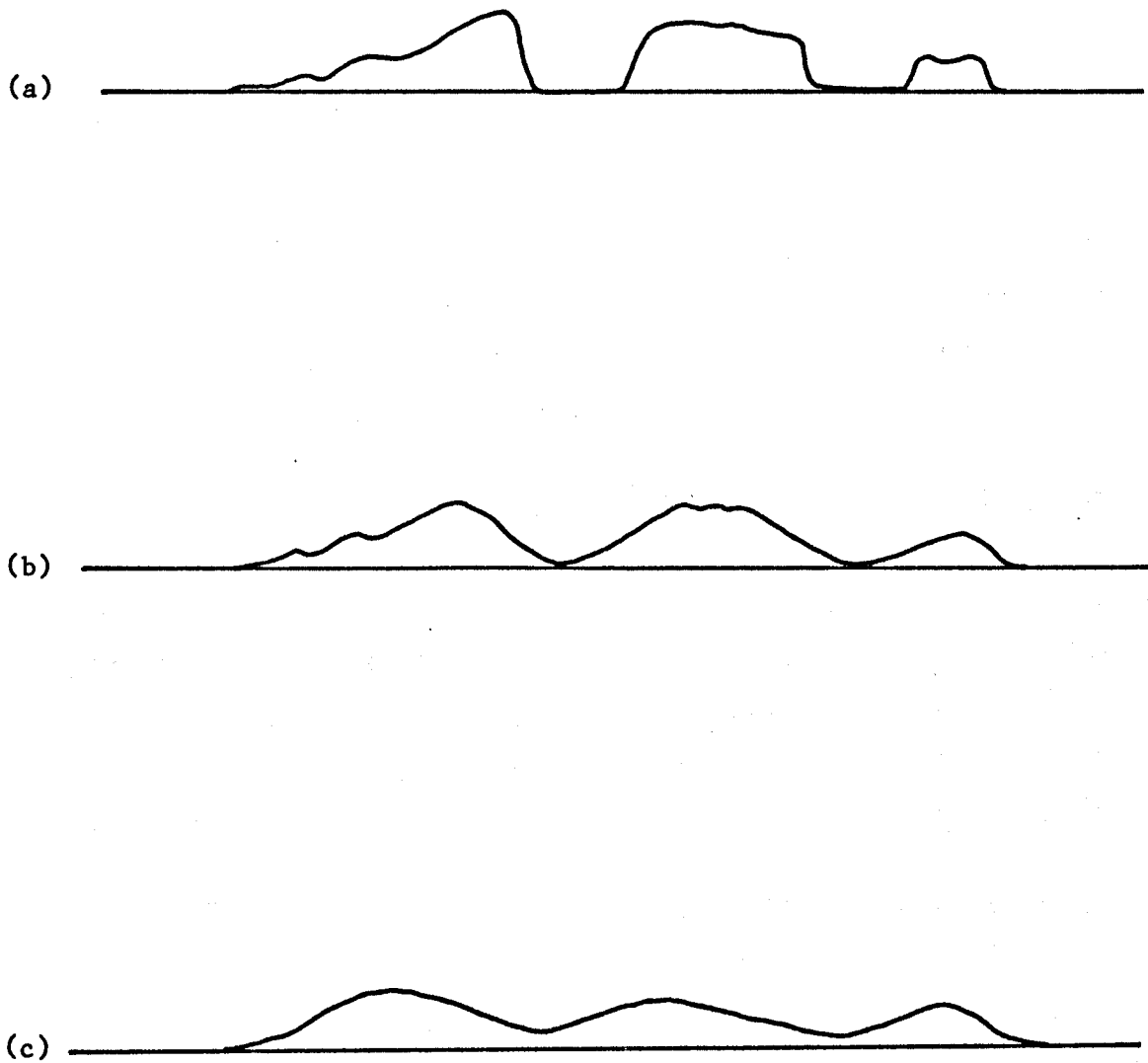


FIGURE 5.11

Effect of image focus on chopping action. Signal envelope is shown for image progressively further out of focus. Object at 2 m, lens focussed at (a) 2 m (b) 2.5 m (c) 3.0 m.

For the north-south component (Channel 1)

$$R = 10 \text{ m}, \quad f = 100 \text{ mm}, \quad d = 4 \text{ mm}, \quad \tau = \tau_c = 0.16 \pm .005 \text{ secs.}$$

Substituting these values in equation (5.7) the north-south component V_{NS} of target velocity is obtained

$$V_{NS} = 2.5 \pm 0.1 \text{ ms}^{-1}$$

Inspection of the 'on time' in relation to the slide orientation shows that this component was directed southerly.

For the east-west component (Channel 2)

$$R = 10 \text{ m}, \quad f = 100 \text{ mm}, \quad d = 4 \text{ mm},$$

$$\tau_a = 0.07 \pm .005 \text{ secs.}, \quad \tau_b = 0.075 \pm 0.005 \text{ secs.}$$

Average value of $\tau = 0.0725 \pm .0025 \text{ secs.}$ substituting the values above in equation (5.7) gives the east-west component as

$$V_{EW} = 5.5 \pm 0.15 \text{ ms}^{-1}$$

Inspection of the 'on time' in this case showed the component to be directed westerly. Combining the two components into a target speed V at an angle θ to the north-south axis gives

$$V = (V_{NS}^2 + V_{EW}^2)^{\frac{1}{2}} \tag{5.8}$$

$$\theta = \tan^{-1} \left(\frac{V_{EW}}{V_{NS}} \right) \tag{5.9}$$

Substituting the calculated values for V_{NS} and V_{EW} gives,

$$V = 6.0 \pm 0.3 \text{ ms}^{-1}$$

$$\theta = 65.5 \pm 1.0^\circ$$

that is, the target was moving at a speed of $6.0 \pm 0.3 \text{ ms}^{-1}$ on a bearing of $245 \pm 1.0^\circ$.

Many other records have been analysed in this way (Section 7.2) primarily to validate the assumption, used in the calculation of the aerial density, that insects fly predominantly downwind. As a result of these analyses several shortcomings in the method were identified. These are noted in Section 7.2.

5.5 TOWARDS AUTOMATIC IN-FIELD DATA ANALYSIS

The analysis methods described above require a substantial amount of trained operator participation, particularly in the discrimination between 'good' and 'bad' spectra and in the measurement of the 'on' and 'off' times. Analysis of recorded data has been tedious and time consuming. For example, the routine spectrum analysis of one channel of an eight hour data tape can take up to 12 hours. For this reason all the data analysis has been performed in England 'after the event'. Automatic in-field analysis therefore represents a very desirable objective not only for the operator time saved but also for the reduced feedback time between

the experiments and their results. It would allow interpretation of results in the field so that changes to the observational strategy could be made if necessary.

It is envisaged that the automatic system will digitise the incoming signals, perform a spectrum analysis, decide whether the signal was caused by an insect and if it was to note the fundamental wing beat frequency and its time of occurrence. It is likely that the system would consist of an analogue to digital converter and an FFT module under the control of a mini computer. The design of the computer software which discriminates between individual signals and decides which are acceptable is expected to be the most difficult part of the exercise.

The aerial densities are calculated from the wing beat frequency data by counting the number during a specified period and dividing by the volume of air sampled. In this case it is imagined that the volume sample rate will be calculated from nomograms or look-up tables based on the results in Section 5.2 rather than repeating the complete iterative program for each measurement.

CHAPTER 6

LABORATORY STUDIES

6.1 TETHERED FLIGHT EXPERIMENTS

6.1.1 Background

The experiments described in this section were performed at the Kenyan Agricultural Research Institute (KARI) during March and April 1978. They formed part of the University of York's contribution to the Centre for Overseas Pest Research (COPR) Armyworm Research Project which is described in Section 7.1. The insect activity in 1978 was unusually low and so the opportunity was taken to do laboratory based studies on both locally caught and laboratory reared specimens, particularly Armyworm moths (spodoptera exempta) together with some other locally occurring species.

6.1.2 Variation of Wing Beat Frequency With Wing Length

The approximately inverse relationship between wing beat frequency and wing length (Figure 1.1) has already been described (Section 1.3) and can be represented mathematically by the following power law

$$f = c l^{-p} \quad (6.1)$$

where f is the wing beat frequency

l is the wing length

c, p are constants depending on the species considered.

Schaefer (1976) found $p = 0.78$ for grasshoppers and locusts. Weis Fogh (1956) introduced the concept of "length index" in his extensive studies of the flight mechanics of the Desert Locust (*Schistocerca gregaria*). The length index L was calculated from the forewing (eleytron) length E and the hind femur length F using the equation

$$L = (E F)^{\frac{1}{2}} \quad (6.2)$$

The "length index" therefore represented a measure of the size of the locust, but can be assumed to be proportional to the wing length l . Weis Fogh (1956) deduced the relationship between f and l for the locust from energetic principles to be

$$f = c l^{-0.67} \quad (6.3)$$

This dependence was verified experimentally for locusts flying (tethered) in a wind tunnel (Weis Fogh, 1956).

The experiments described here were designed to investigate whether a similar relationship could be established for night flying moths in Kenya. The equipment used for the experiments is shown in Figure 6.1. The insects (predominantly moths) were mounted on a thin, stiff rubber tube (Hellermen Sleeve) using a very low vacuum. Before mounting, the insects were cooled in the freezing compartment of a refrigerator for about 10 minutes to reduce their activity. In this way they could be mounted carefully on the dorsal side of the thorax just below the head. This mounting technique appeared to

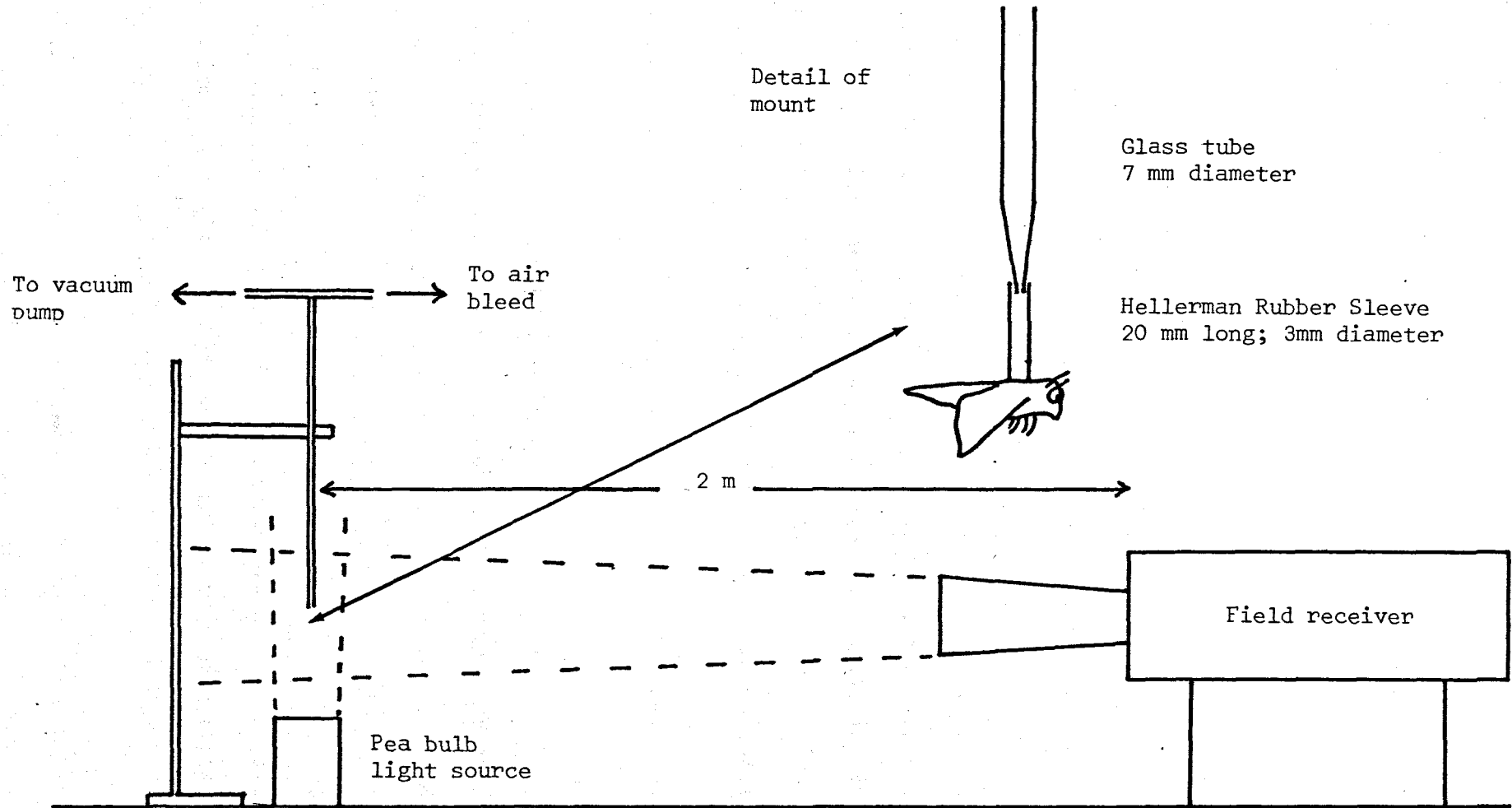


FIGURE 6.1

Layout of experimental system for tethered flight studies at K A R I, Kenya

cause no obstruction to the wing action and the degree of vacuum could be easily adjusted (with an air bleed) so that the insects showed no signs of discomfort. The specimens, once mounted, were allowed to warm up to ambient temperature. A few of them required an airflow from a small fan before they would fly. Most, however, would fly as soon as they were warm enough and would stop when a small piece of tissue was placed for their legs to grip. Removal of the tissue initiated flying again.

The results from specimens flown in these experiments are summarised in Appendix C4. Fifty specimens actually flew out of about 100 which were mounted; of the 50 fliers about 35 gave useful results. Figure 6.2 shows a scatter plot of wing beat frequency against wing length. Regression analysis of these data shows no evidence for a relationship of the form of (6.1). Analysis of the data for spodoptera exempta moths alone suggests a possible increase in frequency with increasing wing length, but it is only significant at the 90% level and the resulting regression line

$$f = 34.6 l^{.454}$$

explains only 21% of the variance.

These results should be accepted with reservation for two reasons. Firstly a large number of different species were used, and secondly, although the mounting technique allowed the moths to flap unhindered it was not possible to check whether they were actually producing positive lift. Only when an insect is producing lift equal to its own weight can it be considered to be flying normally.

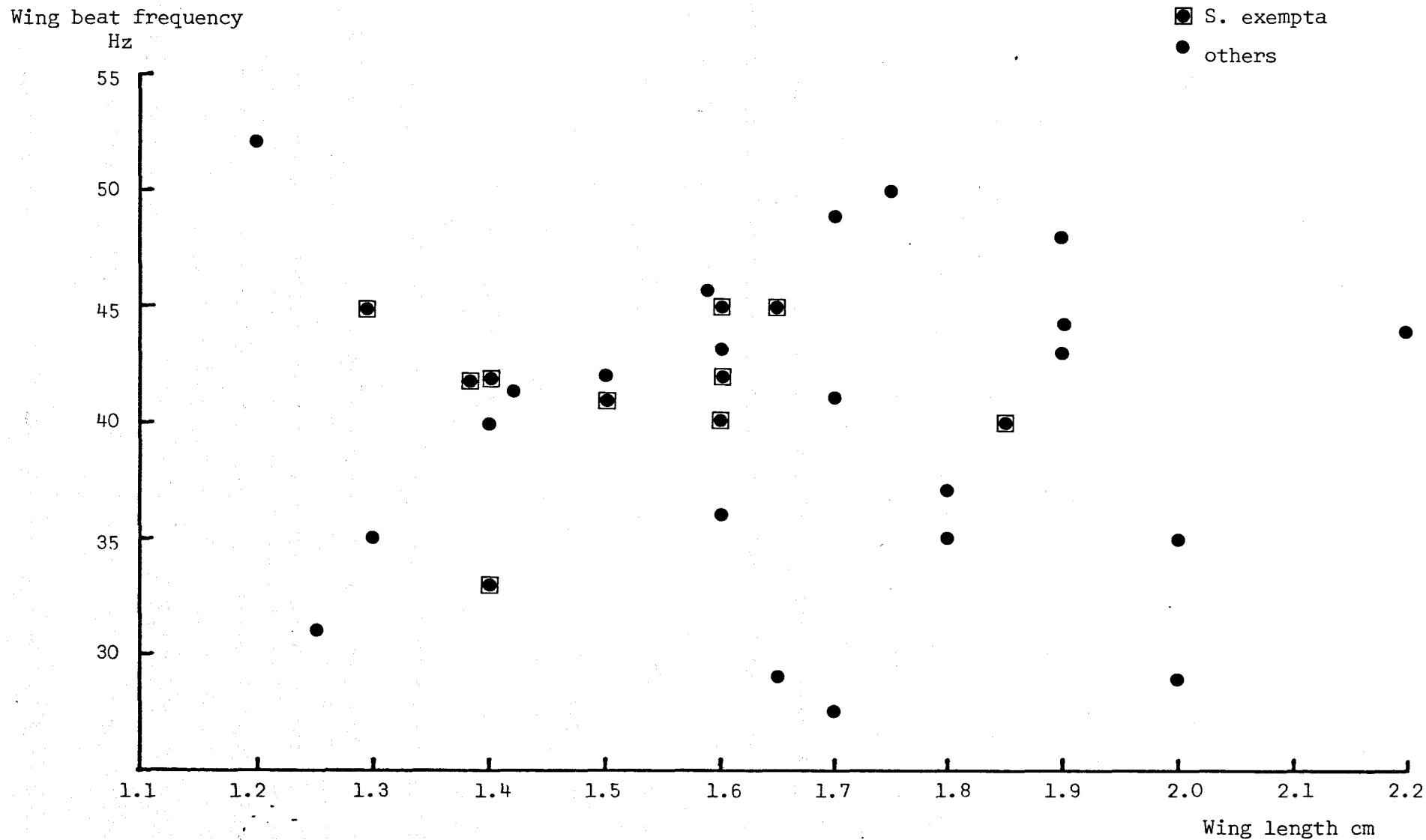


FIGURE 6.2 Variation of wing beat frequency with wing length from laboratory tethered flight experiments

This aspect has been considered in recent work done by Cooter. In Kenya (April 1979) he carried out experiments to determine the wing beat frequencies of s. exempta sized moths (Cooter 1979). The moths were mounted on a novel flight balance and frequency measurements were only made on those which produced positive lift. He used laboratory reared s. exempta specimens and other common, similarly sized species which were caught at a light trap as required. As with the present work he found no correlation between wing beat frequency and wing length. He did however find a substantial decline in wing beat frequency during the first eight minutes of flight (at a rate of 0.42 Hz min^{-1}) followed by a much slower decrease for the rest of the flight (up to 2 hours duration) of 0.05 Hz min^{-1} .

In the following year Cooter used freshly caught moths from outbreak areas and in this case found a correlation of the form (Cooter, pers comm)

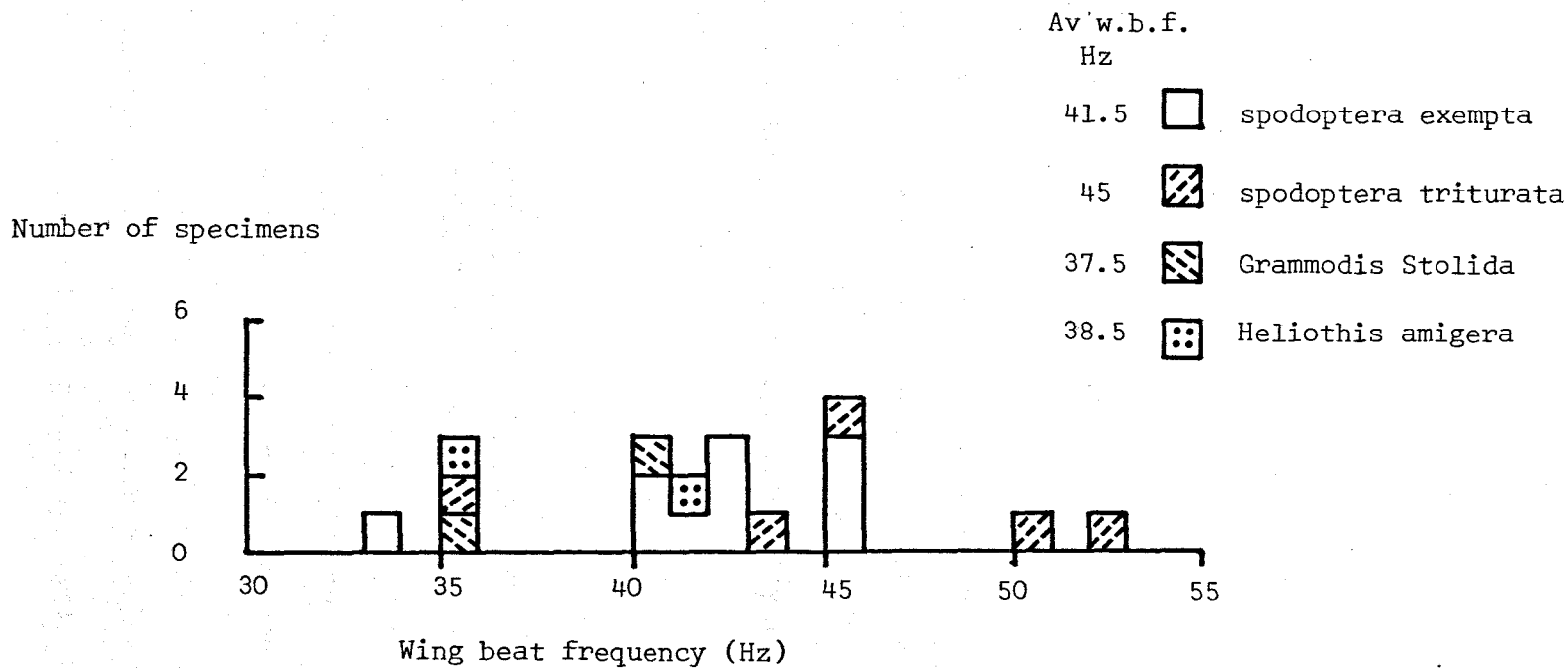
$$f = c l^{-0.45}$$

The reason for the difference in results between the two years has not yet been established.

6.1.3 Wing Beat Frequency As An Aid To Species Identification

In this investigation the data from the preceding section has been used to test whether the wing beat frequencies of s. exempta moths could be distinguished from those of other species which are found in similar habitats. The data are presented in the form of a

FIGURE 6.3 . Wing beat frequency related to species for the laboratory tethered flight specimens



histogram (Figure 6.3). The small number of specimens make it difficult to conclude much. However, it is clear that all but one of the s. exempta specimens fall in the range 40 - 45 Hz and that there is a well defined difference between the mean frequencies of s. exempta ($\bar{f} = 41.5$ Hz) and s. triturrata ($\bar{f} = 45.0$ Hz).

In 1979 Cooter found the mean wing beat frequency of the laboratory reared specimens to be 40.5 Hz (S.D. = 4.4 Hz), and concluded that there was no way of identifying s. exempta from other similarly sized moths on the basis of wing beat frequency alone. Cooter's corresponding figure for the field specimens in 1980 was 45.0 Hz. No explanation of this difference can be made until all the data have been fully analysed.

Measuring the wing beat frequencies of tethered insects is difficult and, at best, only gives the probable range in which the "natural" frequencies will lie. There is in fact some evidence to suggest that laboratory measured frequencies are systematically lower than naturally occurring ones (Baker, Gewecke and Cooter, in press).

6.1.4 Variation of The Received Signal With Relative Position of Transmitter, Insect and Receiver

The shape of the received signal from an insect for one wing beat cycle is termed the wing beat pattern. This was found to change considerably with the aspect of the insect presented to the receiver.

Using the experimental configuration shown in Figure 6.1, the moth was rotated about the vertical axis of the mount in 15° steps from the insect being aligned perpendicularly to the optical axis of

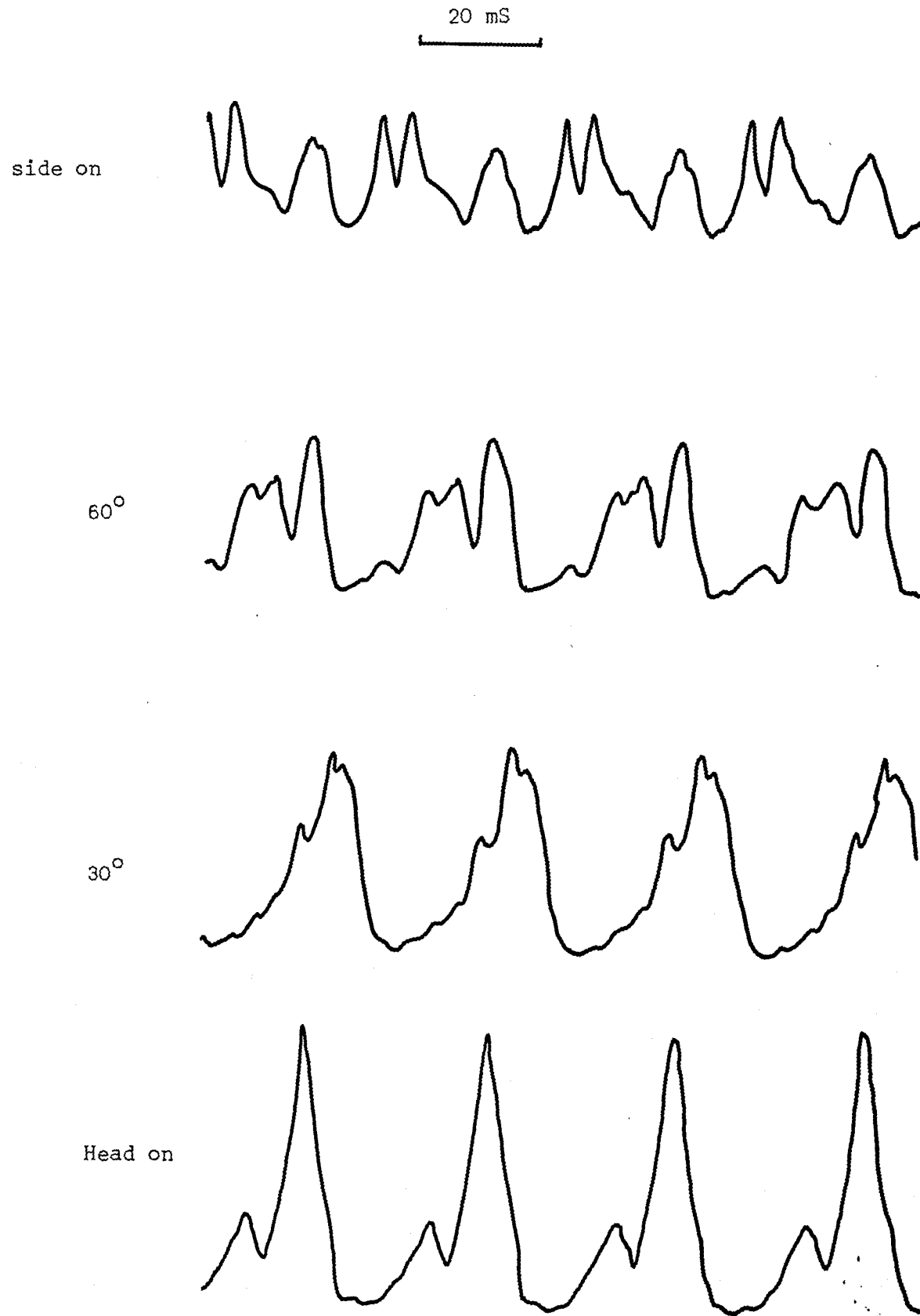
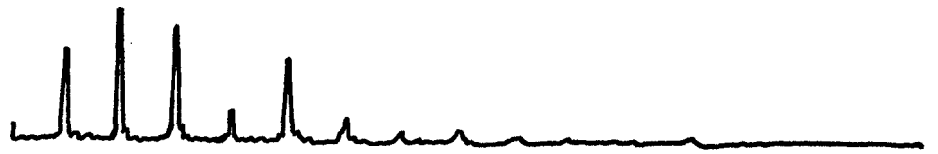
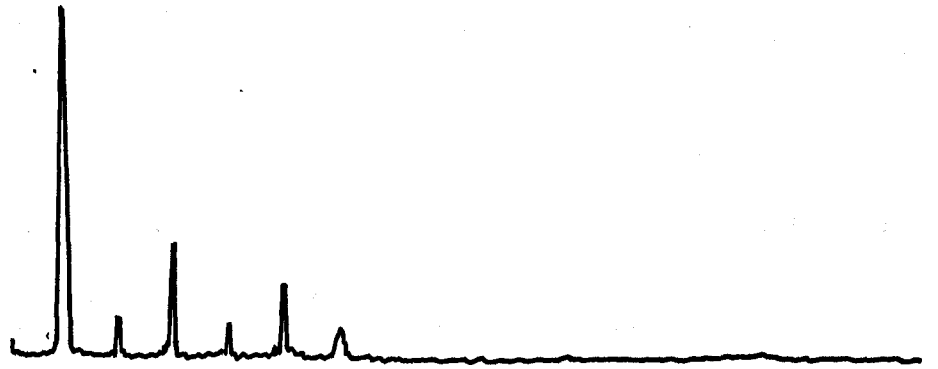


FIGURE 6.4 Variation of wing beat pattern with aspect of moth presented to receiver

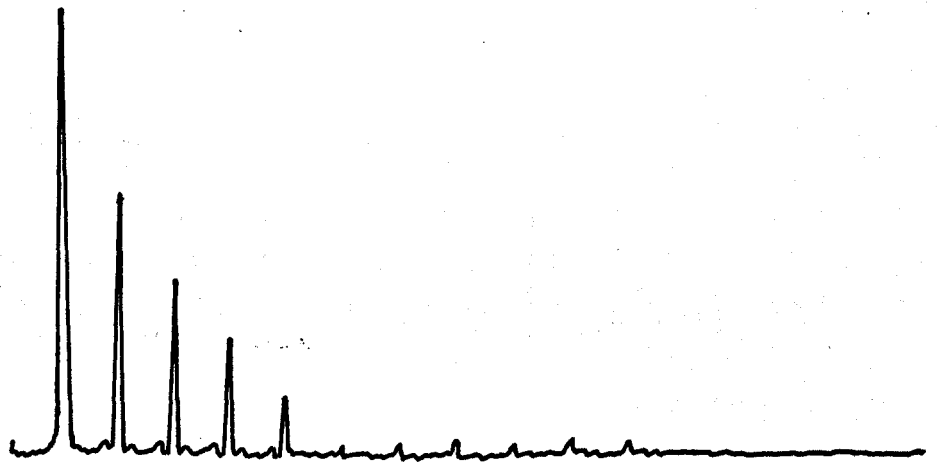
Side on



60°



30°



Head on

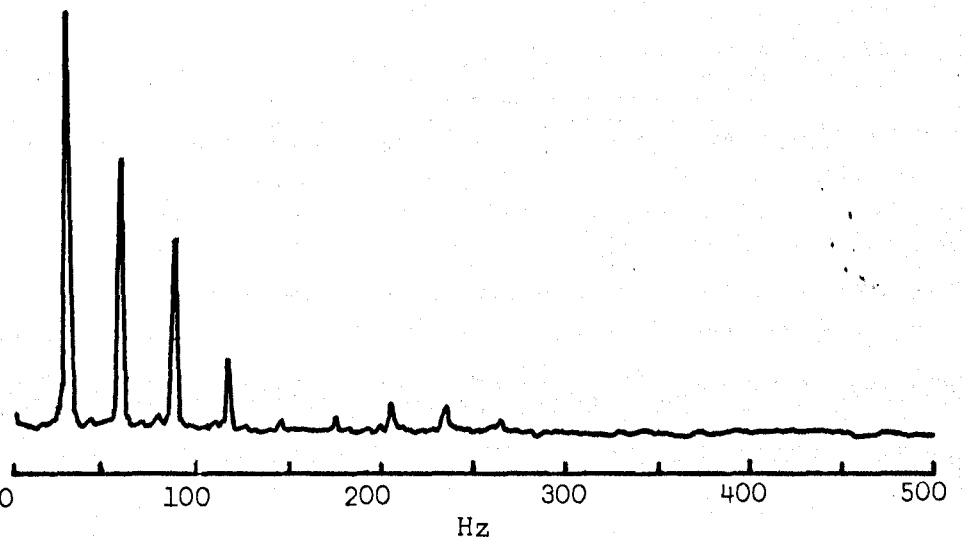


FIGURE 6.5

Frequency spectra of the wing beat patterns shown in Figure 6.4, showing the variation in harmonic content with aspect.

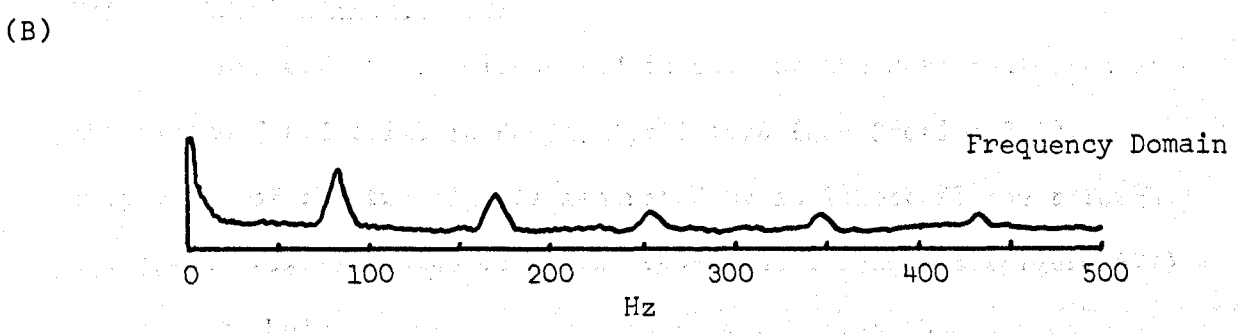
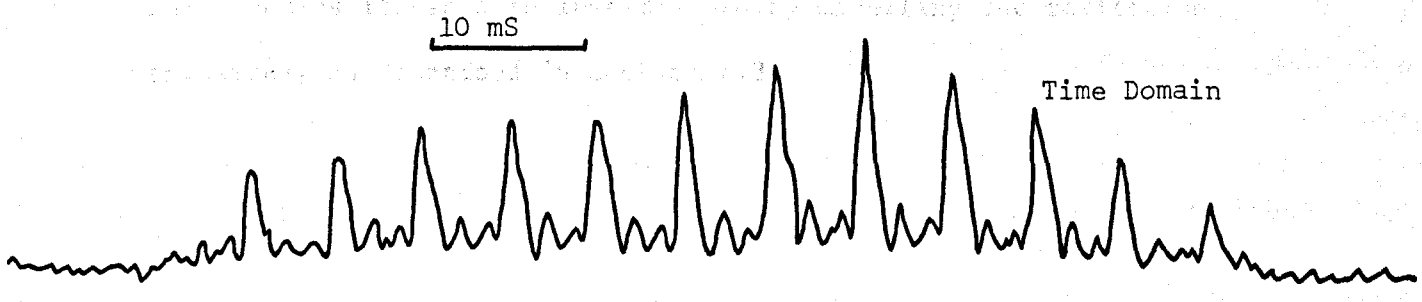
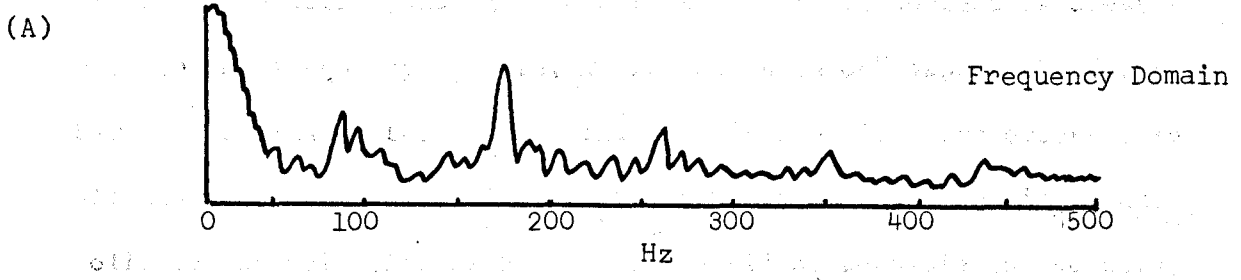
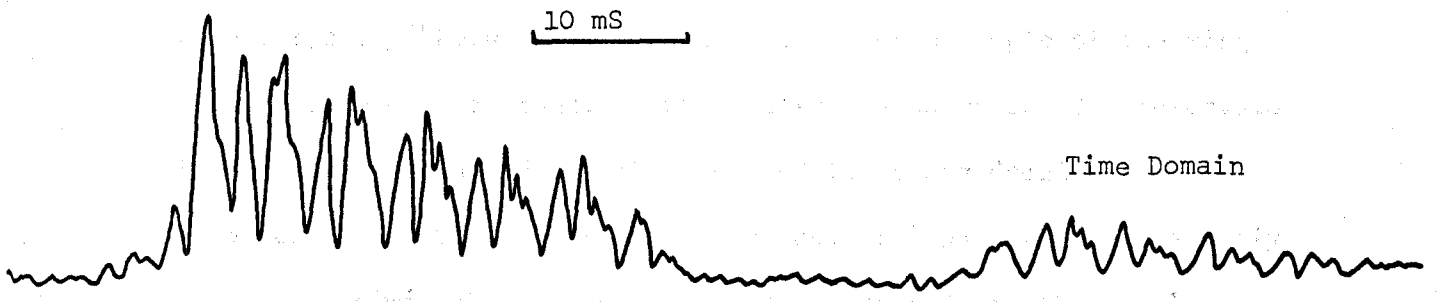


FIGURE 6.6 TWO EXAMPLES OF TYPICAL SIGNALS IN THE TIME AND FREQUENCY DOMAINS, ILLUSTRATING DIFFERENT HARMONIC CONTENTS. IN (A) THE FIRST HARMONIC DOMINATES THE FUNDAMENTAL

the receiver ("side on") to the insect being aligned along the receiver axis ("head on"). At each position a sample of the wing beat pattern was recorded. The results are shown for 30° intervals in Figures 6.4 and 6.5, in the time and frequency domains respectively. The main peak in the "head on" pattern progressively splits and diminishes as the specimen is rotated and the small peak grows. The corresponding change in the harmonic content is clearly seen in the frequency spectra, where, at "side on" aspect the first harmonic dominates the fundamental. This behaviour was observed in all the specimens and a similar effect has been noted in field data collected in Mali (Figure 6.6). It should be possible to use this effect to deduce the orientation of flying moths. The mechanism which causes it has been investigated by modelling the reflection processes, as described in Section 6.3.

6.2 POLARISATION EFFECT

This effect was discovered in some of the data collected at the Kiboko field trial in Kenya, April 1978 (see Section 7.1). Inspection of the two signals generated by an insect flying through the sample volume monitored by the two-channel receiver (Figure 6.7) shows that their patterns do not always match even though they are both derived from the same image. This was unexpected and two explanations were considered.

(a) It was due to variations in sensitivity across the two photocathodes. Very large variations would be required to account for the different patterns seen in Figure 6.7 and experiments performed to

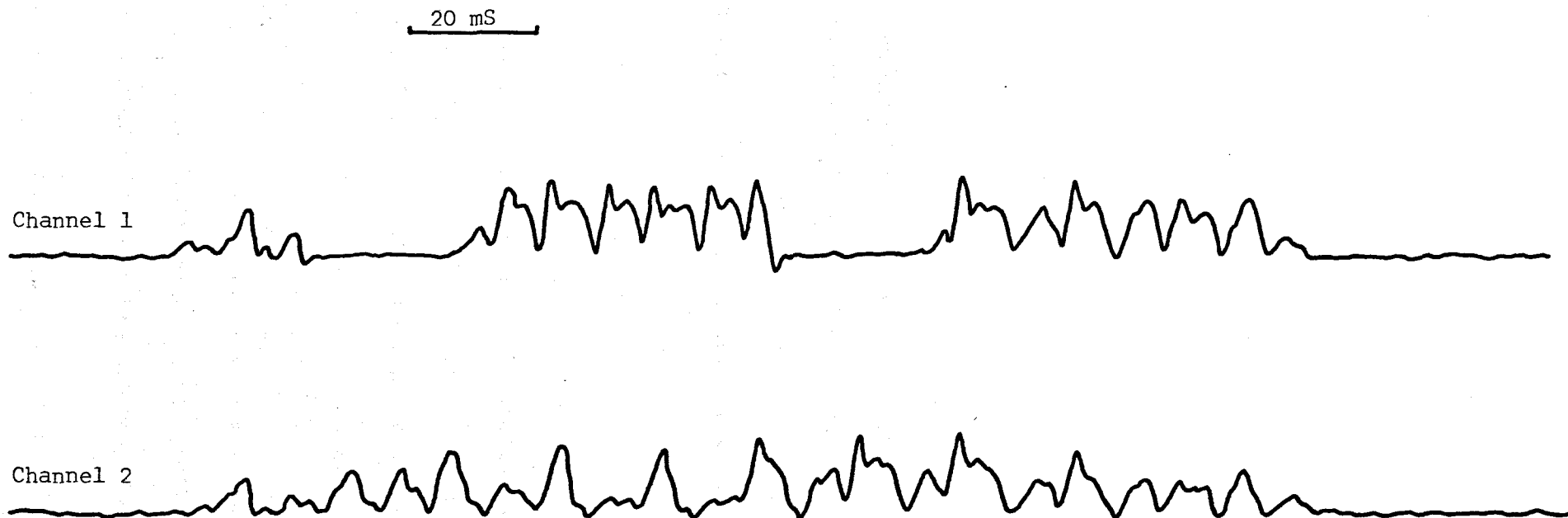


FIGURE 6.7

A typical signal from Kiboko field trial. Wing beat modulation and intercepts are clearly demonstrated. Different wing beat patterns between the two channels are also seen in parts of the record.

test this hypothesis (Section 6.4) showed that this was not the cause.

(b) It was a polarisation effect. The beam splitter in the two-channel receiver has a reflection coefficient which varies with the angle of polarisation of the incident light. Consequently the relative amplitudes of the signals from the two channels will vary with the state of polarisation of the scattered light from the flying insect.

A program of work to test the latter hypothesis was initiated which consisted of (i) laboratory experiments to investigate whether the polarisation of the reflected light from an insect varied during the wing beat cycle, and (ii) computer modelling of the reflection of light during the wing beat cycle using measured reflection coefficients for the insect wings (see Section 6.3).

The laboratory experiments were planned to follow closely the experimental method used previously (Section 6.1). However, because the experiments could be performed at close range there was no need for the high sensitivity of the field receivers. A new receiver was therefore designed which used silicon photovoltaic cells as detectors and had the facility for analysing the polarisation of the light incident on the detectors.

The internal layout of the laboratory receiver is shown in Plate 12. A standard 35 mm camera lens (50 mm focal length) was used to produce an image of the tethered insect. The image beam was split with a small beam splitter and the two images were made to focus on the surfaces of two photovoltaic cells. These cells had active areas of 1 cm^2 and were housed within aluminium blocks to reduce electrical

"pick up". Also mounted within the aluminium block was a polaroid window in front of the photovoltaic cell. It was possible to rotate the window by a spindle on the outside of the receiver via a worm gear mechanism within the block. One rotation of the spindle rotated the direction of polarisation of the window through 18° (a gear reduction of 1 : 20). The signal currents from the photovoltaic cells were amplified by two current-to-voltage amplifiers (Appendix A2) mounted within the receiver.

Initial experiments were carried out with this receiver as part of a third year undergraduate project and are reported elsewhere (A.B. Rafferty, Third Year Project, 1979). The work included digitisation of the signals for computer analysis.

Some success has been achieved in duplicating the 'polarisation effect' in the laboratory. Figure 6.8 shows a record from the laboratory system of a s. exempta moth in tethered flight. The polarisers were removed for this experiment and so the system was exactly similar to the two channel field receiver. The main peak in the lower trace can be seen to be partially split. The difference between the two traces is small compared to that seen in the field data. Laboratory measurements have shown (Section 6.3) that the amorphous texture of the moth wing is a very poor polariser compared, for example, to the glass-like surface of a grasshopper's hind wing. It is therefore thought likely that the insect responsible for the signal in Figure 6.7 was a grasshopper, and that the effect is small for moths.

20 mS

Channel 1



Channel 2



FIGURE 6.8

Recorded signal from a laboratory simulation experiment using a *Spodoptera Exempta* moth on the suction mount. In channel 2 the main peak is partially split.

6.3 COMPUTER SIMULATION OF RECEIVED SIGNALS

The objective of this work was to model the scattering of light from a flying insect so that the aspect and polarisation effects might be better understood.

6.3.1 Scattering and Reflectivity Properties of Insect Wings

The model required knowledge of the scattering properties and reflection coefficient of the insect wing. These parameters were measured experimentally for the fore and hind wings of s. exempta and Schistocerca gregaria. These two species were considered to be representative of the two major insect types of interest.

The measurements were made using the experimental layout shown in Figure 6.9. Each Wing for study was mounted flat on matt black cardboard which was secured to the vertical face of a glass block positioned at the centre of a turntable. A narrow (2 mm diam.) beam from a helium-neon laser was made incident on the wing and the scattered light was detected by a photomultiplier tube behind a narrow aperture (angular width 2°). The angle of incidence θ_I , was varied by rotating the turntable and the angle of reflection θ_R defined by the detector was changed by rotating the detector assembly around the turntable at a fixed radial distance.

The scattering characteristic of each wing was obtained by measuring the light scattered as a function of the angle of reflection for selected angles of incidence ($\theta_I = 15^\circ, 30^\circ, 45^\circ, 60^\circ, 75^\circ$). Sample results from the hind wings of the two species are shown in Figure 6.10 for $\theta_I = 45^\circ$. The scattering from the amorphous moth

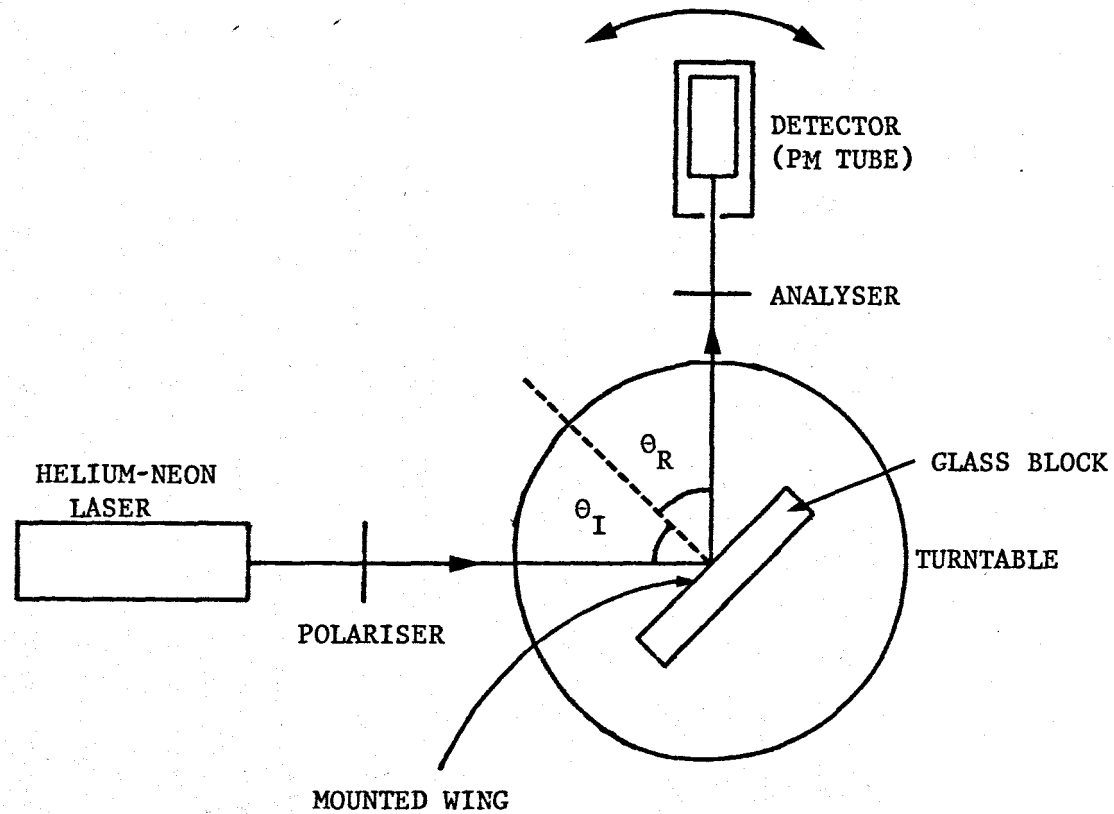


FIGURE 6.9 Experimental layout for reflectivity and scattering experiments

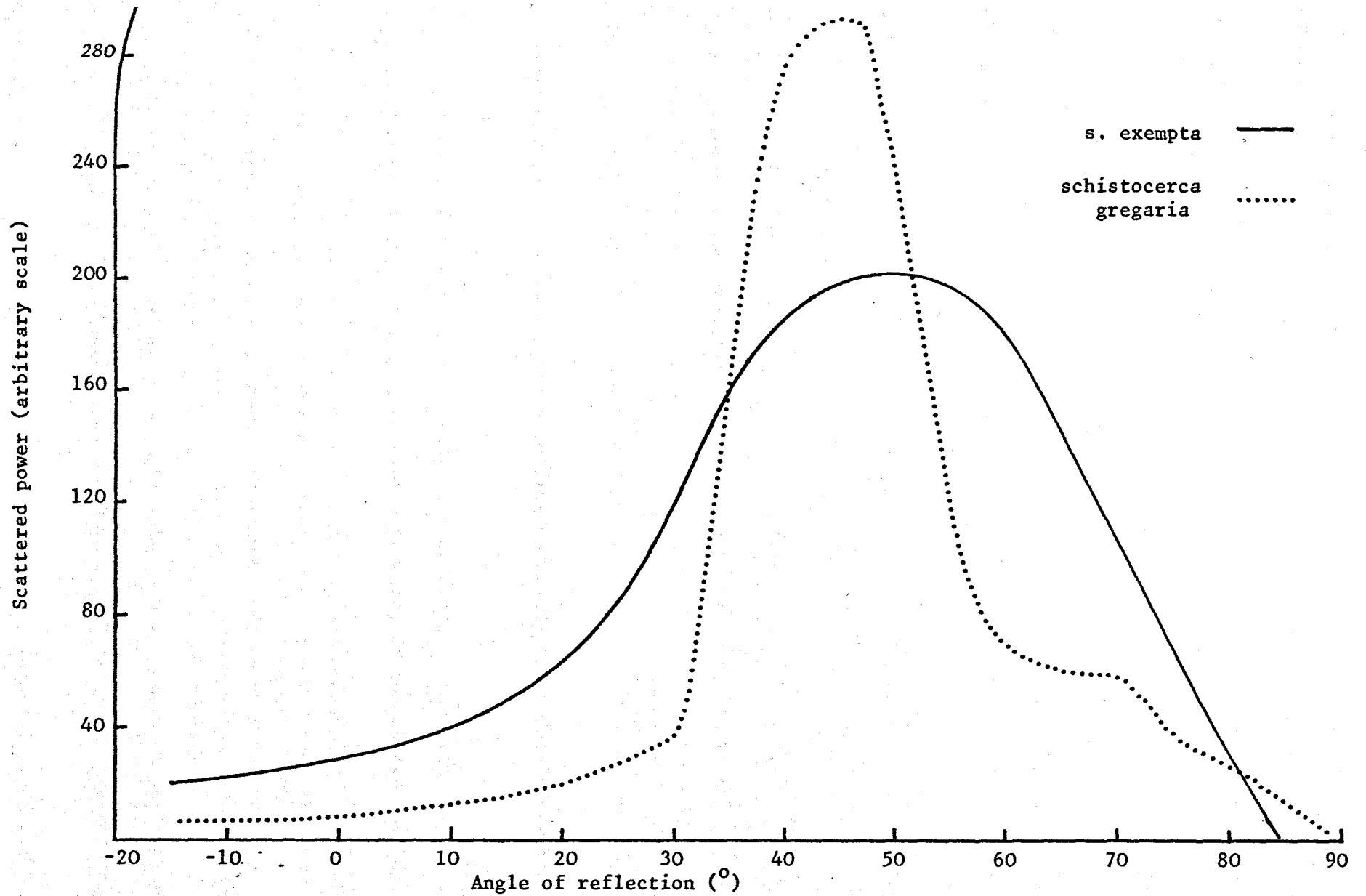


FIGURE 6.10 Scattering characteristics for the hind wings of *s. exempta* and *schistocerca gregaria* for an angle of incidence of 45°.

wing is clearly more diffuse than that from the specular locust wing.

The full width at half maximum of the scattering characteristics for each wing was not found to change dramatically with angle of incidence. Therefore, to simplify the calculations the FWHM at $\theta_I = 45^\circ$ was assumed to be characteristic of scattering for each wing. The results are summarised in Table 6 .

TABLE 6

FWHM OF SCATTERING CHARACTERISTIC
AT $\theta_I = 45^\circ$

<u>INSECT SPECIES</u>	<u>FORE WING</u>	<u>HIND WING</u>
s. <u>exempta</u>	22.0 $^\circ$	42.5 $^\circ$
<u>schistocerca gregaria</u>	22.0 $^\circ$	17.5 $^\circ$

The measurements were made on the upper surface of each wing in question. The lower surface of the s. exempta fore wing had the same surface as the upper and lower surfaces of the hind wing. It was considered unlikely, using the geometry of the operational system, to receive reflections from the upper surfaces of an insect's wings, and so in the case of s. exempta only the value for the hind wing was needed in the calculations. The lower surface of the fore wing of schistocerca gregaria was very similar to the upper surface and the two surfaces of the hind wing were the same. In the model, the scattering from schistocerca gregaria was therefore characterised by

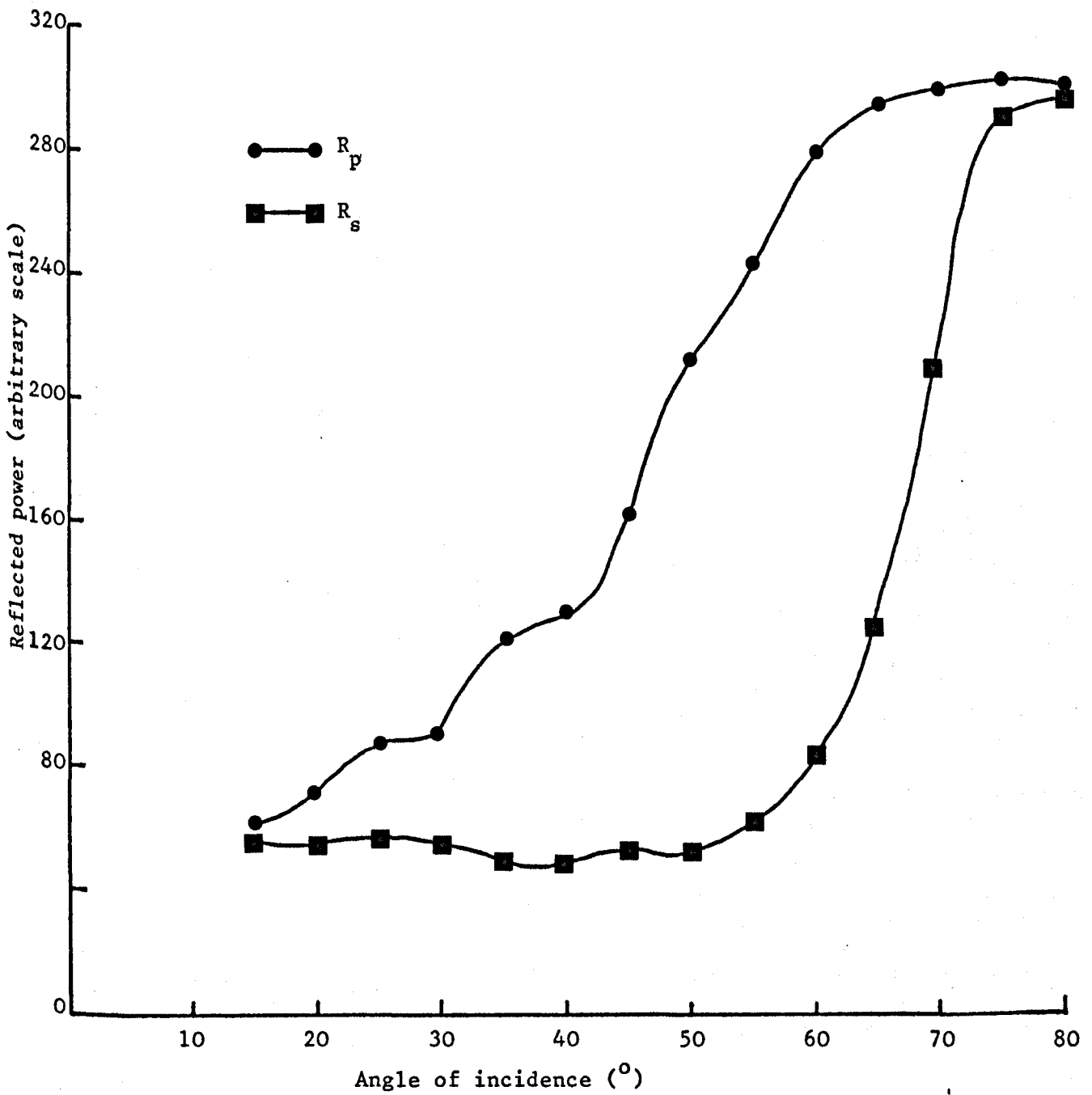


FIGURE 6.11(a) Reflection coefficients R_p and R_s for the hind wing of s. exempta.

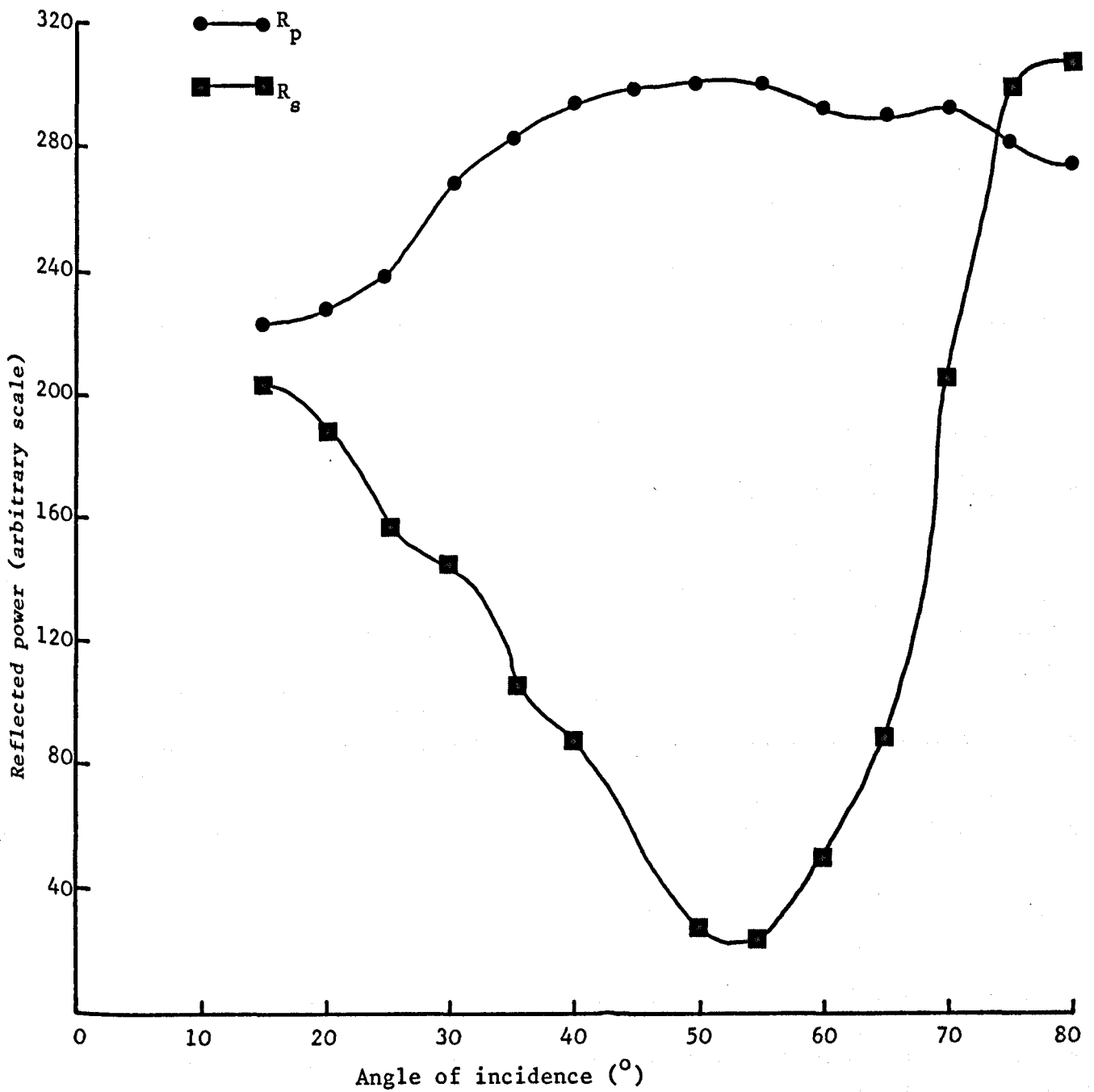


FIGURE 6.11(b)

Reflection coefficients R_p and R_s for the hind wing of Schistocerca gregaria.

the average value of the fore and hind wings.

The reflection coefficients, R_p and R_s corresponding to light polarised perpendicular and parallel to the wing surface, respectively, were measured using the same experimental arrangement (Figure 6.9). The powers reflected in the direction $\theta_R = \theta_I$ were measured for angles of incidence in the range $15^\circ - 80^\circ$. Results for the two hind wings are shown in Figure 6.11. There is a strong Brewster effect in the case of schistocerca gregaria (c.f. a glass surface) but not for s. exempta.

For the same reasons as described above these results were considered typical of the two types of insect, and used in the model which is described in the next section.

6.3.2 Computer Model of Flapping Flight

The simple model described here was developed only as far as was necessary to show the important features of the polarisation and aspect effects.

The model consisted of a pair of wings, each of area A_R , which were hinged along a horizontal axis and moved in the manner shown in Figure 6.12. The wings were assumed to be rigid and planar, and to flap in a sinusoidal manner i.e. the angle THETA between each wing and the vertical plane at time TIME was given by

$$\text{THETA} = 90 \left(1 - \cos \left(360 \times \frac{\text{TIME}}{\text{PERIOD}} \right) \right) \quad (6.2)$$

where the PERIOD is the wing beat period.

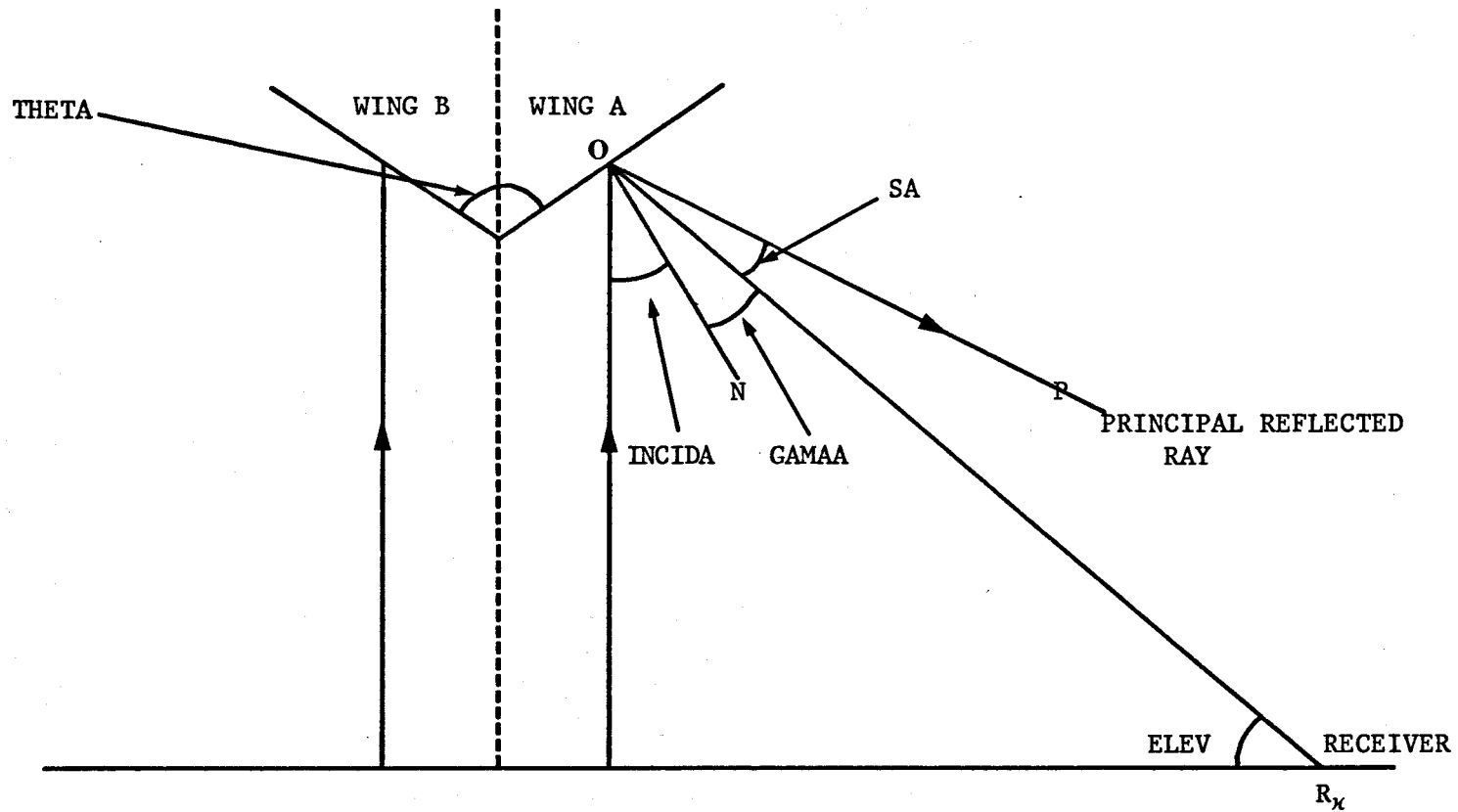


FIGURE 6.12 Geometry of the flapping flight model

The illuminating beam was made to be vertical with horizontal dimensions much larger than those of the wings. The receiver was placed initially at position R_x , viewing the transmitter beam at an angle of elevation $ELEV$. The program calculated the power received by the receiver from the two wings in the following way.

For a given wing angle $THETA$ the angles of incidence of the transmitter beam on the two wings were calculated thus

$$\begin{aligned} INCID A &= 90 - THETA \\ INCID B &= THETA - 90 \end{aligned} \tag{6.3}$$

The value of the reflection coefficients RP and RS were then computed from polynomial representations of the experimental results obtained above using the absolute value of $INCIDA$ or $INCIDB$. Considering now only wing A for simplicity the values of RP and RS were used to calculate the powers of the respective polarisation components reflected in the direction OP defined by $REFA = INCIDA$. The next step was to compute the angle between OP and OR_x , so that the power scattered in the direction of the receiver could be calculated. From simple geometry,

$$GAMAA = THETA - ELEV \tag{6.4}$$

and the scattering angle SA is given by

$$SA = INCIDA - GAMAA \tag{6.5}$$

The power scattered in direction SA away from the primary ray was

then computed from a Gaussian fit to the scattering characteristics measured above. For both s. exempta and schistocerca gregaria Gaussian profiles with half widths equal to the measured values were found to fit the experimental data to an accuracy of approximately 10%. The S-component of the power scattered by wing A into the receiver was therefore given by

$$RECDAS = RS \times SCATA \times AREA \quad (6.6)$$

$$\text{where } SCATA = \text{EXP} \left\{ -\frac{1}{2} \left[\frac{SA \times 2.354}{(FWHM)} \right]^2 \right\} \quad (6.7)$$

$$\text{and } AREA = \text{SIN}(THETA) \quad (6.8)$$

Similar equations can be written for the p-component and for wing B. The total power received was then computed from

$$RECDT = RECDTS + RECDTP \quad (6.9)$$

where RECDTS and RECDTP are the total S- and p- components of the power received, and can be written as

$$RECDTS = RECDAS + RECDBS \quad (6.10)$$

$$RECDTP = RECDAP + RECDBP \quad (6.11)$$

where RECDAS is the received s-component from wing A and the other terms are defined similarly.

The computer program thus calculated the expected received power during the wing beat cycle by incrementing TIME .

Figure 6.13 shows results for a pair of wings with characteristics of s. exempta viewed at a received elevation of $ELEV = 45^\circ$. In both the p- and s- components the two peaks are seen on both the downbeat (first half of displayed period) and the upbeat, demonstrating the symmetry inherent in this model. Of the two peaks on the downbeat the first one is due to reflection from wing A and the second from wing B. It is clear from this picture that if the receiver was looking 'head on' then the contribution from each wing would be in phase and only one peak would result. This can be crudely simulated by progressively increasing the receiver elevation until $ELEV = 90^\circ$ (equivalent to directly 'head on') (see Figure 6.14). The origin of the aspect effect is therefore evident. It is due to out of phase reflections from each wing on the downbeat, as seen from the side, which when viewed from 'head on' are in phase. The small peak following the split peak seen in the experimental results (Figure 6.4) is not simulated here, but is thought to be due to a complex 'feathering' action of the non-rigid wings on the upstroke.

The limitations of this model namely, (a) no consideration of wing bending and (b) no distinction between upstroke and downstroke, are clearly evident in the resulting patterns. However no attempt was made to improve since it had successfully described the basic scattering mechanism in its simple form.

Figure 6.15 shows the p- and s- components for the case of wings with the characteristics of schistocerca gregaria. From the strong Brewster effect in the reflectivity coefficients some difference between the received p- and s- components might have

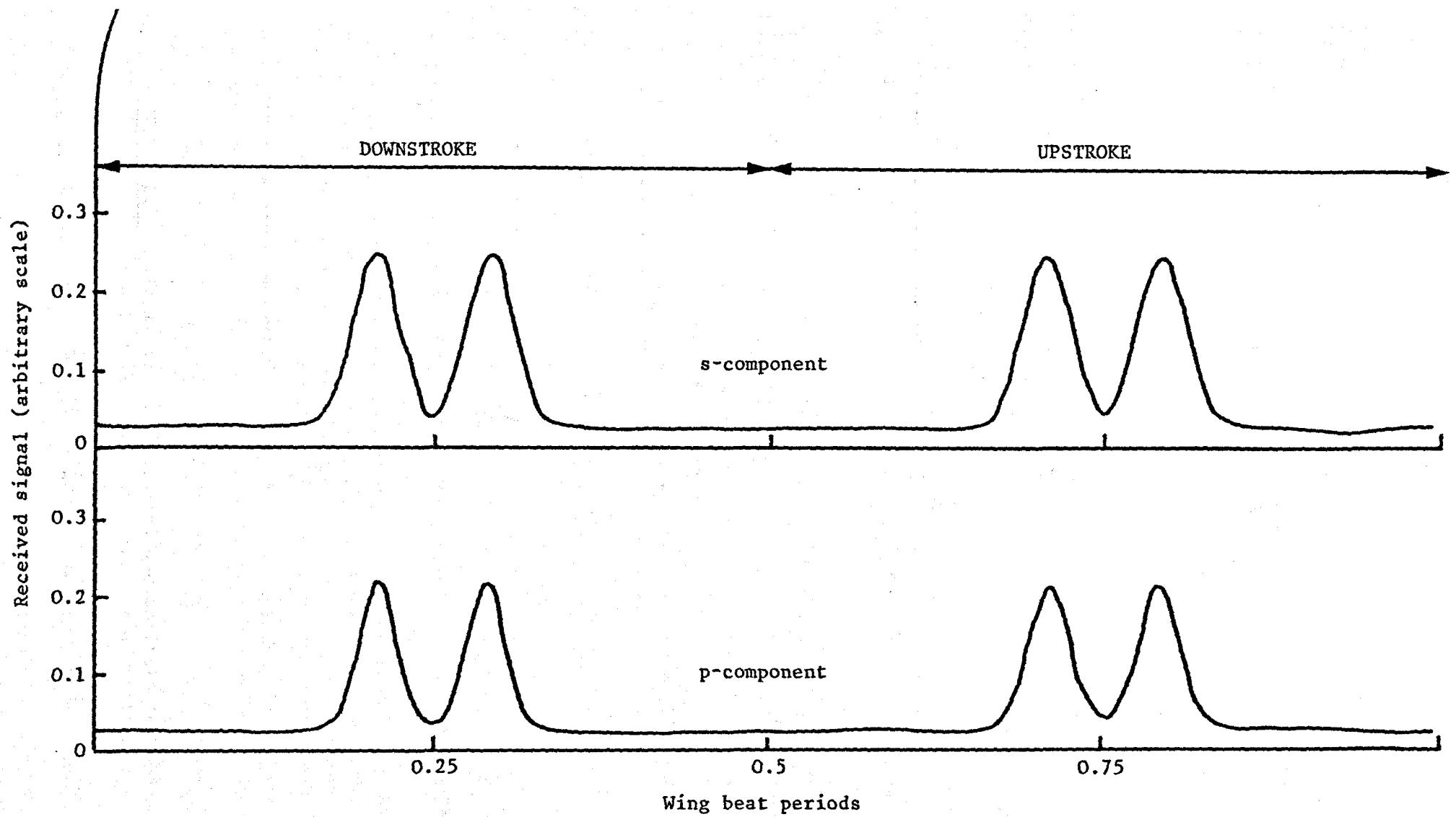


FIGURE 6.13

Computer simulation of received signal from a s. exempta-type insect

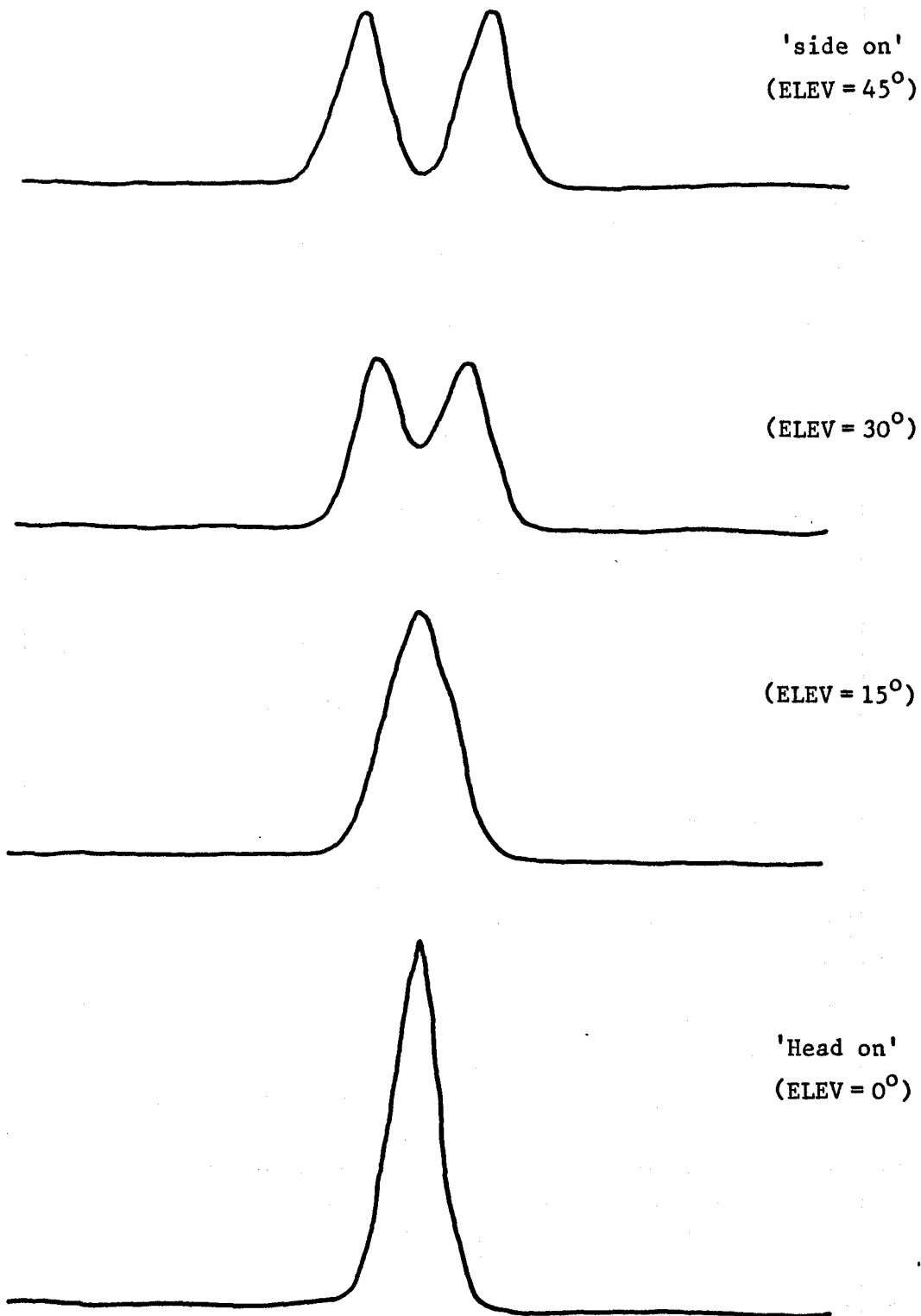


FIGURE 6.14

Computer simulation of the splitting of the main peak on the downbeat, as a function of the receiver aspect. (c.f. Figure 6.4)

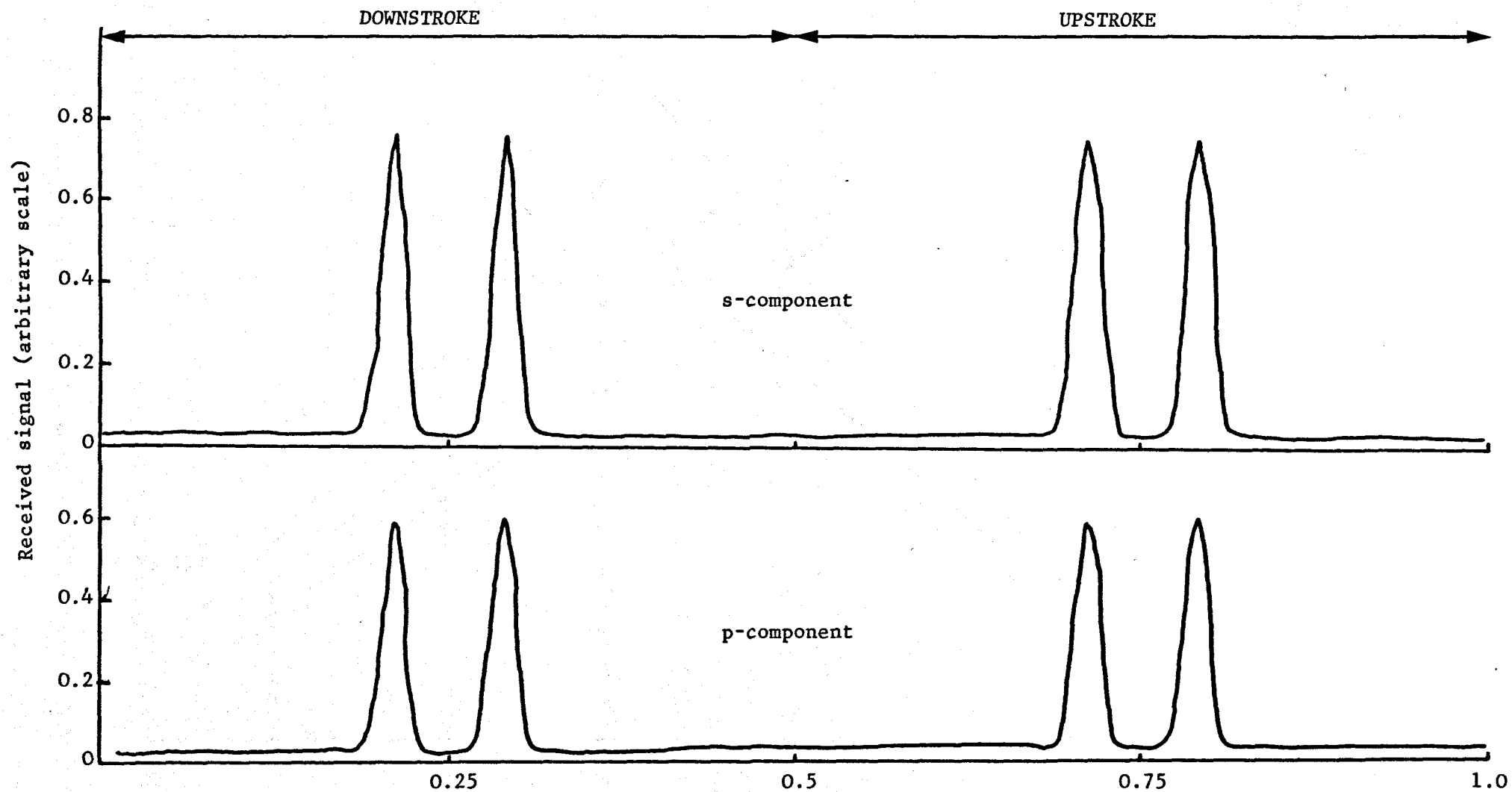


FIGURE 6.15

Computer simulation of received signal
from schistocerca gregaria-type insect

θ_B - Brewster angle
for locust wing

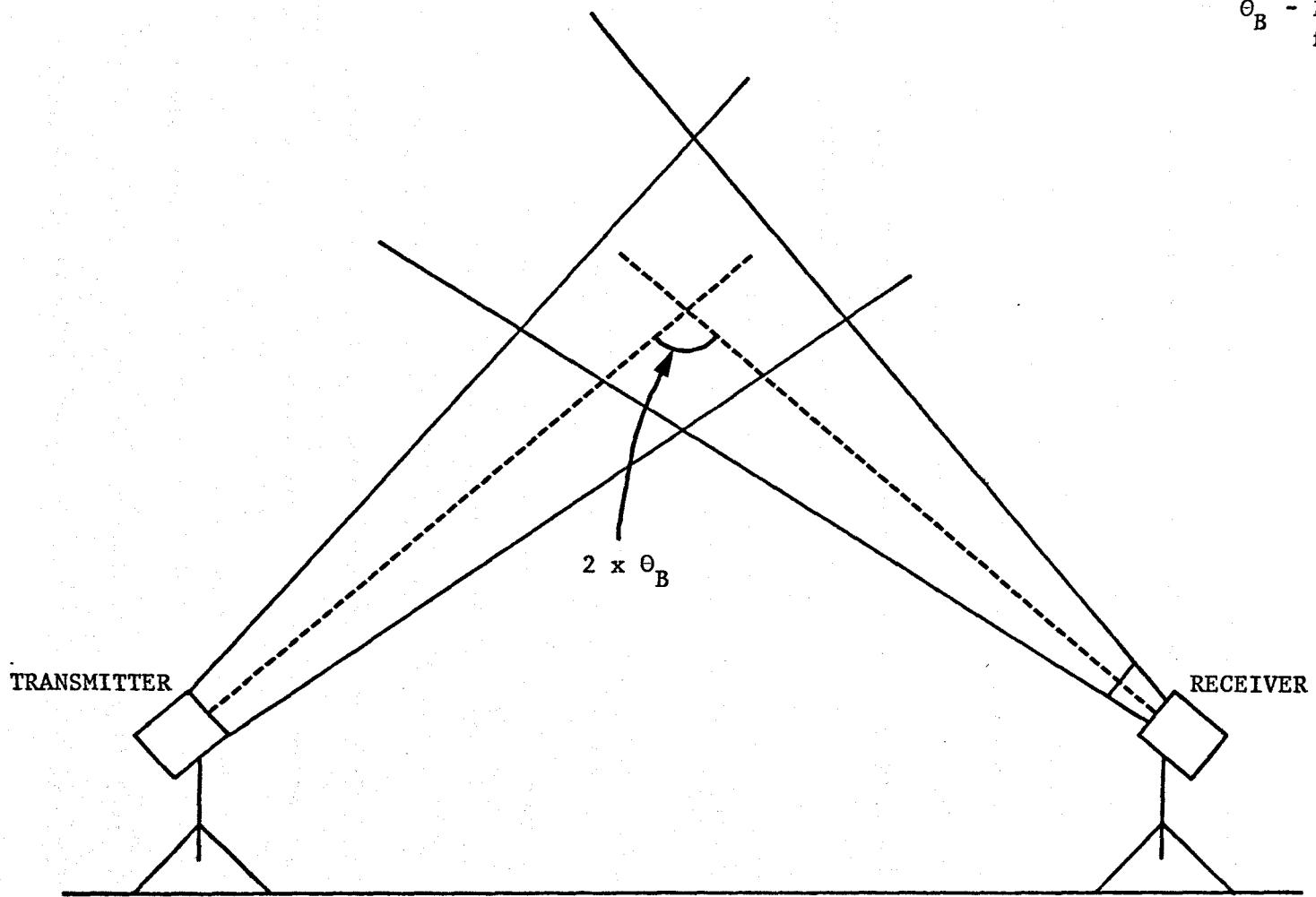


FIGURE 6.16

Receiver-transmitter geometry for differentiating between reflected p- and s- components.

been expected, there is clearly none. This, however, is not surprising since in this geometry, for $ELEV = 45^\circ$, no significant power is received for angles of incidence greater than 22.5° . Therefore the large difference between the values of RP and RS at the Brewster angle (angle of incidence equals 50°) never affects the received power. For the difference between RP and RS to affect the results the angle between receiver and transmitter (TOR) has to be equal to twice the Brewster angle.

This would require the geometry shown in Figure 6.16. In this case it should be feasible to differentiate between moth and locust types on the basis that for locust types the received s- and p- components would be widely different and for moths they would be approximately similar. This may provide a valuable aid to species identification in future work.

6.4 VARIATION OF RESPONSIVITY ACROSS PHOTOMULTIPLIER PHOTOCATHODE

The variation of responsivity across the photocathode of the photomultiplier tubes used in the optical system was investigated for two reasons. Firstly, to validate the assumption made in Section 2.3.1 that the receiver gain in an optical system is constant across its field of view. Secondly, to confirm that variations in responsivity were not the cause of the 'polarisation effect' (Section 6.2).

A block diagram of the equipment used in these experiments is shown in Figure 6.17. A gantry was scanned across the field of view

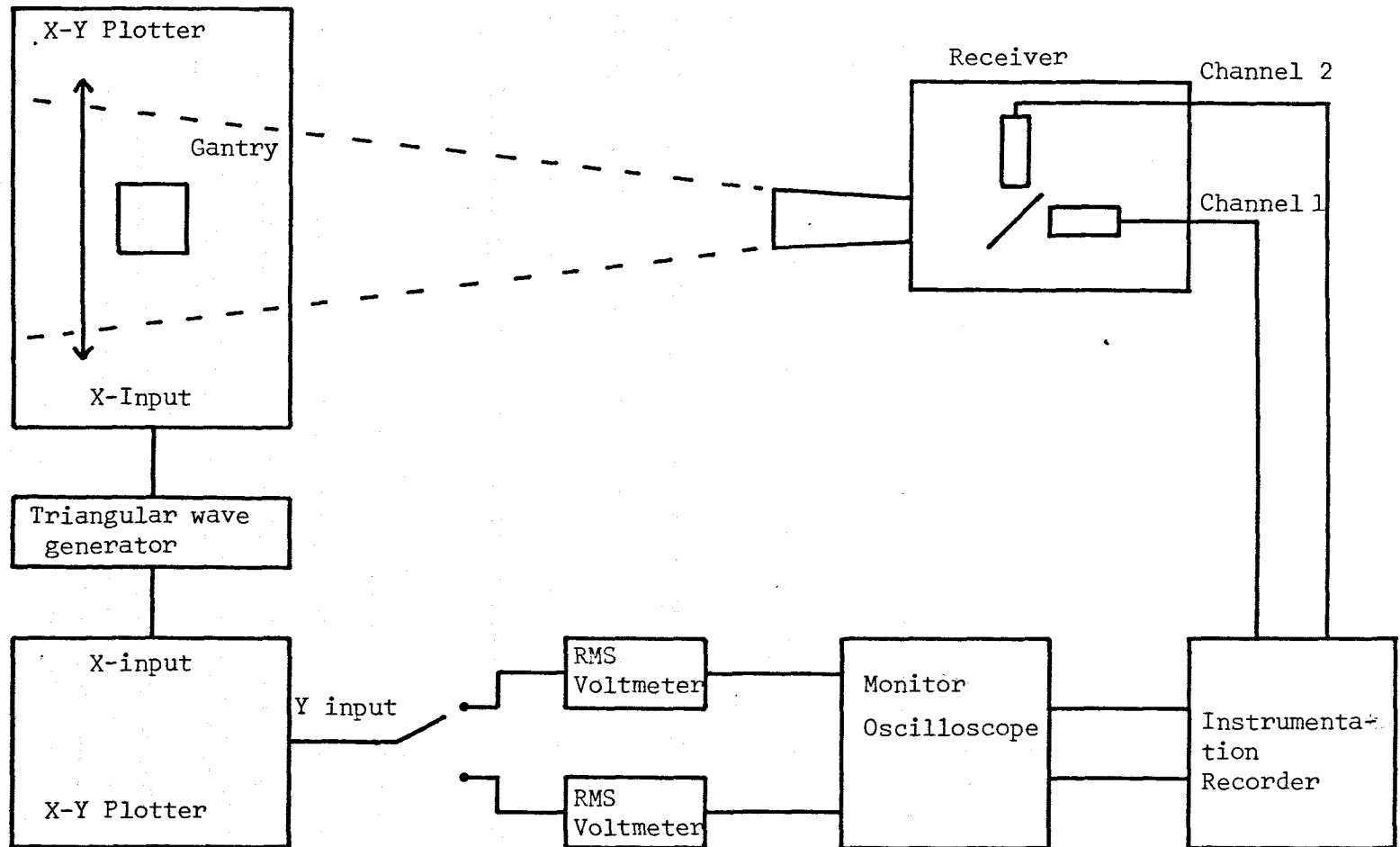


FIGURE 6.17 Block diagram of equipment used to measure photocathode responsivity profiles

of the receiver at a range of 2 m. The scanning action was produced by mounting the gantry on the X drive of an X-Y graph plotter, which was driven by a very low frequency triangular wave. The calibration unit (Section 4.5.1) was mounted on the gantry and provided a chopped reference signal.

The r.m.s. value of the resulting signal from either photomultiplier tube was applied to the Y input of another X-Y plotter whose X-base was driven in synchronism with the scanning action. The tube gain was kept constant and the photocathode responsivity was thus plotted against position.

Responsivity profiles for two different EMI type 9558B photomultiplier tubes are presented in Figures 6.18 and 6.19. These measurements were made using light in the waveband 700 - 850 nm. Smaller variations were observed when higher energy (visible light) photons were used (Figure 6.20). It is thought that this is due to the lower energy photons being more sensitive to variations in the photocathode work function.

These results show conclusively that the 'polarisation effect' is not due to spatial variations in photocathode responsivity. Not only are the variations too small to account for the large differences seen in Figure 6.7, but also it is noted that the 'polarisation effect' has a cyclic nature (seen in Figures 6.7 and 6.8). It is impossible that this could be associated with the spatial characteristics of the photocathode.

The assumption that the receiver gain is constant across the field of view is considered valid in the light of these results. This is true provided that an optical mask is used in the receiver to

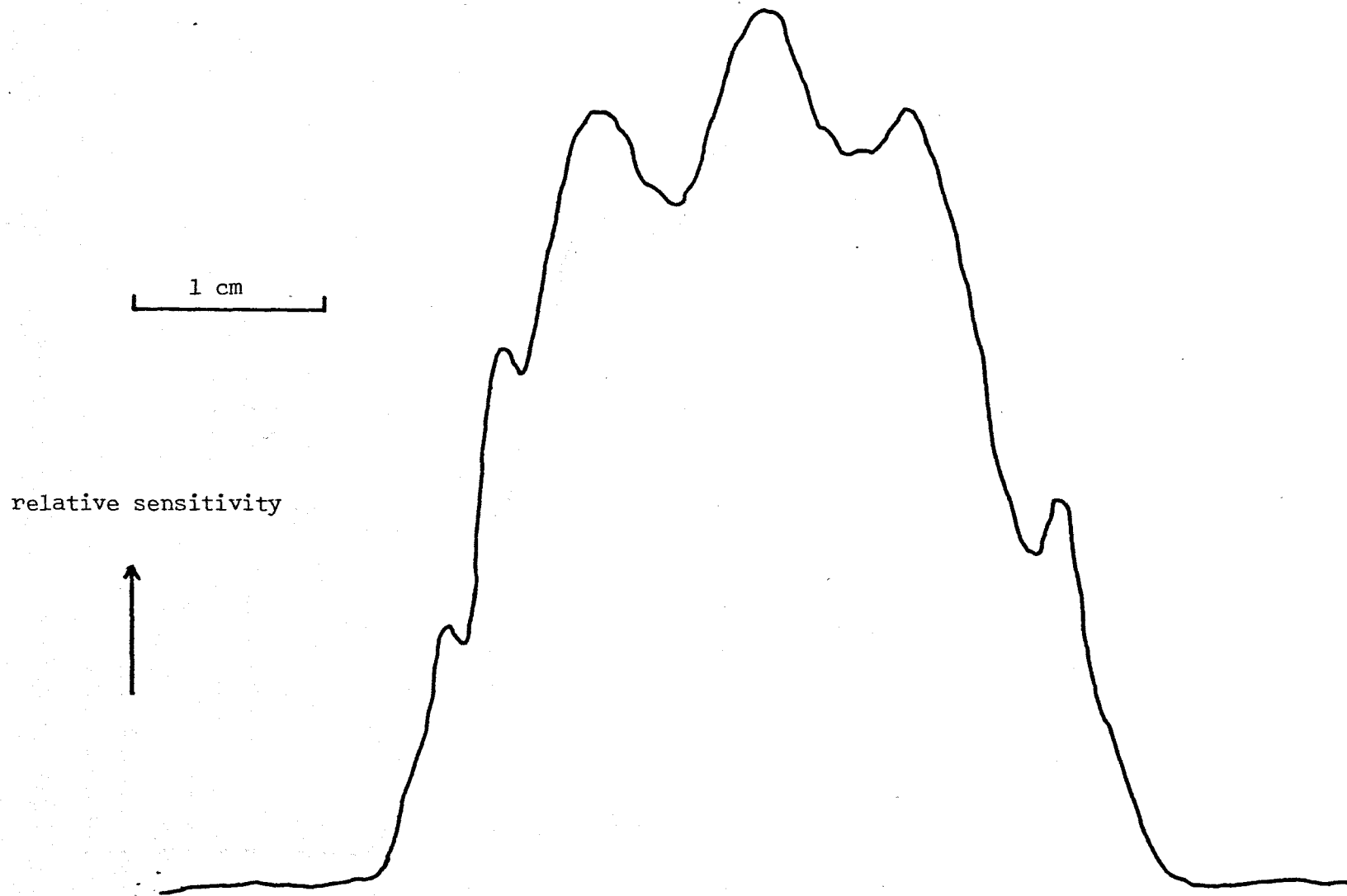


FIGURE 6.18 Variation of sensitivity across the photocathode of EMI photomultiplier tube type 9558B (Ser. No. 25700) measured using light in band 700 - 850 nm.

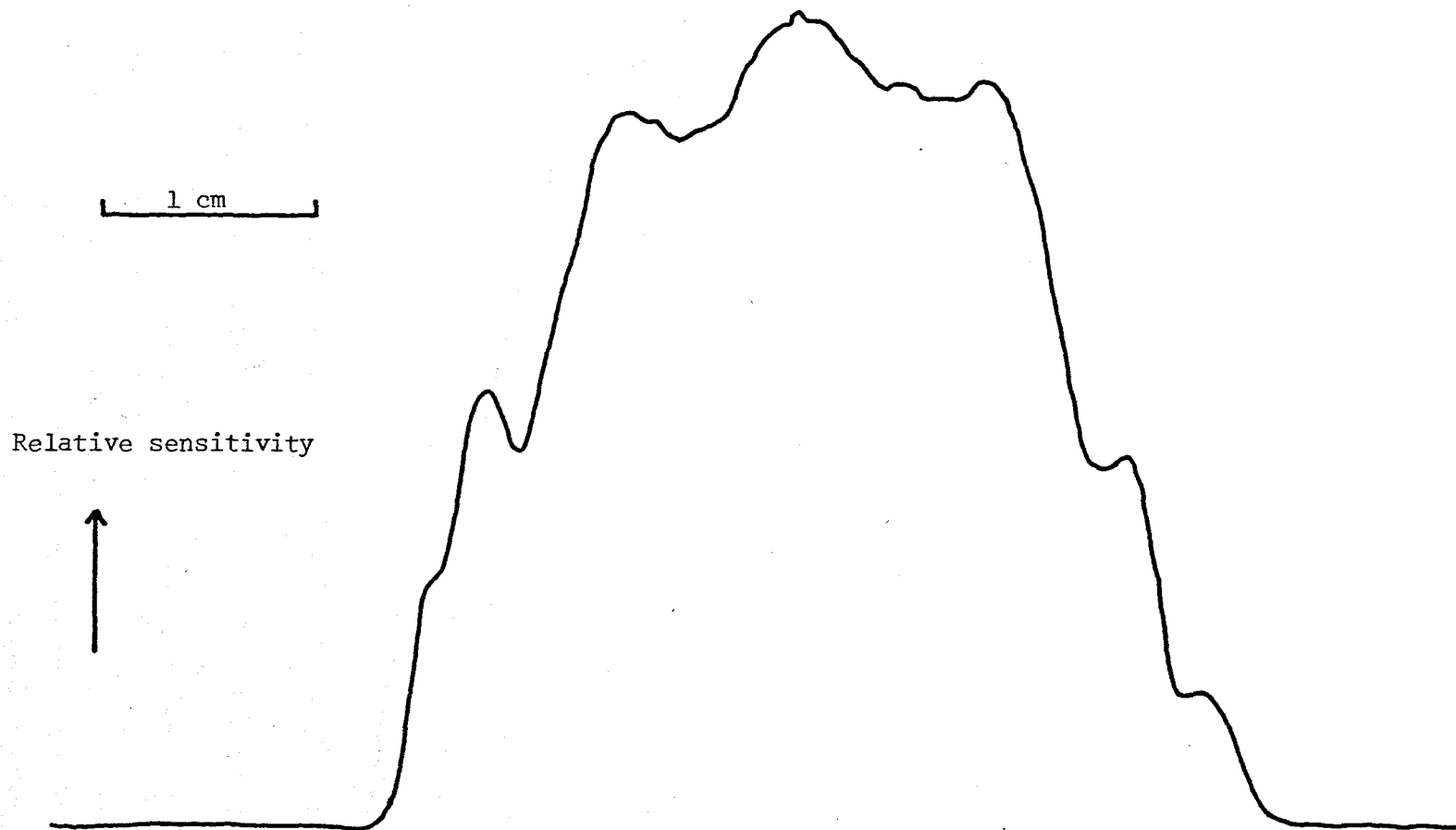


FIGURE 6.19 Variation of sensitivity across the photocathode of EMI photomultiplier tube type 9558B (Ser. No 25725) measured using light in band 700 - 850 nm.

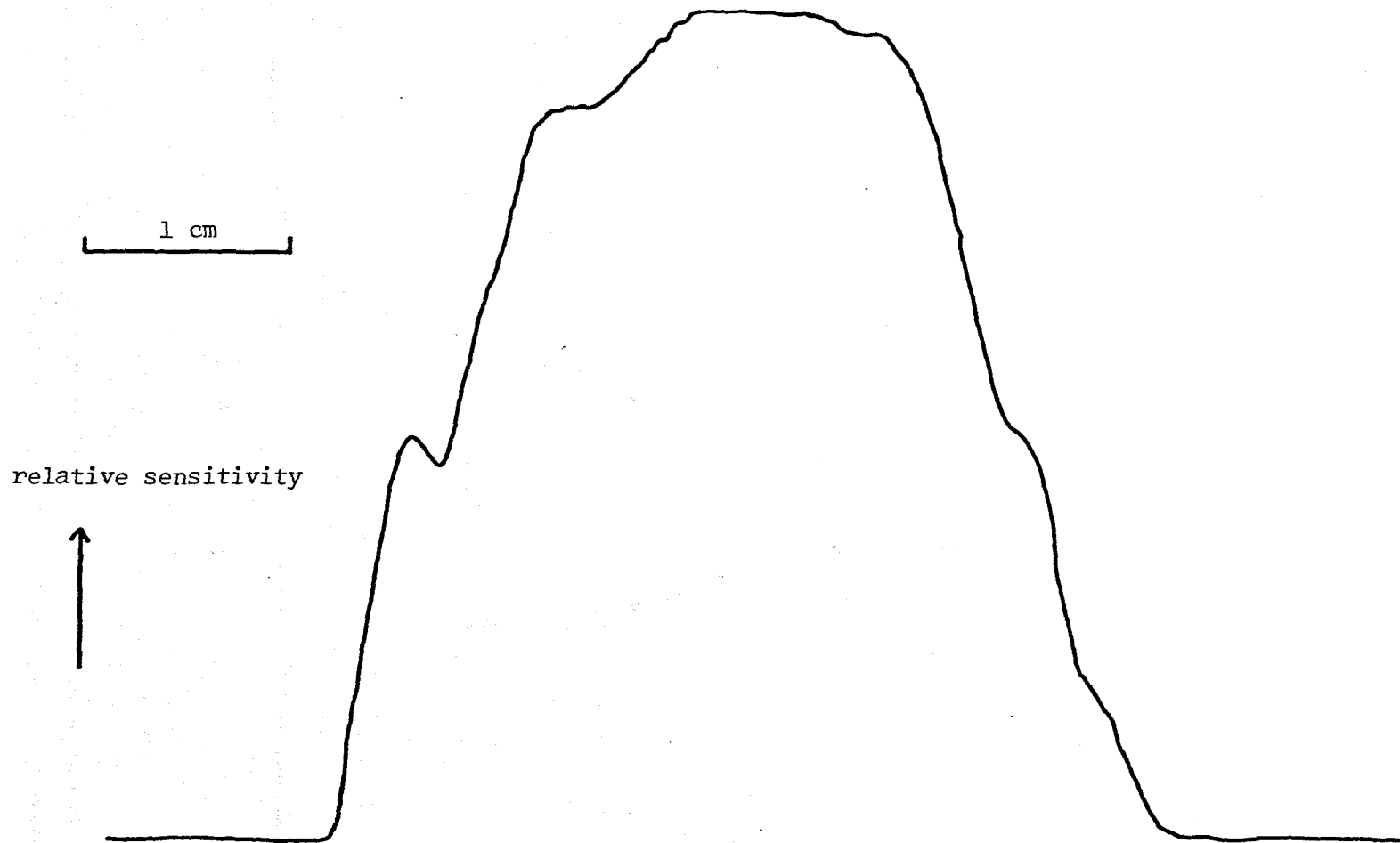


FIGURE 6.20 Variation of sensitivity across the photocathode of EMI photomultiplier tube type 9558B (Ser. No. 25700) measured using unfiltered tungsten source at 3000°K

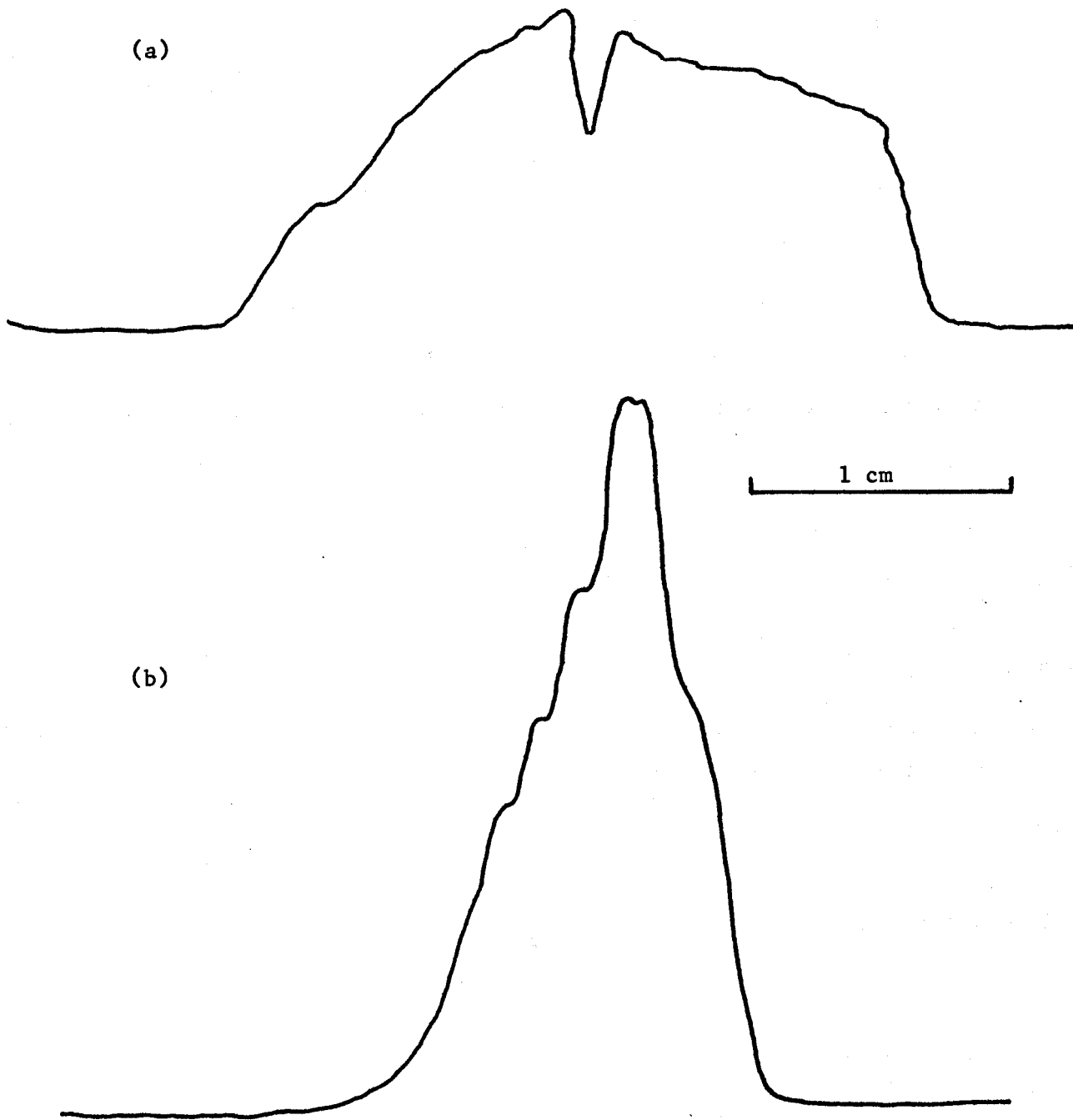


FIGURE 6.21

Sensitivity profiles across a Russian photo-multiplier tube (type FEU-28) in perpendicular directions.

restrict the sensitive area to the central portion where the variations are less than 10%.

This method was also used to evaluate the suitability for our purpose of a sparsely documented Russian photomultiplier (type FEU-28). The results for this tube are shown in Figure 6.21. The narrow width of the photocathode in one direction (which could not be deduced by inspection) made the tube unsuitable for our use. The unsuitability was compounded by the poor anode sensitivity of the tube, which was three orders of magnitude less than that of the EMI 9558B.

CHAPTER 7

RESULTS

7.1 REVIEW OF FIELD WORK UNDERTAKEN

7.1.1 Background

The optical system has been used on collaborative field projects with the COPR Radar Group in Kenya and Mali. Three projects were conducted in Kenya as part of the COPR Armyworm Research Programme, described in Section 1.5 and a fourth formed part of the COPR/OCALAV Grasshopper Research Project in Mali, W. Africa. These are described in chronological order below.

7.1.2 Armyworm Studies, Kenya, March - April, 1978

This field trial formed part of the COPR/DLCOEA/KARI Joint Armyworm Research Project, which had been set up to study the population dynamics of the East African Armyworm Moth (spodopetera exempta). It was planned to use radar to try and answer the question "What proportion of an emergent population of Armyworm Moths engage in long distance flight?". In this plan the optical system was to supplement the radar observations at low altitude. It was not intended to operate the radar for this first season. The opportunity was, however, taken to evaluate the prototype optical system in field conditions and to collect preliminary data.

The operation was based at the Kenyan Agricultural Research Institute, Muguga, 20 miles outside Nairobi. The Institute provided laboratory facilities for experiments and was a good base from which field expeditions could be mounted.

The Armyworm "season" (approximately from March - April in Kenya) was biologically unusual in 1978, probably because of abnormally high rainfall in the preceding six months. No Armyworm outbreaks were reported and the general insect activity (moths and grasshoppers) was very low. Field observations were therefore difficult and much of the work was carried out in the laboratory, which is described in Sections 6.1 and 6.2.

Two small field trials were mounted to evaluate the prototype. For convenience, the first experiments were performed close to the Institute at Muguga. Local insect activity was low for the reasons already mentioned coupled with low night time temperatures (the Institute is at 7000' ASL). However, the opportunity was taken to "run-up" the system and check its sensitivity using the artificial insect target (Section 4.5.3). The size of the vane had been adjusted in the laboratory to give comparable signals to s. exempta moths.

The transmitter and two channel receiver were separated by 20 m and arranged to look horizontally so that the sample volume was positioned at a range of 20 m from both the receiver and the transmitter. The artificial insect target was swung through the sample volume to simulate the passage of an insect. The result of one of these transects is shown in Figure 7.1. The modulation from

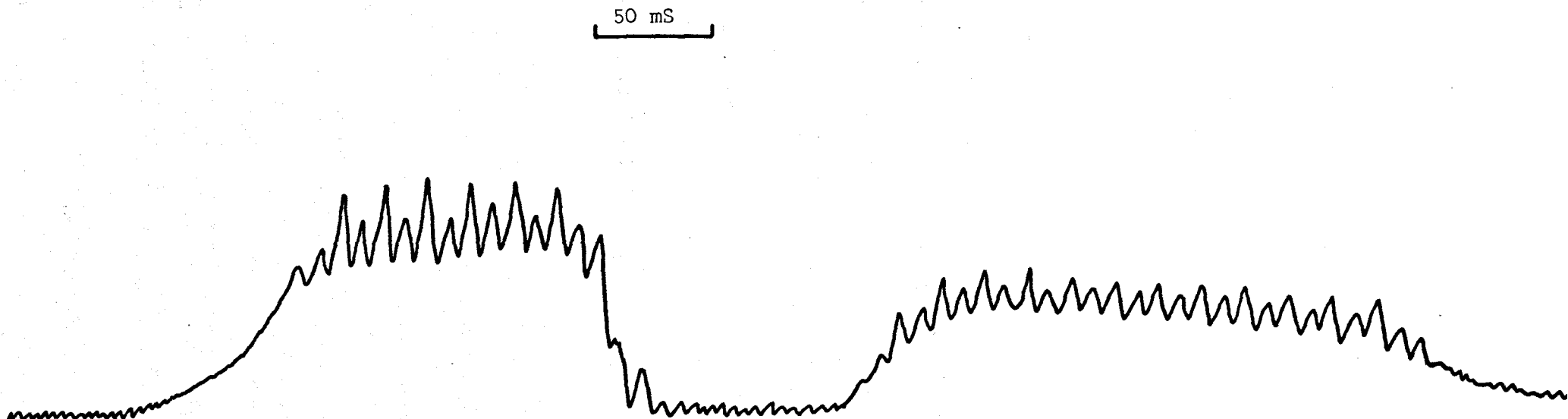


FIGURE 7.1

Artificial insect target swinging through the sample volume. Modulation and intercepts are clearly shown. The high dc component of the signal arises from the large body of the target.

the rotating vane and the chopping action of the optical mask are clearly seen. The large d.c. component is due to reflection from the body of the motor (Section 4.5.3). The narrowest transmitter beamwidth (0.035 rad.) was used for this experiment (Figure 4.4).

The received power P_R is related to the signal voltage v_s by equation (7.1) namely

$$P_R = \frac{v_s}{r R \mu} \quad (7.1)$$

where r is feedback resistor

R is responsivity of photocathode

μ is photomultiplier gain.

Substituting the following values

$$v_s = 2.0 \text{ v}$$

$$r = 5.6 \times 10^6$$

$$\mu = 10^6$$

$$R = 8.0 \times 10^{-3} \text{ A W}^{-1}$$

gives

$$\underline{P_R = 4.4 \times 10^{-11} \text{ W}} \quad .$$

We calculate the power received from the target on axis at a range as follows.

Power reflected by target

$$P_{REF} = I_{20} \times A \times \sigma \quad (7.2)$$

where I_{20} is the on axis intensity at a range of 20 m

A is the open wing area of s. exempta

σ is the reflectivity of wings.

Power incident on detector assuming that the energy is scattered by the target into a hemisphere is given by

$$P_R = P_{REF} \times \frac{d^2 K}{8 h^2} \quad (7.3)$$

where d is the diameter of receiver lens

K is the transmission of the optics

h is the receiver-target range.

Combining (7.2) and (7.3) and writing the intensity at 20 m in terms of the measured on axis intensity at 10 m gives

$$P_R = I_{10} \left(\frac{10}{20} \right)^2 \frac{A d^2 K \sigma}{8 h^2} \quad (7.4)$$

Using the following values

$$I_{10} = 4.5 \text{ W m}^{-2}$$

$$A = 2 \times 10^{-4} \text{ m}^2$$

$$d = 6.0 \times 10^{-2} \text{ m}$$

$$K = 0.5$$

$$\sigma = 0.2$$

$$h = 20 \text{ m}$$

the received power has been calculated to be

$$\underline{P_R = 2.5 \times 10^{-11} \text{ W}}$$

The agreement between the received power calculated from the measured signal voltage and that expected theoretically is considered good, and validates the assumptions made.

The second field experiment was based at the Kiboko Range Research Station (3000' ASL), where the insect activity was higher than at Muguga because of the warmer night-time temperatures. A number of specimen results were obtained and valuable experience with the equipment was gained. However because of the unusually low activity no operational trials were possible. Instead these were postponed for the Mali project

7.1.3 Grasshopper Studies, September - November, 1978, Mali

The prototype system was deployed as part of the COPR/OCLALAV Grasshopper project in Mali, September 1978. The project had been set up to study the southerly migration of Sahelian grasshoppers. Nightly radar observations of overflight and local take off were made, and correlated with light trap catches and ground sampling of the grasshopper population. The results of previous radar work are reported elsewhere (Riley and Reynolds, 1979). For the optical system, the project represented an opportunity to test the operational strategy and if possible to supplement the radar observations usefully at low level.

Field operation of the prototype optical system required equipment (mobile laboratory and generator) earmarked for use with the second mobile radar station. Operations were therefore

conducted early in the project and ceased before the second radar was deployed. An extended Landrover was used as the laboratory and the internal air conditioner unit was found to be essential for the reliable operation of the recording electronics. Mains power was derived from a 2kVA petrol generator. The experimental site was positioned approximately 100 m south of the radar laboratory (Plate 13).

The two-channel receiver was used for this work. Initially a static configuration was tried in which different heights were sampled sequentially by incrementing the angle of elevation of the transmitter, while the receiver looked vertically. This strategy was found impractical for the two reasons listed below.

(i) The dwell time at each level had to be long (15 - 30 minutes) to collect a useful sample. Consequently measurements of the height profile were unsatisfactory because the different samples could not be related closely enough to each other in time.

(ii) The operations required the continuous participation of at least two personnel. This was impractical for observations over extended periods:

A horizontally-looking monostatic configuration was therefore used for this work (Plate 14). The beams of the closely spaced receiver and transmitter were arranged to overlap over a large distance to give a reasonable sample rate of activity at ground level. The data collected are summarised in Appendix C1 and some of the results are presented in Section 7.3.

The project provided valuable operational experience from which the following conclusions were drawn.



PLATE 13 Optical site, Mali 1978 (the radar site can be seen in the background).

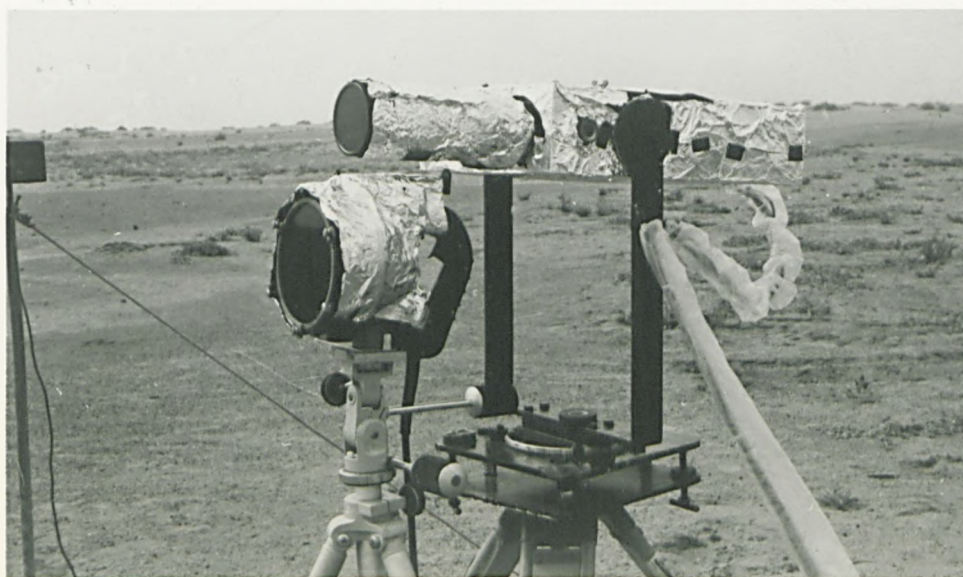


PLATE 14 The monostatic configuration of transmitter and receiver used in the Malian field trial.

(a) Aerial density and wing beat frequency were the most important parameters for supplementing the radar observations. Insect speed and direction were of secondary importance.

(b) The sequential height sampling idea was impractical.

As a result of these findings it was decided to use several single channel receivers to measure wing beat frequency and aerial density continuously at selected heights whilst the two channel receiver measured insect speed and direction when necessary.

7.1.4 Armyworm Studies March - April, 1979; Kenya

This project formed the first joint radar/optical field study of the COPR/KARI/DLCOEA Armyworm Research Project, (Section 1.5).

The African Armyworm occurs in outbreaks with peak densities of 100 larvae per m² over areas of 10 - 50 km² (Brown, Betts and Rainey, 1969). The larvae, when fully grown, pupate in the ground and emerge after about 10 days as adult moths. The biology of the African Armyworm is well described by Brown, Betts and Rainey (1969). Their extensive studies indicated that the emerging moths climbed up grass stems and spent two hours drying their wings out before embarking on their migratory flights, which were predominantly downwind. It was thus considered likely that areas of high larval density would, after the appropriate time interval, have large numbers of moths taking off from them. For the radar this would have made identification reasonably simple. However, shortly before the actual experiments visual observations were made at an outbreak

site which were inconsistent with this simple picture (Rose and Dewhurst, 1979). It was found that after drying their wings the moths flew to nearby trees in which they spent their first night. The moths left the trees before dawn and found somewhere to hide for the day. It was on the following night that they appeared to undertake serious flight. The unfortunate result of this "Tree Phenomena" was that the ground densities were redistributed and could not be easily related to the aerial densities just after take off. This meant that the problems of radar identification were increased.

The following observations were planned at the outbreak site (Figure 7.2).

(i) Visual ground based observations

Estimates of emergence rate and numbers taking off from selected sites were to be made by the entomological team during the night.

(ii) Optical observations

Wing beat frequency distributions and aerial densities were to be measured at three different heights (10 m, 20 m and 30 m AGL).

(iii) Overlooking radar observations

Observations of aerial activity from approximately 50 m AGL upwards. Direction and rates of displacement and wing beat frequency distribution were also to be measured.

(iv) Downrange radar observations

It was planned to position a second ("downrange") radar approximately 20 km downwind of the outbreak site. It was hoped to be able to observe the overflight of moths which had taken off from the outbreak site and flown downwind.

A suitable outbreak site was discovered in the East African

METHODS OF OBSERVATION

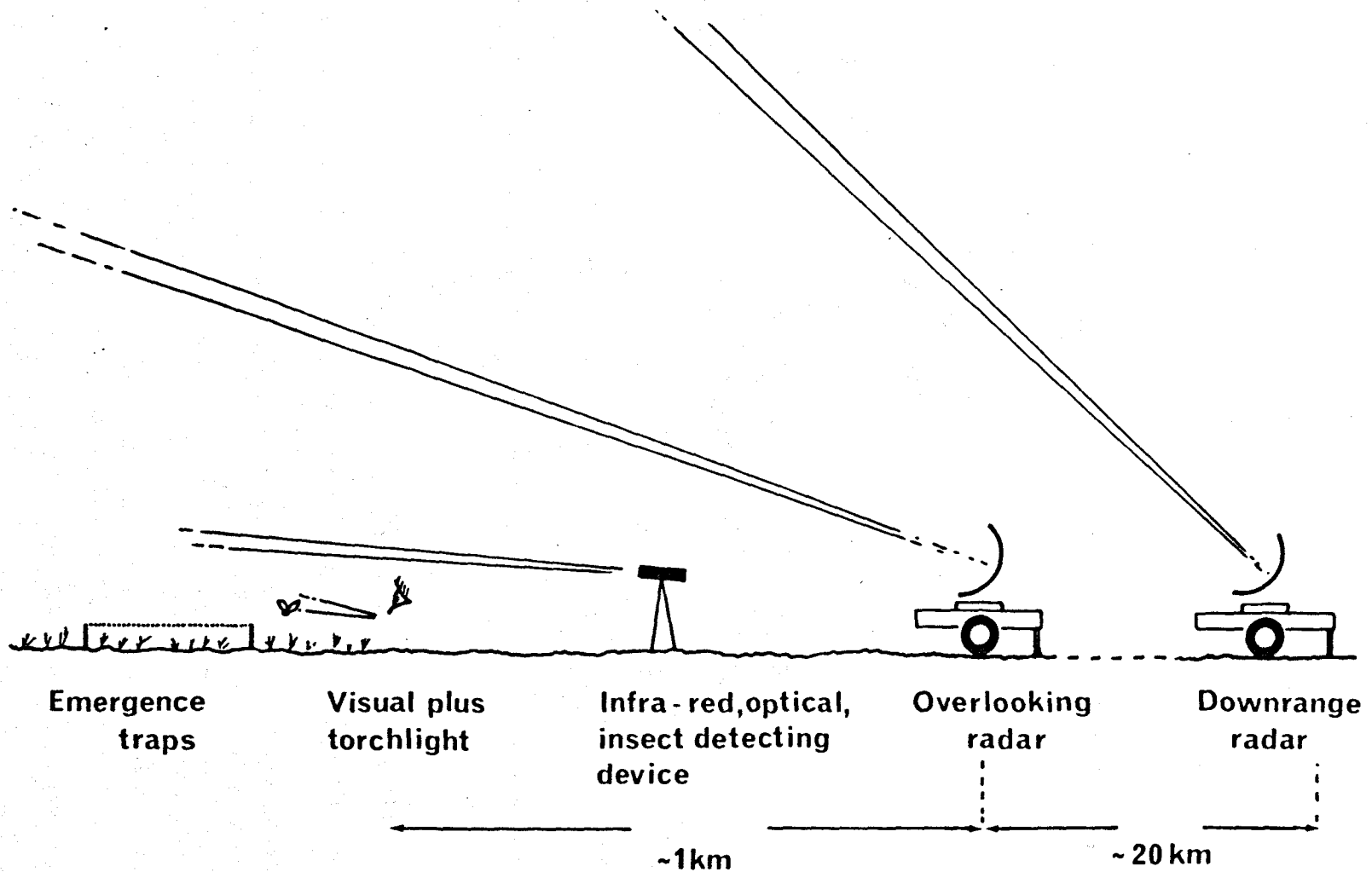


FIGURE 7.2 Observational methods for Armyworm studies, Kenya 1979.

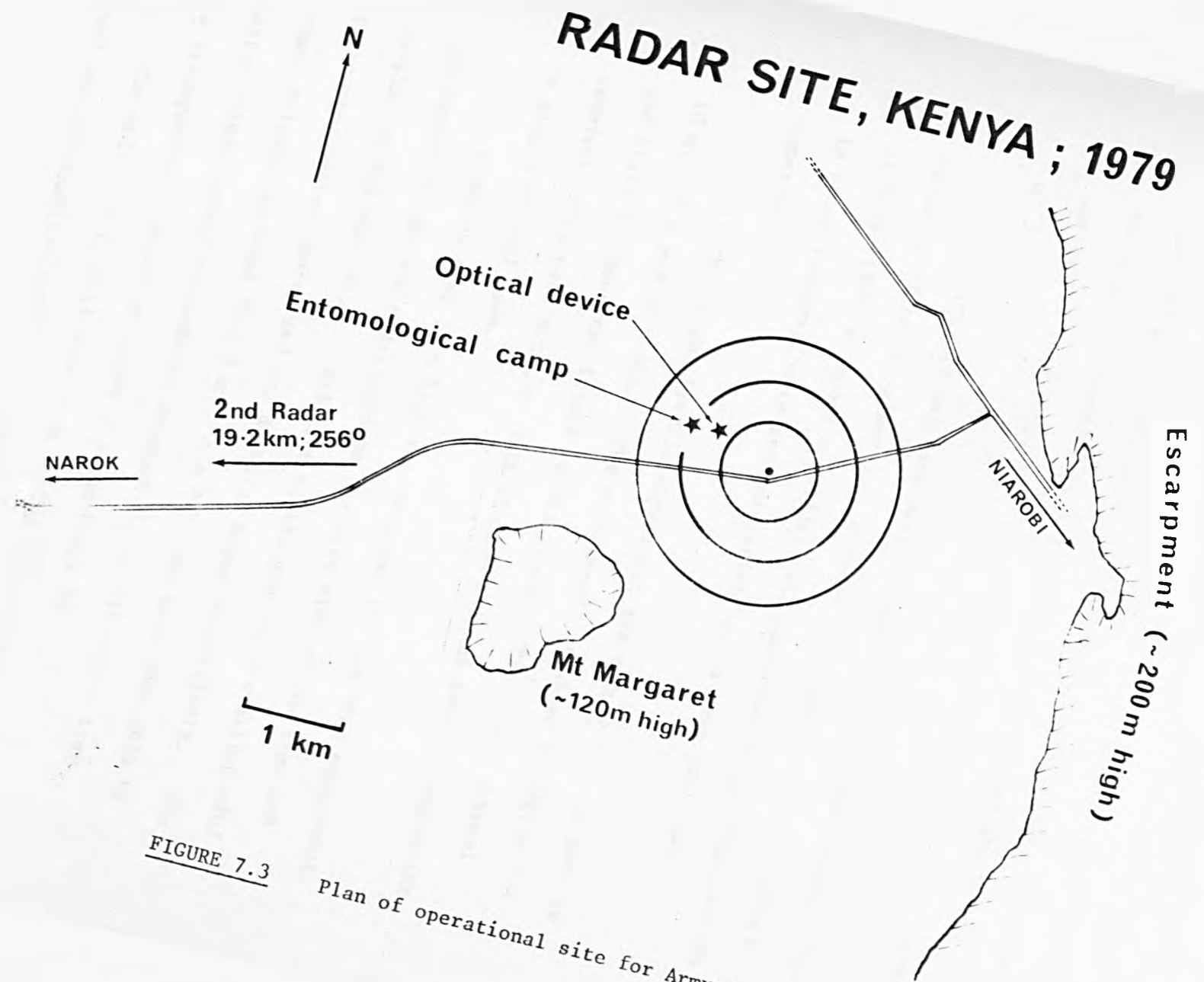


FIGURE 7.3 Plan of operational site for Armyworm studies, Kenya 1979.

Rift Valley about 30 miles north of Nairobi. It was first reported to KARI and then surveyed by Dr. Rose and the radar/optical team to estimate its extent and larval densities. The latter varied from 1.0 - 100 m⁻², the highest being found on the verges along the Narok road and around the edges of some small maize fields. A plan of the site is presented in Figure 7.3. The optical system was positioned in a large area of moderate infestation (10 - 15 larvae m⁻²).

Initially only one optical experiment had been planned (the height profile experiment). However in response to the findings of Rose (1980) a second experiment was performed whose objective was to study immigration to and emigration from a tree (the tree experiment).

In the height profile experiment the sample volumes were at 10 m, 20 m and 30 m AGL. The arrangement is shown in Figure 7.4 and Plate 15 shows the layout in the field. Two single channel receivers were used together with the two channel receiver operating in single channel mode.

A nearby tree 10 m high was selected for the tree experiment. One sample volume was positioned on the east side of the tree and another on the west side. Relative to the general prevailing wind these represented the upwind and downwind edges respectively. The sample volumes extended from 2 m to 8 m AGL, and were thus able to monitor either upwind or downwind movement in or out of the tree. This arrangement is shown in Figure 7.5 and Plate 16.

The radar and optical data from this project have been analysed and the complete results are presented elsewhere (Riley,



PLATE 15 Equipment used in the height profile experiment, Mt. Margaret site, Kenya 1979.

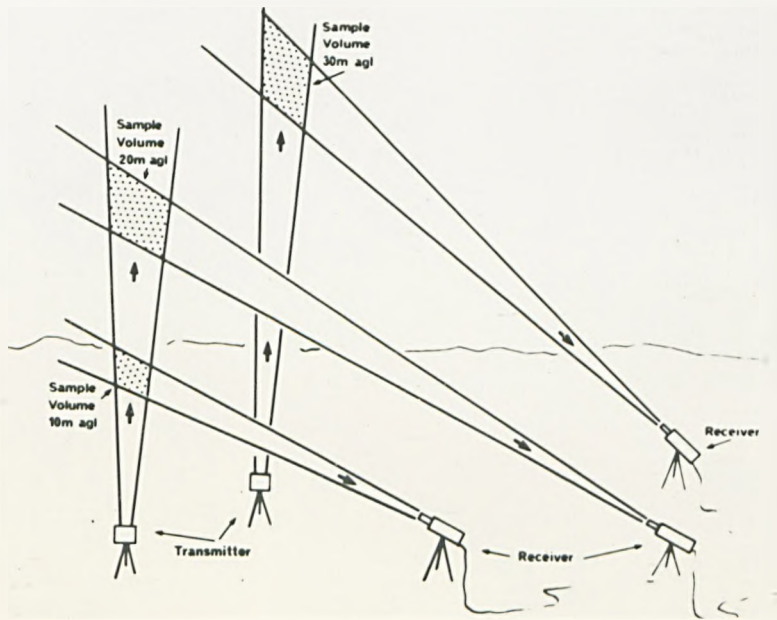


FIGURE 7.4 Schematic diagram showing the arrangement of the sample volumes for the height profile experiment. Mt. Margaret site, Kenya 1979.



PLATE 16 The layout of the equipment for the tree experiment, Mt. Margaret site, Kenya 1979.

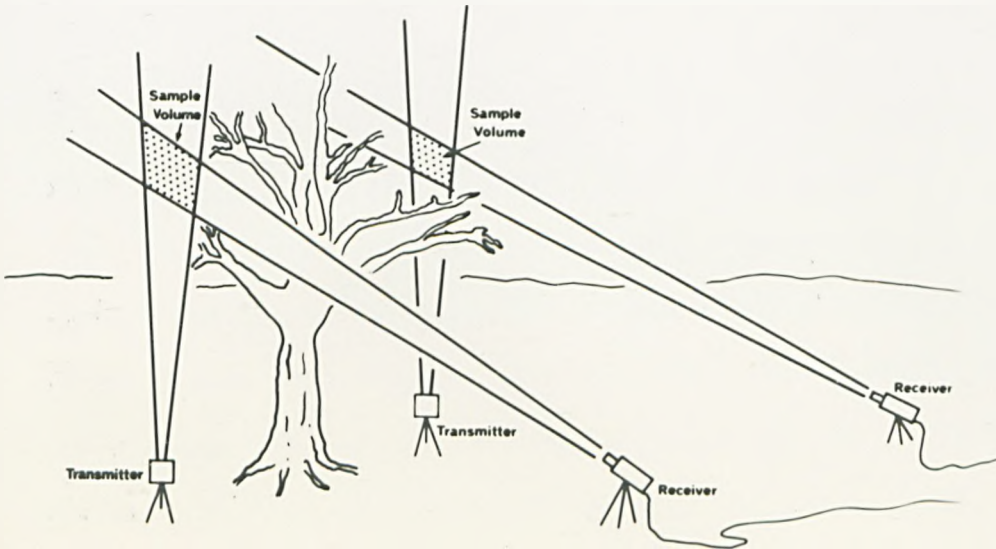


FIGURE 7.5 Schematic diagram showing the positions of the sample volumes for the tree experiment, Mt. Margaret site, Kenya 1979.

Reynolds and Farmery, 1981). Some of these are presented in Section 7.3 to illustrate the potential of the system and the collected data are summarised in Appendix C2.

During this first season of Armyworm studies two shortcomings were identified in the operation of the optical system. Firstly, it became apparent that for the system to be useful it had to monitor the three sample volumes continuously throughout the period 1900 - 0600 hours on at least eight consecutive days. The system had therefore to be largely automatic since only one operator was available. This stimulated the construction of the auto-eht unit and the counter system (Section 4.4).

Secondly, it is during the Armyworm season that the long rains begin. Operations were often disturbed by heavy rain storms and so, to prevent water getting into the receivers or cracking the hot infra-red glass filters on the transmitter, weather shrouds were introduced for the 1980 season.

7.1.5 Armyworm Studies February - April 1980; Kenya

This project represented the second season of joint radar/optical studies for the COPR/KARI/DLCOEA Armyworm Research Project, and carried on from the work done in 1979. Two findings of that work affected the optical strategy for this project. First, Armyworm Moths had not been found to dominate the aerial fauna in 1979. This had made identification more difficult and so the optical system was to make more measurements of moths flying close to the ground

which could be visually identified. Second, the results of the height profile experiment had not shown any significantly different behaviour between 10 - 30 m AGL. Changes in aerial activity were reflected to a greater or lesser extent at all three levels. It was therefore decided to examine the activity closer to the ground to ascertain whether there were significant differences in activity in that region.

Two outbreaks were studied during the 1980 season, namely the Lukenya Hill outbreak and the Hopcraft Ranch outbreak. Most of the analysis has been directed toward the Hopcraft Ranch outbreak and so only this will be described here.

The outbreak covered an area of approximately 40 km² on the Athi Plains 50 km south of Nairobi. The optical site was positioned 1 km north of the overlooking radar and 500 m west of the entomological camp, in an area of high larval infestation (Figure 7.6). The operational system was the final one developed (Section 4.4) which incorporated the improvements identified in the previous work, viz: automatic photomultiplier gain control, real time counter system and weather shrouds.

The system continued to operate satisfactorily during periods of rain, although insects could not be detected in very heavy rain. Wind speed and direction were measured continuously throughout the operational period at 2 m and 10 m AGL using wind vane and anemometer sensors mounted on a portable mast (Plate 17).

Observations of insect speed and direction were made at selected times for comparison with the wind velocity data. These

KENYA 1980; Hopcraft Ranch

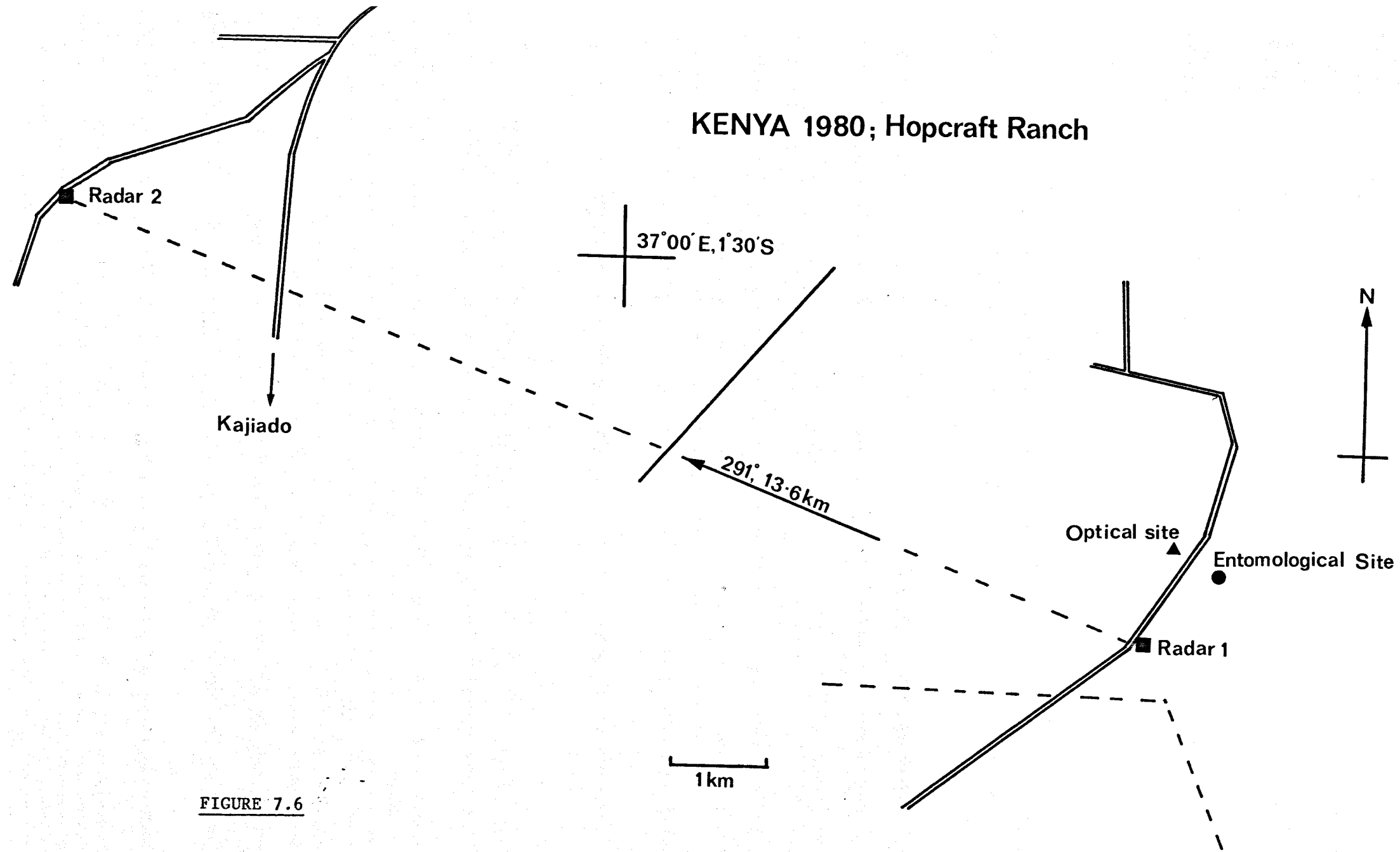


FIGURE 7.6



PLATE 17 The anemometer mast. Wind speed and direction sensors were positioned at 2 m and 10 m AGL.

results are presented in Section 7.2.

The sample volumes for the height profile experiment at the Hopcraft Ranch outbreak were centred at 2 m ("ground level"), 10 m and 20 m AGL. Results from the Lukenya Hill and Hopcraft Ranch outbreaks are presented in Section 7.3 and the collected data are summarised in Appendix C3.

7.2 MEASUREMENTS OF INSECT SPEED AND DIRECTION

The two channel receiver was operated at the Hopcraft Ranch outbreak site during the period 3 - 5 April 1980 (incl.). Measurements of insect speed and direction were made at selected times during the operational period at 10 m AGL. As a result of recorder failure the observations could not be made at the optimal times. The two consequences of this restriction were that the insect densities were not as high as would have been preferred, and that the relatively high background illumination decreased the horizontal dimension of the sample volume (Section 5.2). The number of intercepts on each signal were therefore reduced, which often prevented averaging of the "off time" (Section 4.2.2).

The wind direction for these measurements was predominantly easterly. Intercepts were therefore made only on the east-west channel and not on the north-south channel (Section 5.4). The spacing of the opaque bars meant that in this case the westerly heading of the targets could be only estimated to an accuracy of $\pm 10^\circ$.

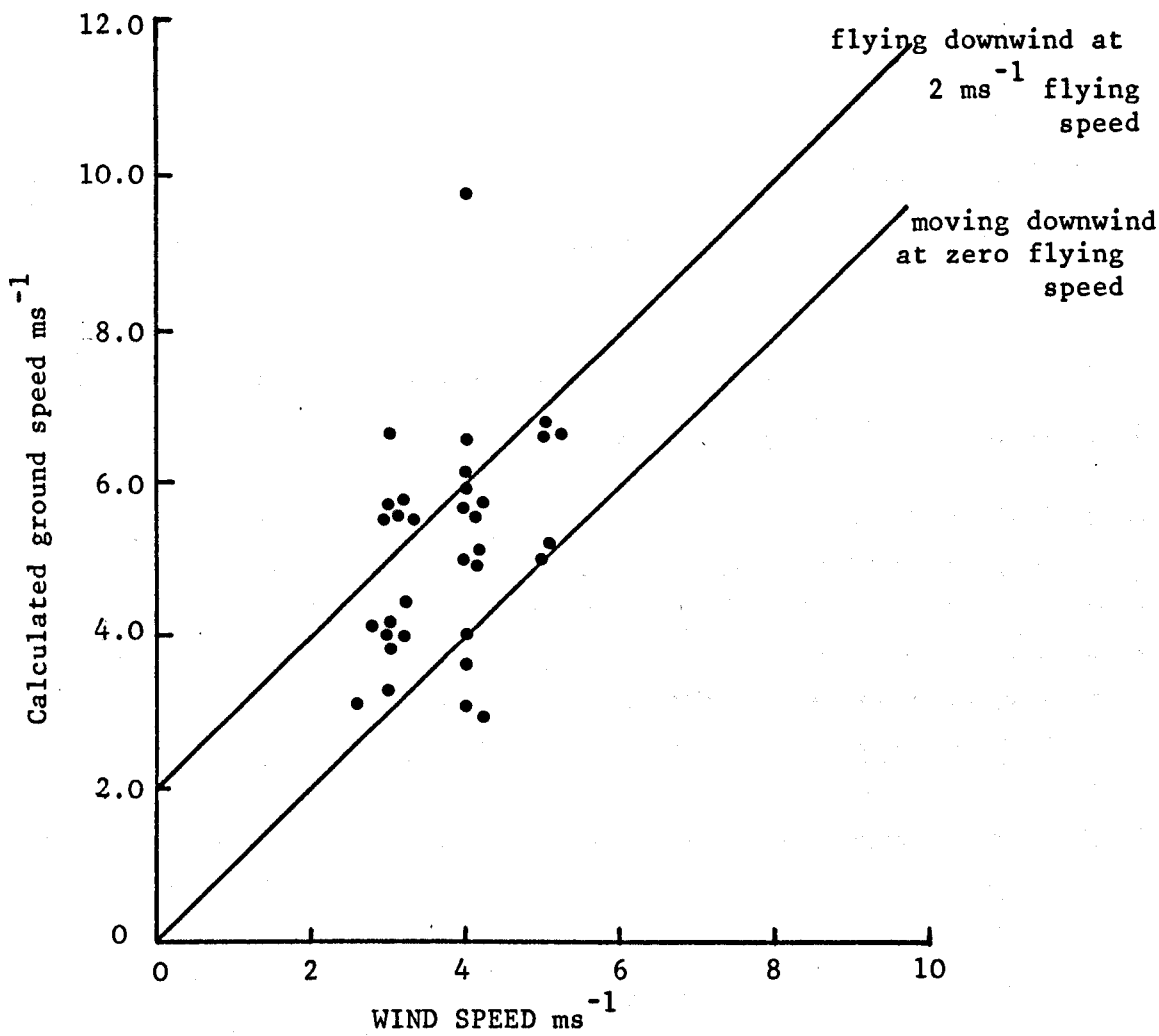


FIGURE 7.7 Measured insect ground speed against wind speed. (Data from 4.4.80, Hopcraft Ranch, Kenya.)

The westerly-directed ground speeds of the insects have been calculated by the method shown in Section 5.4 and are plotted as a function of the easterly wind speed in Figure 7.7. The relationship for (a) an insect being blown downwind with no flying speed, and (b) an insect flying at 2 ms^{-1} downwind are shown as solid lines. It can be seen that in nearly all cases the insects are flying downwind and that most (~70%) of the targets have flying speeds between $1 - 3 \text{ ms}^{-1}$. The assumption made in Section 2.4 that the Armyworm Moths fly predominantly downwind at 2 ms^{-1} is therefore considered reasonable.

The analysis of these results has demonstrated the weaknesses of this technique for measuring target speed and direction. In particular it is clear that the sample volume should be larger so that the insect is likely to cross more "on-off" cycles during a transect of the sample volume. The width of the "on time" can be halved to reduce the directional uncertainty when the image is moving approximately parallel to the length of the bars in one direction. There is however a minimum width for the "on and off times", which is set by the condition that the on and off periods should not be confused with the wing beat period.

7.3 RESULTS FROM FIELD STUDIES

7.3.1 Aerial Density Measurements

(a) Low altitude density profile

The aerial densities recorded at the Mt. Margaret site for

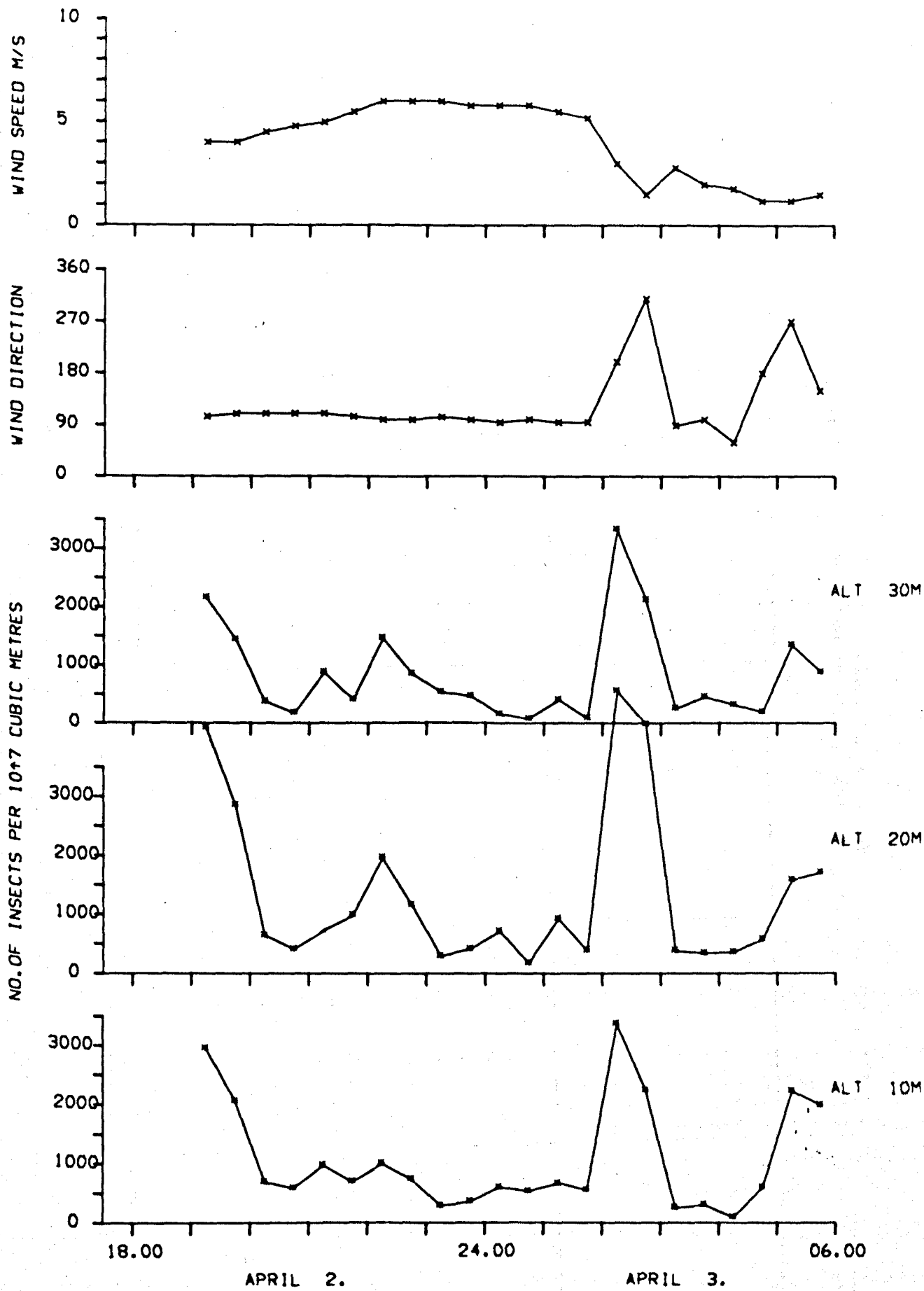


FIGURE 7.8 Variation of aerial density during night of 2 - 3 April 1979 at Mt. Margaret Outbreak site with concurrent wind speed and direction measurements

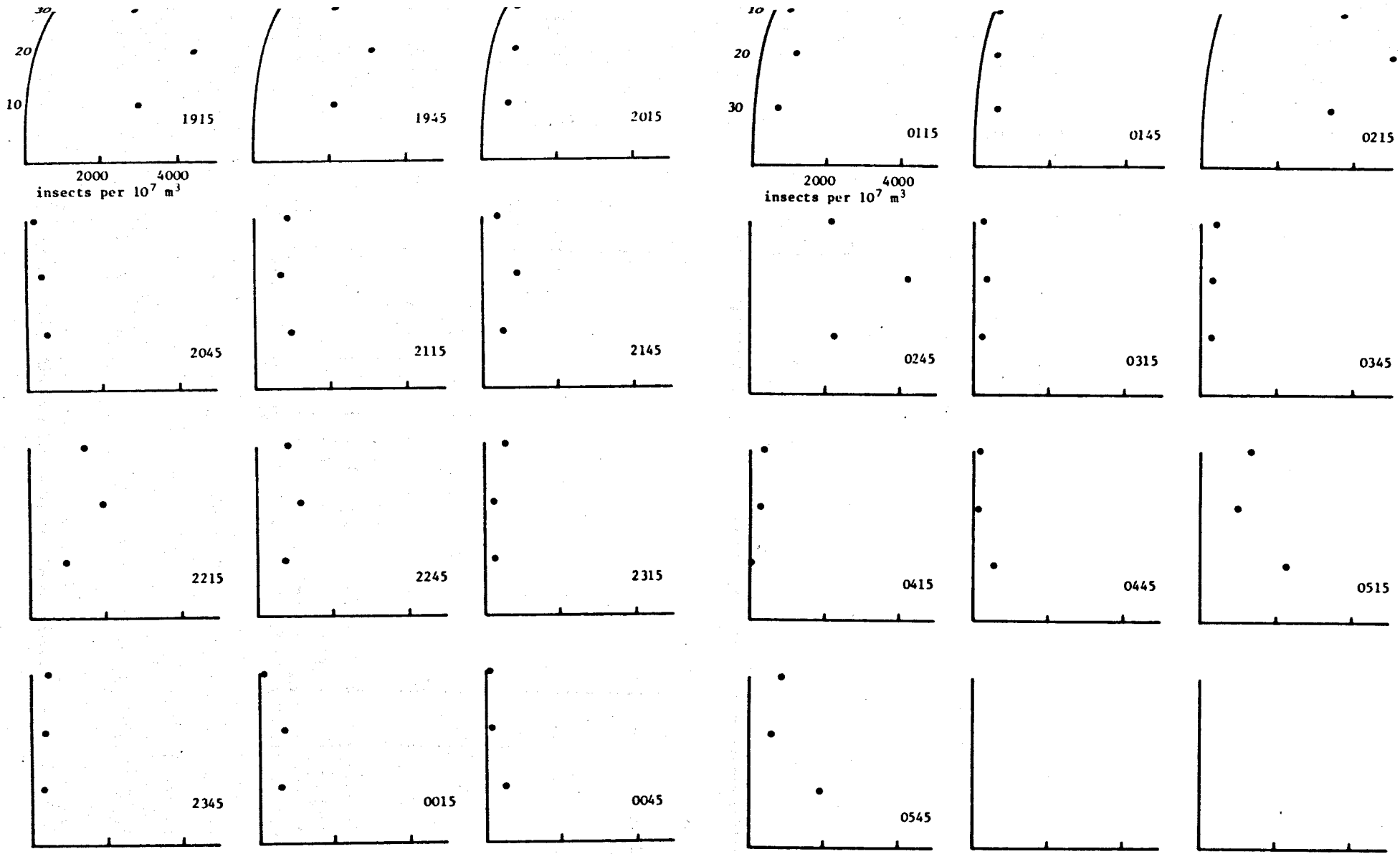


FIGURE 7.9

Height profiles of aerial density plotted at half-hourly intervals for 2 - 3 April 1979 at Mt. Margaret site, Kenya,

MOUNT MARGARET, KENYA

2/3 APRIL 1979

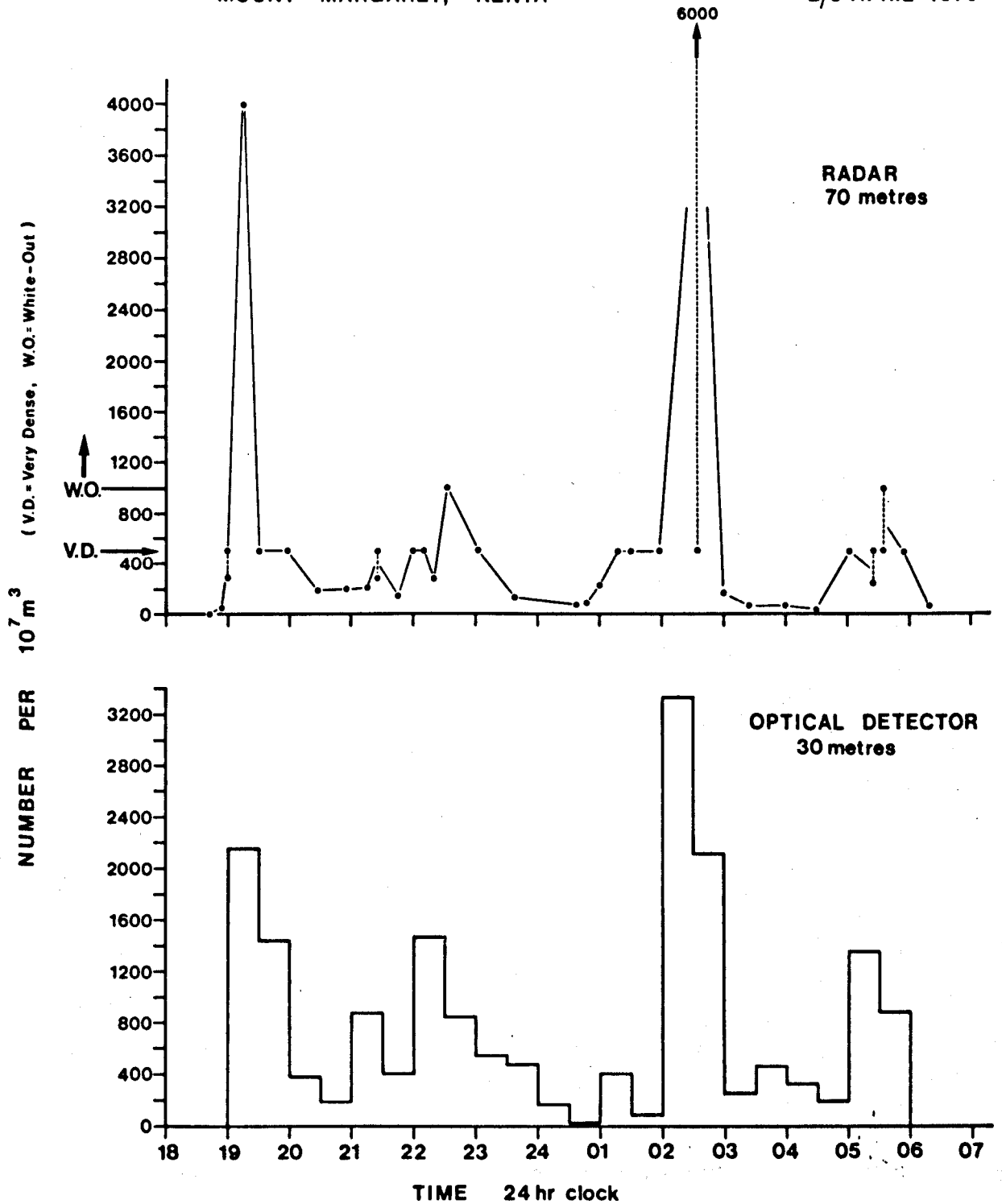


FIGURE 7.10

Comparison between aerial densities measured by the radar and optical system.

FIGURE 7.11

AERIAL DENSITY vs TIME FOR 5-6 APRIL 1980, HOPCRAFT RANCH

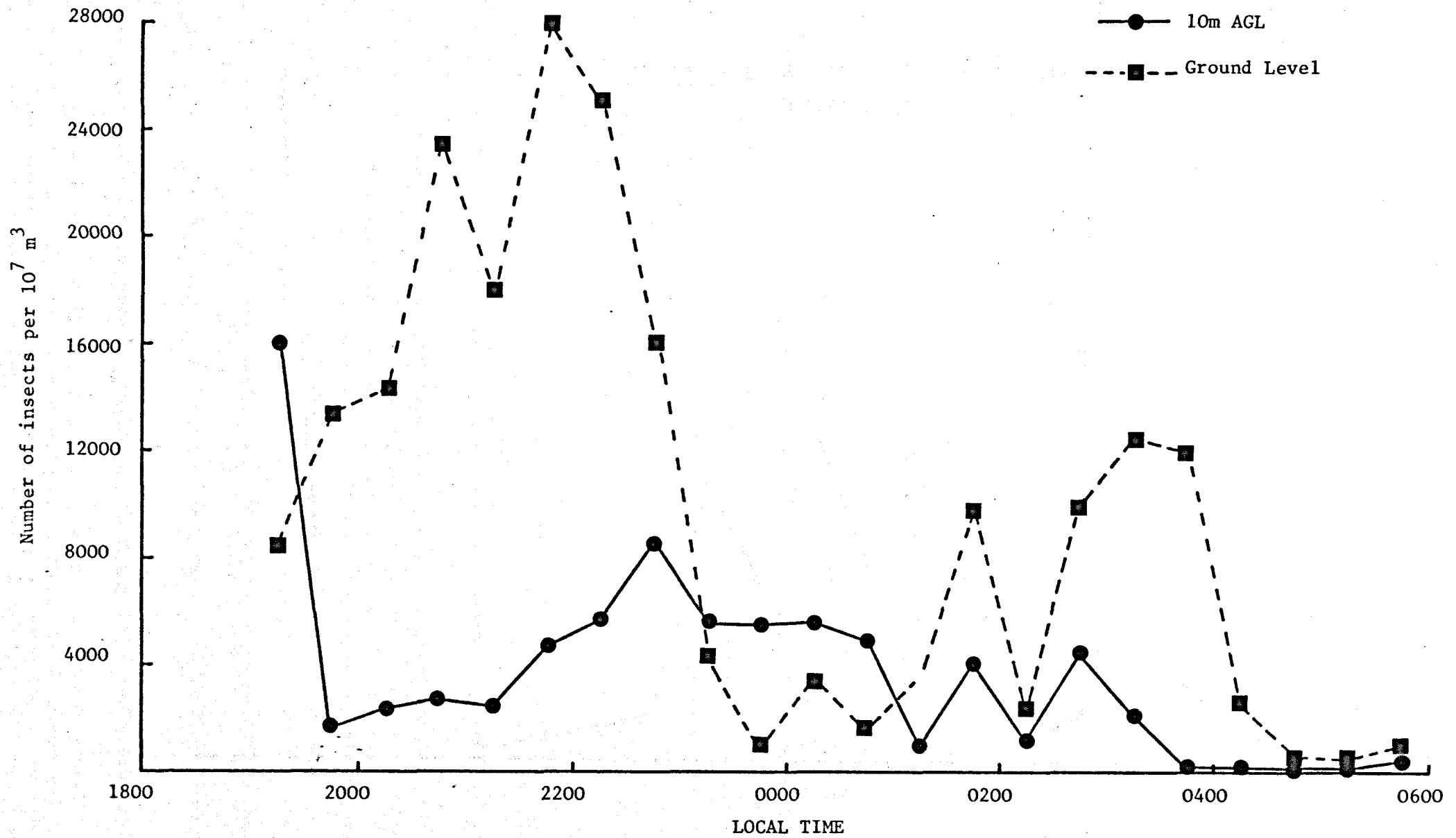
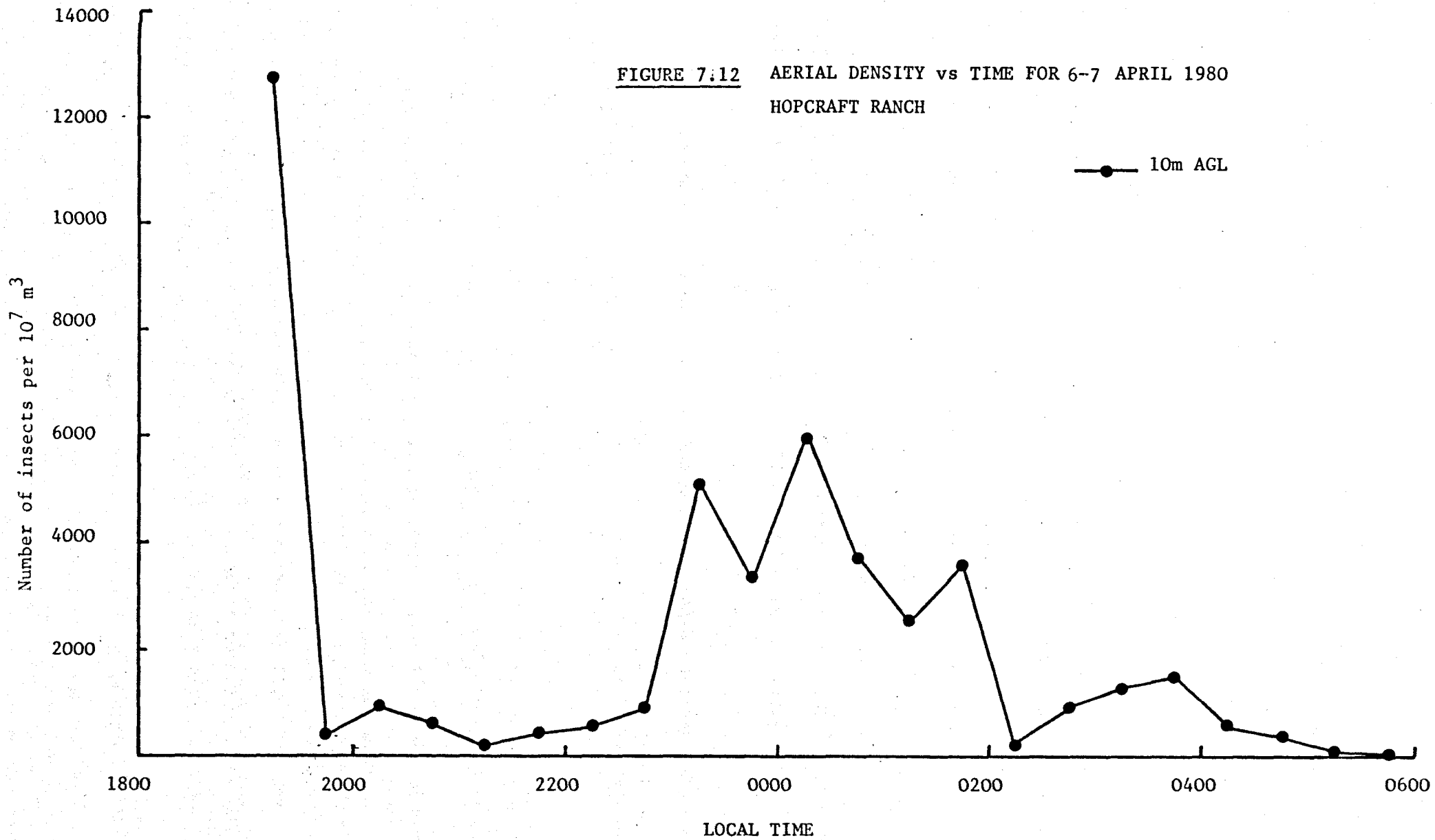


FIGURE 7.12 AERIAL DENSITY vs TIME FOR 6-7 APRIL 1980
HOPCRAFT RANCH



the night of 2 - 3 April 1979 are shown in Figure 7.8. The structure of the activity at the three levels is similar although the absolute densities differ slightly. The same data presented in height profile form (Figure 7.9) support the hypothesis that in this region the aerial activity does not change much with height.

Further evidence for this view comes from Figure 7.10 where the optical observations at 30 m AGL are compared to the radar observations at 70 m. Very close agreement is seen between the two patterns of activity and the measured densities are comparable.

The situation is different below 10 m AGL. Figure 7.11 shows the aerial densities recorded at Hopcraft Ranch for the night of 5 - 6 April. The general pattern of activity at 10 m AGL is similar to that in Figure 7.8 (see 7.3.1(b)) but the activity at "ground level" (2 m AGL) is distinctly different. This was found to be the case on many occasions at the Hopcraft Ranch outbreak. I hold the view that the Armyworm activity is approximately similar in the height range 10 - 70 m AGL but that distinct differences in activity are seen close to the ground.

7.3.1(b) General pattern of Armyworm activity at low altitude

Figures 7.8, 7.11 and 7.12 illustrate the general pattern of Armyworm activity as seen by the optical system. At 10 m and above a characteristic decrease in density is seen between 19.35 hours and 19.45 hours. This represents the end of the dusk take off, which was observed by the radar to begin at 18.55 hours, about twenty minutes after

sunset. The onset of the dusk take off was not detected optically due to the high background illumination. The decline was normally followed by a period of low activity from 20.00 hours to at least 21.00 hours and often longer. This lull in activity is thought to be due to the fact that most of the moths capable of flight have flown away in the dusk flight. The freshly emerging moths were seen to congregate in the trees from 19.30 hours onwards (Rose, Pers comm). This post-emergent flight from the ground into the trees is probably responsible for the increase in detected activity at "ground level". The nightly emergence reaches a peak at about 20.00 hours and all moths have left the ground by 00.00 hours (Rose, pers comm and 1979), which explains the sharp decline in "ground level" activity at 23.30 hours in Figure 7.11.

Some of the moths remain in the trees throughout the night, others appear to leave the trees in synchronised departures. These may be the cause of the "plume" activity seen by the radar (Riley, Reynolds and Farmery, 1981). This increase in activity from about 21.00 hours is reflected in the optical data from 10 m AGL and above, and persists generally for about three hours. The activity after 00.00 hours at 10 m AGL is generally lower reflecting the reduced amount of "plume" activity. The large peak seen in Figure 7.8 is a meteorological effect described in 7.3.1(c),

At the Mt. Margaret site there was a characteristic increase in activity at 10 m AGL and above just prior to dawn, probably due to moths suddenly leaving the trees. This was not seen at the Hopcraft outbreak, instead moths were observed to leave the trees

steadily from about 01.00 hours onwards (Rose, pers comm). This departure fits well with the increase in activity at "ground level" which finished approximately when the trees were depleted at 05.00 hours.

7.3.1(c) Meteorological effects

Radar observations have shown that flying insects are often concentrated in areas of atmospheric convergence (e.g. Schaefer, 1976 and 1980). In particular, locally high aerial densities have been associated with meteorological phenomena such as wind shift lines, cold fronts, storm outflows and sea breeze fronts. The use of insects as tracers has opened new possibilities for the study of these phenomena.

The optical system has on several occasions detected the increase in aerial density associated with wind shift lines. Such an event is documented in Figures 7.8 and 7.10. A sudden increase in density is seen at all heights from 10 - 30 m AGL and on the radar at 70 m AGL at approximately 02.15 hours. It is very well correlated with the change in wind direction and drop in wind speed shown on the concurrent anemograph record in Figure 7.8.

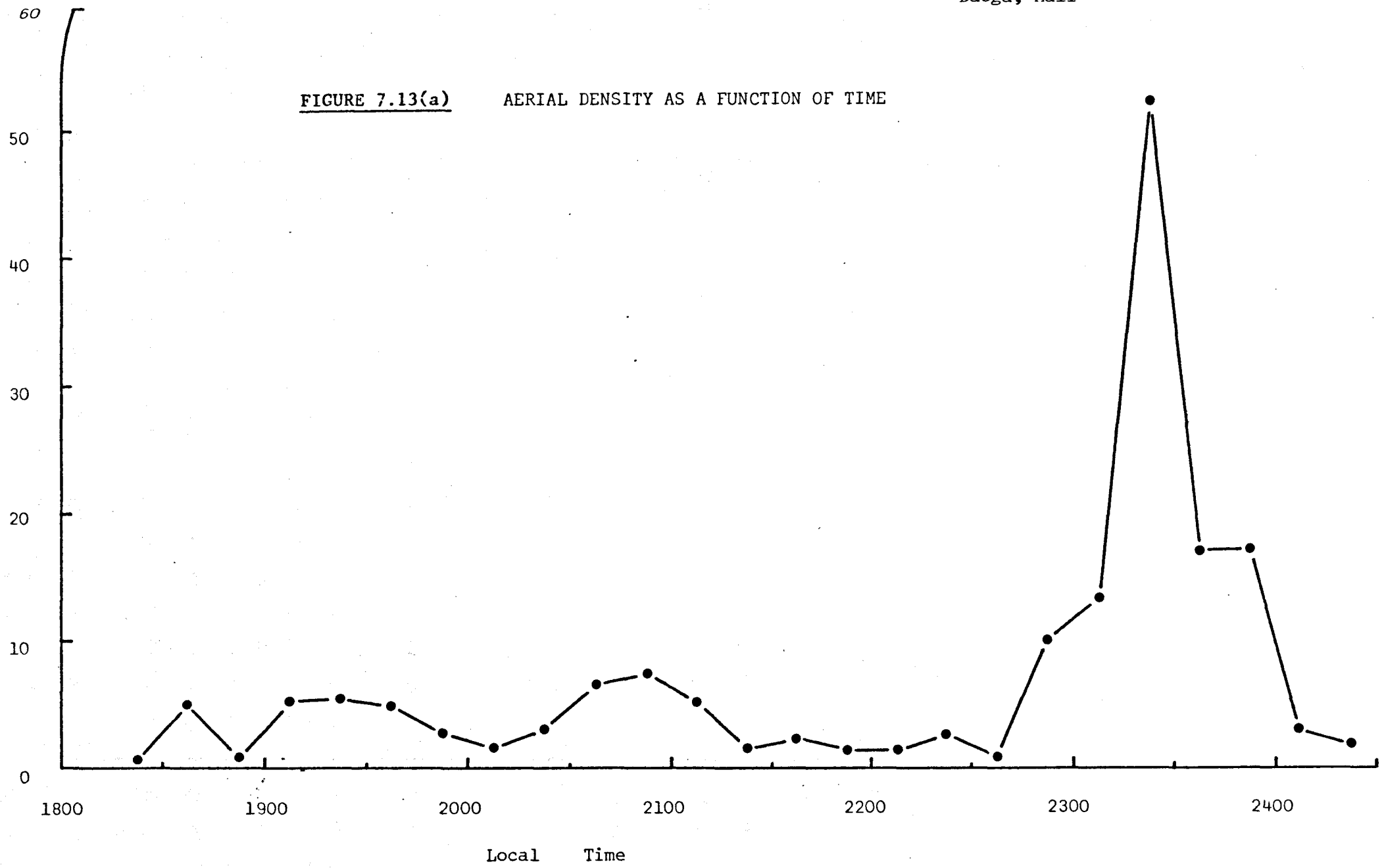
Data from the grasshopper studies in Mali provide another example (Figure 7.13(a)). In this case a dramatic increase in ground level density is well correlated with a distinct change in wind direction at about 23.30 hours (Figure 7.13(b)).

The optical system has the disadvantage of not being able to show the extent or structure of these meteorological phenomena as the radar can. It has however demonstrated that the effects extend down to very low altitude (~ 10 m AGL) and it offers the possibility of

Aerial Density
 $\times 10^{-5} \text{ m}^{-3}$

Friday 29 September 1978
Daoga, Mali

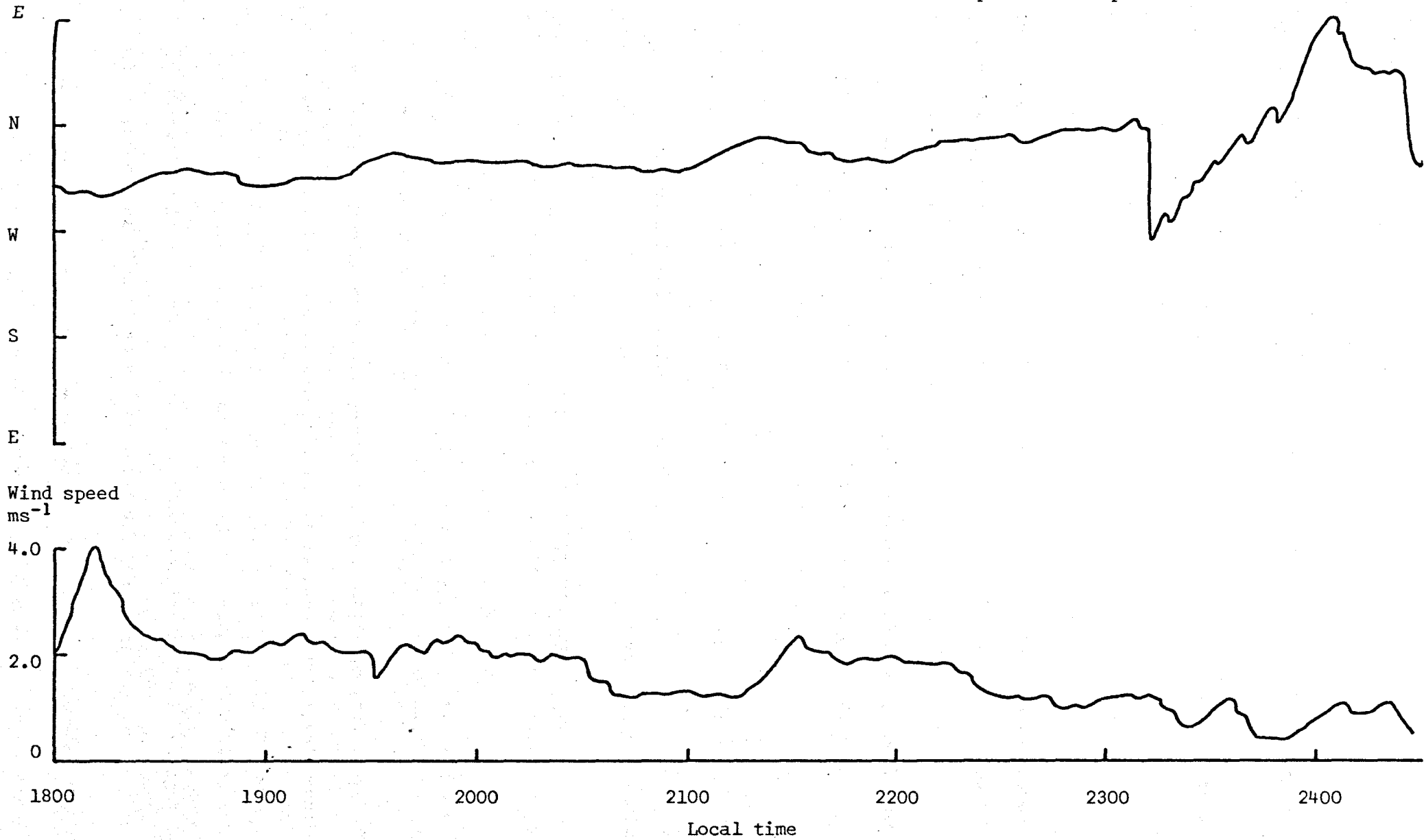
FIGURE 7.13(a) AERIAL DENSITY AS A FUNCTION OF TIME



Wind direction

FIGURE 7.13(b)

Wind Speed and direction for the
observational period 29 September 1978



comparing the insect wing beat frequencies inside and outside of the concentrations.

Observers of Armyworm flight have often noted high densities of flying moths during heavy rain. Unlike the radar, the optical system can operate satisfactorily during rain and increased densities of flying moths have been measured close to the ground. Radar observations made just after the passage of a rainstorm show reduced aerial densities compared to those prior to the rain (Riley, Pers comm). It is therefore suggested that the increased activity associated with rain observed at ground level both visually and by the optical system is due to the insects descending to low altitude rather than more insects being stimulated to fly.

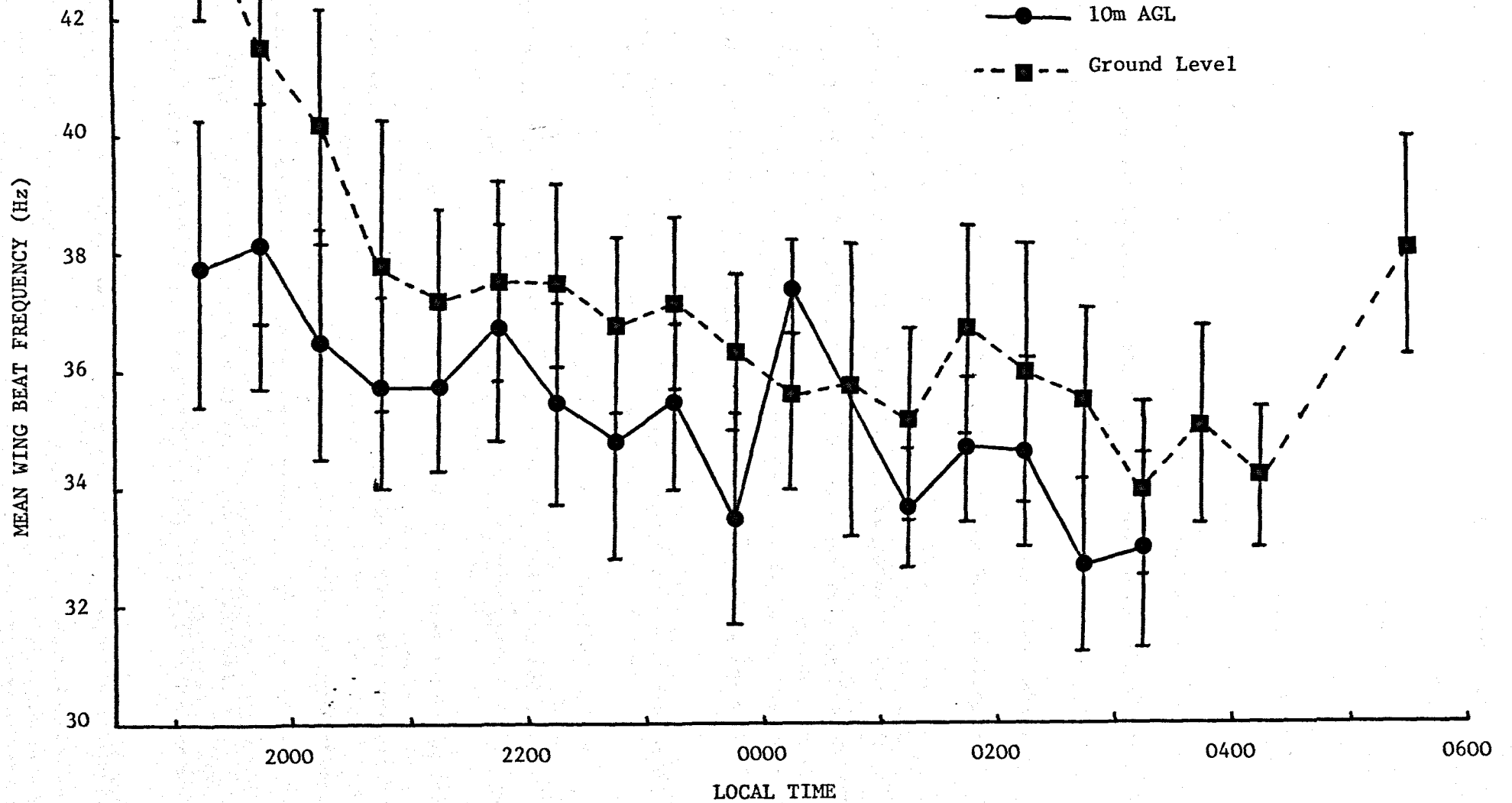
7.3.2 Wing Beat Frequency Measurements

7.3.2(a) Effect of temperature on wing beat frequency

The means and standard deviations of the wing beat frequencies occurring in half hour periods at the "ground" (2 m) and 10 m levels have been plotted against time in Figure 7.14 for the night of 5 - 6 April 1980 at Hopcraft Ranch. The "ground level" data show a significant drop in mean frequency during the period 19.15 - 21.15 hours with a subsequent slow decline. It is considered likely that this fall was due to the effect of ambient air temperature on the wing beat frequency of flying moths, since the air temperature was falling in a similar manner during the same period. It is thought that the effect was probably not caused by a changing aerial

46

FIGURE 7.14 MEAN WING BEAT FREQUENCY OF HALF-HOURLY PERIODS vs TIME
(Data from 5-6 April 1980, Hopcraft Ranch)



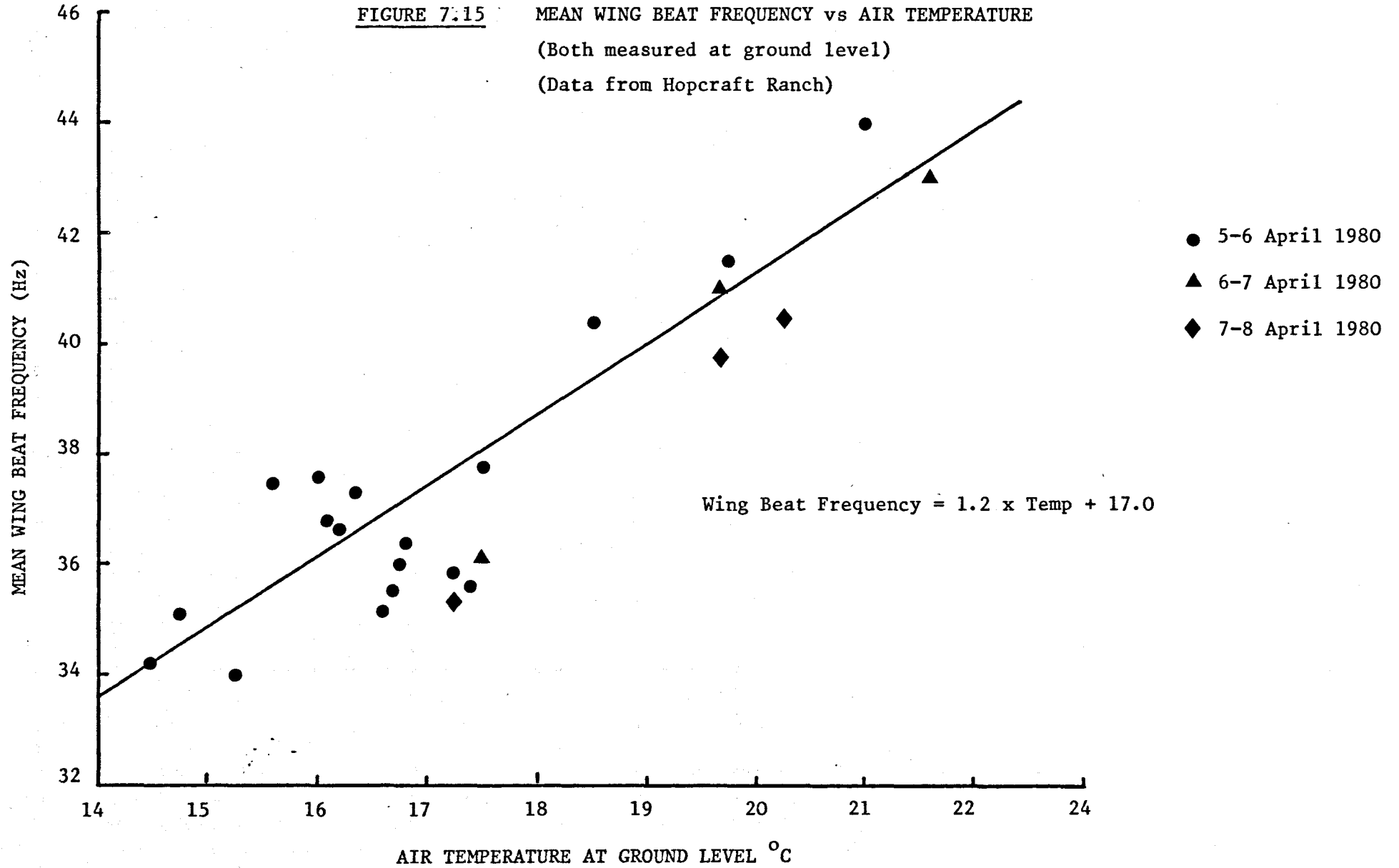
population, for two reasons. Firstly, the wing beat frequency showed a steady decline rather than the abrupt jump which would be expected had an influx of different insects occurred. Secondly, if instead, the aerial population had changed its composition slowly then the standard deviations of the samples would have increased to a maximum when the population mix was 50/50. The observed behaviour of the standard deviations is clearly more consistent with the hypothesis that the population changed its mean wing beat frequency.

This possible correlation between wing beat frequency and temperature is shown more clearly in Figure 7.15. The mean wing beat frequency for a series of half hour periods has been plotted against mean air temperature (as measured in a Stevenson Screen at 2 m AGL) during each period. The least square regression line has a gradient of 1.2 Hz per $^{\circ}\text{C}$ with a 95% confidence interval of 0.9 - 1.5 Hz per $^{\circ}\text{C}$, and explains 72% of the variance.

A similar effect was observed in the data collected at the Mt. Margaret site. Figure 7.16 shows the mean wing beat frequencies for hourly periods plotted against mean air temperature for each period. In this case the regression line had a gradient of 1.8 Hz per $^{\circ}\text{C}$ and it explained 84% of the variance. Inclusion of radar observations for the same period did not significantly affect the result.

Both sets of field results indicate strongly that the wing beat frequencies of small moths (thought to be predominantly Armyworm) are dependent on ambient air temperature. Tethered flight studies in the field further support this assertion. Cooter (unpublished results) flew field captured Armyworm Moths on a novel flight balance

FIGURE 7:15 MEAN WING BEAT FREQUENCY vs AIR TEMPERATURE
(Both measured at ground level)
(Data from Hopcraft Ranch)



which allowed wing beat frequency and lift to be measured simultaneously. Wing beat frequencies were only measured for those specimens that produced positive lift. He found a correlation between wing beat frequency and temperature of 0.45 Hz per °C which was significant at the 5% level.

The wing beat frequencies of large grasshoppers, locusts and the larger moths e.g. Hawk Moths) are thought to be largely independent of temperature. The effect of temperature on wing beat frequency depends on the mechanism of the wing stroke (Sotavalta, 1964) and probably on the ability of the insects to maintain their thoracic temperature independent of the air temperature. Small insects have a larger surface area to body weight ratio than larger insects and are therefore more likely to be affected by the ambient temperature. Sawedal and Hall (1979) found chironomids (midges) which had wing beat frequencies of about 500 Hz to have temperature coefficients of approximately 8 Hz per °C. The Gypsy Moth was found to be unable to regulate its thoracic temperature and to have a temperature coefficient of wing beat frequency of 0.45 Hz per °C (Casey, 1979). In addition Schaefer (1976) has suggested that the wing beat frequencies of small grasshoppers (e.g. *Aiolopus simulatrix*) decrease with decreasing temperature. The results reported here represent the first field observations of the effect in small moths.

This apparent dependence of the Armyworm wing beat frequency on ambient temperature causes problems for the identification of armyworm moths, which is the topic considered in the next section.

7.3.2(b) Identification

At its conception it was envisaged that the optical system would prove useful as an aid to radar identification of flying insects. Results are presented below to show the extent to which it has been successful in this aim.

Figure 7.17 shows the wing beat frequency distributions obtained for the period 01.00 - 02.00 hours on 2 - 3 April 1979 at the Mt. Margaret site. The radar signatures were obtained at the lowest altitude accessible (65 m AGL) directly above the optical site. During the period in question Armyworm Moths were seen by torchlight to be numerically dominant in the air a few metres above ground level. The wing beat frequency distribution recorded for the lowest altitude (10 m AGL) which was monitored by the optical system was therefore assumed to be characteristic of Armyworm. In Figure 7.17 it can be seen that the shape and position of the distributions attributable to Armyworm Moths was preserved at all the altitudes measured. This remarkable similarity between the distributions obtained by the optical system and the radar strongly suggest that the species composition did not change appreciably with altitude.

The spectral range (36 - 44 Hz) occupied by the moths assumed to be Armyworm in Figure 7.17 agrees very well with the range found for Armyworm Moths in tethered flight by Cooter (1979) of $40 \text{ Hz} \pm 4 \text{ Hz}$.

Figure 7.17 should be compared to Figure 7.18 which shows the wing beat frequency distributions for the same night during the dusk

Wingbeat frequency distributions for 2/3 April 1979 0100 - 0200 hours

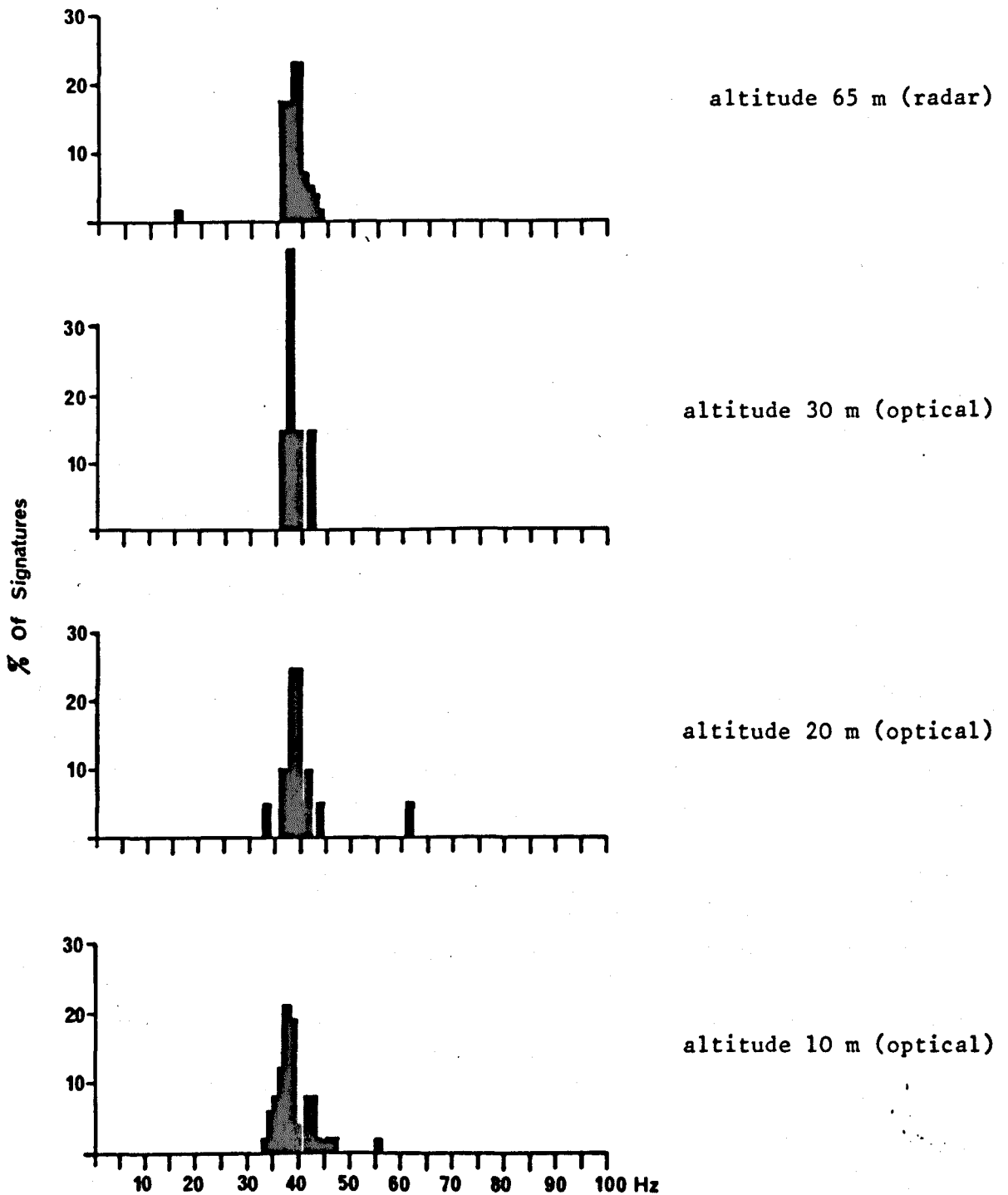


FIGURE 7.17

Comparison of optical and radar wing beat frequency distributions measured at different altitudes (Data from Mt. Margaret site, Kenya.

Wing beat frequency distributions for 2/3 April 1979 1910 - 2000 hours

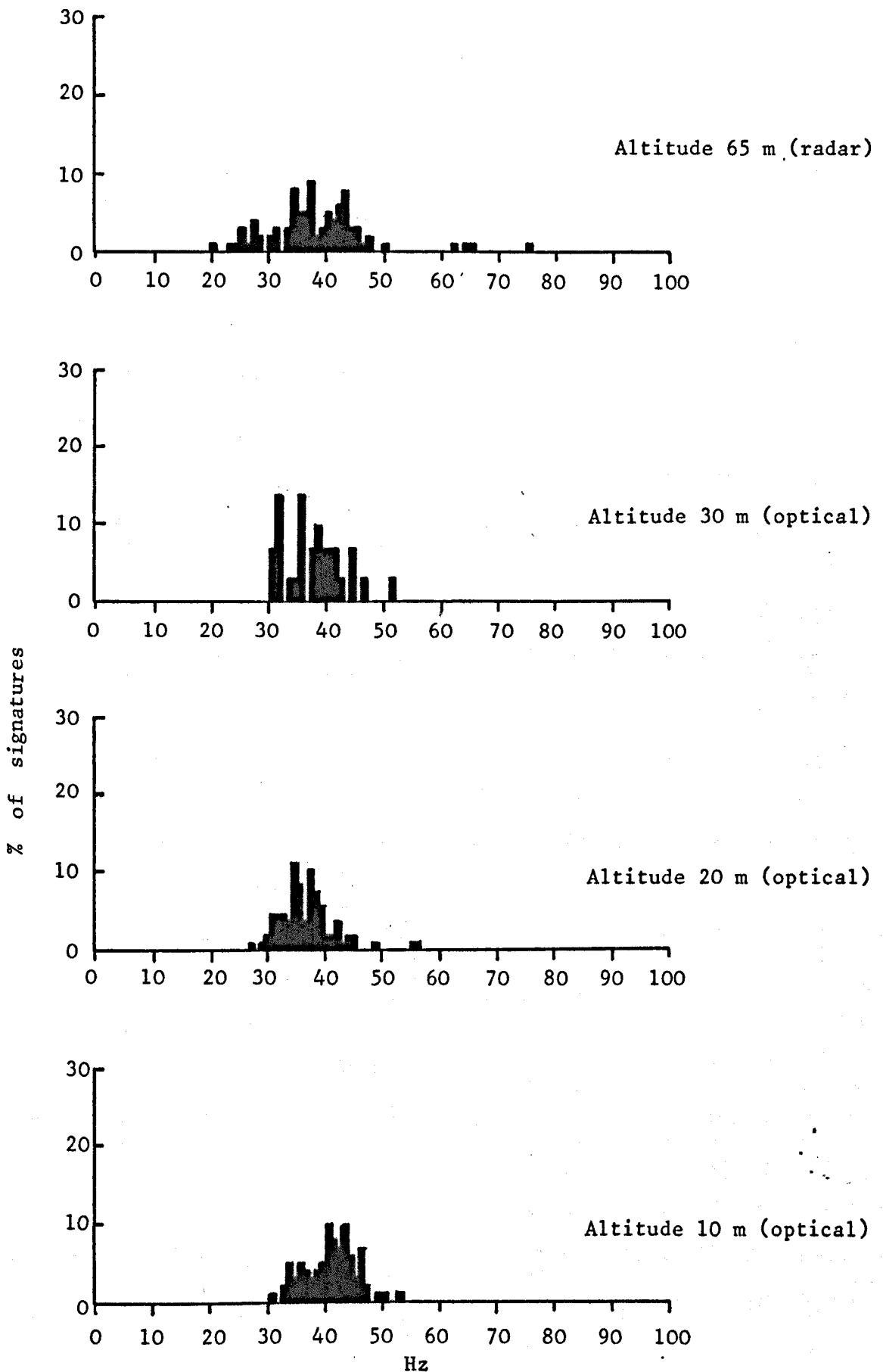


FIGURE 7.18 Comparison of optical and radar wing beat frequency distributions measured at different altitudes (Data from Mt. Margaret site, Kenya)

RADIO SOUNDINGS: MOUNT MARGARET, KENYA

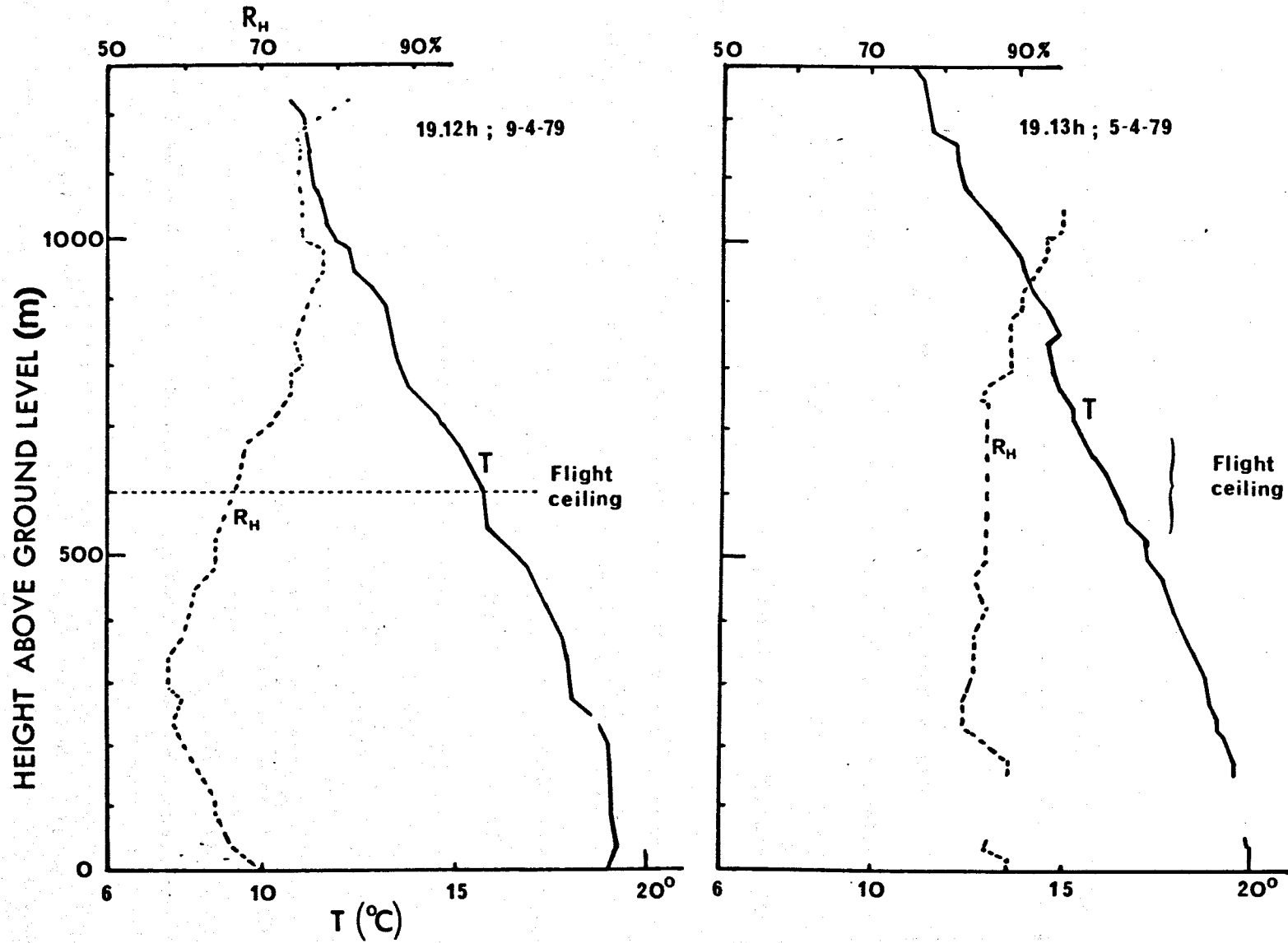


FIGURE 7.19 Examples of air temperature profiles obtained from radiosonde measurements

take off period 19.10 ~ 20.00 hours. The radar and optical distributions are all comparatively broad, which is believed to reflect the large number of different species which were seen to be active during the early evening period.

The effect of temperature on the interpretation of these results is not considered serious since the temperature difference over the height range of 65 m measured with a radiosonde was found to be less than 0.5 °C on two typical occasions (Figure 7.19).

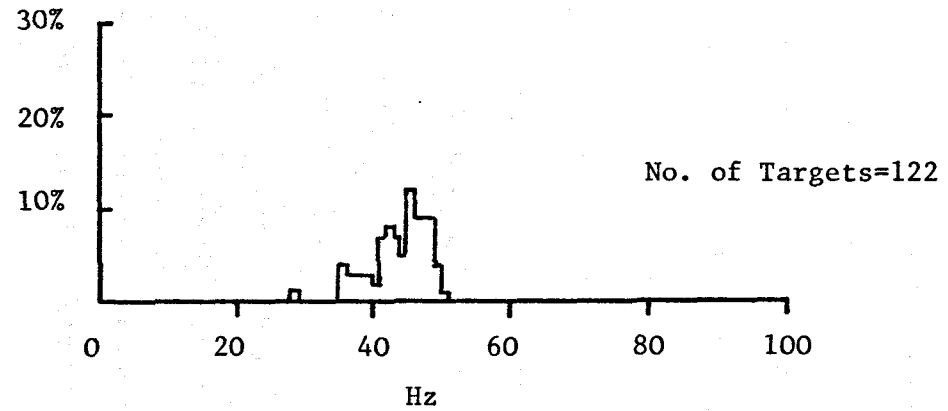
7.3.2(c) Wing beat frequency as a function of wing length

The results of tethered flight experiments to investigate the relationship between wing length and wing beat frequency for small moths are described in Section 6.1; results from field studies are presented below.

An experiment to measure the wing beat frequency of moths flying downwind of a pheromone trap was performed at the Lukenya Hill outbreak on 2 - 3 March and 3 - 4 March 1980. Large numbers of sexually mature Armyworm Moths were in the area. Some of these had originated from the outbreak and others were thought to be immigrants.

A sample volume was positioned about 1.5 m downwind of, and at the same height (2 m AGL) as a "Delta" type pheromone trap. The moths (exclusively male Armyworm) flew upwind toward the trap. They steadily reduced ground speed as they approached the trap and consequently moved through the sample volume very slowly. Sometimes they would stop completely and hold station in the wind. It was

(a) Wing Beat Frequency Distribution



(b) Wing Length Distribution

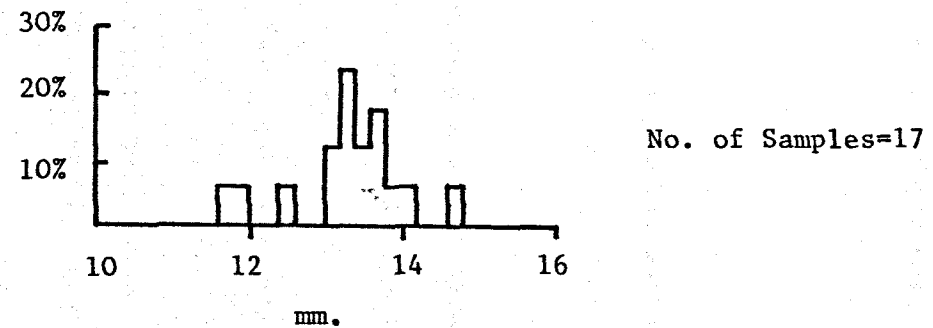


FIGURE 7.20 RESULTS OF THE PHEROMONE TRAP EXPERIMENT (Data from 2-3 March 1980, Lukenya Hill)

therefore possible to obtain unusually long signatures from these insects. A proportion of the insects which flew through the sample volume continued on and were caught in the trap. These were later collected and their wing lengths measured. It was considered reasonable to assume that the wing length distribution obtained was representative of the moths flying through the sample volume, since the efficiency of the trap was not known to be dependent on wing length.

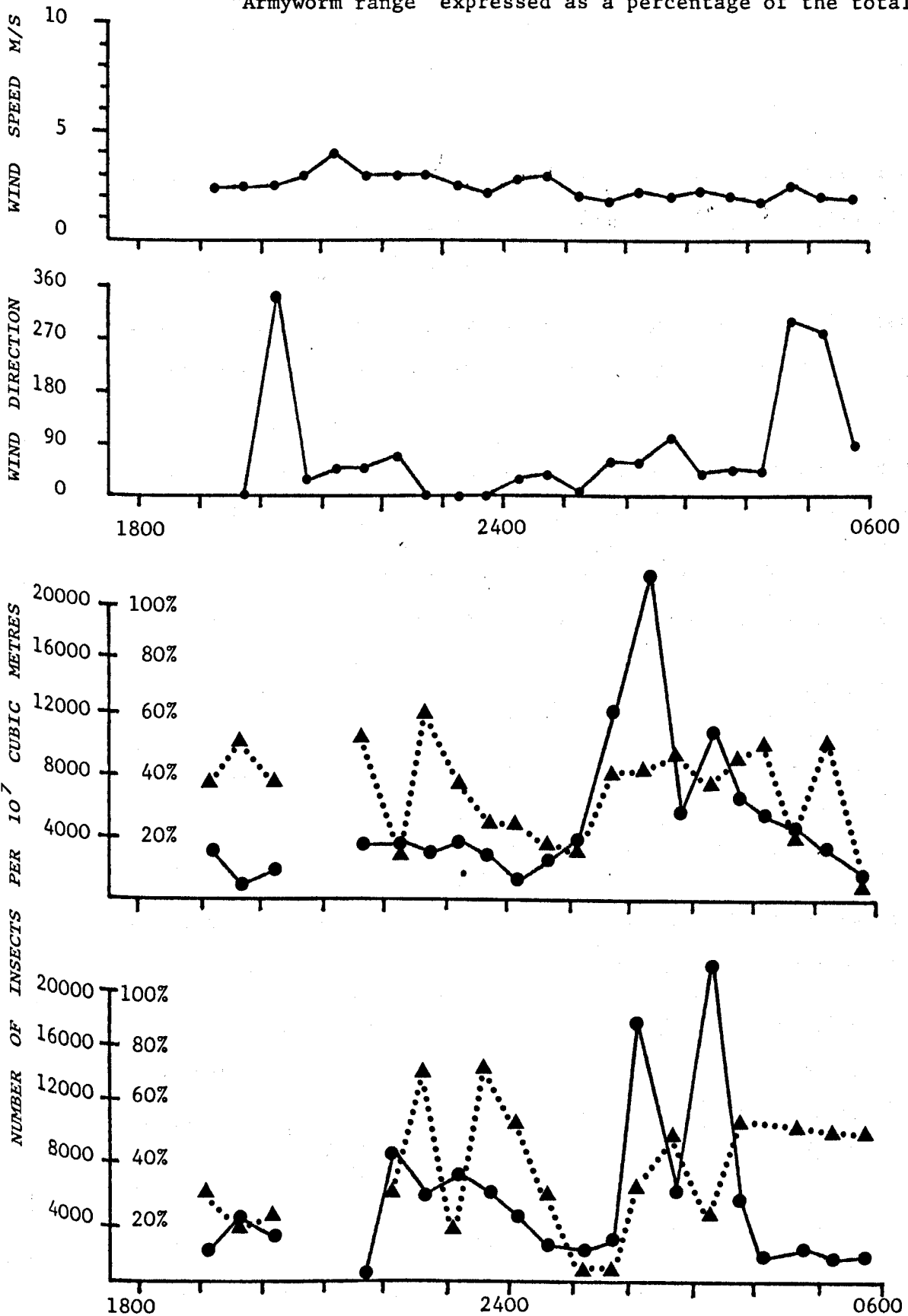
Some of the results of this experiment are presented in Figure 7.20. Both wing beat frequency and wing length distributions appear very slightly bimodal, possibly reflecting the two different populations mentioned above. The wing beat frequencies are generally high compared to those of moths flying normally, their mean being about 45 Hz. This could be due to the degree of sexual stimulation or a higher flapping rate required to hold station. The frequencies of a few moths varied while they were in the sample volume, but the majority did not. This indicates that power output and flight control for the moth may be controlled by wing profile rather than wing beat frequency (c.f. variable pitch propellor), though at the moment this is only a tentative suggestion. It could be equally argued that most moths made a smooth straight approach. A few odd ones may have been caught in gusts or eddies and compensated by varying wing beat frequency, but the majority did not have to.

7.3.3 Aggregation of Moths in Trees

The objective of the "Tree Experiment" described in

FIGURE 7.21 TREE EXPERIMENT 6-7 APRIL, MT MARGARET KENYA 1979

●—● Total aerial density
 ▲....▲ Number of insects with wing beat frequency in the "Armyworm range" expressed as a percentage of the total number.



Section 7.1.4 was to study the movement of Armyworm Moths to and from a tree at an outbreak site following the observations by Rose (1979) of the aggregation of moths in trees.

The temporal variation in aerial density on the "upwind" and "downwind" edges of the tree for the 6 - 7 April 1979 at the Mt. Margaret site is shown in Figure 7.21. Interpretation of these results is complicated by the variability of the wind direction. Changes in wind direction from the prevailing easterly direction meant that the sample volumes were no longer monitoring the appropriate activity. However general features can be deduced, in particular, it is seen that the activity on both sides of the tree was greatest between 01.30 and 04.00 hours. This fits well with the data in Figure 7.11 which shows ground level activity to peak during this period, probably the result of moths leaving the tree.

The frequency band assumed characteristic of Armyworm for the Mt. Margaret outbreak was 36 - 44 Hz at an air temperature of 19°C. The proportion of frequencies within this band (adjusted for air temperature using the results of Figure 7.15) have been plotted on Figure 7.21. The proportion of Armyworm-sized targets was generally low, reflecting the small numbers of Armyworm Moths visually observed on the tree (<10 at any one time). It was apparent that the rate of emergence in the area of the optical site had dropped considerably. (Moths had first been seen emerging in the area on 2nd April.) Visual inspection of the tree did however show that the tree contained two other moth species in large numbers. These species were respectively slightly larger and smaller than Armyworm Moths. The

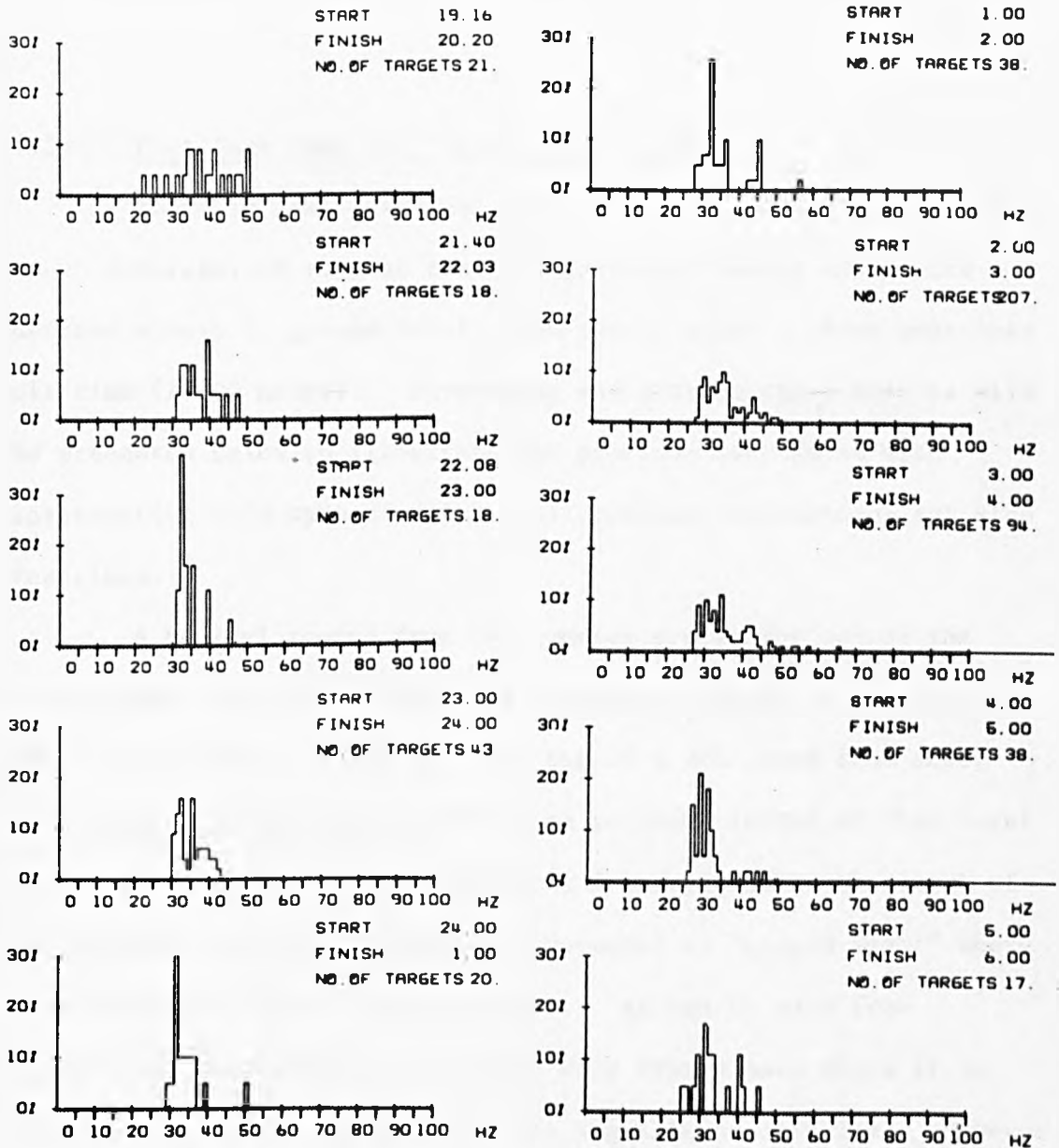


FIGURE 7.22 Wing beat frequency distributions from the tree experiment, 6-7 April 1979, Mt. Margaret site, Kenya.

wing beat frequency distributions for this night (Figure 7.22) show a bimodal structure, particularly in the period 01.00 - 04.00 hours. It seems that the results reflected the activity of these two species and their preponderance over the Armyworm population.

7.3.4 Post Dusk Take Off "Descending Flight"

There is some evidence, from data collected at the Hopcraft Ranch outbreak, to suggest that a significant number of insects descend slowly to ground level about twenty minutes after peak take off time (19.00 hours). Supporting and contradictory results will be presented below to illustrate the problems associated with interpreting this type of data. Alternative explanations are also described.

A typical record from the counter system for one of the seven nights that this effect was observed is shown in Figure 7.23. Insects were detected initially at the 10 m AGL level from about 19.14 hours onwards and the flurry of activity lasted at that level for about 11 minutes. Approximately 9 minutes after the start of the activity at 10 m, signals were detected at "ground level" where they persisted for at least one hour. As can be seen from Figure 7.23 the timings are at best very approximate since it is difficult to define the onset of the significant activity. However, the general effect could be interpreted as a band of insects descending slowly from above the 10 m level to ground level and then milling about. The descent rate calculated from the time delay between the

occurrence of the first signals at each level was, for the 5 - 6 April, in the range $0.8 - 1.6 \text{ m min}^{-1}$, depending on the exact choice of start time at "ground level". An estimate of the depth of the band was made in the following way;

let the depth of insect band be $d \text{ m}$
 let the depth of 10 m sample volume be $g \text{ m}$
 let the descent rate be $v \text{ ms}^{-1}$
 let the time for which targets were
 detected at the 10 m level be $t \text{ s}$.

Then

$$\frac{d + g}{t} = v$$

or $d = vt - g$ (7.1)

Substituting measured values for 5 - 6 April we obtain

$$1.0 \text{ m} < d < 10.0 \text{ m}$$

Although the analysis is very crude it does indicate that the band is surprisingly shallow.

Table 7 lists the times for when this "descending flight" was observed. The evidence for this being a real effect is supported by data from 9 - 10 April 1980 when it was not observed. Instead activity was seen to occur at both levels practically simultaneously. This change in behaviour was possibly related to the fact that the Armyworm emergence had almost finished by this date.

TABLE 7

EVIDENCE FOR "DESCENDING FLIGHT"; HOPCRAFT RANCH

DATE	ARRIVAL TIME AT 10m AGL	ARRIVAL TIME GROUND LEVEL	DESCENT TIME (minutes)
2.4.80	19.16	19.26	10.0
3.4.80	19.14	19.20	6.0
4.4.80	19.16	19.34	8.0
5.4.80	19.14	19.23	9.0
6.4.80	19.18	19.23	5.0
7.4.80	19.07	19.13	6.0
8.4.80	19.12	19.18	6.0
9.4.80	19.05	19.05	0.0 *

* Effect not observed on this night

The timings at the two levels are very approximate but the general effect is clear, viz. targets detected at 10 m AGL before targets at "ground level" even though the "ground level" receiver was more sensitive than that at 10 m. The most obvious interpretation is in terms of a descending flight. There is, however, contradictory evidence for this simplistic view. Firstly, it is hard to imagine how the band could be so shallow, and if indeed the insects had taken off with the rest at about 19.00 hours then they would have originated from approximately 5 km upwind of the site. The outbreak site was not known to extend this far, though of course it is not

certain that they took off with the rest. They could have been part of a later, lower altitude local flight.

One of the critical tests for the theory is whether the target detected at 10 m AGL and at "ground level" came from the same population. The means and standard deviations of the wing beat frequencies of the two samples are shown in Figure 7.23. The 8 Hz difference in means cannot easily be explained in terms of a temperature effect since the required temperature gradient of -1°C per metre is very unlikely. It is possible to postulate a slower flapping rate in the descent which speeds up as the insects approach the ground and level out, but a problem is found in the standard deviations of the two samples. If the two samples were from the same population then the standard deviations would be expected to be similar. In this case they are not. It therefore seems likely that the two levels were not monitoring the same band of insects passing them both. An alternative and more plausible explanation is required for why insects should be consistently detected at 10 m AGL before they were detected at "ground level". Two possible explanations are described here.

The targets detected at 10 m AGL could have originated from a well defined source area upwind of the site, the upwind distance being calculated from the time taken to climb to 10 m AGL, assuming a reasonable climb rate of 0.5 ms^{-1} , and the horizontal wind speed. This positions the source area ~ 50 m east of the optical site, which may indicate that it was associated with the high larval densities found along the road edge in that area. The well defined source area would mean that nothing would be detected at the position of the

ground level sensor. The activity detected later at this level could be due to the start of milling activity of moths either not involved in the take off or freshly emerged.

The second theory involves the flight of moths from the trees. At dusk moths were seen to accumulate in trees for short periods prior to taking off on serious flights. This flight from daytime hiding places to the trees took place when neither "ground level" nor 10 m AGL sensor was sufficiently sensitive to detect it (because of high background illumination). The activity detected later at 10 m AGL may be due to insects taking off from the trees, which because they are already 3 - 4 m AGL do not intercept the "ground level" sensor at 2 m AGL. The activity at "ground level" which follows could be explained in a similar way to the first proposal. Confirmatory evidence for this explanation could come from the entomological observations of activity on the trees.

It is clear that the initial interpretation, made in the field, that the pattern of activity represented a descending flight was incorrect. This demonstrates the caution that is required when interpreting this type of data, and that more reliable explanations can be developed by considering additional data from other sources (e.g. entomological and meteorological observations).

7.4 CONCLUSIONS

The speed and direction measurement of insect displacements at 10 m AGL have shown that insects fly predominantly downwind at low

altitude. This represents similar behaviour to that seen by the radar at higher altitudes (Schaefer, 1976; Riley and Reynolds, 1979), and has been used to simplify the calculation of aerial density (Section 2.4).

The aerial density profile of Armyworm Moths has been found to be approximately constant in the height range 10 - 70 m AGL. This indicates strongly that altitude causes no significant change in behaviour within this region. Closer to the ground (2 m AGL), however, the activity has been found to follow a substantially different pattern. It is thought likely that the ground level activity is influenced strongly by very local flight to and from trees following emergence, whereas that at 10 m and above represents flights of longer range and duration leading to significant displacements.

On several occasions the optical system has detected the passage of wind shift lines by the associated increase in the aerial density of flying insects. These observations have conclusively demonstrated the fact that the effect of the wind shift line on insect density extends down to at least 10 m AGL. Light trap catches have shown similar increases well correlated with concentrations of insects observed by radar (Greenbank, Schaefer and Rainey, 1980) but in these cases it was not possible to deduce the flying height of the captured insects.

At Armyworm outbreak sites not only has the optical system been able to demonstrate a fairly constant level of insect activity from 10 m AGL up to altitudes accessible to radar (70 m AGL) but it has, using wing beat frequency data, been able to show that the size

structure of the airborne population is also effectively constant. It can therefore be assumed that the radar has been seeing a representative sample of the airborne population. By comparing the optical wing beat frequency distributions of moths visually confirmed to be Armyworm with those obtained by the radar it has been possible positively to identify Armyworm activity at higher altitudes.

Results from two seasons' work have shown that the Armyworm wing beat frequency increases with increasing temperature. Similar results have been found for small moths in the laboratory, but these optical data represent the first supporting evidence from the field.

The optical system has been used to monitor the approach of male Armyworm Moths to a pheromone trap. The initial studies have shown the considerable potential of the system for the study of insect flight mechanics and in particular the use of wing beat frequency by the insect as a means of controlling power output to hold station.

CHAPTER 8

CONCLUSIONS AND FUTURE PROSPECTS

The high rate of world population growth is putting an increasing demand on world food production. The reduction of crop losses due to insect pests has been shown to offer an important method for easing the situation. However, it is crucially important to understand the population dynamics of an insect pest before successful pest control is possible. In particular, for those insects which have a flying phase in their life cycle, information about the role of flight in their population dynamics is of utmost importance for the formulation of an effective control strategy.

Remote sensing using 3 cm wavelength radar has been shown to provide previously unobtainable insight into insect flight behaviour. The limitations of radar have, however, been clearly identified and an optical system was proposed to supplement the radar observations at low altitude and to help with the question of target identification.

The performance of a suitable optical system has been analysed and design criteria were established that were compatible with the requirement that the system should operate in hostile field conditions. A prototype system was constructed, and developed into a fully operational unit with the benefit of experience gained on field trials. Throughout the development emphasis has been placed on the compromise between technical sophistication and the ability

to obtain entomologically useful results.

The sample of field results presented in this thesis have shown conclusively (Section 7.4) that the optical system has performed according to the original specifications and that it has made a valuable contribution to the understanding of the flight behaviour of the Armyworm Moth (s. exempta).

It should be stressed that the optical system has shown that, in the case of Armyworm flight from an outbreak site, the activity observed by the radar is representative of that down to 10 m AGL. It is only very close to the ground (~ 2 m AGL) that activity patterns differ. This is a considerable step forward since previously it was impossible to assert whether the activity observed by radar was at all characteristic of the whole population.

The laboratory and computer studies of the nature of the signal received from a flying insect have revealed two important effects. Firstly, it has been shown that the harmonic content of the signal may be used to deduce the insect orientation relative to the receiver. Secondly, the analysis of the polarisation of the reflected light from an insect may provide a method for discriminating between moths and grasshoppers.

It is clear that the major limitation of the optical system described here is its susceptibility to background illumination. The analysis presented has shown that the intrinsic advantages offered by the narrow spectral width of laser sources cannot be fully exploited in this type of system because of the relatively large sample volumes used. It is likely that independence from effects of

background illumination could be best achieved by operating at a wavelength at which there is no radiation from the sky at ground level. The 250 - 270 nm ozone absorption band offers this opportunity. A lower cost interim solution for reducing the system's susceptibility to background radiation using modulated transmitters has been presented in this thesis.

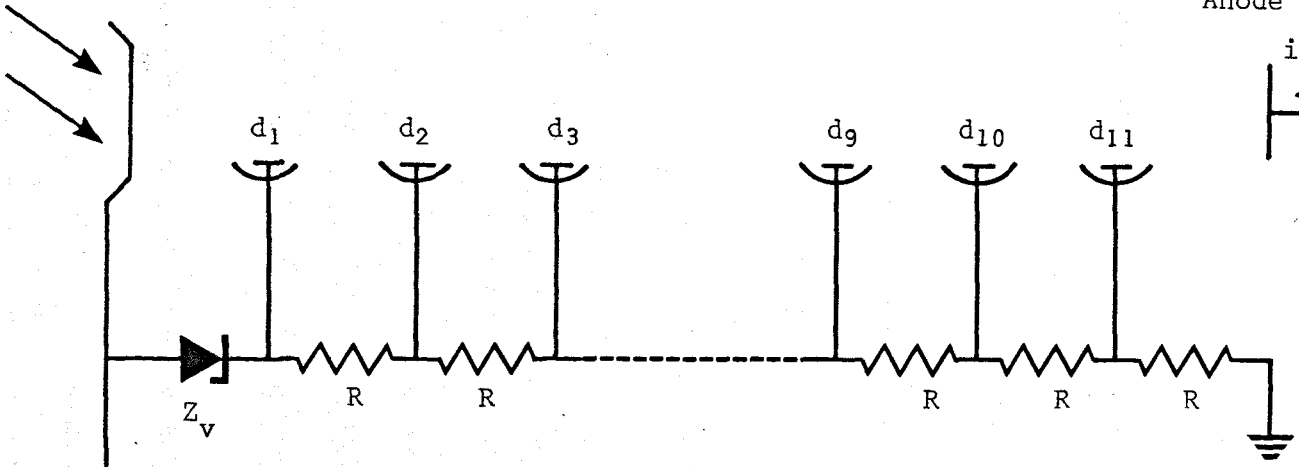
Experience has shown that the potential of the optical system (and of the radar) could be substantially increased by employing in-field automatic data analysis. The possibility of interpreting the results as they happen would represent an extremely attractive feature, particularly to entomologists who are traditionally used to more rapid feedback between experiments and results.

It is hoped that the ideas and systems developed in this work will find wide application in the study of insect flight. It is envisaged that the understanding gained will lead to more integrated control strategies which are more appropriate to present day problems.

In summary I claim to have identified a problem, proposed a solution and developed an operational system which has been shown to produce important results which were previously unobtainable.

APPENDIX A1

Photocathode



Dynode number d_n
Dynode resistor $R = 47k\Omega$
Zener Diode $Z_v = 150$ volts

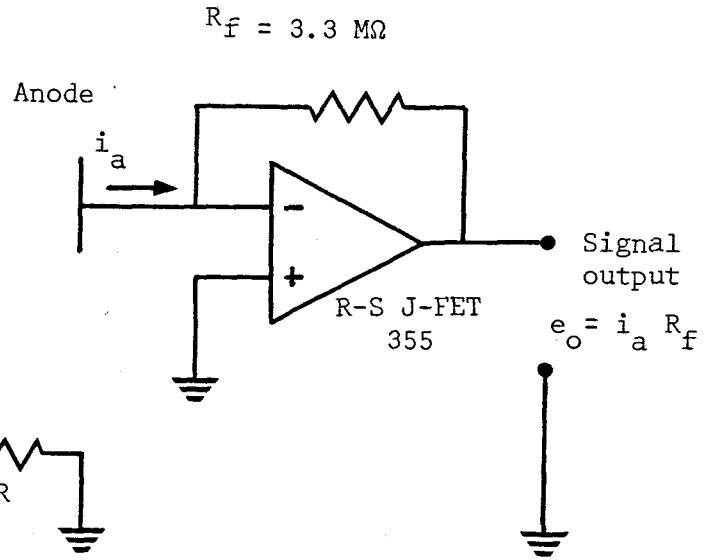


FIGURE A1 Photomultiplier Circuit (EMI type 9558B)

APPENDIX A2

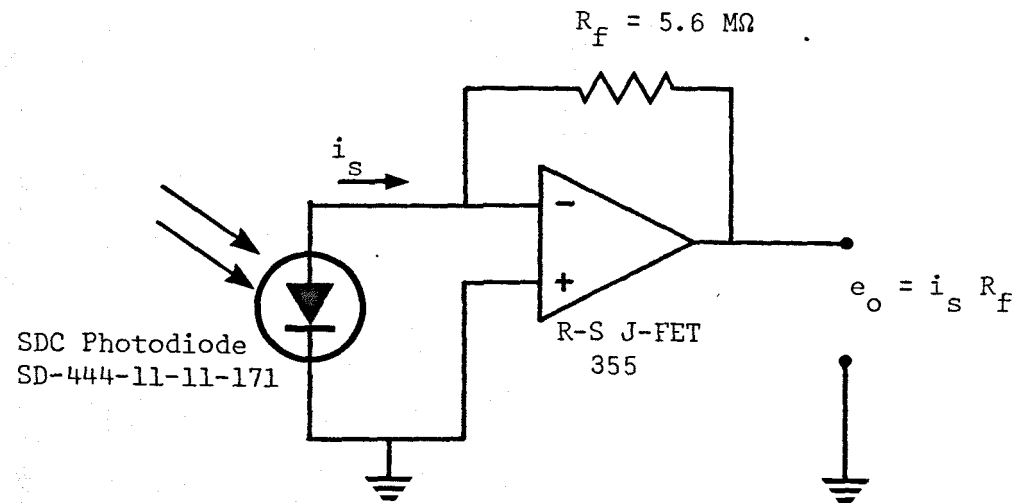


FIGURE A2 Photodiode connected to current to voltage amplifier (photovoltaic configuration)

APPENDIX A3

APPENDIX A3

A block diagram of one channel of the automatic eht system is shown in Figure A3. The principle of operation is similar to that of the low level radiometer (Appendix D).

The photomultiplier anode current i_a is fed into a current to voltage amplifier to generate the voltage e_a (see Appendix A1). This voltage consists of a d.c. level on which white noise is superimposed. It is therefore passed through an R.C. Filter with a time constant of approximately one second to provide a smooth voltage level. The voltage e_a is then compared to a reference voltage e_r in a differential amplifier. The value of e_r is set to be equivalent to an anode current of $0.33\mu\text{A}$. The output of the differential amplifier, e_d is given by

$$e_d = 10 (e_r - e_a) \quad (\text{A1})$$

The voltage e_d is then compared to two fixed voltages e_f and $-e_f$. If e_d is more positive than e_f then comparator A closes reed switch S_A . If, alternatively e_d is more negative than $-e_f$ then comparator B closes reed switch S_B . The closing of switches S_A and S_B allows the capacitor C_2 to charge or discharge through resistor R_2 . The maximum capacitor voltage is clamped at V_z volts by a zener diode. The voltage on the capacitor is buffered and fed to the programming input of a Brandenburg 479 N photomultiplier power supply module. This module produces an eht output proportional to the programming voltage input. The eht output

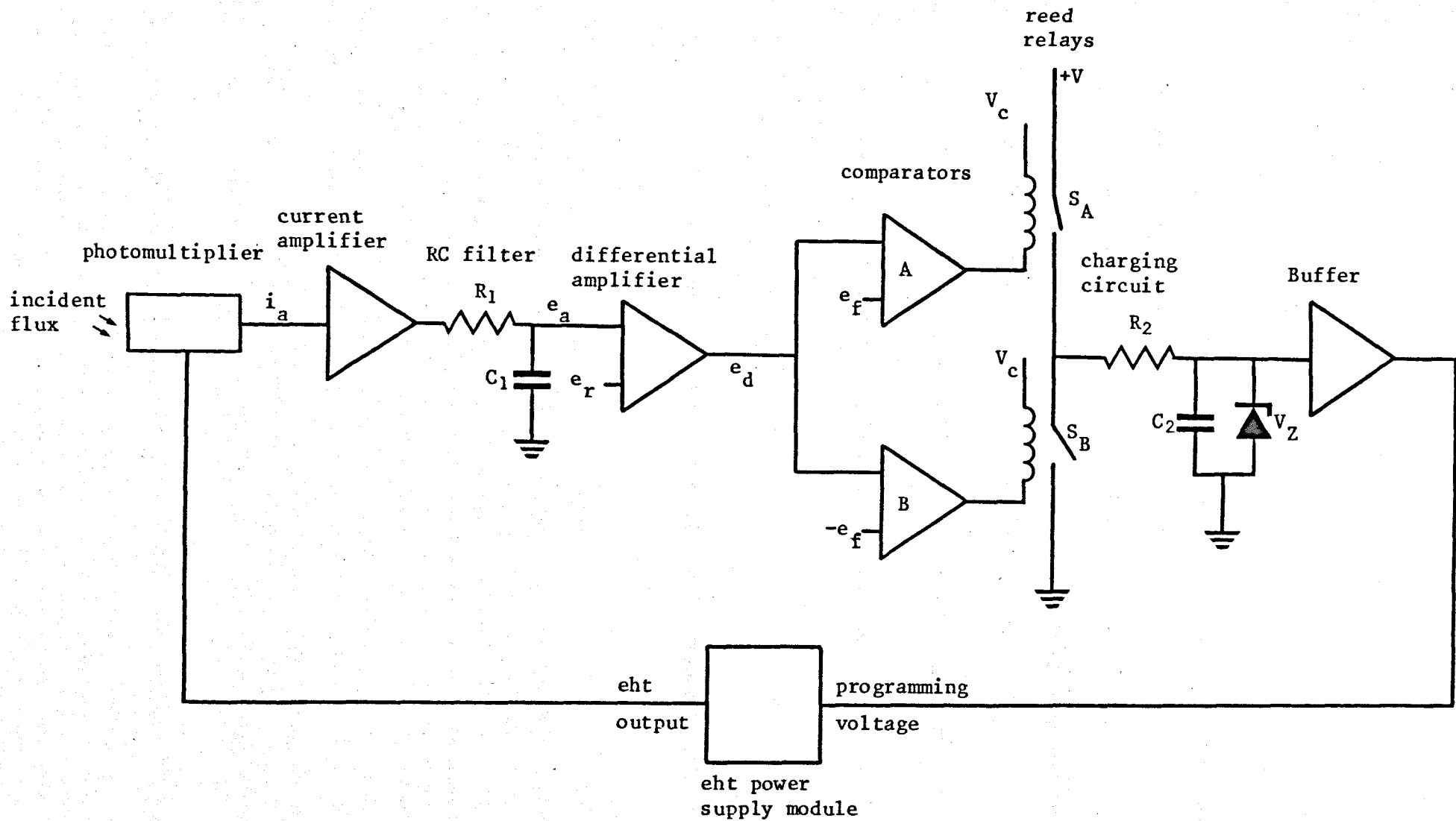


FIGURE A3
BLOCK DIAGRAM OF AUTO EHT UNIT (ONE CHANNEL)

of this module is applied to the photomultiplier tube.

Consider the case with no eht voltage applied to the tube. The anode current $i_a = 0$ and hence $e_a = 0$ and the value of e_d will be

$$e_d \gg e_f$$

(the voltages $\pm e_f$ are used to prevent 'chatter' in this feedback system and are set equal to ± 0.1 volt).

The switch S_A therefore closes and the capacitor C_2 begins to charge, which in turn increases the eht voltage applied to the tube. The charging continues until the condition

$$e_d < e_f$$

is reached. The switch S_A opens and the eht voltage remains constant so long as

$$e_d < e_f$$

If, for example, the incident flux increases, the anode current increases and

$$e_d < -e_f$$

the switch S_B then closes and capacitor C_2 discharges through R_2 . The discharge continues until the eht has been reduced sufficiently to regain the condition

$$e_d < |e_f|$$

The value of e_a is thus held constant within the range $e_r \pm \frac{e_f}{10}$

which represents an accuracy of 1%.

The zener diode prevents the programming voltage from exceeding the value corresponding to the maximum permissible eht voltage for the tube. At high illumination the eht voltage is reduced below that of the zener diode in the dynode chain (Appendix A1) and the tube is effectively switched off, thus preventing damage.

APPENDIX A4

APPENDIX A4

THE COUNTER SYSTEM

In the counter system (Figure A4) the signal from the photomultiplier tube (via the frequency calibration unit) is fed into a buffer followed by a 300 Hz filter, which mimics the bandwidth of the tape recorder. The filtered signal is then compared to a preselected threshold level (approximately twice the noise level above the background level). Each time the signal rises above the threshold level indicating the presence of a target in the sample volume the monostable is triggered. This in turn energises a relay in the event recorder which makes a mark on pressure sensitive paper. A retriggerable monostable is used with a time constant of 0.25 seconds so that rapid fluctuations in the received signal (for example, the wing beat action) cannot be counted as 'events'. CMOS components have been used where possible because of their simpler power supply requirements and reduced power consumption.

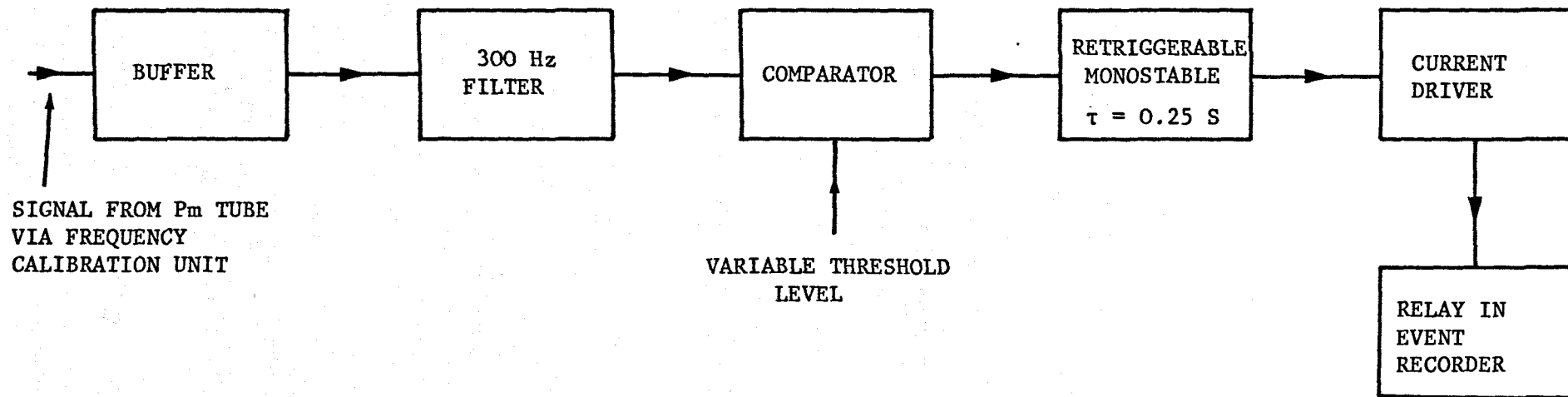


FIGURE A4 Block diagram of one channel of the counter system

APPENDIX A5

APPENDIX A5

FREQUENCY CALIBRATION UNIT

A block diagram of the frequency calibration unit is shown in Figure A5. A 100 kHz sine wave is first squared off by a Schmidt trigger and then divided by 2048 using a 12-bit counter. The resulting 48.82 Hz square wave is used as the calibration signal to check the tape recorder speed-

A precision timer produces a one second duration pulse every 15 minutes. This is used to energise the coil of a 4-pole, 2-way relay. The signal from the photomultiplier tube on each channel is interrupted and the calibration frequency switched in. This occurs on all four channels. The amplitude of the calibration frequency is arranged to be greater than the counter threshold so that the regular calibration signals are counted as events and produce 15 minute timing marks on the paper record.

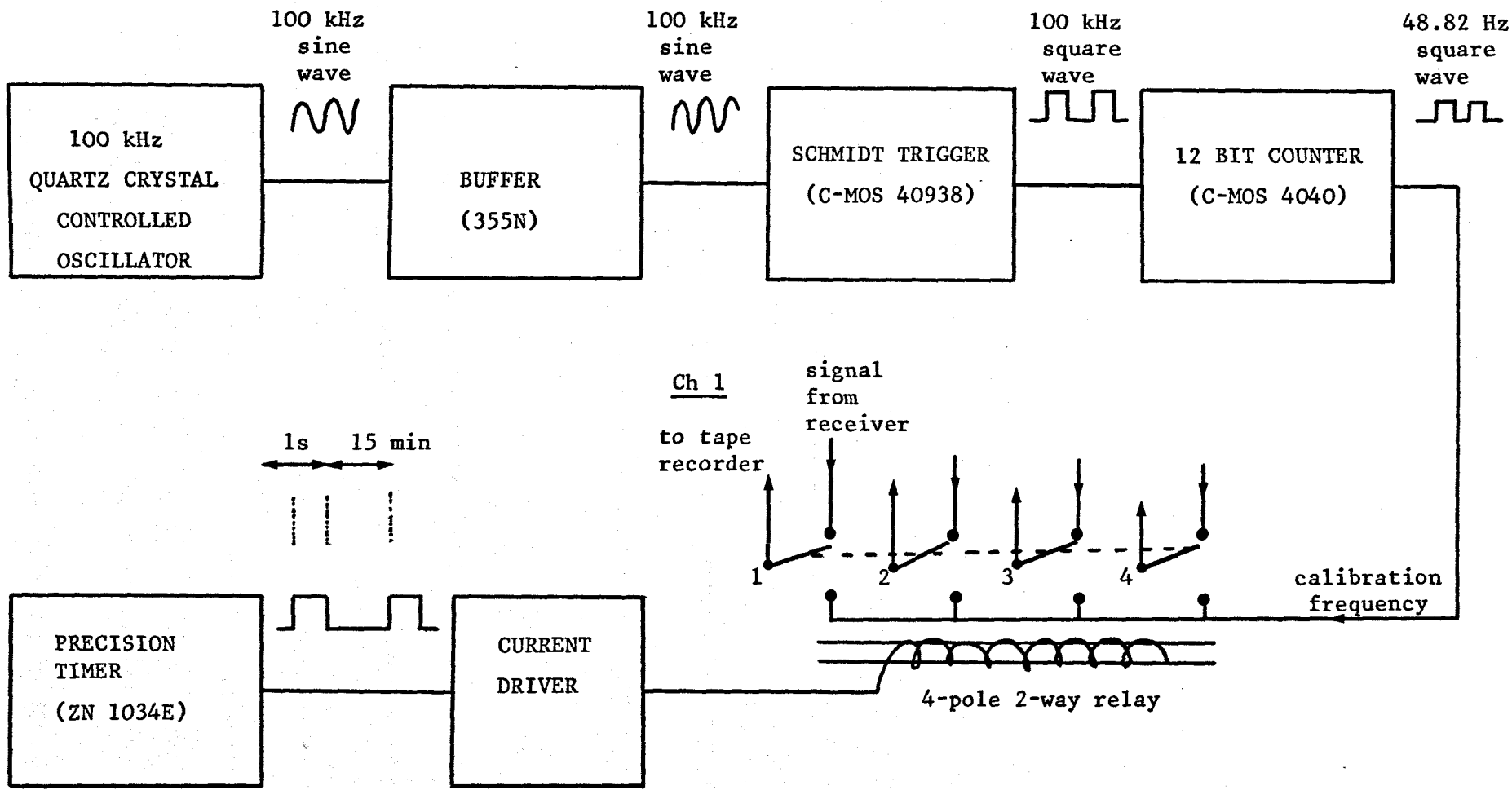


FIGURE A5 Block diagram of frequency calibration unit

APPENDIX B

APPENDIX B

RECORDER NOISE

The signal-to-noise ratio S_N (in dB's) of the Racal Store 4 instrumentation recorder is defined by the manufacturerers as

$$S_N = 20 \log_{10} \frac{V_S}{V_N} \quad (B1)$$

where V_S is the rms value of the sine wave whose amplitude is equal to the maximum recorder output.

V_N is the rms value of the noise voltage at the output.

In order to accommodate the largest likely signals, the 5 v input range was used on the recorder. The replay output range was set at 1.0 v, giving an input/output attenuation factor of 5 .

At the replay speed of $15/16$ ips the manufacturers quote the 1.0 dB bandwidth of the recorder as 313 Hz and the signal-to-noise ratio as 45 dB. Assuming the value of $V_S = 1.0$ v set above, the rms output noise voltage has been calculated to be $V_N = 4$ mV . This is equivalent to a peak-peak noise voltage of about 12 mV . The measured value for the recorder used in this work was $V_N = 30$ mV . This noise voltage was obtained using high quality instrumentation tape (manufactured by 3M Ltd.), and was found to be reproducible without sign of degradation with time. The discrepancy between the measured and manufacturerers derived figures for the output noise voltage is considered to be due to inferior machine performance.

During analysis only signals with amplitudes greater than twice the output noise voltage were counted (Section 5.3). The minimum detectable signal amplitude at the input to be recorded (i.e. at the output of the photomultiplier current to voltage amplifier) was therefore effectively limited to 0.3 v by the input-output attenuation factor of 5 .

In the analysis of Section 2.3 the performance of the photomultiplier tube was shown to be limited by the noise generated by background radiation. For a spectral bandwidth of 150 nm the generated photocathode current was found to be

$$i_b = 10^{-12} \text{ A .}$$

The rms shot noise current associated with this background current is

$$i_N = (2eB i_b)^{\frac{1}{2}}$$

using the following values

$$e = 1.6 \times 10^{-19} \text{ C}$$

$$B = 300 \text{ Hz}$$

gives

$$i_N = 10^{-14} \text{ A .}$$

Assuming the maximum likely photomultiplier gain to be 10^6 the noise current at the anode is

$$i_{N_A} = 10^{-8} \text{ A .}$$

At the output of the current to voltage amplifier (feedback resistor = 5.6 M Ω) the rms noise voltage is

$$V_N = 60 \text{ m V}$$

The peak to peak noise voltage generated by the background radiation is thus approximately 170 m V . This value is approximately half that generated by the recorder (300 mV).

It can therefore be concluded that, in practice, the minimum detectable signal is limited by recorder noise rather than noise generated by the receiving system.

APPENDIX C

APPENDIX C1 SUMMARY OF COLLECTED DATA MALI 1978

Date	Tape No.	Tape Footage	Start time	Finish time	Comments
20.9.78	3	0			Running up using standard source
21.9.78	3				Running up using artificial insect on tethered balloon
22.9.78	3	100-450			Insect signals: trying different geometries: some good signals
23.9.78	3	480-860			Attempt at normal operations. Mid-evening change from bi-static to monostatic configuration
24.9.78	3 4	900-end 0-350	1800	2300	Front reported by radar
25.9.78	4	370-773	1800	2025	Initial test with artificial insect at 40 m range. Low insect activity for rest of evening
26.9.78	4	800-1480	1830	2110	Initial test with artificial insect: a few good signals. Low activity.
27.9.78	3	0-450	1830	2000	Tape 3 inadvertently over-recorded. Labelled 'tape 5'; very low activity
28.9.78	5	0-1154	1815	2215	Moderate to high activity; concentration reported at 2125-2130
29.9.78	6	0-1730	1815	0030	Perfect evening operation; dramatic increase in numbers at 2300
30.9.78	6 7	1750-1971 0-76 76-340 350-415 417-453	1825	2200	A few good signals Attempts at tethered flight Normal observations Poor Aldis beam plot Good Aldis beam plot
1.10.78	7	500-800	1822	2137	Whole evening plagued by series of generator and equipment failures. Poor data

APPENDIX C2 Summary of Collected Data Kenya 1979.

Configuration	Date	Tape No.	Tape footage	Start time	Finish time	Remarks
monostatic	30.3.79	10	11 - 16	-	-	Testing system with artificial moth
Height profile Mk 1	31.3.79	10	30 - 80	1916	1927	Testing operational configuration, rain
Height profile Mk 1	1.4.79	10	100 - 956	1900	2218	
			960 - 1020	2245	2258	
Height profile Mk 1	2.4.79		1021 - 1051	0045	0051	'Dawn flush'
			1060 - 1195	0530	0600	
Height profile Mk 2	2.4.79	11	0000 - end	1910	0136) Good observations
	3.4.79	12	0000 - 1355	0145	0635	
Height profile Mk 2	3.4.79	12	1360 - end	1910	2043	rain
		13	0000 - 356	2046	2150	
	4.4.79		370 - 512 520 - 1609	0105 0205	0134 0600	
Height profile Mk 2	4.4.79	14	0000 - 418	1921	2051	rain
	5.4.79		418 - 583	0528	0602	'Dawn flush'
Height profile Mk 2, from 0430 onwards chan (1) in tree config.	5.4.79	14	600 - 888	1902	2004	rain
			900 - 941	2124	2132	rain
	6.4.79		943 - 1220 1230 - 1792	0248 0358	0347 0559	Interrupted by rain Good observations

APPENDIX C2 (cont'd.)

Configuration	Date	Tape No.	Tape footage	Start time	Finish time	Remarks
Tree ch. 1 west ch. 2 east	6.4.79	15	0000 - 302 303 - 416 430 - 1764	1916 2139 2208	2020 2203 0255	Aldis failure
	7.4.79	16	0000 - 841	0300	0600	
Tree ch. 1 west ch. 2 east	7.4.79	16	850 - 1792 0000 - 35	1910 2240	2233 0035	Battery charge ch. 2 interrupted
	8.4.79	18	540 - end 0000 - 168	0051 0524	0519 0600	frequently until 0430
Tree ch. 1 west	8.4.79	18	200 - end	1915	0055	at start demonstration of recorder noise level poor data
		19	0000 - 1405	0100	0600	

APPENDIX C3 Kenya 1980 Summary of Collected Data

OUTBREAK 1. LUKENYA SITE

Date	Tape No.	Start time	Finish time	Start Footage	Finish Footage	Configuration	Remarks
25.2.80	20	2005	0643	0000	2295	setting up: from 2121 (356) Ch. 1 at 10 m; Ch. 3 at 20 m until 0250 (1900) then d/w of tree	activity at 10 m d/w edge not defined due to light winds
26.2.80	21	1915	0330	0000	end	Ch. 1, 20m until 2230 then at 10 m (defoc aldis)	good data from tree
	22	0335	0618	0000	762	Ch. 2 d/w tree (defoc aldis) Ch. 3 grd. level (defoc aldis)	
27.2.80	22	1915	0035	800	end	Ch. 1 10m (defoc aldis) Ch. 2 d/w tree (defoc aldis)	10 m O.K. later on tree good grd level poor
	23	0040	0630	0000	1675	Ch. 3 grd level (defoc aldis)	
28.2.80	23	1915	2142	1660	end	Ch. 1 10 m (defoc aldis)	10 m O.K.
	24	2145	0545	0000	end	Ch. 2 d/w tree (defoc aldis)	tree good
	25	0550	0619	0000	135	Ch. 3 grd level (defoc aldis)	grd level poor
29.2.80	25	1912	0255	150	end	Ch. 1 10 m (defoc aldis)	some rain
	26	0300	0618	0000	925	Ch. 2 d/w tree (defoc aldis) switched to Ch. 4 at 400 Ch. 3 grd level (defoc aldis)	calm conditions most of night

APPENDIX C3 (cont'd.)

OUTBREAK 1. LUKENYA SITE (cont'd.)

Date	Tape No.	Start time	Finish time	Start Footage	Finish Footage	Configuration	Remarks
1.3.80	26	1957	0046	950	end	Ch. 1 20m (foc aldis)	low activity detected
	27	0048	0617	0000	1537	Ch. 4 d/w tree (defoc aldis) Ch. 3 grd level (defoc aldis)	fairly bright moonlight frequent rain (storm at normal start time)
2.3.80	27	1900	2145	1550	end	Ch. 1 10 m (foc aldis)	many signals from pheromone trap
	28	2146	0602	0000	end	Ch. 3 d/w tree (defoc aldis)	trap
	29	0605	0617	0000	60	Ch. 3 grd level (defoc aldis) Ch. 4 switched to pheromone trap at 1958 (1810)	rain
3.3.80	29	1910	0315	70	end	Ch. 1 10 m (foc aldis)	frequent rain
	30	0507	6616	0000	320	Ch. 4 Pheromone trap (defoc aldis) Ch. 3 grd level	lots of activity at pheromone trap

APPENDIX C3 (cont'd.)

OUTBREAK 2 HOPCRAFT RANCH

Date	Tape No.	Start time	Finish time	Start Footage	Finish Footage	Configuration	Remarks
31.3.80	31	1915	2200	0000	735	Ch. 3 at 10 m from start (defoc aldis) Ch. 2 20 m from 1950 (156) (foc aldis)	not much activity early closedown after β -light experiments
1.4.80	31	1910	0040	750	end	Ch. 1 20 m (foc aldis)	
	32	0045	0615	0000	1550	Ch. 2 3m (defoc aldis) Ch. 3 10 m (foc aldis)	not much activity
2.4.80	32	1910	2142	1600	end	Ch. 1 20 m (foc aldis)	'descending' flight
	33	2145	0553	-0005	end	Ch. 2 3 m (defoc aldis)	observed at 1920
	34	0555	0610	0000	70	Ch. 3 10m (foc aldis)	emergence $\sim 1 \text{ m}^{-2}$
3.4.80	34	1910	0300	100	end		'descending' flight
	35	0303	0605	0000	859	standard	2-ch recordings made on cassette
4.4.80	35	1910	0008	900	end		'descending' flight
	36	0610	0605	0000	1660	standard	highest emergence to date: good activity
5.4.80	36	1910	2117	1700	end		'descending' flight
	37	2120	0533	0000	end	standard	good activity
	38	0535	0605	0000	142		2-ch on cassette

APPENDIX C3 (cont'd.)

OUTBREAK 2 HOPCRAFT RANCH (cont'd.)

Date	Tape No.	Start time	Finish time	Start Footage	Finish Footage	Configuration	Remarks
6.4.80	38	1910	0247	150	end	standard	'descending' flight good activity
	39	0250	0615	0000	948		
7.4.80	39	1910	2348	1000	end	standard	descent earlier lightening rain towards morning
	40	2350	0605	0000	1745		
8.4.80	40	1905	2053	1800	end	standard	'descending' flight lightening some rain
	41	2055	0513	0000	end		
	42	0515	0605	0000	241		
9.4.80	42	1905	0217	300	end	standard	some lower Wbf's at 1910, descending flight not obvious lots of lightening
	43	0220	0640	0000	1234		

APPENDIX C4

SUMMARY OF MOTHS FLOWN IN LABORATORY, MUGUGA, KENYA, MARCH 1978

Trace No	Wing beat frequency Hz	Moth No	Wing length cm	Weight mg	Species
6	65				
7	50				
17	40	M6	1.4	44.2	Grammodis Stolidia
18	30	M7	1.7	34	Hypens Abyssinalis
19	35	M8	1.3	43	Grammodis Stolidia
20	37	M9	1.8	107	Plusia Limbirenia
21	48	M10	1.9	77.8	Plusia Acuta
22	29	M11	2.0	42.4	Plusia Acuta
23	33	M12	1.4	45.8	Spodoptera Exempta (M)
24	45	M13	1.65	84	Spodoptera Exempta (M)
29	42	M14	1.60	78.7	Spodoptera Exempta (M)
31	46	M15	1.85	66.7	Spodoptera Exempta (M)
32	41	M16	1.50	67.2	Spodoptera Exempta (M)
41	40	M17	1.60	84.7	Spodoptera Exempta (F)
42	45	M18	1.6	72.5	Spodoptera Exempta (F)
43	45	M20	1.3	50	Spodoptera Exempta (F)
46	42	M22	1.4	61	Spodoptera Exempta (M)
47	42	M23	1.4	53	Spodoptera Exempta (M)
48	49	M28	1.7	96	
49	45	M29	1.9	122	Spodoptera Triturata (M)
50	31	M30	1.25	14	Hypens Jussalis
51	43	M31	1.9	97	Spodoptera Triturata
52	52	M32	1.2	82	Spodoptera Triturata (M)
54	35	M33	2.0	168	Heliothis Amigera
56	50	M34	1.75	88	Spodoptera Triturata (M)
57	29	M37	1.65	57	Margaronia Unionalis

/continued

APPENDIX C4 (cont'd.)

Summary of moths flown in laboratory, Muguga, Kenya, March 1978

Trace No	Wing beat frequency Hz	Moth No	Wing length cm	Weight mg	Species
60	43	M38	1.40	60	
61	36	M39	1.60	86	Spodoptera Exempta (M)
62	44	M40	2.20	179	
63	45	M41	1.60	58	
64	45	M42	1.90	-	
66	43	M43	1.60	62	
67	41	M44	1.70	99	Heliothis Amigera
68	42	M45	1.5	76	Spodoptera Capicola (F)
69	35	M47	1.80	92	Spodoptera Triturata (F)

APPENDIX D

1. Introduction

Radar observations have revealed two aspects of insect flight which may be dependent on irradiance. Firstly it is possible that the level of nocturnal irradiance could affect the ability of night flying insects to adopt a measure of common orientation (Riley 1975). Secondly, the synchronised take-off of many night flying insects shortly after sunset (Schaefer 1976, Riley and Reynolds 1979) may possibly be triggered by falling levels of irradiance. For the further study of both these phenomena we required a sensitive, continuously recording radiometer with wide dynamic range suitable for field operation. No commercial instrument with such a specification was available and what follows is our solution to the problem. It is expected that the instrument will find application in many other areas, such as astronomical and night airglow studies.

2. Design requirements

For the application envisaged it was decided that the instrument should satisfy the following criteria.

It should:

- (1) Continuously and automatically measure irradiance in the visual waveband, from sunset until dawn.
- (2) Be sensitive enough to detect varying degrees of starlight obscuration by cloud.
- (3) Tolerate hostile environmental conditions.
- (4) Be reasonably compact and simple to operate.

At sunset, clear sky irradiance in the waveband 375-825 nm (an

extended version of the visual waveband, defined by our detector response) is approximately 0.1 Wm^{-2} and the value for unobscured starlight is approximately 10^{-5} Wm^{-2} . However, we chose the minimum irradiance to be detected by the photometer as $2.0 \cdot 10^{-6} \text{ Wm}^{-2}$ so that it would be possible to resolve different degrees of starlight obscuration. The instrument thus had to have a dynamic range of at least five decades.

3. Prototype design

Several different detectors were considered for the radiometer before the present system was finalised. Although the detectivity of some solid state detectors e.g. low noise silicon photodiodes was just sufficient for our purpose, we considered them unsuitable because they have to be used in a 'switched range' mode to give the necessary dynamic range. Such a method (Callaghan 1964) is inappropriate to automatic operation.

The very high detectivity (typically $D^* = 10^{16} \text{ W}^{-1} \text{ Hz}^{\frac{1}{2}}$) and effectively noise-free gain of photomultiplier tubes meant that these tubes easily yield adequate sensitivity and in fact they have been used in several night photometers (Buyal'skii et al 1977, Treanor and Salpeter 1972, Kulkarnie 1970). However these instruments were unsuitable for automatic operation because they depended on some form of range switching.

Our design has overcome this limitation by exploiting the exponential gain function of the photomultiplier tube (Figure D1). We have put the photomultiplier tube in a feedback system in which the applied EHT, and therefore the gain of the tube is automatically adjusted so that the anode current is maintained at a fixed value,

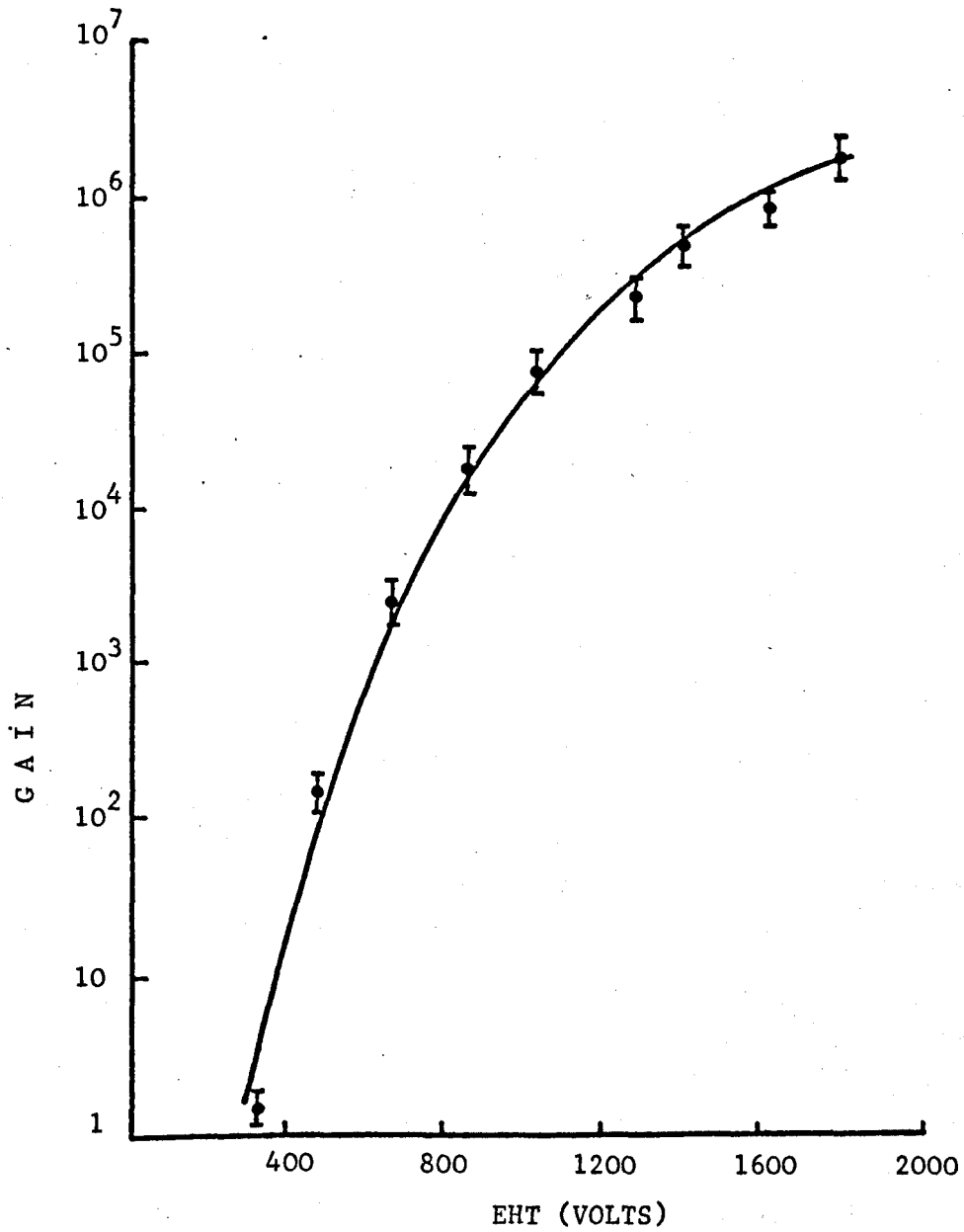


FIGURE D1

Gain as a function of applied EHT voltage for an 11-stage photomultiplier tube (EMI type 9558B).

for a wide range of irradiance. The EHT required is then a convenient measure of the logarithm of incident power. It has been noted (Ovchinnikov et al 1974) that variations in photomultiplier gain can change the spectral responsivity of the photocathode, but this effect is not however considered to be significant in our system.

4. Prototype Instrument

4.1 Circuit description

A block diagram of the prototype instrument is shown in Figure D2. The photomultiplier tube is an EMI type 9558B with S20 photocathode. The dynode chain is standard. The cathode to first dynode voltage is stabilised at 150 v by zener diode and the other dynodes are interconnected via equal value fixed resistors.

The photomultiplier anode current flows into a current-to-voltage amplifier. The resulting voltage, e_a is compared to a reference voltage, e_r (corresponding to an anode current of 0.3 μ A) using a differential amplifier. The output of the differential amplifier e_d is then sensed by two comparators A and B. These have fixed reference voltages of 0.1 v and -0.1 v respectively to reduce 'chatter' in the feedback system. The comparators control reed relays which allow a capacitor C_2 to either charge or discharge through a resistor R_2 . The voltage on the capacitor is buffered and forms the output of the radiometer. It also forms the programming voltage for a Brandenburg 479N EHT power supply module, and thus controls the EHT applied to the photomultiplier, and hence its gain.

4.2 Method of operation

If the anode current is less than the preselected value, the

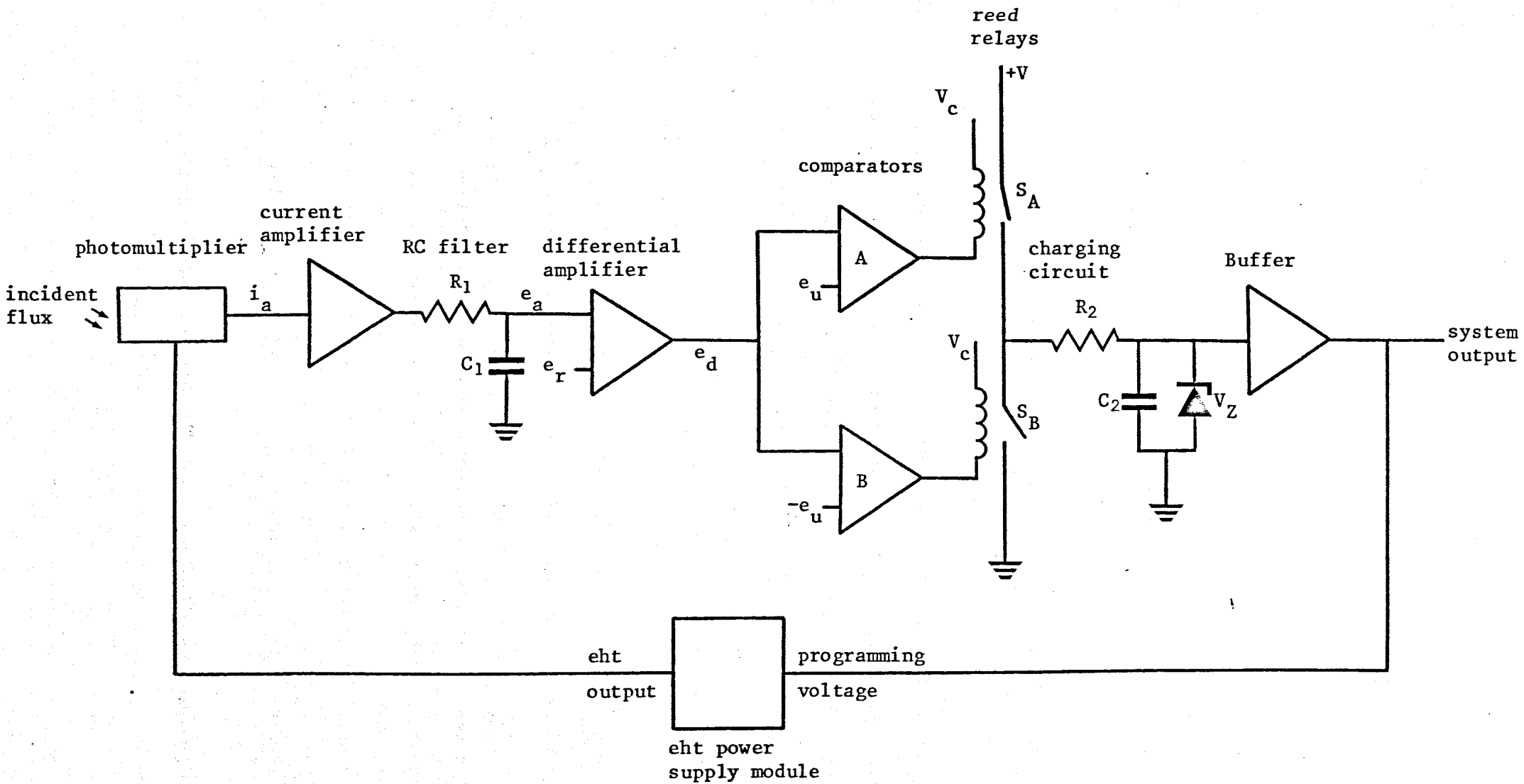


FIGURE D2
BLOCK DIAGRAM OF LOW LEVEL RADIOMETER

output of the differential amplifier is positive and comparator A closes switch S_A . Capacitor C charges up with time constant R_2C_2 . This in turn increases the programming voltage and the EHT applied to the tube. The gain of the tube increases and for the given incident power, so does the anode current. The process continues until the anode current equals the reference value. The system reacts to high anode current in a reverse manner by reducing the applied EHT.

Two safeguards have been designed into the system. The voltage on the capacitor C which forms the programming voltage is limited by a zener diode to a value corresponding to the maximum permissible EHT voltage for the tube. Also, since the EHT output for zero programming voltage is 130 v, the inclusion of the 150 v zener diode effectively switches the tube off for EHT values less than 150 v. This protects the tube against high anode currents in bright sunlight.

The two time constants R_1C_2 and R_2C_2 are both equal to 10 seconds.

5. Calibration

The calibration of the radiometer was made with the assumption that the spectral responsivity for the photomultiplier S20 photocathode and the spectral distribution of nocturnal irradiance could be adequately represented by the functions shown in Figures D3 and D4. Three distinct stages were used in the calibration.

(a) Calibration of radiometer output in terms of photocathode current

The power incident on the photomultiplier photocathode from a helium-neon laser (632 nm) was varied over a wide range of values by using calibrated neutral density filters. The radiometer output was noted

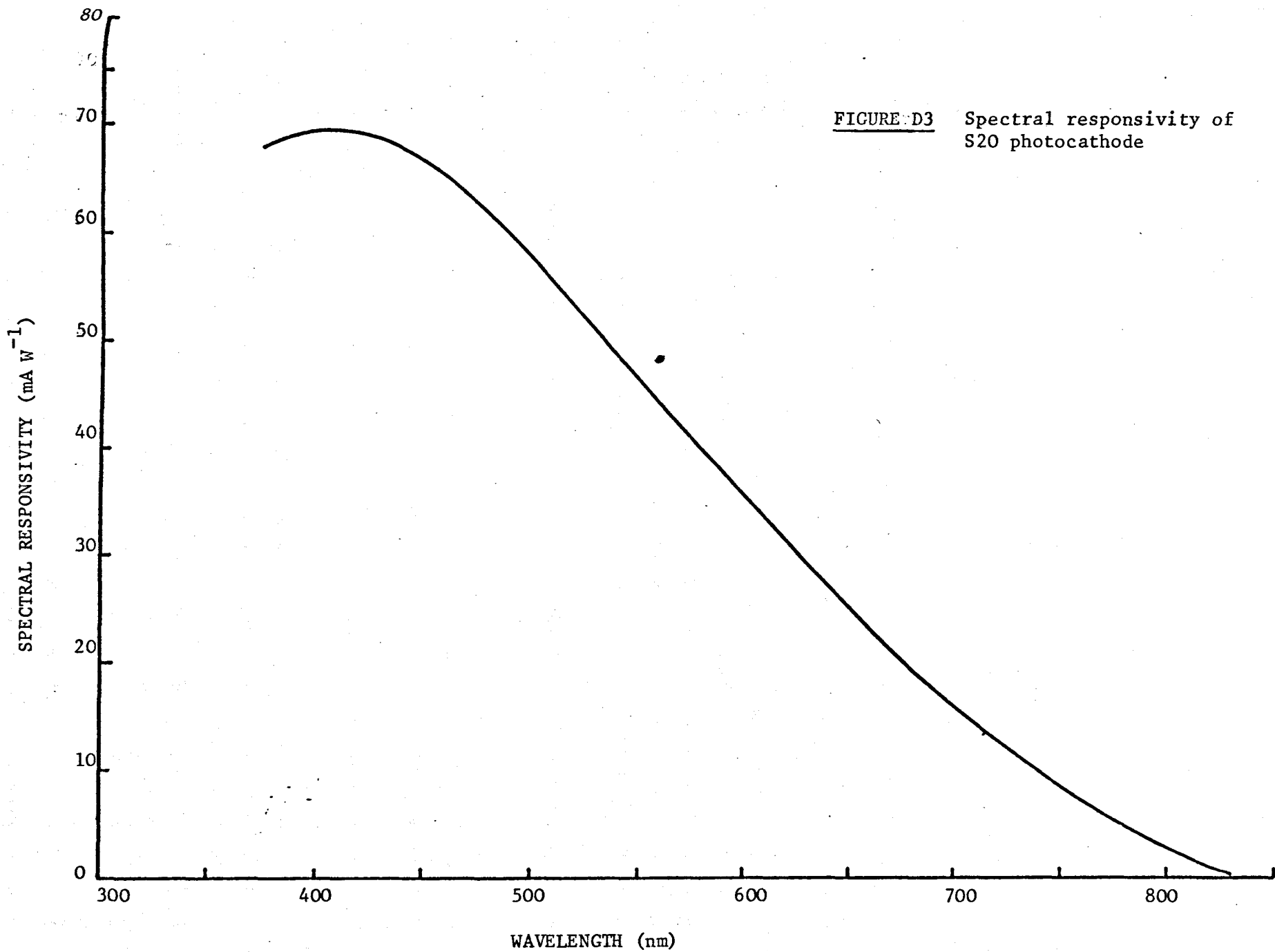
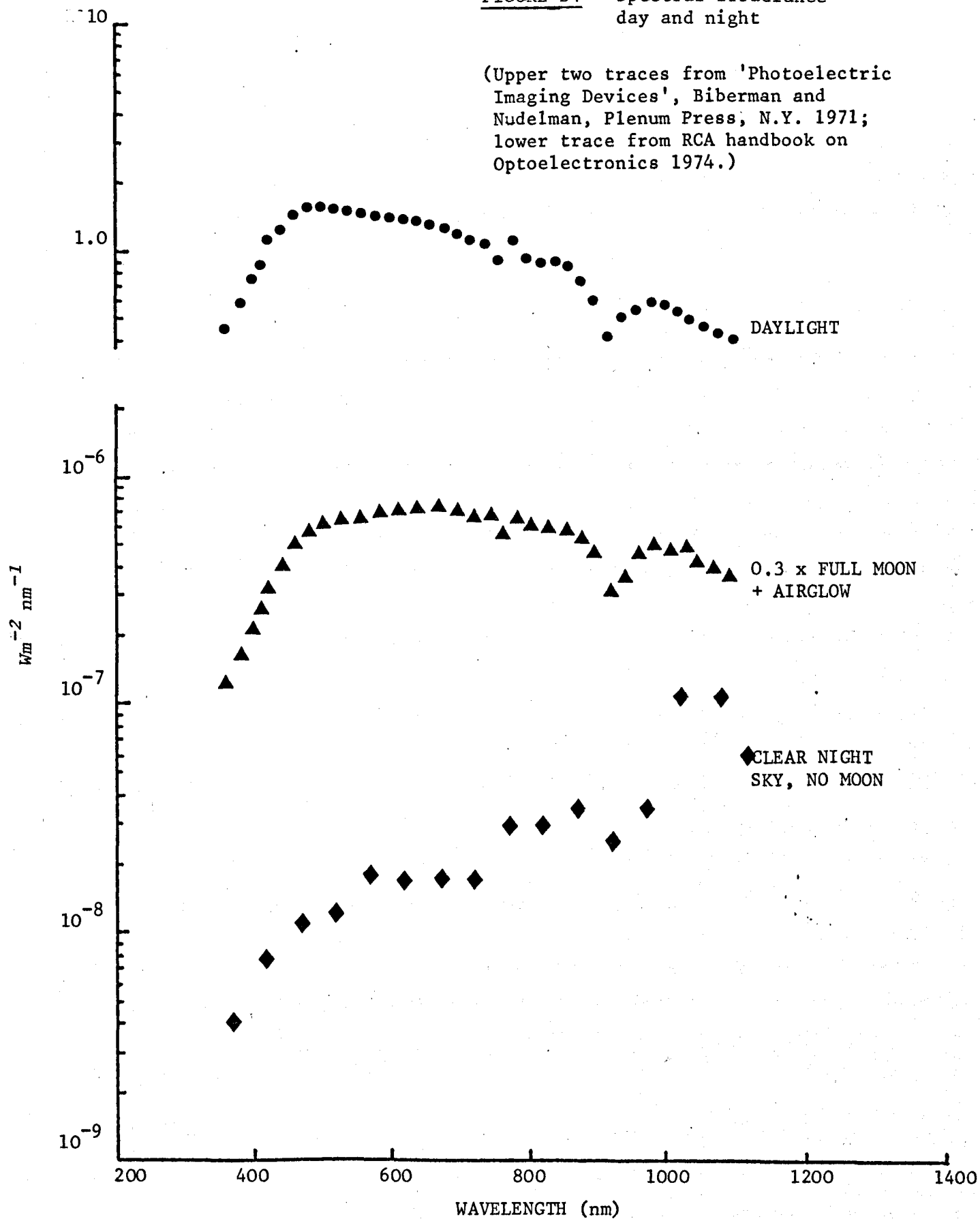


FIGURE D3 Spectral responsivity of S20 photocathode

FIGURE D4 Spectral Irradiance
day and night

(Upper two traces from 'Photoelectric
Imaging Devices', Biberman and
Nudelman, Plenum Press, N.Y. 1971;
lower trace from RCA handbook on
Optoelectronics 1974.)



for each incident power. This procedure effectively calibrated the radiometer output voltage (e_o) in terms of photocathode current since this current, i_p could be calculated from the known incident power, P_{in} by the equation:

$$i_p = P_{in} \times R_{632} \quad (D1)$$

Where R_{632} is the responsivity of the photocathode at 632 nm.

The relation: $i_p = f(e_o)$ was thus determined.

(b) Calculation of effective responsivity of S20 photocathode for nocturnal irradiance

The next step was to calculate the photocathode current generated for a given nocturnal irradiance. If the spectral irradiance of nocturnal light is $E(\lambda)$, and the spectral responsivity of the S20 photocathode is $R(\lambda)$ then the photocathode current generated is given by i_E where

$$i_E = A \int_{\lambda_1}^{\lambda_2} E(\lambda) R(\lambda) d\lambda \quad (D2)$$

Where λ_1 λ_2 are the lower and upper limits of the detector response and A is the illuminated photocathode area.

The total power incident in the waveband is given by

$$P_T = A \int_{\lambda_1}^{\lambda_2} E(\lambda) d\lambda \quad (D3)$$

and hence the effective responsivity of the photocathode for nocturnal irradiance is

$$R_{\text{eff}} = \frac{A \int_{\lambda_1}^{\lambda_2} E(\lambda) R(\lambda) d\lambda}{A \int_{\lambda_1}^{\lambda_2} E(\lambda) d\lambda} AW^{-1} \quad (\text{D4})$$

It is assumed that the form of $E(\lambda)$ does not change significantly through the night.

(c) Calibration of radiometer output in terms of irradiance

Finally the steps (a) & (b) were combined to produce a relation between radiometer output (e_o) and incident irradiance (E). Thus from (a):

$$i_p = f(e_o) \quad (\text{D5})$$

But also
$$i_p = \{E\} \times \{A\} \times R_{\text{eff}} \quad (\text{D6})$$

where $E \text{ Wm}^{-2}$ is the total nocturnal irradiance in the range 375-825 nm.

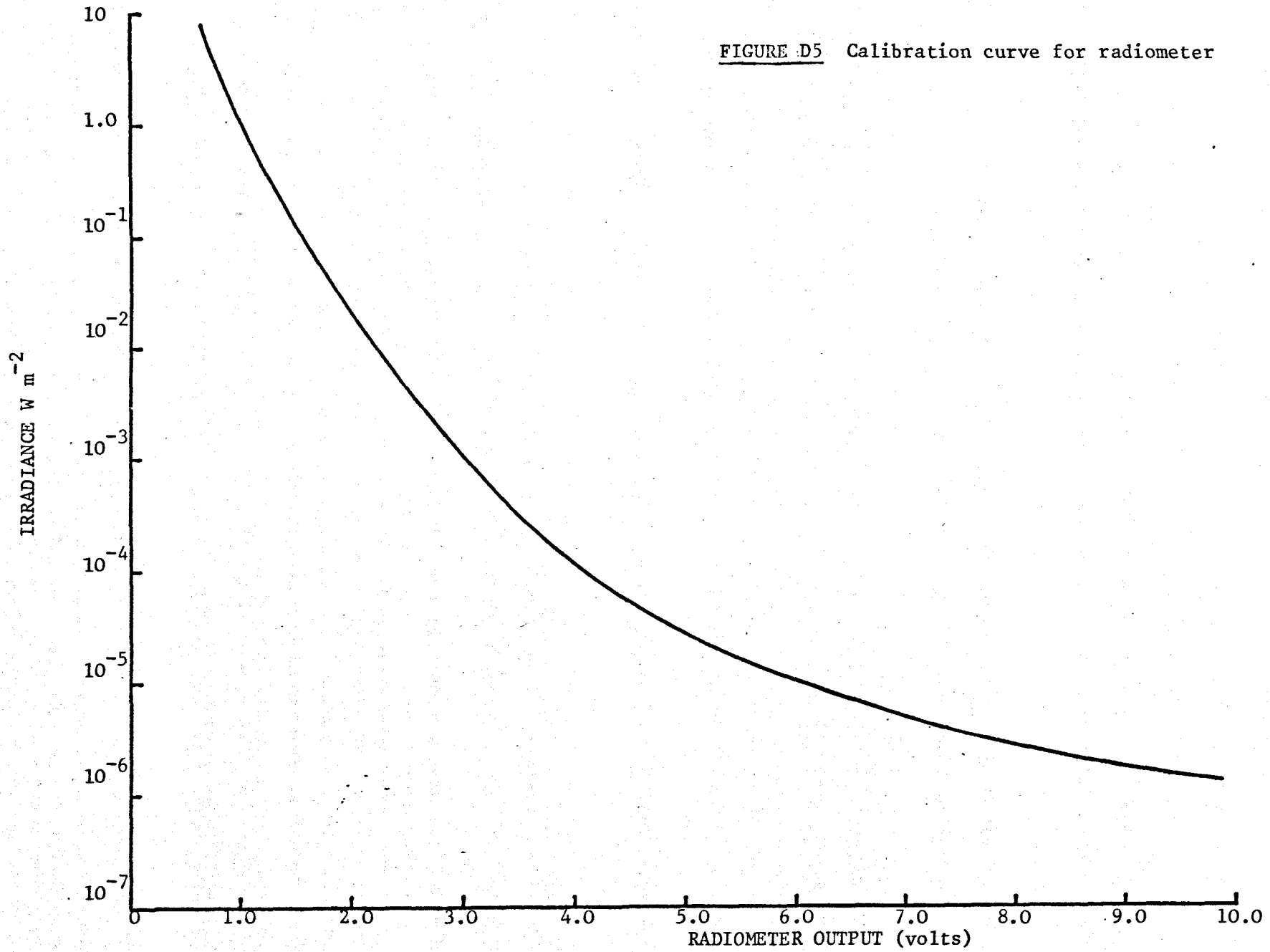
Hence:

$$E = \frac{f(e_o)}{\{A\} \times R_{\text{eff}}} \quad (\text{D7})$$

This equation (D7) calibrates the radiometer output (e_o) in terms of irradiance in the waveband 375-825 nm using the measured photocathode current/radiometer output characteristic.

The instrument in this form was however about three decades too sensitive. A neutral density and diffuser combination reduced the sensitivity by the required amount and the final calibration is shown in Figure D5.

FIGURE D5 Calibration curve for radiometer



6. Field operation

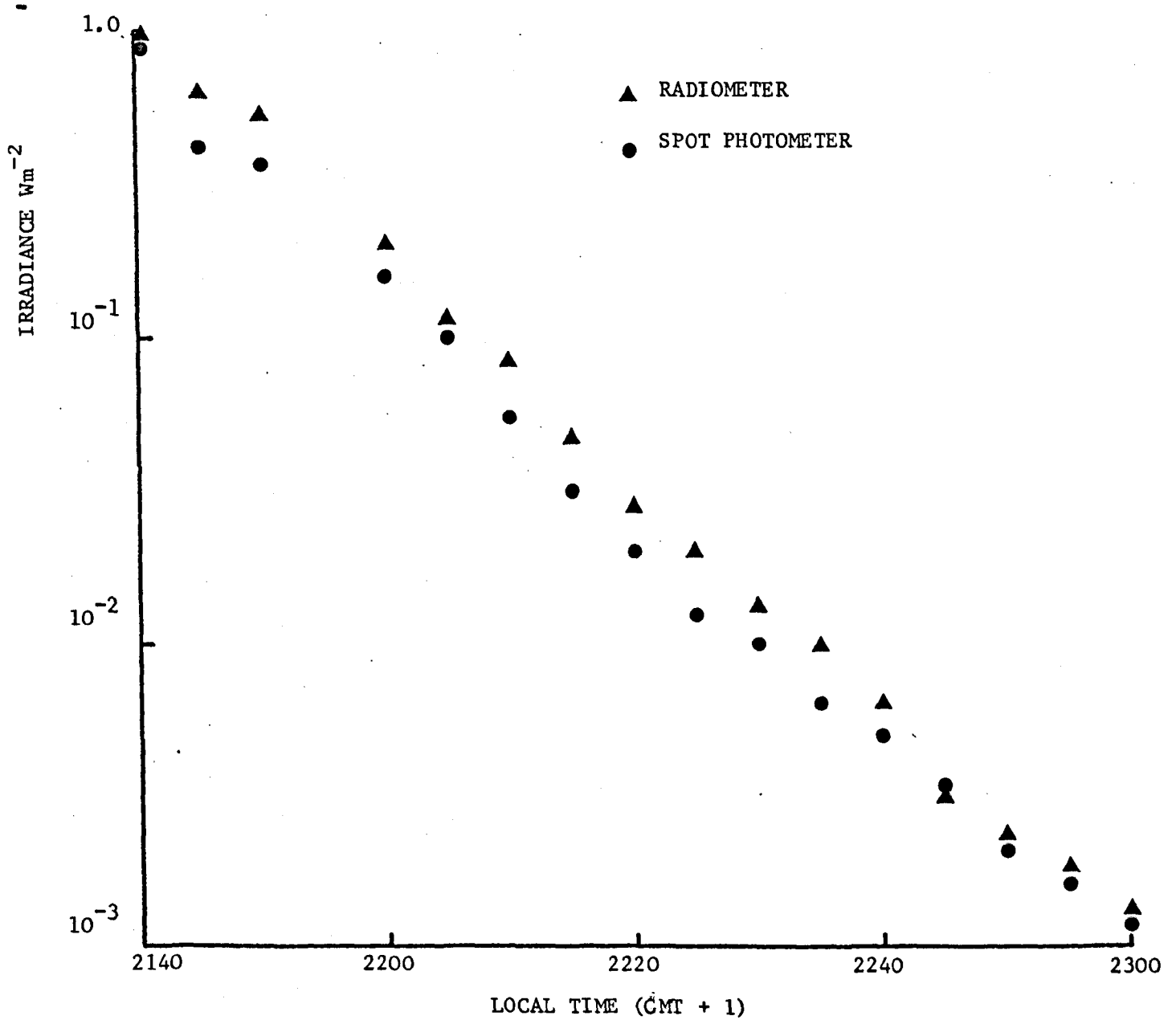
The prototype instrument was designed to run on either 240 v ac or 24 v dc. The sensor head containing photomultiplier tube and current amplifier was made from aluminium as a hermetically sealed unit (Plate 1). HT and signal cables connected it to the control box. The instrument received its first field trial in Kenya (1980), where it operated reliably for a period of 21 days.

In Kenya the decrease in irradiance after sunset is very rapid and so it was difficult to make sufficient synchronised measurements with a spot photometer for useful comparison. This experiment was therefore performed instead in England where the decrease is slower. The results are shown in Figure D6 for the period where their respective ranges overlap. It may be seen that the results are in excellent agreement.

7. Conclusion

The design of a simple radiometer has been described which has a continuous output over five decades and a minimum sensitivity equivalent to obscured starlight. The design exploits the high detectivity and exponential gain function of a photomultiplier tube. The instrument has been tested in arduous field conditions and specimen results have been compared with measurements from a commercial photometer. The total cost of components for the radiometer is approximately £500.

FIGURE D6: Comparison of radiometer
spot photometer measurements
for post-sunset period,
5 July 1980



APPENDIX E

APPENDIX E

IMPROVED BACKGROUND DISCRIMINATION

It has been noted in this work that one of the most serious limitations of the optical system which has been developed is its susceptibility to background radiation. This problem is a direct result of the broad spectral bandwidth (150 nm) of the radiation and the wide receiver field of view employed. Laser systems can be largely independent of background radiation (Lawrence, Crownfield and McCormick, 1967) but in this application their intrinsic advantages cannot be fully exploited (Section 3.5).

The problem of susceptibility to background radiation has manifested itself in two ways. Firstly, observations have been limited at dusk and dawn; during periods of very bright moonlight the effective sample volume has been reduced considerably. Secondly, scattered moonlight from passing clouds has sometimes injected a low frequency noise component into the system, thus degrading the recorded data.

The partial solution described below uses a modulated transmitter in conjunction with a receiver tuned to radiation with the appropriate modulation. This approach discriminates against background illumination but does not make the receiver independent of it. It would still be possible to saturate the receiver with high background illumination, but it should be possible to extend the operations into high background illumination levels since the chopped system gives an improved signal-to-noise ratio.

The idea is to modulate the intensity of the transmitted beam at some frequency f_0 and to tune the receiver to be sensitive only to radiation with that modulation frequency.

In order to preserve the wing beat frequency information the source must be modulated at a frequency f_0 given by

$$f_0 = 10 (W b f)_{\max}$$

where $(W b f)_{\max}$ is the maximum wing beat frequency to be detected, which for the present work is 100 Hz. The required modulation frequency is therefore 1 kHz.

In the present system a tungsten filament forms the source. It is not possible to electrically modulate such a source at this frequency because of the thermal inertia of the filament. Mechanical modulation is possible but since the source is large, such things as chopper discs would be unpractical at this frequency. Electro-optical modulators such as the Kerr Cell or Pocket Cell are available but these are invariably expensive and not field compatible.

Xenon flashtubes are by their nature electrically modulated and they emit substantially in the 700 - 850 nm range (Figure E1). Normally the flash rate for a Xenon flash tube is limited to about 50 Hz by the recovery time of Xenon ions. However Xenon flash and short arc tubes can be operated in the 'simmer mode' to increase their modulation rate. In this mode the discharge is established by a high voltage spike and then maintained by a small d.c. current. The light output of the tube is modulated by applying high current pulses to the tube at the required frequency. This method has advantages besides just making high modulation rates possible. The pulse-pulse stability

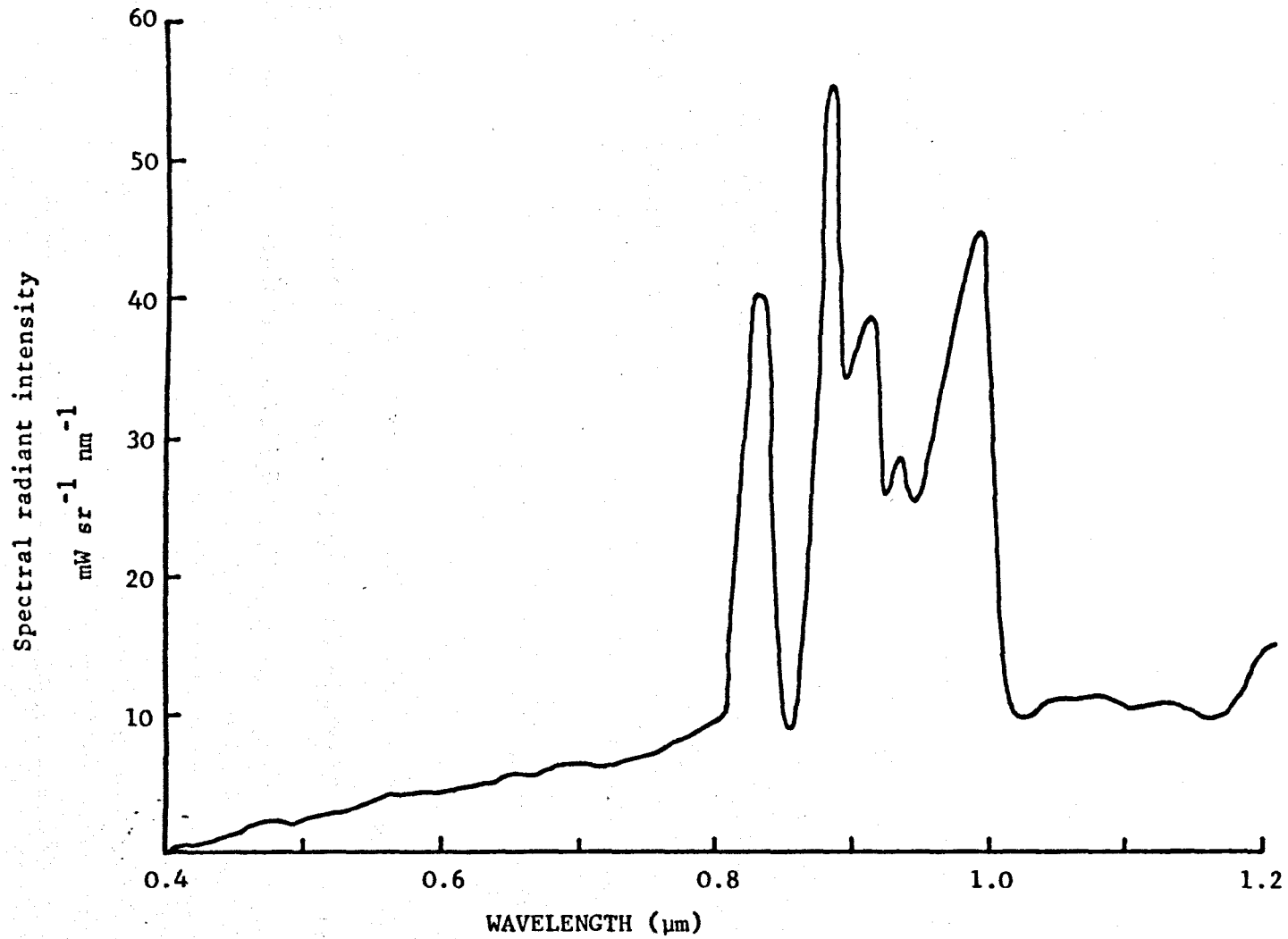


Figure E 1 Emission Spectra of 150w Xenon Short Arc
(from R.C.A. Optoelectronic Handbook, 1974)

of the light output is much improved and lamp life is increased.

Signal-noise considerations

Let average power input to lamp be P Watts

let pulse length be τ sec

let pulse repetition frequency be f

let efficiency of lamp in region 700 - 850 nm be η

then peak pulse power P_p is given by

$$P_p = \frac{P\eta}{\tau f} \quad (E1)$$

Energy per pulse

$$E_p = P_p \tau$$

$$E_p = \frac{P\eta}{f} \quad (E2)$$

No. of photons/pulse

$$N_p = \frac{E_p}{\epsilon} \quad \epsilon - \text{energy/photon}$$

$$N_p = \frac{P\eta\lambda}{fhc} \quad (E3)$$

No. of photons received from exempta sized target at 30 m range with 3° transmitter beamwidth is given by

$$N_{pR} = FN_p \quad \text{where } \gamma \text{ is range factor}$$

$$N_{pR} = \frac{F P \eta \lambda \gamma}{f h c} \quad (E4)$$

Calculate N_{PR} for

$$\underline{N_{PR} = 3.1 \times 10^7 \text{ per pulse}}$$

$$y = 10^{-12}$$

$$\eta = 0.1$$

$$P = 80 \text{ W}$$

$$\lambda = 775 \text{ nm}$$

$$f = 10^3 \text{ Hz}$$

$$h = 6.6 \times 10^{-34} \text{ Js}$$

$$c = 3 \times 10^8 \text{ ms}^{-1}$$

Photomultiplier dark current

Anode dark current $\sim 10 \text{ nA}$

Cathode dark current $\sim \frac{10^{-8}}{G} \text{ A}$ where G is tube gain

$$i_c \sim \frac{10^{-8}}{5 \times 10^5} \sim \underline{2 \times 10^{-14} \text{ A}}$$

This is equivalent to N_c photons/sec where

$$N_c = \frac{i_c \lambda}{R h c}$$

$$= \frac{2 \times 10^{-14} \cdot 775 \times 10^{-9}}{7 \times 10^{-3} \cdot 6.6 \times 10^{-34} \cdot 3 \times 10^8}$$

$$\underline{N_c = 1.18 \times 10^7 \text{ s}^{-1}}$$

The noise current generated by the dark current is given by

$$i_n = (2eBi_c)^{\frac{1}{2}}$$

B - bandwidth

e - electrical charge

$$i_n = (2 \times 1.6 \times 10^{-19} \cdot 300 \cdot 2 \times 10^{-14})^{\frac{1}{2}}$$

$$= (1.92 \times 10^{-30})^{\frac{1}{2}}$$

$$= \underline{1.4 \times 10^{-15} \text{ A.}}$$

This is equivalent to a photon flux of

$$N_{C_n} = \frac{1.4 \times 10^{-15}}{R \cdot 2 \times 10^{-19}}$$

$$\text{photon en} = 2 \times 10^{-19} \text{ J}$$

$$= \frac{1.4 \times 10^{-15}}{8 \times 10^{-3} \cdot 2 \times 10^{-19}}$$

$$\underline{N_{C_n} = 1.4 \times 10^6 \text{ sec}^{-1}}$$

Background illumination

From night sky, background flux is

$$H = 10^{-8} \text{ W m}^{-2} \text{ sr}^{-1} \text{ nm}^{-1}$$

if field of view of receiver is α° , aperture diameter d , then flux in waveband 700 - 850 nm is given by

$$P_B = H \frac{\pi d^2}{4} \frac{\pi (\alpha/56)^2}{4} \cdot 150 \cdot W$$

$$= \underline{8.1 \times 10^{-11} \text{ W}}$$

This is equivalent to N_B photons sec^{-1} where

$$N_B = \frac{P_B}{\epsilon}$$

$$= \frac{8.1 \times 10^{-11}}{2 \times 10^{-19}}$$

$$\underline{N_B = 4 \times 10^8 \text{ s}^{-1}}$$

The incident power generates a photo-current given by

$$i_b = \frac{P_B}{R}$$

$$= 8.1 \times 10^{-11} \cdot 7 \times 10^{-3}$$

$$\underline{i_b = 5.7 \times 10^{-13} \text{ A}}$$

the shot noise associated with this is given by

$$i_{b_n} = (2 e B i_b)^{\frac{1}{2}}$$

$$= (2 \cdot 1.6 \times 10^{-19} \cdot 300 \cdot 5.7 \times 10^{-13})^{\frac{1}{2}}$$

$$= \underline{7.4 \times 10^{-15} \text{ A}}$$

in terms of an incident photon rate this is

$$N_{b_n} = \frac{i_{b_n}}{R \epsilon}$$

$$N_{b_n} = \frac{7.4 \times 10^{-15}}{7 \times 10^{-3} \cdot 2 \times 10^{-19}}$$

$$\underline{N_{b_n} = 5.2 \times 10^6 \text{ s}^{-1}}$$

In summary

$$\text{Signal} = 3.1 \times 10^7 \text{ per pulse } (N_s)$$

$$\text{Dark current} + \text{B/ground} = 4.12 \times 10^8 \text{ per sec. } (N_c + N_B)$$

Signal/noise ratio for phase sensitive detector

P.S.D. has bandwidth of 300 Hz.

i.e. the time constant is 3.3 mS

which means that the p.s.d. averages over 3 signal pulses.

The signal n_s is then

$$n_s = 3 \times 3.1 \times 10^7 \text{ photons}$$

The total dark current + background flux in the averaging period is given by n_x

$$n_x = 4.12 \times 10^8 \cdot 3.3 \times 10^{-3}$$

$$\text{therefore total noise} = n_s + n_x$$

$$\begin{aligned} \text{Signal noise ratio} &= \frac{n_s}{n_s + n_x} \\ &= \frac{9.3 \times 10^7}{9.3 \times 10^7 + 1.35 \times 10^6} \\ &= \frac{9.3 \times 10^7}{9.43 \times 10^7} \\ &= \frac{9.3 \times 10^7}{9.7 \times 10^7} \\ &= \underline{9.5 \times 10^3} \end{aligned}$$

Which means that observations can be continued during higher levels of background illumination than previously possible.

Simmer mode operation - design considerations

A block diagram of a simmer supply circuit is shown in Figure E2. The lamp is ignited by a high voltage pulse from the trigger pulse generator. The diode train prevents this from being dissipated in the energy storage capacitor. Once ignited a low voltage d.c. discharge is kept alive in the tube by a continuous low current from the simmer power supply. This power supply should include an inductive output impedance so that it is protected from fast rising pulses applied to the lamp. The d.c. power supply charges the energy storage capacitor through a resistor R.

The lamp pulsing is controlled by the power pulse initiator which triggers the SCR to conduct, thereby delivering a large current pulse to the lamp. The diode train limits the current pulse to half a sine wave and prevents oscillation.

Consider a PSA 80 short arc tube (from Messrs. ILC). This is capable of 80 W average power output. Operating at 50 W this gives for a p.r.f. of 1 kHz and pulse length of 250 μ s a peak pulse power of 200 W. The energy per pulse is 50 mJ.

Energy stored in capacitor

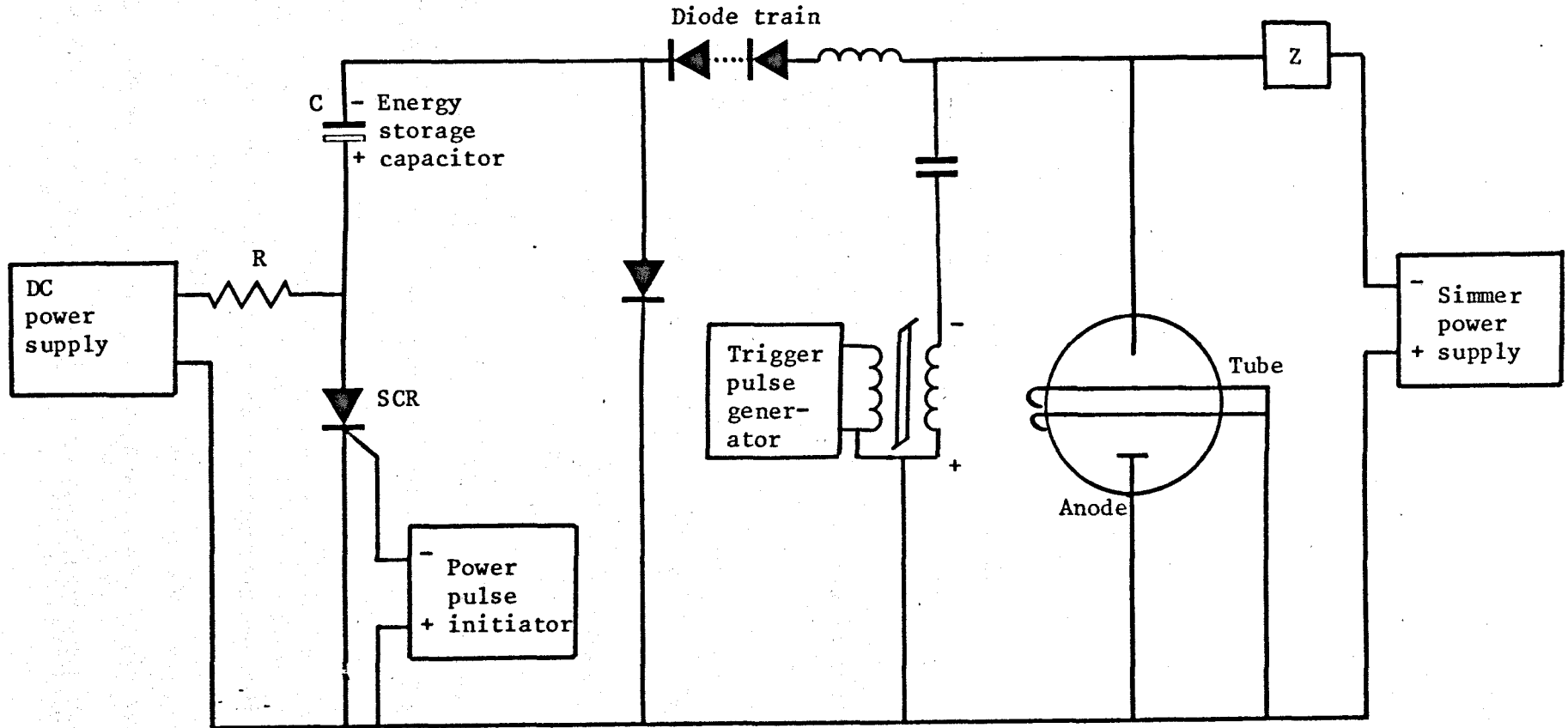
$$= \frac{1}{2}CV^2 \text{ J.} \quad \begin{array}{l} C - \text{farads} \\ V - \text{volts} \end{array}$$

$$\text{Put } C = 10^{-5} \text{ F}$$

$$\frac{1}{2} 10^{-5} V^2 = 5 \cdot 10^{-2}$$

$$\underline{V = 100 \text{ volts}}$$

FIGURE E2
BLOCK DIAGRAM OF SIMMER POWER SUPPLY



This is acceptable. The recommended voltage for the tube is 150 volts but it can be lower for simmer operation. Therefore the d.c. power supply and simmer power supplies must both supply 100 volts.

Charging time for the 10 μ F capacitor in series with resistor R is approx $T = 5 \times RC$ sec

Now $T = 7.5 \times 10^{-4}$ s for complete charging between pulses

$$\text{then } R = \frac{7.5 \times 10^{-4}}{5 \times 10^{-5}}$$

$$\underline{R = 15 \Omega}$$

The peak charging current will be $\frac{100}{15.0} = 6.6$ amps.

The average current output of the power supply will be \bar{I} where

$$\begin{aligned} \bar{I} &= fq & q - \text{charge on capacitor } C \\ &= fCV \\ &= 10^3 \cdot 10^{-5} \cdot 10^2 \end{aligned}$$

$$\underline{\bar{I} = 1.0 \text{ A}}$$

The average power output of the power supply \bar{P} will be

$$\bar{P} = 100 \cdot 1.0 \text{ W}$$

$$\underline{\bar{P} = 100 \text{ W}}$$

Design points

The power supplies need not be very accurately smoothed since in one case it is only charging a capacitor and in the other it is providing a low power discharge. They could for example consist of a mains transformer providing 115 V a.c. with a full wave rectifier

capable of supplying in one case up to 7 amps.

Charging power supply

E.g.	1000 VA auto transformer	£32.00
	Bridge rectifier 6.6 A av current	£ 3.00
	Smoothing capacitor 100 μ F	£ 1.00

Thus typical cost of this power supply will be about £50.00

Simmer power supply

	100 VA auto transformer	£ 8.00
	Bridge rectifier	£ 1.00
	Smoothing capacitor 100 μ F	£1.00

say £15.00 for this power supply.

Trigger Pulse generator

Since this is used only to initiate the discharge, it does not need to have a high specification. A high performance car ignition coil would be suitable, manually switched. Typical cost £40.00.

S.C.R. and power pulse initiator

The power pulse initiator is basically an oscillator at 1 kHz which controls the S.C.R. gate. It needs to supply approximately 3.0 v at 50 mA to switch suitable S.C.R.'s.

Typical cost of oscillator	£10.00
Typical cost of S.C.R.	£ 1.00

Diode train and inductors

These are basically inexpensive

Typical cost of power silicon diode	£ 1.00
-------------------------------------	--------

inductors can be made or bought

Short arc tube

ILC PSA 80 short arc tube

£100.00

Total cost of flash lamp and driving circuit (not including reflectors) is estimated at £250.00

The receivers would also have to be modified with phase sensitive detectors to process the chopped signals. The capital cost of purpose built units is not high ~ £20 - 30 per channel.

REFERENCES

- Baron S. (1972) The Desert Locust, Publ. Eyre Methuen, London, (1972).
- Brown E.S., Betts E, and Rainey R.C. (1969) Seasonal changes in the distribution of the African Armyworm (s. exempta) with special reference to E. Africa Bull. entomol. Res 58 661-728, 1969.
- Buyal'skii V.V., Koschavtsev N.F. and Pavlov V.A. (1977) Photometer for measuring the natural night illumination in the 0.4 - 1.2 m Technol 44 pp. 404-406, 1977.
- Callahan P.S. (1964) An inexpensive actinometer for continuous field recording of moonlight, daylight or low intensity evening light. J. Econ. Ent. 57 pp 758-760, 1964.
- Casey T.M. (1980) Flight energetics and heat exchange of Gypsy Moths in relation to air temperature. J. exp. biol. 88 133-145, 1980.
- Couter (1979) Unpublished COPR report on visit to Kenya to measure wing beat frequencies of s. exempta and moths of similar size, April 1979.
- Cramer H.H. (1967) Plant protection and world crop protection Farbenfabriken Bayer AG, Leverkusen, West Germany, 1967.
- Crawford A.B. (1949) Radar reflections in the lower atmosphere Proc. IRE 37 pp 404-405, 1949.
- Eastwood E. (1967) Radar Ornithology, Methuen, London 1967.
- Elterman L. (1966) Aerosol measurements in the troposphere and stratosphere. Appl. Opt. 5 1769-1776.
- Engstrom R.W. (1947) Multiplier photo-tube characteristics. Application to low light levels. J. Opt. Soc. Am. 37 420.
- Enochson L.D. and Otnes R.K. (1968) Programming and analysis for digital time series data. Publ. Shock and Vibration Centre Information Centre, United States Department of Defence, 1968.

- EMI (1979) EMI Photomultiplier tube manual.
EMI Series POOL/E79.
- Farmery M.J. and Sills E.C. (1976) Field studies of Aphid flight activity in the Sudan Gezira. E.P.R.G. report, Cranfield Institute of Technology, U.K. Jan. 1976.
- Fiocco G. and Smullin L.D. (1963) Detection of scattering layers in the upper atmosphere by optical radar. Nature (London) 199 1275-1276.
- Forsythe W.E. and Adams E.Q. (1945) Radiating characteristics of Tungsten and Tungsten Lamps. J. Opt. Soc. Amer. Vol. 35, 1108-113.
- Friedland S.S., Katzenstein J. and Zatzick (1956) Pulsed searchlighting of the atmosphere. J. Geophys. Res., 61 415-434.
- Gauthreaux S.A. (1969) A portable ceilometer technique for studying low level nocturnal migration. Bird Banding 40 309-320.
- Greenbank D.O., Schaefer G.W. and Rainey R.C. (1980) Spruce Budworm, moth flight and dispersal: New understanding from canopy observations, radar and aircraft. Mem. Ent. Soc. Can., 110 1-49.
- Greenwalt C.H. (1962) Dimensional relationships for flying animals. Smithsonian Misc. Collection 144 2 Apr. 1962.
- Headley J.C. (1972) Economics of agricultural pest control. A. Rev. Ent. 17 273-286.
- Hulbert E.O. (1937) Observations of a searchlight beam to an altitude of 28 km. J. Opt. Soc. Am. 27 377-382.
- Johnson C.A. (1960) A basis for a general system of insect migration by flight. Nature (London) 186 348-350.
- (1963) Physiological factors in insect migration by flight. Nature (London) 198 423-427.
- (1966) A functional system of adaptive dispersal by flight. A. Rev. Ent. 11 233-260.
- (1969) Migration and dispersal of insects by flight. Methuen, London, 1969.

- Joyce R.J.V. (1976) Insect flight in relation to problems of pest control. In R.C. Rainey (ed), Insect Flight Symposium. R. Ent. Soc. (Lond.) 135-155.
- Kulkarni P.V. (1970) A direct calibrating type night airglow photometer. Annales de Geophys 25 747-751.
- Lack D and Varley G.C. (1945) Detection of birds by radar. Nature (London) 156 446.
- Langar H., Hamann B. and Meinecke C.C. (1979) Tetrachromic visual system in the moth s. exempta. J. Comp. Physiol. 129 235-239.
- Lawrence J.D., Crownfield F.R. and McCormick M.P. (1967) Optical measurements of the atmosphere. NASA contract report NASA CR-729.
- Malthus T.R. (1798) Principle of Population. In Population, the first Essay. University of Michigan Press 1959.
- Miller C.A. (1971) The Spruce Budworm in Eastern North America. Proc. Tall Timbers Conf. on Ecological Animal Control by Habitat Management: 169-177.
- Morris R.F. (1963) The dynamics of epidemic Spruce Budworm populations. Mem. Ent. Soc. Can., No. 31: 332 pp.
- Morton G.A. and Mitchell J.A. (1949) Nucleonics 4 1 1949.
- Muzumdar S., Bhaskara Rao N.S. and Gupta G.R. (1965) Radar and synoptic study of locust swarms over Delhi. W.M.O. Tech. Note 69 162-188.
- N.A.S. (1975) Population and food, Committee on World Food, health and population. National Academy of Sciences Washington D.C. 1975.
- Ovchinnikov V.M., Gorlacker G.A. and Man'ko A.E. (1974) Automatic Control of photomultiplier gain using an optron. Sov. J. Opt. Technol. 41 236-237.
- Pimentel D and Pimentel M (1978) Dimensions of the world food problem and losses to pests. In World Food, Pest Losses and the Environment Ed. D. Pimentel. A.A.A.S. Selected Symp. No. 13 1978.

- Rainey R.C. (1955) Observation of desert locust swarms by radar. Nature (London) 175 77.
- Ramana Murty B.H.V., Roy A.K., Biswass K.R. and Khemani L.T. (1964) Observations of flying locusts by radar. J. Sci. Ind. Res. New Delhi 23 289-296.
- Richards I.R. (1955) Photoelectric cell measurements of insects in flight. Nature (London) 175 128.
- Riley J.R. (1974) Radar observations of individual desert locusts. Bull. Ent. Res. 64 19-32.
- (1975) Collective orientation in night flying insects. Nature (London) 253 113-114.
- (1979a) Quantitative analysis of radar returns from insects. In C.R. Vaughn, W. Wolf and W. Klassen (eds.) Proc. Workshop on Radar, Insect population and Pest Management held 2-4 May 1978 Wallops Flight Centre, Wallops Island, Virginia.
- (1979b) Radar as an aid to the study of insect flight. Handbook on Biotelemetry and Radio tracking. Pergamon Press, Oxford 1979.
- Riley J.R. and Reynolds D. (1979) Radar based studies of the migratory flight of grasshoppers in the middle Niger area of Mali, West Africa. Proc. R. Soc. B 204 67-82.
- Roach F.E. (1963) The Nightglow. Adv. Elec. Electr. Phys. 18 1-44
- Roffey J. (1963) Observations on night flight in the Desert Locust. Anti Locust Bull. 39 1-32 ALRC London.
- (1969) Radar studies of the Desert Locust, Niger, Sept. - Oct. 1968. ALRC Occasional Report No. 17.
- (1972) Radar studies of insects. PANS 18 303-309.
- Rose D.J.W. (1979a) Warning system for Armyworm in East Africa: Physical and biological considerations. Proc. IX Int. Cong. on Plant Protection, Washington.

- Ross D.J.W. (1979b) The significance of low density populations of the African Armyworm (s. exempta). Phil. trans. R. Soc. B287 393-402.
- Rose D.J.W. and Dewhurst C.H. (1979) The African Armyworm (s. exempta) Congregation of moths in trees before flight. Ent. exp. and appl. 26 346-348.
- Ross M. (1966) Laser Receivers. John Wiley, N.Y. 1966.
- Sawedal I and Hall R. (1979) Flight tone as a taxonomic character in Chironomidae. Entomol. Scand. Supp. 10 139-144.
- Schaefer G.W. (1969) Radar studies of locust, moth and butterfly migration in the Sahara. Proc. R. Ent. Soc. (Lond.) 34 39-40.
- (1971) Preliminary report on radar field expedition March 4-16 1971. CSIRO Division of Entomology, Canberra, Australia.
- (1976) Radar observations of insect flight. In R.C. Rainey (ed.), Insect Flight Symp. R. Ent. Soc. (London) 157-197.
- Shockly and Pierce J.R. (1938) Proc. I.R.E. 26 321.
- Smith R.F. and Calvert D.J. (1978) In D. Pimentel (ed.) World Food, Pest Losses and the Environment. A.A.A.S. Select Symp. No. 13 1978 .
- Taylor L.R. (1958) Aphid dispersal and diurnal periodicity. Proc. Linn.Soc. Cand. 169 67-73.
- Treanor P.J. and Salpeter E. (1972) A portable night sky Photometer. Observatory 92 96-99.
- U.S.D.A. (1965) Losses in agriculture. Handbook No. 291, United States Department of Agriculture Agricultural Research Service, Washington, D.C. 1965.
- Young (1972) Photomultiplier tubes and their application. EMI tube division publ. ref: R/P055T 72.